

THE UNIVERSITY OF CHICAGO

SUBDUCTION AND UPLIFT OF CONTINENTAL CRUST IN THE INDIA-ASIA
COLLISION ZONE: CLUMPED-ISOTOPE PALEOTHERMOMETRY AND
PALEOALTIMETRY OF THE LHASA BLOCK, SOUTHERN TIBET

A DISSERTATION SUBMITTED TO
THE FACULTY OF THE DIVISION OF THE PHYSICAL SCIENCES
IN CANDIDACY FOR THE DEGREE OF
DOCTOR OF PHILOSOPHY

DEPARTMENT OF THE GEOPHYSICAL SCIENCES

BY

MIQUELA INGALLS

CHICAGO, ILLINOIS

JUNE 2017

Copyright © 2017 by Miquela Ingalls

All Rights Reserved

For my Aunt Deb,

who whispered “PhD, PhD, PhD”

to an infant in 1989.

Here’s our dissertation.

TABLE OF CONTENTS

LIST OF FIGURES	viii
LIST OF TABLES	x
ACKNOWLEDGMENTS	xi
ABSTRACT	xiii
1 INTRODUCTION	1
1.1 Overview	1
1.2 Paleoelevation & Paleothermometry	2
1.3 Continental Mass Balance	10
1.4 Carbonate Diagenesis and the Proxy Record	11
2 PALEOCENE TO PLIOCENE HIGH ELEVATION OF SOUTHERN TIBET: IMPLICATIONS FOR TECTONIC MODELS OF INDIA-ASIA COLLISION, CENOZOIC CLIMATE, AND GEOCHEMICAL WEATHERING	14
2.1 Abstract	14
2.2 Introduction	15
2.2.1 A case for multiple proxies in reconstructions of ancient topography and environments	17
2.2.2 Geologic Setting	19
2.3 Methods	26
2.3.1 Sample Preparation	26
2.3.2 Standard stable isotope measurements	27
2.3.3 Clumped isotope (Δ_{47}) analyses	28
2.3.4 $^{40}\text{Ar}/^{39}\text{Ar}$ geochronology	31
2.3.5 Apatite (U-Th)/He thermochronometry	31
2.4 Discussion of results	33
2.4.1 Geochronology and thermochronometry	33
2.4.2 $\delta^{13}\text{C}$, $\delta^{18}\text{O}$ and clumped isotope-derived temperatures	33
2.4.3 Paleocene to Pliocene stable isotope paleoelevation of the Lhasa Terrane	41
2.5 High elevation southern margin of Eurasia	48
2.5.1 Prior work on pre-collisional topography	50
2.5.2 Past models of the regional tectonic history of the Lhasa Block	52
2.6 The impact of evaporative enrichment of surface waters on paleo-elevation estimates	54
2.7 Cenozoic climate	56
2.7.1 Tectonic-weathering-climate feedbacks	57
2.8 Conclusions	61

3	NORTH, SOUTH, EAST AND WEST: CLUMPED ISOTOPE PALEOTHERMOMETRY AND STABLE ISOTOPE PALEOALTIMETRY OF THE LHASA BLOCK	63
3.1	Abstract	63
3.2	Introduction	64
3.2.1	Geologic Setting	66
3.3	Methods	71
3.4	Results	72
3.4.1	Oxygen and carbon isotopes	72
3.4.2	Clumped isotope thermometry	73
3.4.3	Elevations	75
3.5	Discussion	76
3.5.1	$\delta^{18}\text{O}$ versus δD : Multi-proxy approach to reconstructing ancient rain-water in arid climates	76
3.5.2	Near-modern elevations (>4 km) across the Lhasa terrane in the mid-Eocene	79
3.6	Conclusions	87
4	BALANCING CRUSTAL MASS VIA SUBDUCTION DURING CONTINENTAL COLLISIONS	88
4.1	Abstract	88
4.2	Introduction	88
4.2.1	Mass balance in an active collision zone	89
4.3	Paleogeography of the India-Asia Collision	92
4.3.1	Age of initiation of the India-Asia continent-continent collision	92
4.3.2	Geometry of Greater India constrained by Gondwanan reconstructions	94
4.4	Bootstrap estimate of areal, volume and mass convergence since onset of collision	94
4.4.1	Assignment of crustal thickness	97
4.4.2	Contributions of the components of the mass balance equation	99
4.5	Discussion and Conclusions	101
4.5.1	Half of pre-collisional continental crust absent from the surface of the Earth	101
4.5.2	Subduction of continental crust	101
4.5.3	Crustal mass loss	103
4.5.4	Comparison of our mass balance calculations with those of Yakovlev and Clark	104
5	CRYPTIC CARBONATE DIAGENESIS AND Δ_{47} THERMOMETRY: INFORMING COMPLEX THERMAL HISTORIES WITH A VARIABLY ALTERED PROXY RECORD	107
5.1	Introduction	107
5.2	Geologic Setting	111
5.2.1	Xigaze forearc basin	111
5.2.2	Tso Jiangding Group	113
5.3	Methods	113
5.3.1	Sample collection	113

5.3.2	Micro-sampling	114
5.3.3	Stable isotope and clumped-isotope measurements	114
5.3.4	Traditional screening tools for carbonate diagenesis	114
5.4	The motivating samples	119
5.4.1	Thermal history of the Jialazi Fm precludes a potential sea level precipitation proxy (δD_p) for syn-collisional Tibetan paleoaltimetry	119
5.4.2	Field and hand sample observations as related to water:rock ratios	120
5.4.3	Cathodoluminescence	122
5.4.4	Isotopic results	123
5.5	Isotopic theory	127
5.5.1	Water-rock isotopic exchange during carbonate recrystallization	127
5.5.2	Solid-state internal isotopic exchange	127
5.6	Using carbonate clumped isotope thermometry and solid-state reordering kinetics to constrain sedimentary basin thermal histories: Results & discussion	131
5.6.1	Water-rock reactions: Calculations of early- and late-stage oxygen isotopic exchange between H_2O and CO_3^{2-} during burial diagenesis	134
5.6.2	Solid state reordering modeling	148
5.7	Refining diagenetic pathways to constrain diagenetic history	153
5.8	Summary: Seemingly contradictory isotopic, thermal, and textural data require a cryptic alteration mechanism	154
5.8.1	Next steps: Micro-analytical techniques for identifying cryptic carbonate alteration	155
5.9	Conclusions	159
6	CONCLUSIONS	160
6.1	Major results and conclusions	160
6.2	Broad implications of this work	162
	APPENDIX A ANALYTICAL DETAILS	164
A.1	Tests on Δ_{47} clean up	164
A.2	Corrections and Quality Control Checks on the MAT253	168
A.3	Equilibrated gases and calcite standards	174
	APPENDIX B PALEOALTIMETRY MODEL PARAMETERS	181
	APPENDIX C PALEO GEOGRAPHY AND CRUSTAL GEOMETRY OF THE INDIAN AND EURASIAN CONTINENTAL CRUST	183
C.1	Age of Initiation of the Continent-Continent Collision in the India Asia System	183
C.2	Greater Indian Basin	184
C.3	Greater India constrained by Gondwanan reconstructions	186
C.4	Bootstrap estimate of uncertainties of areal convergence since onset of collision	187
C.5	Collisional crustal volume	187
C.6	Erosional mass flux	188
C.7	Tables related to plate rotations	189

APPENDIX D ADDITIONAL TABLES	199
REFERENCES	213

LIST OF FIGURES

1.1	Map of India-Asia convergence zone.	3
1.2	Schematic diagram of Rayleigh distillation, carbonate precipitation, and stable isotope paleoaltimetry theory.	6
2.1	Maps of the sampled regions	18
2.2	Stratigraphic section of the Nianbo Formation in the Penbo Basin	20
2.3	Stratigraphic section of the Nianbo Formation in the Oiyug Basin.	22
2.4	Inverse isochron plot of potassium feldspar Ar/Ar age.	24
2.5	Clumped isotope-derived paleotemperatures of samples from the Penbo Basin with relative age.	35
2.6	Clumped isotope-derived paleotemperatures of samples from the Oiyug Basin with relative age.	36
2.7	Paleocene-Eocene elevation reconstruction of the Penbo basin.	45
2.8	Cenozoic elevation reconstruction of the Oiyug basin, southern Tibet.	47
2.9	Effects of evaporation on siderites (dark red square), calcites (dark red circles) and leaf wax (blue-green diamonds) from the same sedimentary horizon.	54
2.10	The Cenozoic marine Sr isotope record in relation to source flux compositions.	60
3.1	Map of paleoaltimetry studies and sampling localities.	65
3.2	Stratigraphy and sample localities for the Lunpola basin.	68
3.3	Modern Amu Xun basin topography and sampling locality.	69
3.4	Measured and sampled stratigraphy in the Amu Xun, Tibet.	70
3.5	Carbonate oxygen and carbon stable isotope data from the Amu Xun and Lunpola basins.	73
3.6	Carbonate oxygen and Δ_{47} data from the Amu Xun and Lunpola basins.	74
3.7	Elevation reconstruction of the Lunpola basin and Nianbo Formation in the Amu Xun, Penbo, and Oiyug basins.	77
3.8	Leaf wax-derived δD_w versus carbonate-derived $\delta^{18}O_w$ for Lunpola samples relative to the GMWL.	78
3.9	Cenozoic elevation reconstruction of northern and southern regions of the Lhasa block (LB) and the eastern Tibetan Plateau (TP).	81
4.1	Paleogeographic and paleothickness reconstructions of the Himalaya-Tibet orogen.	91
4.2	Continental thickness and mass convergence.	97
4.3	Schematic tectonic cross-section of India, the Himalayan orogenic prism, and southern Tibet during lower crustal subduction.	102
5.1	Two modes of isotopic alteration during carbonate diagenesis.	108
5.2	Petrographic screening of fossiliferous limestones of the Tso Jiangding Group.	110
5.3	Map of Xigaze Forearc strata in study area adapted from Orme et al. (2014).	111
5.4	Cross sectional cut of Tethyan marine carbonate sample T0702-18.	115
5.5	Scanning electron microscopy (SEM) images of Tethyan marine carbonates.	117
5.6	Paired plane polar light (PPL) and cathodoluminescent (CL) petrographic images.	121

5.7	Stable isotope values of Jialazi Formation marine carbonates compared to expected values.	124
5.8	Within-sample Δ_{47} and stable isotopic variability.	126
5.9	Time-temperature schematic diagram of bond ordering behavior during burial and exhumation.	129
5.10	Schematic diagrams of potential diagenetic and isotopic alteration pathways. . .	133
5.11	Water-rock oxygen isotope exchange at shallow and deep burial conditions. . . .	139
5.12	Water-rock oxygen isotope exchange of marine carbonate at varying burial depths and temperatures.	141
5.13	Equilibrium oxygen isotopic composition of water and carbonate at varying values of N.	145
5.14	Effect of maximum burial temperature and integrated time above “threshold” temperature on apparent “lock-in” $T(\Delta_{47})$	150
5.15	One thermal history yields three unique apparent equilibrium $T(\Delta_{47})$ based on material-specific Arrhenius parameters.	152
A.1	Empirical transfer functions for each analytical period.	180
D.1	Petrography of Penbo basin carbonates.	200
D.2	Petrography of Oiyug basin carbonates.	201

LIST OF TABLES

4.1	Local convergence length of continental crust along the Indus Yarlung Suture since the onset of India-Asia collision.	96
A.1	All clumped isotope measurements run on standard materials during the analytical period in which Oiyug and Penbo basin measurements were made.	165
A.2	Once- and twice-cleaned sample analyses.	169
A.3	Sample gases re-equilibrated at 26, 60, and 1000°C.	171
A.4	Equilibrated gases.	175
C.1	Pairwise plate rotations.	190
C.2	Rotations of India with respect to Eurasia.	195
C.3	India-Eurasia convergence and rotation data.	197
D.1	Stable isotope data for all carbonates and calculated paleo-elevations of the Penbo Basin.	202
D.2	Stable isotope data for all carbonates and calculated paleo-elevations of the Oiyug Basin.	205
D.3	Stable isotope data for the subset of samples with Δ_{47} measurements from Oiyug and Penbo localities.	206
D.4	Carbon, oxygen, and hydrogen stable isotope values, and calculated paleo-elevations of the Lunpola basin.	207
D.5	Carbon and oxygen stable isotope values, and calculated paleo-elevations, from Nianbo Formation in the Amu Xun.	208
D.6	Single crystal zircon (U-Th)/He cooling ages for igneous samples from the Oiyug and Penbo basins.	209
D.7	$^{40}\text{Ar}/^{39}\text{Ar}$ inverse isochron age for the base of the Rigongla Formation, Oiyug basin.	210
D.8	Lithologies, sample locations, and carbon and oxygen stable isotope data for the Tso Jiangding.	211
D.9	All Δ_{47} measurements of the Tso Jiangding samples.	212

ACKNOWLEDGMENTS

First, I owe a great deal to my adviser, David Rowley, for providing me the freedom to wander with my waxing and waning curiosities to come to this body of work. Your passion for whatever you are working on is infectious and inspiring. The endless nature of your knowledge never ceases to amaze, and I hope I absorbed a fraction of it. I would also like to thank my external committee member and friend, Brian Currie, for recognizing the importance of getting your boots on the outcrop, and providing a field refuge away from Chicago. Thanks for showing me my first paleosol, hours of conversation at MUGFS and elsewhere, and introducing me to great people. Your overwhelming belief in me is truly appreciated.

I owe several members of the Colman lab gratitude. I would like to thank Albert for pushing me to be a careful and thorough scientist, and for compassionate support throughout my time at Chicago. Gerry, there would be no geochemistry in this dissertation without you. Thank you for keeping all of the moving parts turning, for being a creative problem solver, and for the laughs. Bo and Aric, thanks for being superb role models and training me on various techniques. And Sora, thank you for being my sounding board, both as a mentor and a dear friend.

There are many additional folks at UChicago who have helped me along the way and deserve thanks. Thank you to the GeoSci support staff, David Taylor, Katie Casey, Brian Lynch, and Jess Valle, for smooth workings behind the scene. Thank you to committee members Frank Richter and Nicolas Dauphas for important critical feedback and asking the right questions. Perhaps most crucial to this process was the support of my friends in the department: Lily, Andrew, Bethany, and Caitlin, to name a few. Thanks for helping me laugh at difficult situations, closed door conversations, and many beers. I owe a great deal of thanks to my dear friends Martha and Allie for being my constants, and an endless source of support and happiness. And of course, Stewart, for being my cheer captain, partner in life, and humoring me in making our home a menagerie of wild beasts.

I thank Roy Plotnick and Kathleen Ritterbush for assistance with petrographic analyses at the University of Illinois-Chicago, and Shanying Li at Miami University. I owe thanks to numerous collaborators for conversations about this work and various scientific contributions: Pratigya Polissar, Devon Orme, Marissa Tremblay, Jenn Schmidt, and David Mayer, to name a few. I would like to thank Xu Qiang for negotiating field logistics for my two seasons in Tibet. Finally, I owe a HUGE thank you to my field assistant, Madison Ball, for being a trooper at 18000ft, doing some serious geology on no sleep, and providing much-needed dance parties on the outcrop. Shake it off.

The majority of the field work and analyses within this dissertation have been supported by National Science Foundation EAR 0609756 awarded to Brian Currie and 1111274 to David Rowley, as well as Sigma Xi Grant-in-Aid of Research G2016100187643997 and two Geological Society of America Graduate Student Research Grants to Miquela Ingalls. Geochemical analyses were enabled by NSF EAR 0923831 awarded to Albert Colman and David Rowley.

ABSTRACT

The Tibetan Plateau is the greatest concentration of continental crust on Earth, and intimately linked to the quintessential example of continent-continent collision: India and Eurasia. The overarching goal of this thesis is to investigate the distribution of exceptionally thick continental crust and high altitude surfaces from the latest Cretaceous—just prior to onset of collision—to modern day in order to better understand how Earth accommodates continental crustal mass during continental collisions. This goal is achieved by employing stable isotope paleoaltimetry methodology to four Cenozoic sedimentary basins: three just north of the Indus Yarlung Suture within the Linzizhong arc, and one near the boundary of the Lhasa and Qiangtang tectonic blocks. Carbonate ‘clumped’-isotope paleothermometry substantially improves traditional stable isotope paleoaltimetry techniques by providing critical constraints on carbonate formation temperature, and thus, the isotopic composition of ancient meteoric water. The paleo-elevation reconstructions presented in this work reflect the existence of an Andean-type high elevation Linzizhong arc just prior to the onset of collision, and the maintenance of a high altitude land surface throughout the Cenozoic. The northern margin of the Lhasa block has been high since at least the Oligocene, but quite likely much earlier. These paleo-elevation reconstructions together require revision of past tectonic models arguing for a Miocene to Pliocene rapid uplift of the southern Tibetan Plateau, and the paleoclimate and tectonic implications these long-standing models invoke.

Mass balance of the continental crust within the India-Asia domain has been debated for more than thirty years. In this work, I revisit mass balance calculations using our new knowledge of a thick Linzizhong arc prior to onset of collision, and the most up-to-date constraints on paleogeography, plate kinematics, and the age of collision onset. The mass balance calculations yield a $\sim 50\%$ loss of continental crust from within the collisional domain boundaries at the Earth’s surface. We suggest that subduction of continental crust into the mantle beneath Eurasia has been equally important as crustal thickening in accommodating continental mass during India-Asia collision.

Paleoclimatology and paleoaltimetry employ the carbonate oxygen stable isotope record to reconstruct the composition of ancient meteoric water. As such, these techniques require the retention of primary isotopic compositions within authigenic minerals through variably complex thermal histories. The objective of the last section of this work is to identify the effects of shallow-to-deep burial and exhumation—thermal conditions common to areas of geologic interest and exposed strata—on carbonate $\delta^{18}\text{O}$ and Δ_{47} compositions. I use isotopic, geochemical, and optical techniques to identify cryptic recrystallization within marine carbonate that has been pervasively altered in oxygen isotope space but appear otherwise texturally pristine. I propose future work to strengthen our understanding of the effects of cryptic carbonate alteration on marine and terrestrial carbonates and to increase our ability to recognize the textural, chemical, and isotopic fingerprints of cryptic alteration. Our ability to screen for such cryptic alteration is critical for the future use of the carbonate proxy record in geological applications. However, the possibility remains that we may not be able to place sufficient constraints on the thermal and alteration histories of terrestrial carbonates to robustly use their stable isotopic values for paleoclimatology and tectonics.

CHAPTER 1

INTRODUCTION

1.1 Overview

The Tibetan Plateau is the largest concentration of continental crust on Earth. For more than three decades, the Tibetan orogeny has been the focus of natural experiments in tectonics (Ding and Lai, 2003; Currie et al., 2005; Rowley and Currie, 2006; DeCelles et al., 2007, 2011, 2014, 2016; Leary et al., 2016; Huntington et al., 2015; Ingalls et al., 2016b), marine and terrestrial geochemistry (Richter et al., 1992), petrology (Mo et al., 2008; Ding et al., 2005; Lee et al., 2007; Bouilhol et al., 2013), geodynamics (Dupont-Nivet et al., 2010; Nabelek et al., 2009; Molnar and Stock, 2009; Kornfeld et al., 2014), geomorphology (Tremblay et al., 2015; Schmidt et al., 2015; Carrapa et al., 2014; Robinson et al., 2014), and paleoclimate (Licht et al., 2014; Kutzbach et al., 1989; DeCelles et al., 2007). The majority of Tibetan geology research requires or is improved by knowledge of Tibet's pre- to syn-collisional uplift history.

The overarching objective of this work is to provide the most complete record to date of Tibetan continental thickness and elevation through time and space. I focus elevation reconstruction efforts on the Lhasa Block, which was the leading edge of the Eurasian continent during the convergence of India and Asia. Paleoelevations are derived from carbonate-bearing strata recording syn-collisional deposition throughout the Cenozoic.

Additional objectives of this thesis are to:

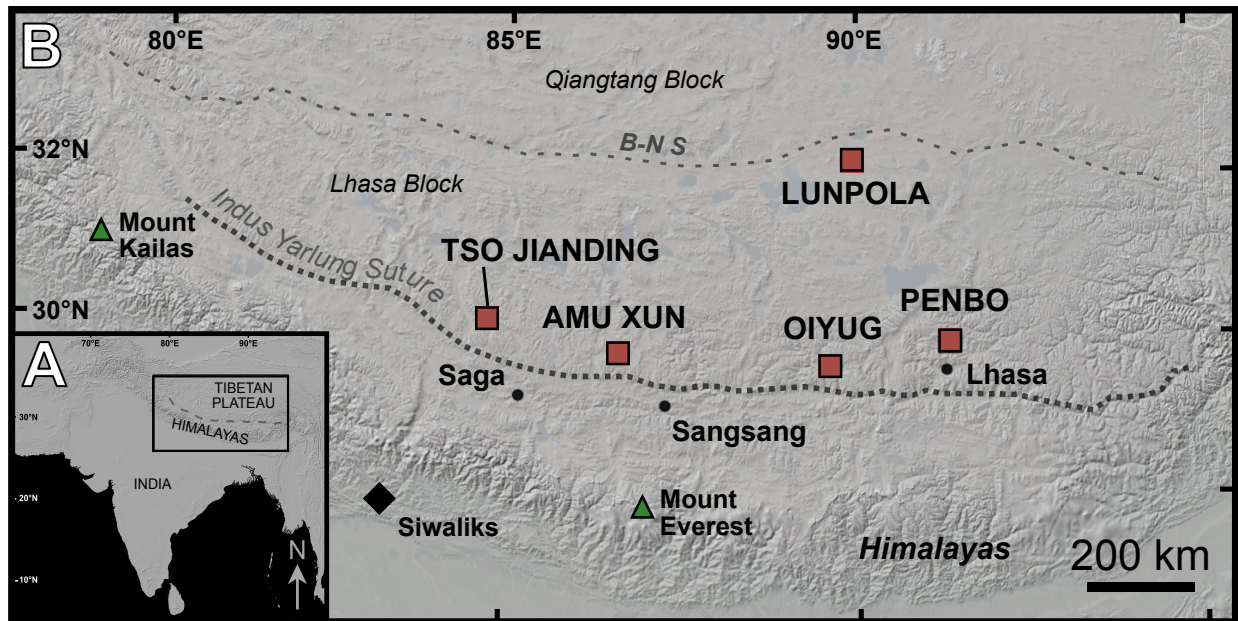
- Balance the pre- and syn-collisional mass of continental crust in the India-Asia convergence zone, and determine the extent of continental recycling during continent-continent collision;
- Consider and revise past tectonic models of Tibetan uplift, and their ties to global climate;

- Identify the effects of shallow-to-deep carbonate burial on Δ_{47} , $\delta^{18}\text{O}$, and $\delta^{13}\text{C}$ values, and reconstruct potential diagenetic pathways and thermal histories using isotopic and geochemical evidence; and
- Propose future work to strengthen our understanding the geochemical, textural, and isotopic effects of cryptic carbonate diagenesis, and increase our ability to recognize the diagenetic fingerprint of cryptic alteration.

1.2 Paleoaltimetry & Paleothermometry

The Indian and Eurasian continents made first contact roughly 60 million years ago (DeCelles et al., 2014), marking the onset of Earth’s archetypical continent-continent collision. Workers have approached paleo-elevation hypotheses with numerous geophysical, paleobotanical, stratigraphic, structural, and isotopic techniques. Each of these approaches require their own caveats and assumptions. Where possible, it is favorable to cross-check and correlate results from multiple techniques and proxy records. In this work, I place critical constraints on the distribution of crustal thickness and land surface elevation across the Lhasa Block. Sampling efforts are focused in four sedimentary basins (Fig. 1.1) that record a composite history of Cenozoic deposition—the geologic era that encompasses the India-Asia collision as well as several important periods of global climate change.

The theory behind stable isotope paleoaltimetry lies in the Rayleigh distillation of oxygen and hydrogen isotopes in precipitation with increasing elevation, and the preservation of precipitation $\delta^{18}\text{O}$ and δD in authigenic minerals (see Fig. 1.2). The “rain out” effect describes the progressive depletion of oxygen-18 and deuterium (^2H) from atmospheric moisture as the vapor reservoir travels over continents and ascends mountain ranges. The water in the carbonate weathering reaction (below) for soil carbonate is often supplied directly from rain water, as opposed to lacustrine settings which derive their water from drainage/runoff from higher elevation sites. Thus it is advantageous to use the pedogenic carbonate oxygen iso-



Explanation

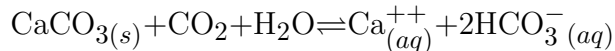
- Study Basins
- Municipality
- ◆ Sea level $\delta^{18}\text{O}_{\text{precipitation}}$ proxy locality

Tectonic Sutures:
B-N S = Bangong-Nujiang Suture Zone
IYS = Indus Yarlung Suture Zone

Figure 1.1 Map of India-Asia convergence zone. **A.** Continental-scale shaded relief map of India and Tibet sourced from the GTOPO30 digital elevation model (DEM). The bold, gray rectangle represents the inset region represented in panel B. **B.** Regional modern elevation distribution of the Lhasa Block and Himalayas. The four paleoaltimetry study basins are noted (Lunpola, Amu Xun, Oiyug, and Penbo), as well as the carbonate diagenesis study site (Tso Jianding). The boundaries (suture zones) between the Indian and Eurasian tectonic plates and the Lhasa and Qiangtang tectonic blocks are marked by a gray dashed line.

topic record when possible because it more directly reflects the oxygen isotopic composition of rainwater at the location and elevation of primary carbonate formation.

Soil, groundwater, and lacustrine carbonates precipitate from carbonate-saturated meteoric water. The general dissolution-precipitation equation that defines carbonate formation (to the left) is:



Pedogenic carbonate formation is driven by the loss of water and CO_2 from soil. Therefore, in most settings, soil carbonate formation occurs predominantly in the summer when soils are warmer and evaporation (E) and evapotranspiration (ET) are more prevalent (Quade et al., 2007). The relative contribution of these processes (F_E/F_{ET}) decreases at deeper soil depths and with increasing rainfall (Quade et al., 2007). Further, although evaporation enriches residual soil water in ^{18}O , evapotranspiration (uptake of water by plant roots from soil) is a non-fractionating process (Quade et al., 2007). In drier climates, evaporative ^{18}O -enrichment is often observed in both soil and lacustrine carbonate, but in wetter climates, where evapotranspiration is the dominant soil carbonate formation process, $\delta^{18}\text{O}_c$ is a more reliable recorder of primary precipitation composition.

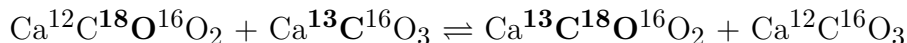
Carbonate production and its kinetics depend on total alkalinity, pH, speciation of dissolved inorganic carbon (DIC), temperature, water availability, and $[\text{Ca}^{2+}]$. Carbonate production in soils and lakes is driven by changes in these chemical properties, as well as microbiological activity (Castanier et al., 1999; Monger et al., 1991), evaporation of surface waters, evapotranspiration (Quade et al., 1989; Monger and Gallegos, 2000), and degassing of soil CO_2 (Mack et al., 1993; Mack, 1992). When carbonate forms, it incorporates oxygen from meteoric water. The relationship between the isotopic compositions of carbonate and its meteoric source water is characterized by a temperature-dependent fractionation factor, $\alpha_{\text{H}_2\text{O}-\text{CO}_3}$ (Kim and O'Neil, 1997).

Elevation estimates derive from the sensitive relationship between elevation and the isotopic composition of precipitation in low-latitude ($<35^\circ\text{N}$) orographic systems (Fig. 1.2).

The water isotope-elevation relationship was originally predicted by atmospheric thermodynamic modeling of the expected lapse rate of water vapor, and calibrated using modern observations (Rowley et al., 2001; Rowley and Garzione, 2007). The model is described in detail in Chapter 2. The elevations calculated using the stable isotope paleoaltimetry model as described in Rowley (2007) (with vapor-ice fractionation) and Ingalls et al. (2017) (without vapor-ice fractionation) represent “precipitation-weighted hypsometric mean elevations.” The meteoric water from which carbonates precipitate could have fallen at any elevation in the drainage system and traveled to a low in basin topography. Thus, we take our elevations to be conservative estimates of the average elevation within the drainage basin.

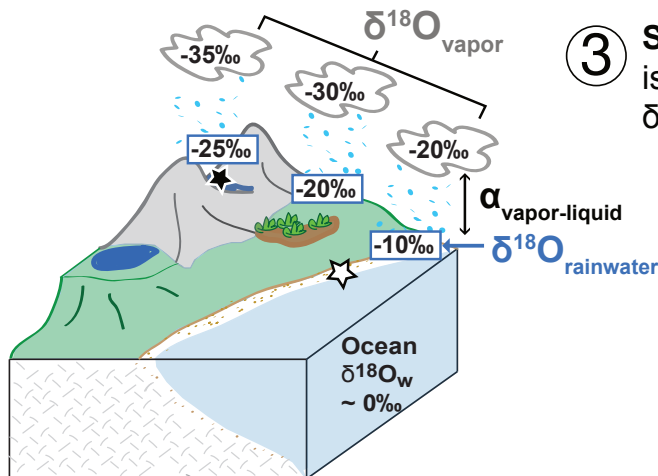
Traditionally, the oxygen isotope ($\delta^{18}\text{O}_{\text{carbonate}}$) thermometer is applied to sediments to estimate past temperatures. Original $\delta^{18}\text{O}$ values are preserved in carbonate minerals that precipitate from meteoric or lake water if there is no post-depositional isotopic exchange. However, $\delta^{18}\text{O}_{\text{carbonate}}$ and $\delta^{18}\text{O}_{\text{water}}$ values are offset by a temperature-dependent fractionation factor, as mentioned above (Kim and O’Neil, 1997). As such, to calculate the isotopic composition of ancient surface water from a carbonate mineral, a temperature must be assumed. Similarly, to use $\delta^{18}\text{O}$ alone as a thermometer, the isotopic composition of the paleo-seawater or lake water ($\delta^{18}\text{O}_{\text{water}}$) from which the carbonate precipitated must be independently known or inferred.

However, a relatively novel technique, ‘clumped’-isotope thermometry, has revolutionized how we measure authigenic mineral formation temperatures and reconstruct past environmental conditions. Clumping refers to the bond ordering of the rare isotopes of carbon (^{13}C) and oxygen (^{18}O) in a carbonate mineral, which relies only on the homogeneous equilibrium of carbonate ions within the mineral, as seen below:

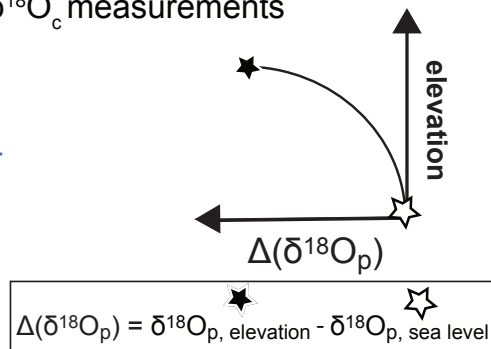


$T(\Delta_{47})$ directly reflects carbonate formation temperature without independent constraints on water isotopes (Eiler, 2011; Ghosh et al., 2006a). In the above equilibrium equation, a

1 Rayleigh Distillation: ^{18}O -depletion of precipitation with increasing elevation



3 Stable isotope paleoaltimetry model: isotopic lapse rate; $\delta^{18}\text{O}_p$ derived from $\delta^{18}\text{O}_c$ measurements



2 Lacustrine and pedogenic carbonate formation from meteoric water

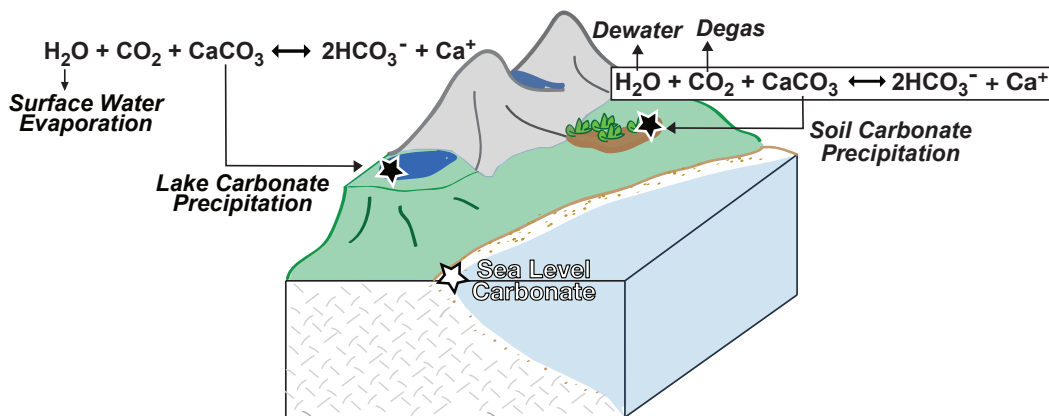


Figure 1.2 Schematic diagram of Rayleigh distillation, carbonate precipitation, and stable isotope paleoaltimetry theory. 1. Rayleigh distillation of a vapor reservoir as it “rains out” over a land surface and over topography. 2. Soil and lake water have a meteoric source. Carbonate precipitation is driven by changes in local lake and soil geochemistry (pH, $[\text{CO}_3^{2-}]$, $[\text{Ca}^{2+}]$, temperature). 3. $\delta^{18}\text{O}$ and $T(\Delta_{47})$ values of authigenic minerals are used to calculate the $\delta^{18}\text{O}$ value of ancient rainwater. The $\Delta(\delta^{18}\text{O}_p)$ value (difference between sea level carbonate and sample at elevation) is fit to a modern-calibrated isotopic lapse rate ($\delta^{18}\text{O}_p/\text{km}$) to reconstruct ancient elevations.

decrease in temperature drives equilibrium to the right in the direction of increased clumping (i.e. greater Δ_{47} , more ^{13}C - ^{18}O bonds). The temperature-dependent relationship of carbonate and water isotopes, as described by a fractionation factor ($\alpha_{H_2O-CO_3}$), has two free variables: $\delta^{18}\text{O}_{water}$ and temperature (Kim and O'Neil, 1997). With the novel Δ_{47} technique, we are able to critically constrain $\delta^{18}\text{O}_{water}$ by providing direct measurements of $\delta^{18}\text{O}_{carb}$ and the mineral formation temperature ($T(\Delta_{47})$). This makes clumped isotope thermometry the ideal tool for terrestrial applications of paleoaltimetry and paleoclimatology.

As demonstrated, elevation and climate proxies are notoriously difficult to disentangle due to the interconnected nature of temperature and elevation. However, in studying elevation and climate proxies in tandem, we possess enormous power to address long-standing tectonic and paleoclimatic hypotheses. Some such questions remaining in the literature relate Tibetan uplift with the onset of the Asian monsoon system (Molnar et al., 1993; Zhang et al., 2015) and to global Cenozoic climate change due to increased silicate weathering (Raymo and Ruddiman, 1992; Raymo et al., 1988; Misra and Froelich, 2012). I outline below the research questions that gave rise to this work, and questions related to the tectonic evolution of the Indian-Eurasian convergent margin, and the role of cryptic carbonate diagenesis in terrestrial applications of clumped isotope thermometry.

The collective focus of the tectonics community on Tibet has significantly enhanced our understanding of crustal response to continental collision (Currie et al., 2005; Rowley and Currie, 2006; DeCelles et al., 2007; Quade et al., 2011; Huntington et al., 2015; Currie et al., 2016; Ingalls et al., 2017), but also has informed current thought and models assigning Tibetan uplift as a driver of atmospheric circulation and monsoon systems and a regulator of global climate by silicate weathering. In Chapters 2 and 3, I detail my work in four basins on the Lhasa Block: the Paleocene-Eocene Penbo basin, the Eocene to Pliocene Oiyug basin, the late Eocene and Oligo-Miocene Lunpola basin, and the nominally Paleocene-Eocene Amu Xun (Fig. 1.1). I employ clumped isotope thermometry and stable isotope

paleoaltimetry to assess past elevations, environmental conditions, and climate. In these chapters, groundwater, lacustrine, and pedogenic carbonates are analyzed for $\delta^{13}\text{C}$, $\delta^{18}\text{O}$, and Δ_{47} in each geologic formation of each measured stratigraphic section for elevation reconstruction.

There are few temperature and elevation proxies robust to secondary effects of the natural Earth system. I petrographically screen for fabrics indicative of secondary crystallization—a red flag for non-primary isotopic compositions. Further consideration is given to isotopic values that may reflect increased aridity, recognized by ^{18}O -enrichment due to evaporation of lake or soil water. In the Oiyug basin, we compare $\delta^{18}\text{O}$ and δD values derived from mixed mineralogies (calcite, dolomite, siderite) and depositional settings (lake sediments, soils, groundwater). A multi-proxy strategy allows for an isotopic assessment of proxy robustness to changing environmental conditions (i.e. aridity) and secondary water-rock interactions by material type. Additionally, isotopic and petrographic analyses of proxy materials from the same strata inform our decisions on which value to accept as primary paleo-precipitation.

My thesis work has increased both the spatial and temporal extent of the land surface elevation reconstructions of the Lhasa Block. In Chapters 2 and 3, I re-assess past models of Tibetan uplift proposed in the literature. The majority of these models assume the southern margin of Eurasia was near sea level at the onset of collision, and either slowly gained crustal thickness as a means of accommodating convergent mass, followed by a rapid uplift ~ 8 Ma due to the removal of a mantle lithospheric root (Molnar et al., 1993), or maintained low elevation until the initiation of normal faulting and rapid exhumation in the Miocene (Harrison et al., 1992). An alternative view is that Mesozoic collisions of the micro-plates that comprise the Tibetan Plateau were enough to thicken the Lhasa Block to ~ 4 km above sea level by north-south thin-skinned shortening (Murphy et al., 1997; England and Searle, 1986). The predominant hypothesized accommodation process is north-south thin-skinned shortening via underthrusting and duplexing of Lhasa terrane rocks beneath the obducted ophiolitic melange associated with the Bangong-Nujiang suture zone (Kapp et al., 2003,

2007).

The elevation reconstructions of four basins presented here are consistently ‘high’ (> 4 km) throughout the Cenozoic. The Penbo basin, which records pre- to syn-collisional deposition in the early Paleocene, yields elevations and temperatures consistent with modern Penbo. The Oiyug basin has been at least 4 km above sea level since the late-Paleocene, and possibly <1.5 km higher than today in the late Miocene. The elevation records of the Amu Xun and Lunpola basins provide corroborating evidence that the Lhasa Block was at high elevation early in the collisional history. The addition of the Lunpola and Amu Xun reconstructions greatly improve our ability to extend that assessment away from Lhasa and the Indus Yarlung Suture (IYS) to the north and west. The agreement between the sedimentary records of the four basins allows us to refute past models of Tibetan tectonics arguing for a late Cenozoic uplift.

In rejecting these models, we must also reconsider their geochemical and physical ties to forcing global Cenozoic cooling due to increased silicate weathering (Raymo and Ruddiman, 1992; Raymo et al., 1988) and strengthening the Asian monsoon (Molnar et al., 1993; Li and Yanai, 1996; Zhang et al., 2015). A change in silicate weathering rate is marked by marine sedimentation rates and offshore clastic sediment accumulation (Clift, 2006). Increased continental weathering influences ocean chemistry and climate on a global scale by imposing a net drawdown of atmospheric CO₂ during multiple intervals of the late Cenozoic (Garziona, 2008; Misra and Froelich, 2012). A tectonic-induced increase in weathering intensity has been argued as the primary driver of late Cenozoic cooling and glaciation (Raymo and Ruddiman, 1992). Given our pre- to syn-collisional elevation reconstruction, it is likely that increased clastic, riverine flux to the Indian ocean (i.e. the late Cretaceous-Cenozoic Sr isotope curve Richter et al. (1992); Zachos et al. (1999)) and changes in seawater chemistry (benthic foram $\delta^7\text{Li}$ Misra and Froelich (2012)) can be attributed to Himalayan uplift alone, not Tibetan. On a more global scale, inflections in the $^{87}\text{Sr}/^{86}\text{Sr}$ curves could be attributed to the significant increase in chemical weathering of continental shield silicates due to high latitude

cooling and ice-sheet growth in the Eocene-Oligocene transition (Zachos et al., 1999), an idea first put forth by Armstrong (1971).

Additionally, the Himalaya-Tibetan orogen is thought to strengthen the Asian monsoon—Earth’s largest monsoon system—by enhancing the high-altitude heat contrast between the land surface and adjacent atmosphere (Li and Yanai, 1996), which drives advection and the formation of a low-pressure cell over the plateau in the summer. An additional argument for plateau-monsoon correlation is that the rain shadow effect of the Himalaya enhances the dryness of air masses over the plateau, further strengthening advection (Ruddiman and Kutzbach, 1989). However, Boos and Kuang (2010, 2013) demonstrate that the high elevation Tibetan Plateau is not the dominant thermal forcing driving the South Asian monsoon. The modern monsoon system can be accurately modeled with or without the Plateau, as long as the Himalayas and Gangdese mountains remain as an orographic barrier, isolating warm, moist air over continental India (Boos and Kuang, 2010).

1.3 Continental Mass Balance

The elevation history of Earth’s largest concentration of continental crust has obvious implications for global climate, but perhaps even greater implications for global tectonics. Previous studies of mass balance in the India-Asia collision have found the crust to be balanced (Richter et al., 1992), unbalanced (van Hinsbergen et al., 2011), or potentially balanced (Yakovlev and Clark, 2014). Discrepant calculations reflect different approaches to tabulating continental mass, but perhaps more importantly, different constraints on paleogeography. In Chapter 4, we fully integrate our calculation with up-to-date constraints on paleogeography and timing of diachronous India-Asia collision onset (Green et al., 2008; DeCelles et al., 2014; Aikman et al., 2008). In this chapter, I consider all possible avenues of continental mass accommodation (crustal thickening, erosion, and tectonic escape) at the Earth’s surface and find nearly half of the pre-collisional Indian and Tibetan continental crust to be missing from the crustal reservoir today. Therefore, the “missing” crust must

have underthrust (i.e. subducted beneath) Eurasia where metamorphism to eclogitic density made part of the Indian continental crust continuously subductable. Previous studies have suggested that piecewise subduction of Indian continental lithosphere may have been a mass accommodation process during India-Asia convergence, but continuous subduction of continental crust has never been considered the dominant accommodation process. We demonstrate that continental subduction is comparable with the accommodation power of crustal thickening and erosion combined.

Direct input of continental-scale volumes of lithophile-rich material should give rise to incompatible trace element contamination of the mantle reservoir. Further, we are interested in the physical expression of continental material subducted from the Paleocene to the present as it can be seen in seismic imaging (Li et al., 2008; Nabelek et al., 2009), and whether recycling of continental crust into the mantle can explain anomalous midocean ridge basalt (MORB) and ocean island basalt (OIB) geochemistry (i.e. elevated incompatible trace element abundances) (Saunders A et al., 1988).

1.4 Carbonate Diagenesis and the Proxy Record

Carbonate clumped isotope paleothermometry, $T(\Delta_{47})$, has improved reconstructions of past climate, tectonics, and ecological and environmental change by providing temperature measurements of carbonate formation. However, carbonate isotopic compositions are highly susceptible to alteration. Δ_{47} can be altered by two known mechanisms: water-rock recrystallization and solid-state reordering of ^{13}C - ^{18}O bonds at high temperature. Until the current work, clumping (Δ_{47}) has been assumed to decrease irreversibly during diagenesis. Thus, the co-occurrence of a high Δ_{47} value and seemingly ‘primary’ carbonate fabrics is typically interpreted to reflect an original mineral formation temperature. However, Chapter 5 explores preliminary results from Tethyan marine carbonates of the Xigaze forearc (southern Tibet) that require an additional alteration mechanism to produce apparent excess Δ_{47} , total oxygen exchange with diagenetic water, and little to no evidence of recrystallization

identifiable by traditional screening tools. The drivers of this cryptic carbonate diagenesis (CCD) and its effects on Δ_{47} are not understood.

The objective of Chapter 5 is to acquire a more rigorous physical and chemical understanding of how a carbonate mineral's burial history is reflected in Δ_{47} measurements. First, I present initial isotopic results and modeling efforts to identify and/or rule out potential diagenetic pathways that could explain our perplexing data. Second, I present a set of micro-analytical techniques for relating minor and trace element distribution, luminescence, micro-scale $\delta^{18}\text{O}$ and $\delta^{13}\text{C}$ measurements (via SIMS), and textural data to Δ_{47} variability on the smallest scale available under current analytical limitations. Techniques are presented as a logical series of diagenetic screening practices to identify CCD, from most widely accessible tools to more costly analyses. This work is an active avenue of research which will be continued in my postdoctoral studies.

In summary, this body of work provides a spatially and temporally comprehensive record of pre- to syn-collisional Lhasa Block elevations. This record reflects the response of the Tibetan continental crust to collision by crustal thickening, and demonstrates that crustal thickening and continental recycling are likely equally important in accommodating convergent mass during the India-Asia collision. A thorough understanding of crustal thickness distribution and extent of high elevation on the Lhasa Block throughout the Cenozoic has been a target of study in the tectonics community for more than three decades. This elevation record will improve our ability to model crustal response to continent-continent collision from continental- to micro-scale structures (Molnar et al., 1993). A projected outcome of the Cenozoic elevation record is to inform more robust assessments of climate-tectonic feedbacks, global distribution of precipitation (atmospheric circulation), and geochemical weathering as related to the Tibetan orogeny.

Further, this work puts forth that wholesale continental crustal recycling was a critical process in accommodating convergent mass during India-Asia collision, and could have been an important process in Earth's past continental collisions.

Finally, although part of the utility and robustness of multi-proxy stable isotope paleoaltimetry is the intimate relationship between climate and elevation proxy records, it is critical to disentangle the isotopic signals of elevation and climate. Additionally, it is absolutely essential to identify all secondary environmental signals (evaporation, transpiration) and diagenetic isotopic and textural signatures (burial, fracturing, recrystallization) that vary from primary meteoric values as reflected in authigenic minerals.

CHAPTER 2

PALEOCENE TO PLIOCENE HIGH ELEVATION OF SOUTHERN TIBET: IMPLICATIONS FOR TECTONIC MODELS OF INDIA-ASIA COLLISION, CENOZOIC CLIMATE, AND GEOCHEMICAL WEATHERING

This work is in review as: Ingalls, M., Rowley, D.B., Olack, G., Currie, B.S., Li, S., Tremblay, M., Shuster, D., Schmidt, J., Zeitler, P., Polissar, P., Ding, L., and Colman, A., Paleocene to Pliocene low-latitude high elevation of southern Tibet: Implications for tectonic models of India-Asia collision, Cenozoic climate, and geochemical weathering, *GSAB*, accepted.

2.1 Abstract

We present the first nearly continuous Cenozoic elevation history from two sedimentary basins on the southern Tibetan Plateau within the latest Cretaceous to Eocene Gangdese arc. Oxygen isotope and Δ_{47} clumped isotope compositions of non-marine carbonates allow us to constrain carbonate formation temperature and reconstruct the paleo-precipitation record of the Eocene to Pliocene Oiyug basin and Paleocene to Eocene Penbo basin. We exploit the systematic decrease of surface temperature and meteoric water $\delta^{18}\text{O}$ with elevation to derive paleo-elevation estimates for these basins. Minimally altered and unaltered pedogenic and lacustrine carbonates from the Oiyug basin yield $\Delta_{47, \text{CDES}}$ values of 0.625 to 0.755, that correspond with temperatures of 1 to 30°C using a Δ_{47} thermometer for low temperature carbonates Zaarur et al. (2013). Similarly, the Penbo Basin yields $\Delta_{47, \text{CDES}}$ values of 0.701 to 0.726, corresponding with temperatures of 6 to 12°C.

Our paleo-elevation estimates for the Eocene to Pliocene Oiyug basin (~6.5 to 4.1 kilometers) support previous evidence (Spicer et al., 2003; Currie et al., 2005; Polissar et al., 2009; Currie et al., 2016) that high elevations were attained in southern Tibet by at least

~30 Ma. Stable isotope results allow for the possibility of significant decrease in elevation during the Miocene as a result of regional extension. In the Penbo basin, our paleo-elevation estimates for the Paleocene to Eocene Nianbo Formation ($4.4 \pm_{-1.7}^{+1.3}$ km) and Eocene Pana Formation ($4.1 \pm_{-1.6}^{+1.2}$ km) extend the altitude record of the southern Plateau to pre-India-Asia collision. These results support the “Lhasaplano” model of an Andean-type continental margin tectonic system.

The rise of the Himalayas and Tibet has often been invoked to understand isotopic proxies for global chemical weathering in the Cenozoic and has constrained the debate on the nature of CO₂-climate-weathering feedbacks. The nature of the Tibetan paleo-elevations from pre- to post-collision, as presented here, indicates that high relief at low latitude prevailed on the Asian margin much earlier than previously thought. Thus high topography alone at low latitude is not sufficient to account for the Cenozoic weathering proxy record.

2.2 Introduction

Recent efforts have established an age of onset of the India-Eurasia continental collision of 56 ± 2 Ma from the Indian deep-water, off-shelf passive continental margin environment represented by Paleocene-Eocene strata near Sangdanlin in south-central Tibet (DeCelles et al., 2014; Hu et al., 2015). Ingalls et al. (2016b) review these and other data to put forth arguments favoring an age of 56 ± 2 Ma for collision of thicker (>20 km) continental crust in the vicinity of Sangdanlin, a younger age of ~ 51 Ma in the Zaskar region farther west (Gaetani and Garzanti, 1991; Green et al., 2008), and an essentially unconstrained 54 ± 4 Ma age nearer to the eastern syntaxis.

The debate over when and how the largest and highest plateau on Earth reached its current altitude has been re-framed in the context of these older dates of collision. This has important implications for tectonics (Le Pichon et al., 1992; Kapp et al., 2007), crustal mass balance considerations (Ingalls et al., 2016b), and feedbacks among tectonics, weathering, climate, and the global carbon cycle, (e.g, (Raymo and Ruddiman, 1992)). In this

paper, we present clumped isotope paleothermometry and stable isotope paleoaltimetry results supporting the existence of an Andean-type continental arc on the southern margin of Eurasia with elevations >4.1 km at ~ 55 Ma, at or just prior to the onset of the India and Eurasia collision in the Penbo/Linzhou region near Lhasa. We also extend the record of the Oiyug Basin, ~ 160 km west of Lhasa, into the Eocene and provide additional support that the Oiyug basin was high throughout the Oligocene to Pliocene. Further, the mean elevation of the Oiyug basin may have been higher than its current elevation of ~ 4.5 km during the late-Miocene (Currie et al., 2016). Our high paleo-elevations agree with aspects of the “Lhasaplano” model (Kapp et al., 2007) a high-standing pre-collision Lhasa terrane and provides additional evidence against models invoking en masse (England and Houseman, 1986; Harrison et al., 1992, 1995; Molnar et al., 1993) or local plateau uplift (Wang et al., 2006) from significantly lower elevations in the Neogene.

Our study of the tectonic history of Penbo and Oiyug Basins provides a framework for the land surface evolution of the southern margin of Eurasia and the sedimentary basins associated with the Linzizhong volcanic arc and younger sedimentary basins during the Cenozoic collisional history spanning ~ 55 Ma to ~ 5 Ma. From the Penbo basin, we present $\delta^{18}\text{O}_c$ measurements on 105 lacustrine, pedogenic, and groundwater calcites. We use clumped-isotope derived mineral formation temperatures from 18 of the calcite samples to calculate the original oxygen isotopic composition of meteoric water ($\delta^{18}\text{O}_w$) from $\delta^{18}\text{O}_c$ measurements. Finally, we assess alteration and secondary calcite precipitation with careful petrographic analyses and characterization of possible diagenesis coupled with our clumped-isotope results.

The Oiyug basin sedimentary record spans nearly the entire Cenozoic, making it a unique site for reconstructing the elevation history of the southern part of the Tibetan Plateau (2.1). Previous paleoaltimetry studies of the basin include paleoenthalpy-derived estimates of ~ 15 Ma elevations from floral physiognomy (Spicer et al., 2003; Khan et al., 2014), oxygen isotope-based estimates from carbonate minerals (Currie et al., 2005, 2016), and compound-

specific δD of leaf wax n-alkanes (Currie et al., 2016). These studies have progressively added archives as a means of testing new proxies and demonstrating internal consistency with prior reconstructions of past hypsometry and environmental conditions. In this paper, we provide new stable isotope data from three Paleogene nonmarine carbonate samples to extend the temporal range of the isotopic record in the Oiyug basin. Additionally, we present clumped isotope estimates of carbonate formation temperatures to better constrain paleo-water isotopic compositions for 34 samples previously analyzed by Currie et al. (2016). These data thus help remove ambiguity as to the potential for biasing paleo-elevation estimates through assumptions regarding carbonate-water fractionation temperatures.

2.2.1 A case for multiple proxies in reconstructions of ancient topography and environments

The exploitation of multiple paleo-elevation and paleo-environmental proxies in a single stratigraphic package allows for calibration and checks among conventional archives. Currie et al. (2016) conducted such a study in the Oiyug basin, characterizing ~ 30 My of relative elevation stasis in the evolving depositional environment of the Oiyug Basin. Currie et al. (2016) synthesized multiple proxies for paleo-meteoric water ($\delta^{18}\text{O}_{\text{FeCO}_3}$, $\delta^{18}\text{O}_{\text{CaCO}_3}$, $\delta D_{\text{leaf wax}}$) to provide mid-Miocene ($5.1^{+1.3}_{-1.9}$ km) and late-Oligocene to mid-Miocene ($4.1^{+1.2}_{-1.6}$ km) paleo-elevation estimates of this region, and a unique opportunity for testing the fidelity of other stable isotope proxies. Khan et al. (2014) determined a mid-Miocene (~ 15 Ma) paleo-elevation of 5.54 ± 0.73 km by reevaluating paleo-enthalpy estimates for a fossil flora locality (Spicer et al., 2003) in the Oiyug Basin relative to new fossil flora localities in the Siwaliks, their sea level proxy.

Clumped isotopes can be powerful in studying the evolution of ancient land surfaces when the original isotopic signature is preserved (Ghosh et al., 2006b; Quade et al., 2007). In this study, we apply calcite Δ_{47} -derived formation temperatures ($T(\Delta_{47})$, Table D.3) to previously published ((Currie et al., 2016), Fig. 2.1) and new oxygen isotopic compositions

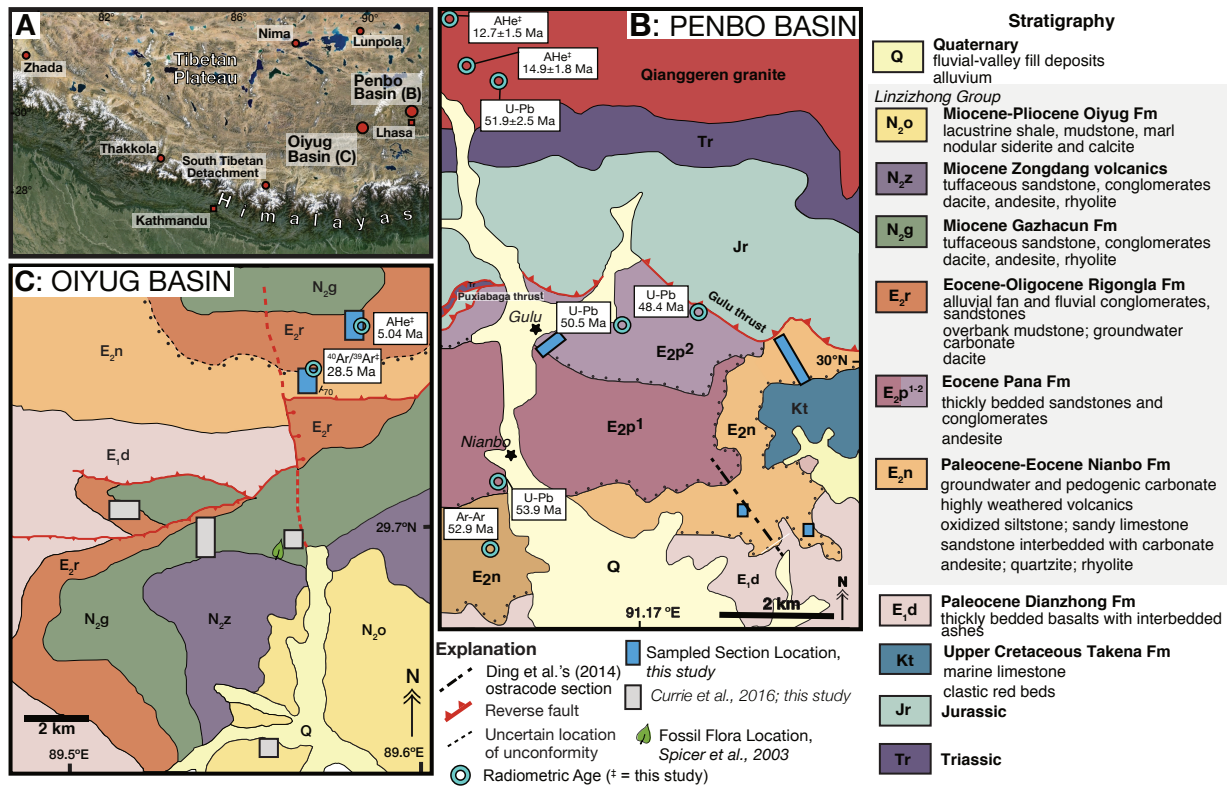


Figure 2.1 Maps of the sampled regions A. Regional Landsat image of the Tibetan Plateau (adapted from Currie et al. (2016)). B. Geologic map of the Linzhou/Penbo region including the Nianbo type section. Map and ages are adapted and sourced from Ding et al. (2014) and He et al. (2007). C. Geologic map of the Oiyug basin displaying measured section locations from Currie et al. (2016) (gray) and this study (blue). The fossil floral locality of Spicer et al. (2003) is depicted as a leaf.

of lacustrine and pedogenic carbonates ($n=141$) to better estimate $\delta^{18}\text{O}_w$ of paleo-waters (Tables D.1 and D.2). $\delta^{18}\text{O}_w$ is the isotopic composition of the water from which the carbonate formed, assuming equilibrium. We use this value to represent the precipitation-weighted hypsometric mean isotopic composition of surface water, which then enters into standard stable isotope paleoaltimetric determinations (Rowley, 2007).

2.2.2 Geologic Setting

Penbo Basin

The Penbo, also referred to as the Linzhou, basin (Fig. 2.1B) is located approximately 35 km north of Lhasa and 75 km north of the Indus Yarlung Suture (IYS). The modern hypsometric mean elevation of the basin drainage area is ~ 4200 m with surrounding peaks < 5300 m. The samples in this study were collected from elevations of 3950 to 4200 m.

This basin exposes a sedimentary and volcanic record spanning pre- to syn-collisional time (~ 67 to ~ 48 Ma) and is the type locality of the non-marine Linzizhong Group (He et al., 2007). Here, the stratigraphic thickness of the Linzizhong Group is approximately 3500 m (He et al., 2007). The volcanism represented by the Linzizhong Group (~ 69 to 43 Ma) and post-Early Cretaceous (< 100 Ma) plutons of the Gangdese belt constitute the subduction-related Linzizhong arc. Neo-Tethyan oceanic lithosphere attached to Indian plate was subducted prior to and during the early stages of continent-continent collision along the Linzizhong arc (Argand, 1924; Dewey and Bird, 1970; Murphy et al., 1997; Ding and Lai, 2003).

We focus our paleo-elevation reconstruction in the Penbo Basin primarily on the ~ 56.5 to ~ 53 Ma Nianbo Fm and the ~ 50 Ma upper Pana Fm because they preserve abundant lacustrine limestone, groundwater and paleosol carbonate nodules, and they have pre- to early syn-collisional depositional ages. The sedimentary rocks of the Nianbo Formation in the Oiyug Basin are mapped as age-correlative with the type Nianbo in the Penbo Basin. The age range of the sampled Nianbo stratigraphy of the Penbo Basin is well constrained by radiometric ages (Ding et al., 2014; He et al., 2007). These ages together with stratigraphic and lithological correlation allow us to place the paleo-altitude results from the Nianbo Formation, discussed below, in the Oiyug Basin into temporal and regional context.

The > 180 meter-thick Paleocene-Eocene Nianbo Fm (Fig. 2.2) conformably and unconformably overlies the Dianzhong Formation, and unconformably overlies the Upper Creta-

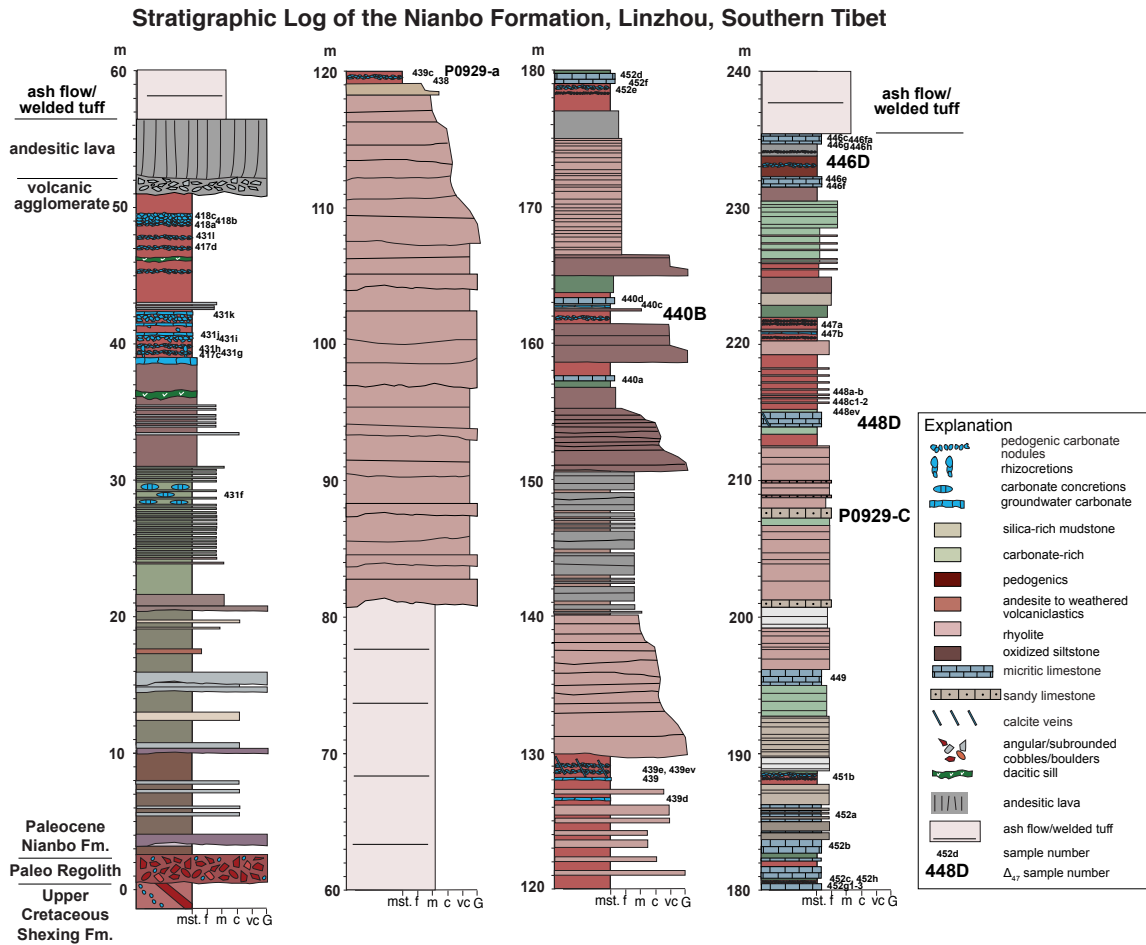


Figure 2.2 Stratigraphic section of the Nianbo Formation in the Penbo Basin. The geographic location for the base of this section is 29.9933°N, 91.2090°E.

ceous Shexing Fm. The Linzizhong Group and particularly the Nianbo Fm are spatially heterogeneous such that no section in the field is representative of all sections. Nonetheless, the overall stratigraphy and sedimentology of the Nianbo Fm can be broken into three lithologic sequences: two upward-fining packages with an ash-flow tuff and massive conglomerate between the two. The lower subunit is dominated by purple and green laminated siltstones and volcanoclastic-dominated sandstones at its base. The siltstones contain nodular carbonate, peds, mottling, and bioturbation, and at least one undeformed snail shell. These are overlain by fine-grained red siltstones abundant in pedogenic carbonate and interbedded with

yellow to brown lacustrine marls. Fossil ostracods are found in the marls. Shell morphology is relatively undeformed but body cavities have sparry calcite infill.

The middle Nianbo subunit is defined by a period of rampant volcanic activity. The volcanic agglomerate base is topped by a 5 meter-thick andesitic lava flow. A 25 meter-thick welded tuff/ash flow tops this sequence, followed by ~ 40 meters of gravel conglomerate.

The basal 10 meters of the upper Nianbo subunit is composed of interbedded red mudstones and medium to very coarse sandstones. The uppermost mudstones contain ground-water carbonate horizons and abundant pedogenic carbonate. Approximately 10 meters of coarse to gravel conglomerate overlies the ped-rich layers. The conglomerate is topped by ~ 10 meters of alternating fine and coarse sandstones. The uppermost ~ 80 meters of the Nianbo are more variable in composition and depositional conditions: fining-upwards conglomerates, meter-thick micritic limestone beds, horizontally laminated medium-grained sandstones, sandy limestones, and paleosol horizons. Ostracods are found in one of the uppermost lacustrine limestone beds, implying a period of relatively shallow and saline lakes (Ding et al., 2014). The majority of the samples used for measuring paleo-elevation of the Nianbo Fm were derived from this upper subunit.

The uppermost preserved rocks of the Linzizhong Group are the Pana Formation, a lower sequence of mostly andesitic volcanics and volcanoclastics overlain by a predominantly lacustrine succession of shales, mudstones, sandstones, and both pedogenic and lacustrine carbonates. The upper subunit of the Pana Formation was deposited between 50.5 ± 2.4 Ma and 48.4 ± 1.0 Ma, as dated by U-Pb zircon laser ablation of interbedded volcanics (Ding et al., 2014).

Oiyug Basin

The Oiyug Basin (Fig. 2.1C), also referred to as the Wuyu Basin, and mischaracterized as the Namling Basin (Spicer et al., 2003) that actually lies slightly farther west, is located 160 km west of Lhasa and 60 km north of the Indus Yarlung Suture (IYS). The basin covers an area

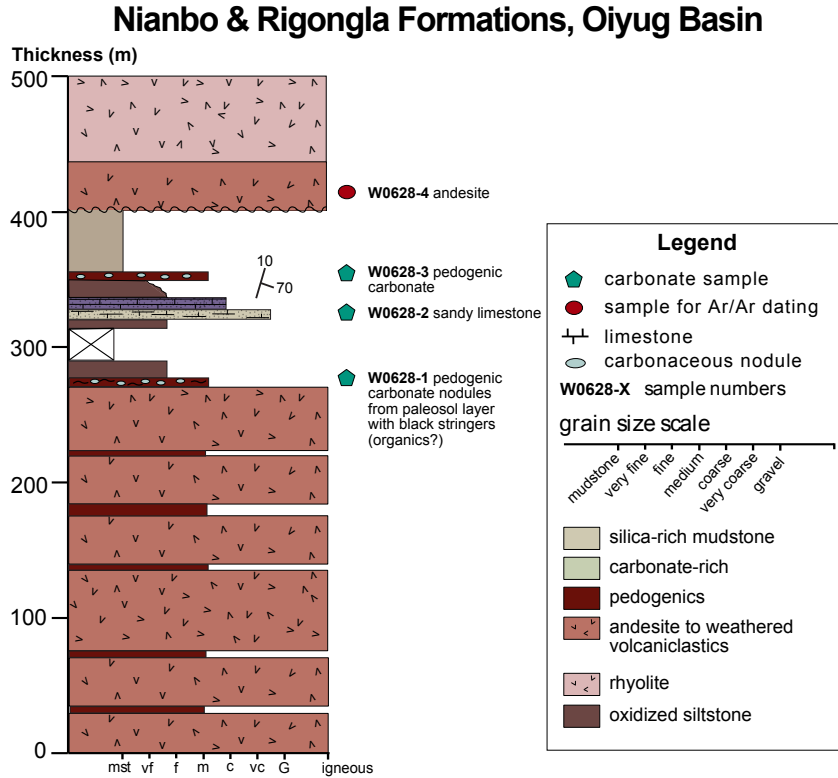


Figure 2.3 **Stratigraphic section of the Nianbo Formation in the Oiyug Basin.** The geographic location for the base of this section is 29.9594°N, 89.7414°E. The x-axis scale refers to grain size, explained in the legend.

of approximately 300 km² (Wang and Chen, 1999) of the Lhasa terrane. Sampled localities are currently at elevations of 4300 to 4400 meters with surrounding elevations >5600 meters. The modern hypsometric mean elevation of the basin drainage area is ~4600 meters.

Paleogene-Neogene strata sampled in the Oiyug Basin consist of the Paleocene-Eocene Nianbo Formation, the Oligocene-Miocene Rigongla Formation, the Miocene Gazhacun Group, and the Miocene-Pliocene Oiyug Formation. In this basin, the Nianbo Formation is comprised of andesite, fluvial volcaniclastics, lacustrine sandstones, mudstones and limestones, and argillaceous/calcareous paleosols. In this study, an approximately 500 meter thick section of the Nianbo Formation was measured in the northern part of the Oiyug Basin (Fig. 2.3). The section is bordered to the south by a low angle thrust fault that places Nianbo sed-

iments above the younger Rigongla Formation. To the north, the section is separated from the overlying Rigongla Formation by an angular unconformity, excising the upper Nianbo and Pana Formations (Fig. 2.1C) from the Oiyug stratigraphy.

The lower parts of the measured Nianbo Formation (Fig. 2.3) consists of ~ 270 m of andesitic volcanoclastic rocks sparsely interbedded with thin (~ 20 to 30 centimeters thick) paleosol horizons. Pedogenic calcite (W0628-1) was collected from a calcareous paleosol ~ 275 meters from the base of the section. Above the volcanics, the Nianbo Formation is dominated by lacustrine limestone, sandstone, and mudstone. The depositional environment is interpreted as marginal lacustrine. The dominant lithology at the base of the thick limestone package is laminated sandy limestone (W0628-2) with very fine-grained calcareous matrix and fine to medium quartz grains. The sandy beds interbedded with the marl limestone cliffs are interpreted as terrestrial alluvium deposited in an offshore to nearshore lake environment (Mack and Rasmussen, 1984). The sedimentology of this sequence and environmental interpretations align with the lithology and sequence stratigraphy of the upper subunit of the Nianbo Formation in the Penbo basin (Ding et al. (2014), this study). Approximately 10 meters above this sampling locality, sandy limestone fines to oxidized siltstone and red mudstone with authigenic calcareous concretions (W0628-3). The Nianbo Formation in the Oiyug Basin is mapped as Paleocene to early Eocene in age. While undated in the immediate study area, U-Pb ages from the Nianbo Formation sampled ~ 40 km to the west near Namling range from 63.78 ± 0.46 Ma to 50.2 ± 2.2 Ma (Wang et al., 2014) in line with dating in the type area in the Penbo Basin to the east.

Rigongla Formation rhyolitic and andesitic volcanoclastic rocks lie unconformably above the described section of Nianbo measured section. A rhyolite (W0628-4) sampled from these volcanics yielded a late Oligocene age of 28.90 ± 1.52 Ma (potassium feldspar $^{40}\text{Ar}/^{39}\text{Ar}$, Table D.7, Figure 2.4), similar to a ~ 31 Ma K-Ar age reported for the lower Rigongla Formation elsewhere in the basin (Zhu et al., 2006). Given these ages, and the ~ 50 Ma age for the upper Nianbo in the region, ~ 20 million years is likely missing at the unconformity

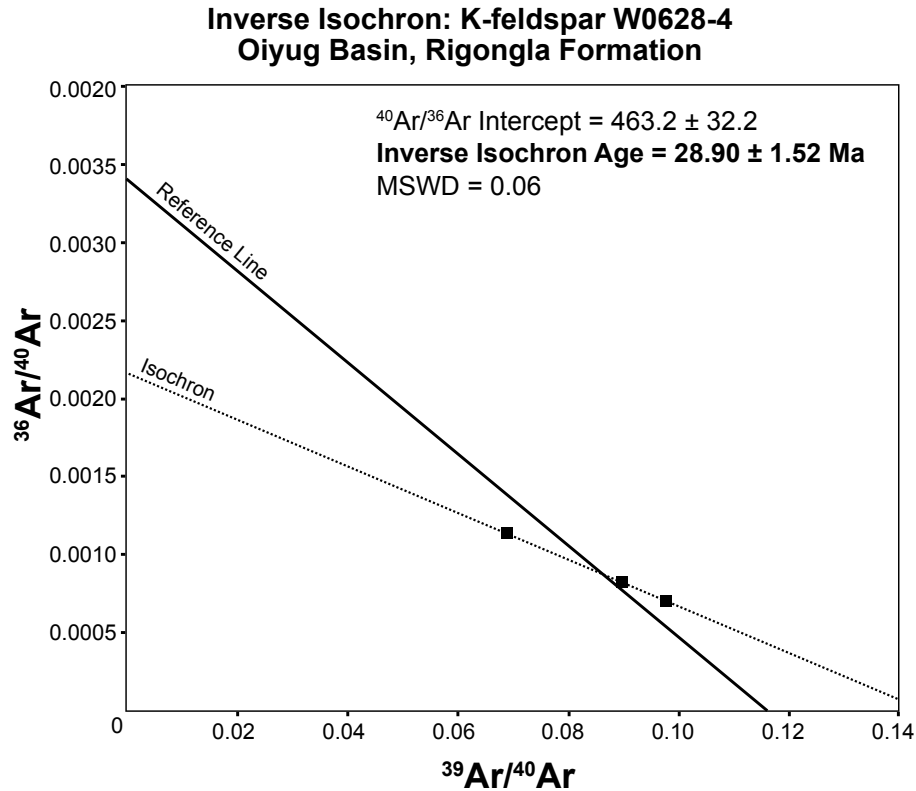


Figure 2.4 Inverse isochron plot of potassium feldspar Ar/Ar age.

between the Nianbo and Rigongla formations in the study area. The Rigongla Formation measured at the headwaters of the Ramaqu, consists of dacitic to andesitic volcanic rocks interbedded with an upward-fining >500 meter thick sedimentary sequence of conglomerates, sandstones, and mudstones (Fig. 2.1C). Paleosol and groundwater carbonate nodules were collected from a ~20 meter thick mudstone horizon between alluvial fan and fluvial channel conglomerate sequences in the Rigongla Formation (Currie et al., 2016). The nodules are texturally micritic and 3 to 15 cm in diameter.

The Gazhacun Group, previously described as the Manxiang Formation (Zhu et al., 2006), directly overlies the volcanics of the upper Rigongla Formation. The base of the Gazhacun Group is comprised of ~140 meters of red and gray overbank mudstones and sparse fluvial channel sandstones and conglomerates (Currie et al., 2016). The overbank mudstones host clay-rich paleosol horizons with well-developed pedogenic calcite nodules

0.25 to 1.5 cm in diameter. The middle Gazhacun is interpreted to record a lacustrine depositional environment, represented by ~225 meters of gray, green, and light red shale and mudstone, and thin beds of siltstone and fine-grained sandstone (Currie et al., 2016). Samples from lacustrine strata of the middle Gazhacun are both early diagenetic calcite and dolomite nodules. Given the paucity of datable volcanics in the Rigongla Formation and lower-middle Gazhacun Group strata, the age of this stratigraphic interval is bracketed between ~29 and 15 Ma (Currie et al., 2016).

The upper Gazhacun Group, measured along the Badamaqen, consists of ~100 meters of tuffaceous conglomerate and fining upwards sandstone, interbedded with carbonaceous siltstone, mudstone, shale, and coal. A siderite nodule (618A) and four shales were collected for isotopic analyses near the top of the floral locality section of Spicer et al. (2003) and Khan et al. (2014).

The age of the top of the upper Gazhacun Group is constrained by $^{40}\text{Ar}/^{39}\text{Ar}$ age of ~15 Ma from felsic tuff deposits within the upper part of the unit and from the base of the overlying Zongdang Group (Spicer et al., 2003). The Zongdang Group consists of ~1900 meters of ash flow tuffs and volcanoclastics (Zhu et al., 2006; Chen et al., 2008). Ash flow tuffs from the uppermost Zongdang Group yielded K-Ar ages ranging from 8.23 ± 0.13 to 7.92 ± 0.15 Ma (Chen et al., 2008).

The upper Miocene-Pliocene Oiyug Formation conformably to unconformably overlies the Zongdang Group. This unit is an ~1 km-thick package of basin-centered lacustrine deposits and associated basin margin fan delta, fluvial, overbank, and swamp deposits (Zhu et al., 2006). The upper Oiyug Formation is dominated by lacustrine marl and mudstone deposits (Currie et al., 2016). Lacustrine marl calcitic limestone, shales, nodular calcite, and nodular siderite were collected for isotopic analyses from the middle to upper Oiyug Formation, with an interpreted depositional age of ~5 Ma (Chen et al., 2008).

2.3 Methods

In this study, we determined the $\delta^{18}\text{O}_c$ and $\delta^{13}\text{C}_c$ composition of 105 carbonate samples collected from Paleocene and Eocene strata in the Penbo basin. Of these samples, 7 were used to determine clumped-isotope estimates of carbonate precipitation temperatures $T(\Delta_{47})$. Currie et al. (2016) previously reported stable isotopic compositions of 33 carbonate samples collected from Oligocene to Pliocene strata in the Oiyug basin. In this study, 3 more samples from Paleogene strata of the Oiyug basin were also measured. In addition, the $T(\Delta_{47})$ of 3 of the Paleogene samples and 9 Oligocene-Miocene samples were determined. We also obtained a potassium feldspar total fusion $^{40}\text{Ar}/^{39}\text{Ar}$ age for Rigongla Formation volcanics in the Oiyug basin in order to provide an upper bound for Nianbo Formation deposition, and measured apatite (U-Th)/He ages for an ash and two granites in the Oiyug and Penbo basins, respectively, in order to constrain burial temperatures.

2.3.1 Sample Preparation

The outer layer of carbonate samples was removed to expose fresh material for stable isotope analysis and making petrographic slides. Samples were powdered using a Foredom TX low speed drill with a Brasseler US#2 HP Round bit at low speed to avoid significant frictional heating and the potential for carbonate C-O bond reordering.

Petrographic slides were made for a subset of samples that appeared minimally or unaltered in hand sample in order to evaluate for visual signs of aqueous alteration (dissolution features, recrystallization textures, secondary carbonates, authigenic metal oxide precipitates, etc.). Tables D.1 and D.2 contain petrographic images of a subset of samples from both basins. The tables also include synopses of the observations made in interpreting textural primacy, the assessment of “primary”, “minor alteration”, or “diagenetic”, and $T(\Delta_{47})$, where applicable.

Petrographic analyses allow distinction between two contrasting textural relationships

among preserved carbonates. One group consists of pedogenic carbonate nodules and lacustrine limestone, some of which preserve ostracods and charophyte debris within a micritic matrix with only very minor spar-filled vugs and/or microspar recrystallization (Tables D.1). This minimally altered group also includes wackestones lacking evidence of secondary recrystallization. The second group, consisting of lacustrine limestone and pedogenic carbonate nodules, is characterized by varying degrees of alteration including extensive development of sparry calcite, oxidation, cross cutting veins, and increase in grain size of the formerly micritic matrix and sparry calcite veins. We discuss our isotopic results with respect to our petrographic assessment of degree of alteration.

For the Penbo Basin, the Δ_{47} analyses were carried out independently from the petrographic observations (isotopic measurements and petrographic observations shared only after both were completed). This blind test was carried out at Miami University as a means of assessing our ability to correctly characterize alteration by petrographic observation. For the Oiyug Basin, petrographic and Δ_{47} analyses were both completed at the University of Chicago.

2.3.2 *Standard stable isotope measurements*

Isotopic measurements were completed in the stable isotope facility in the Department of the Geophysical Sciences at The University of Chicago. All samples were analyzed for calcite $\delta^{18}\text{O}_c$ and $\delta^{13}\text{C}_c$ and weight % CaCO_3 using a Gas Bench II (Thermo, Bremen, Germany) connected to a Delta V Plus (Thermo) stable isotope ratio mass spectrometer. Stable oxygen and carbon isotopic measurements are reported in ‰ using conventional delta notation:

$$\delta^{18}\text{O}_c = \left(\frac{\frac{^{18}\text{O}}{^{16}\text{O}}_{\text{sample}}}{\frac{^{18}\text{O}}{^{16}\text{O}}_{\text{standard}}} - 1 \right) \times 1000\text{‰} \quad (2.1)$$

with analogous formulation for $\delta^{13}\text{C}_c$. Samples were weighed out to yield roughly 100 to 200 μg CaCO_3 equivalent. Comparable size ranges of the isotopic standards NBS-18

($\delta^{13}\text{C} = -5.01\text{‰}$ VPDB; $\delta^{18}\text{O} = -23.20\text{‰}$ VPDB (Coplen et al., 2006)), NBS-19 ($\delta^{13}\text{C} = 1.95\text{‰}$ VPDB; $\delta^{18}\text{O} = -2.19\text{‰}$ VPDB (Gonfiantini, 1983)), and periodically LSVEC ($\delta^{13}\text{C} = -46.6\text{‰}$ VPDB (Coplen et al., 2006)) were interspersed with the Tibetan samples. These standards were used to assess, and correct when needed, for linearity and drift. Results for carbonate $\delta^{13}\text{C}_\text{c}$ and $\delta^{18}\text{O}_\text{c}$ are reported on the VPDB scale ($\pm 0.1\text{‰}$ analytical uncertainty). The calculated values for water in isotopic equilibrium with the carbonate minerals, $\delta^{18}\text{O}_\text{w}$, are reported on the VSMOW scale and based on the Kim and O’Neil (1997) fractionation relationship. $\delta^{18}\text{O}_\text{w}$ compositions are calculated using the mineralogy-specific water-carbonate fractionation factors for calcite, siderite, and dolomite, as follows:

$$1000\ln\alpha_{\text{CaCO}_3\text{-H}_2\text{O}} = (18.03 * 10^3 / T) - 32.42 \text{ (Kim and O’Neil, 1997)}$$

$$1000\ln\alpha_{\text{FeCO}_3\text{-H}_2\text{O}} = (2.62 * 10^6 / T^2) - 2.17 \text{ (Zhang et al., 2001)}$$

$$1000\ln\alpha_{\text{MgCO}_3\text{-H}_2\text{O}} = (2.73 * 10^6 / T^2) + 0.26 \text{ (Vasconcelos et al., 2005)}$$

2.3.3 Clumped isotope (Δ_{47}) analyses

The carbonate clumped isotope thermometer is established using the temperature-dependent enrichment of clumped isotopologues in carbonates, and can be used to determine carbonate mineralization temperature (Ghosh et al., 2006a,b; Eiler, 2007; Huntington et al., 2009). The “clumping” refers to ions or molecules with more than one rare isotope (e.g., a clumped carbonate ion: $^{13}\text{C}^{18}\text{O}^{16}\text{O}_2^{2-}$). The formation of carbonate minerals in internal isotopic equilibrium results in greater clumping at lower temperatures. The clumped isotope composition of carbonates is measured on CO_2 released by phosphoric acid digestion of carbonate minerals. The composition is reported as a Δ_{47} value expressed in units of ‰, where Δ_{47} is defined as the enrichment in clumped CO_2 with molecular mass 47 (dominated by $^{13}\text{C}^{18}\text{O}^{16}\text{O}_2^{2-}$) relative to the amount of clumping expected based on a stochastic distribution of C and O isotopes as measured in the bulk isotopic composition: $\Delta_{47} = (R_{47}/R_{47}^* - 1) * 1,000 \text{‰}$, where $R_{47} = \text{mass } 47 / \text{mass } 44$, and R_{47}^* denotes analogy to R_{47} , but reflects the abundance predicted with a random distribution of isotopes. δ_{47} is defined similarly to $\delta^{13}\text{C}$

and $\delta^{18}\text{O}$, using the abundance ratios of CO_2 isotopologues (rare mass 47 isotopologues compared to the common mass 44 isotopologue) referenced to a working gas that defines “zero”.

Carbonates were digested overnight in 5-7 ml of $\sim 103\%$ anhydrous phosphoric acid at 26°C with acid densities of 1.92 to 1.94 g/cm^3 , verified gravimetrically prior to each use. Following acid digestion, the resultant CO_2 was purified on a glass vacuum line to remove trace water vapor and isobaric contaminants. Gas was transferred through a cryogenic water trap (glass tubing immersed in LN2-ethanol slurry at -80°C) with the CO_2 frozen out (liquid N_2) downstream and with non-condensable gases then pumped away. These non-condensable gases typically gave a pressure of 0.1 to 0.2 Torr in a 250 ml volume segment of the vacuum line and reaction vessel as compared with a CO_2 partial pressure of 80 Torr in 15 ml. The frozen CO_2 sample was isolated from the rest of the system and warmed, with pressure reading serving as a monitor of CO_2 yield from the sample digestion (902 piezo vacuum transducer, MKS Instruments, Andover, MA). Then the CO_2 was passed through a Haysep Q (60/80 mesh, Supelco, Bellefonte, PA, USA) filled U-trap (6 mm i.d., 24 cm packed length) with an approximately 2 cm thick layer of powdered Ag_3PO_4 (Strem Chemicals, Newburyport, MA, USA) mixed with quartz chips at the inlet end. Small quartz wool plugs capped with silver wool plugs were used on both ends of the column to retain fine mesh and powder packing material. The U-trap thus packed served as a chromatography column. We optimized the temperature of CO_2 chromatography by varying temperature of the column ~ 0 to 25°C , and passing gases equilibrated at 25°C and 1000°C through the column. No fractionation of the equilibrated gases occurred during the room temperature trials. The transfer of CO_2 through the column at room temperature was monitored barometrically, and freezing over of CO_2 was continued for approximately 10 minutes beyond the time required for the upstream pressure to reach baseline (40 to 50 minutes total). The collected CO_2 was cryogenically transferred through a second water trap to a cold finger, then isolated and warmed for pressure reading to confirm quantitative transfer. The purified CO_2 was

stored in borosilicate tubes with CTFE valve body and o-ring seal (Kimble-Chase, Vineland, NJ) until loaded into the mass spectrometer sample bellows.

Clumped isotope measurements and traditional carbon and oxygen stable isotope measurements were made on a Finnigan MAT253 set to measure m/z 44 49 ion beams. Oztech (Stafford, AZ, USA) isotopic standard CO₂ tank gas (UOC 1766, $\delta^{13}\text{C}=-3.61\text{‰}$ VPDB, $\delta^{18}\text{O}=24.99\text{‰}$ VSMOW) was used as the working reference gas during clumped isotope analyses, and 47 values were determined with the working gas defining zero.

Following Dennis et al. (2011), raw Δ_{47} values are standardized to gases heated to 1000°C to approximate near random distribution of isotopes, as well as gases equilibrated with waters of known composition at 4, 26, and 60°C. Standardized Δ_{47} values are reported on an “absolute reference frame”, henceforth referred to as the Carbon Dioxide Equilibrium Scale (CDES) following Dennis et al. (2011), allowing for interlaboratory comparison. We routinely measured standard calcite materials (Carrera Marble [CM] and four CaCO₃ materials from ETH-Zurich [ETH1 through 4]) that have been distributed to many clumped isotope facilities for the purpose of inter-laboratory calibrations and measurement comparisons. We also use frequent analyses of these standard materials as a check on internal consistency of repeated measurements within and between analytical periods (Table A.1). Further discussion of quality control checks and corrections applied to measurements made on the MAT253 can be found in the Appendix.

Temperatures were calculated using the Zaarur et al. (2013) paleothermometer. There is presently a consensus in the clumped isotope research community that the conversion of Δ_{47} values to equilibrium temperatures should employ a paleothermometer that was determined on similar sample types and with similar acid digestion temperatures (Huntington et al., 2015; Defliese et al., 2015; Gallagher and Sheldon, 2016; Burgener et al., 2016; Ringham et al., 2016). Our 26°C acid digestion temperatures is essentially the same as the 25°C temperature used for the Zaarur et al. (2013) calibration. Use of this paleothermometer also maintains inter-laboratory consistency with other paleoaltimetry studies on the Tibetan

Plateau (Huntington et al., 2015). Errors are reported for each sample using the standard error of the mean for replicate sample digestions (in this study, Δ_{47} s.e.m. of 0.011 to 0.040), that converts to temperature uncertainties of 2.3 to 8.2°C on the Zaarur et al. (2013) paleothermometer.

2.3.4 $^{40}\text{Ar}/^{39}\text{Ar}$ geochronology

Standard K-feldspar $^{40}\text{Ar}/^{39}\text{Ar}$ total fusion analyses were conducted for sample W0628-4 in the Lehigh University Noble Gas Laboratory. Approximately 2.4 mg of K-feldspar was loaded into an aluminum foil packet and stacked vertically with other unknowns along with GA1550 biotite flux monitor (age = 98.79 Ma) and K_2SO_4 and CaF_2 salts to correct for nucleogenic interferences. Following a cumulative 25-hour irradiation at the USGS Triga reactor, K-feldspars were split into three aliquots, loaded into a sample planchet and brought to vacuum by a turbomolecular pump coupled with a rotary backing pump. Samples were fused using a Merchantek dual UV/ CO_2 laser system. Extracted gas was purified with an SAES getter for 10 minutes. The gas was then measured by an Argus VI magnetic sector mass spectrometer equipped with five faraday cups. Masses 40, 39, 38, 37, and 36 were measured concurrently to enable calculation of the radiogenic ^{40}Ar component and correct for nucleogenic interferences (^{40}Ca , ^{42}Ca , ^{37}Cl , ^{40}K) on Ar isotopes. Raw data was reduced using ArArCalc software (Koppers, 2002) to regress to time-zero beams and to correct for blank, mass discrimination, nucleogenic interferences, and decay following irradiation. K-feldspar $^{40}\text{Ar}/^{39}\text{Ar}$ analytical data are provided in Table D.7. Data for the three aliquots in the inverse isochron plot show a well-fit linear correlation with an $^{40}\text{Ar}/^{39}\text{Ar}$ intercept indicative of a trapped excess Ar component.

2.3.5 Apatite (U-Th)/He thermochronometry

Measurements for apatite (U-Th)/He thermochronometry were made in the Noble Gas Thermochronometry Laboratory at the Berkeley Geochronology Center. A brief description of

the methodology is provided here; for a full description of the measurement procedures, see Tremblay et al. (2015).

Individual, euhedral apatite crystals with no visible fluid or mineral inclusions and equivalent spherical radii of 50 μm or greater were selected, photographed, and measured using a Leica MZ16 stereomicroscope. Individual crystals were loaded into PtIr packets and heated under vacuum to $1050 \pm 50^\circ\text{C}$ for 6 minutes with an 810 nm wavelength diode laser. The extracted gas was spiked with an aliquot of ^3He , purified, and analyzed using a Pfeiffer Prisma quadrupole mass spectrometer QMS 200 under static vacuum. Helium blanks, determined by heating empty PtIr packets, were typically less than 5×10^{-17} moles. To achieve complete helium extraction, each sample was reheated until the ^4He yield was less than 0.5% of the ^4He yield in the first heating step. Molar ^4He abundances were calculated by dividing the measured $^4\text{He}/^3\text{He}$ ratio by the $^4\text{He}/^3\text{He}$ ratio of a manometrically-calibrated ^4He standard gas aliquot spiked with the same molar abundance of ^3He as was the unknown, and multiplying this value by the known ^4He molar abundance of the standard gas.

After degassing, each sample was dissolved in 50 μL of 7N HNO_3 spike solution containing 9.20×10^{-10} mol/L ^{233}U , 9.03×10^{-10} mol/L ^{229}Th , and 6.7% enriched ^{147}Sm spike. Solutions were diluted by a factor of 20 and analyzed on a Thermo Scientific Neptune Plus multicollector ICP-MS with an Aridus2 desolvating nebulizer sample introduction system. To standardize the analyses, we also analyzed a spiked normal solution with known U, Th, and Sm concentrations. Spiked normal solution isotope ratio measurements were reproducible to much better than 0.5% for each element. (U-Th)/He ages were calculated using blank corrected ^4He , ^{147}Sm , ^{232}Th , and ^{238}U abundances. Raw ages were corrected for alpha ejection effects after Farley et al. (1996).

2.4 Discussion of results

2.4.1 Geochronology and thermochronometry

All geochronological and thermochronometric data can be found in Tables D.6 and D.7. Apatite grains picked from an ash in the Oligocene Rigongla Formation in the Oiyug Basin (Fig. 2.1C) yielded a U-Th/He age of 5.04 ± 0.65 Ma. A rhyolite immediately above the Rigongla-Nianbo unconformity provides an $^{40}\text{Ar}/^{39}\text{Ar}$ K-feldspar age of 28.90 ± 1.52 Ma (Fig. 2.4), providing a minimum age of the underlying Nianbo Formation. Apatite grains from two granites just north of the Penbo Basin, L0706-2 and L0706-3, yielded U-Th/He ages of 14.86 ± 1.83 Ma and 12.74 ± 1.47 Ma (1σ), respectively.

2.4.2 $\delta^{13}\text{C}$, $\delta^{18}\text{O}$ and clumped isotope-derived temperatures

Penbo Basin

All carbonate oxygen and carbon isotopic compositions are reported on the VPDB scale. The oxygen isotopic compositions of all 68 calcites sampled from the Pana and Nianbo Formations in the Penbo basin range from -22.8 to $-9.4 \pm 0.1\text{‰}$, with mean values of $-14.0 \pm 1.2\text{‰}$ and $-15.1 \pm 2.1\text{‰}$ (1σ), respectively (Table D.1). The carbon isotopic compositions range from -10.4 to -0.1‰ . The mean $\delta^{13}\text{C}_c$ for all calcites of the Pana and Nianbo Formations vary by 1.5‰ , with values of $-6.0 \pm 1.5\text{‰}$ and $-4.5 \pm 2.3\text{‰}$ (1σ), respectively. Pedogenic and lacustrine carbonate typically derive their carbon from different sources and precipitate under different environmental conditions, thus providing additional information for environmental reconstructions. As such, it is worth noting isotopic variability between lithologies. The mean $\delta^{13}\text{C}_c$ values for paleosol carbonate in the Paleocene-Eocene Nianbo and Eocene Pana Formations are $-6.9 \pm 0.8\text{‰}$ and $-5.4 \pm 2.2\text{‰}$, respectively. The mean $\delta^{13}\text{C}_c$ values for lacustrine carbonate are $-5.7 \pm 1.8\text{‰}$ and $-3.2 \pm 1.7\text{‰}$.

In the subset of samples with clumped isotope measurements and petrographic character-

ization, both the "primary" carbonates and those with more extensive signs of recrystallization span -12 to -18‰ in $\delta^{18}\text{O}_c$ space. The three unaltered or minimally altered carbonates from the Nianbo Formation record $\Delta_{47,CDES}$ values of 0.700 to 0.730 ± 0.020 (D.3). These carbonates yield $T(\Delta_{47})$ of 6 to 12°C (Fig. 2.5). As described in the Methods section, we interpret these as primary carbonate reflecting original depositional temperatures. Four pedogenic and lacustrine carbonates exhibit more extensive recrystallization in thin section. These altered carbonates have $\Delta_{47,CDES}$ values of 0.540 to 0.590 ± 0.010 with corresponding paleo-temperatures from 41 to 55°C . The upper end of this temperature range is similar to those determined from visual Thermal Alteration Index values for organics sampled from the base of the Penbo section. These values correspond with vitrinite reflectance values (R0) of 0.4% to 0.5%, indicating burial temperatures ranging from 53 to 75°C (Barker, 1988).

The observed variability in both $\delta^{18}\text{O}_c$ and Δ_{47} does not display any stratigraphic trend that can be attributed to progressive burial diagenesis with depth (Fig. 6). The samples that show petrographic and Δ_{47} signs of alteration are not appreciably shifted in $\delta^{18}\text{O}_c$, implying that the alteration in these samples was rock-buffered, i.e. carbonate buffered the oxygen isotopic composition relative to the small amount of water present in the system. We emphasize paleo-elevations derived from samples with Δ_{47} analyses (Table D.3), but include data from all samples (measured $\delta^{18}\text{O}_c$ only) under the assumption that any alteration took place in a rock-buffered system. The remainder of the discussion of the Penbo basin samples will focus on the implications of the isotopic compositions of the minimally altered, micritic carbonates.

Oiyug Basin

Table D.3 provides $\delta^{13}\text{C}_{\text{CO}_3}$, $\delta^{18}\text{O}_{\text{CO}_3}$, $\delta^{18}\text{O}_{\text{CO}_2}$, Δ_{47} , and Δ_{47} measurements for the eleven Oiyug Basin samples selected for clumped isotope analyses. Traditional oxygen and carbon isotopic compositions of the entire Oiyug Basin sample set are reported in Table D.2. Isotopic variations were assessed for trends with location in section (relative age) and sediment type.

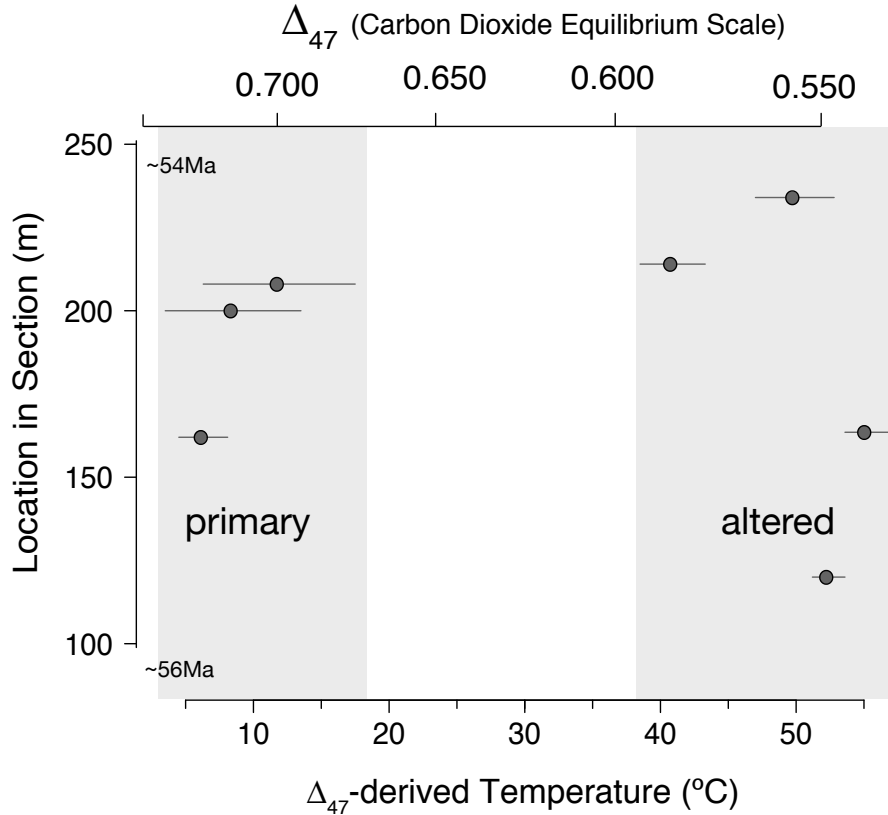


Figure 2.5 **Clumped isotope-derived paleotemperatures of samples from the Penbo Basin with relative age.** Ages are based on location in stratigraphic section and interbedded ashes. Δ_{47} is reported in CDES (carbon dioxide equilibrium scale) reference frame (Dennis et al., 2011). Error bars represent $\pm 1\sigma$ of all replicate analyses of each sample (n listed in Table D.3).

Oxygen analyses of siderites and dolomites from the Oiyug basin yield discrepant results from the dominant calcite mineralogy. For example, calcites from the Oiyug Formation (~ 8.1 to 2.5 Ma, Chen et al. (2008)) yield $\delta^{18}\text{O}_c$ and $\delta^{13}\text{C}$ values of -28.0 to $-27.4 \pm 0.1\text{‰}$ and -0.1 to 1.3‰ VPDB, and the siderite nodule, -10.8‰ and 12.9‰ . As such, siderites and dolomites are considered separately in this study.

Calcites from the Gazhacun Group (>15.03 Ma, Spicer et al. (2003)) yield mean $\delta^{18}\text{O}_c$ and $\delta^{13}\text{C}_c$ values of $-18.8 \pm 2.6\text{‰}$ (ranging -21.1 to -11.6‰) and $-6.3 \pm 1.6\text{‰}$ (ranging -8.0 to -2.5‰). Dolomites from the Gazhacun Group yield mean $\delta^{18}\text{O}_c$ and $\delta^{13}\text{C}_c$ values

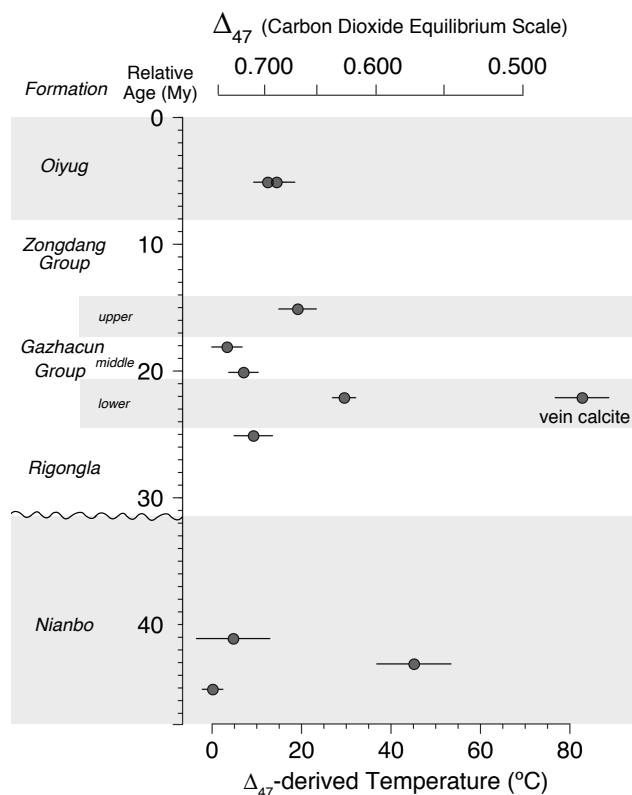


Figure 2.6 **Clumped isotope-derived paleotemperatures of samples from the Oiyug Basin with relative age.** Ages are based on location in stratigraphic section and interbedded ashes. Δ_{47} is reported in CDES (carbon dioxide equilibrium scale) reference frame (Dennis et al., 2011). Error bars represent $\pm 1\sigma$ of all replicate analyses of each sample (n listed in Table D.3).

of $-6.9 \pm 2.3\text{‰}$ (ranging -11.3 to -5.5‰) and $-6.8 \pm 2.4\text{‰}$ (ranging -11.3 to -5.1‰). One lacustrine siderite from the top of the Gazhacun Group yields $\delta^{18}\text{O}_c$ and $\delta^{13}\text{C}_c$ values of -17.1‰ and 4.2‰ , respectively. The mean $\delta^{18}\text{O}_c$ and $\delta^{13}\text{C}_c$ values of calcite in the Rigongla Formation (31.4 to 15.1 Ma, Zhu et al. (2006)) are $-16.4 \pm 4.0\text{‰}$ (ranging -20.4 to -11.9‰) and $-3.9 \pm 1.4\text{‰}$ (ranging -6.2 to -2.6‰). Calcites from the Nianbo Formation (63.8 to 50.2 Ma, Wang et al. (2014)) yield slightly more depleted $\delta^{18}\text{O}_c$ of -24.9 to $-18.6 \pm 0.1\text{‰}$. The mean $\delta^{13}\text{C}_c$ value of the Nianbo Formation is $-3.0 \pm 1.4\text{‰}$, which agrees within error with the carbon isotope values of the Nianbo Formation in the Penbo basin.

Eight of the pedogenic, groundwater, and lacustrine calcites yield $\Delta_{47,\text{CDES}}$ measurements ranging from 0.625 to 0.755. These values correlate to temperatures that range from 30°C to 1°C (Fig. 2.6), which are in the realm of plausible low-latitude, high-elevation surface temperatures (Lawrimore et al., 2011).

A vein calcite (543Av) from the Lower Gazhacun Formation yields a low Δ_{47} value of

0.467±0.014 and corresponding higher temperature of 83.3±6.0°C (±s.e.m., n=2). This vein was sub-sampled from pedogenic calcite 543A, which yielded a Δ_{47} value of 0.625±0.010 and paleo-temperature of 30.1±2.6°C (±s.e.m., n=4). Even if this pedogenic calcite precipitated at the warmest part of the day during the warmest month of the year, 30°C is likely warm for >4 km elevation. There are at least two plausible scenarios that would result in a soil carbonate T(Δ_{47}) greater than mean air temperature:

(1) Pedogenic T(Δ_{47}), on average, exceeds mean summer air temperature by 3 to 5°C (Hough et al., 2014), and mean annual air temperature by 10 to 15°C due to summertime bias in soil carbonate formation (Quade et al., 2013) and increased solar heating of the soil surface (Passey et al., 2010). Applying the latter offset, the air temperature above the location of soil carbonate formation would have been 15 to 20°C. While seasonality may have the dominant effect on soil carbonate Δ_{47} (Passey et al., 2010; Suarez et al., 2011; Peters et al., 2013; Quade et al., 2013; Hough et al., 2014), Δ_{47} also varies with soil depth and duration of shade cover (Quade et al., 2013), soil moisture as it relates to the timing of carbonate formation (Burgener et al., 2016), and local soil hydrology (Ringham et al., 2016). This is to say, at the same elevation and atmospheric temperature, but under variable environmental conditions, two pedogenic calcites could record significantly different Δ_{47} values. For example, the two pedogenic calcites most proximal to 543A, within the Gazhacun Formation and 40 meters below in the Rigongla Formation, yield T(Δ_{47}) values of 7.6±3.3°C and 9.8±4.3°C, respectively. Therefore, it is reasonable to believe that the air temperature above soil carbonate 543A was much cooler than 30°C.

(2) The bulk rock could have experienced low-grade alteration and partial recrystallization under high temperature associated with the calcite vein (543Av). Even so, there are significant differences between $\delta^{18}\text{O}_{\text{Cc}}$ and Δ_{47} of 543A and 543Av, suggesting that the alteration was not pervasive enough to cause extensive bond reordering or bulk isotopic resetting of the whole rock.

Marl calcite W0628-2 of the Nianbo Formation is also interpreted as diagenetically altered

based on a Δ_{47} value of 0.572 ± 0.027 (\pm s.e.m., $n=3$) and corresponding paleo-temperature of $45.7 \pm 8.3^\circ\text{C}$. However, the other two samples from the Nianbo Formation, W0628-1 and W0628-3, yield Δ_{47} values of 0.755 ± 0.011 ($n=6$) and 0.738 ± 0.040 ($n=3$), corresponding to plausible surface temperatures, $0.7 \pm 2.3^\circ\text{C}$ and $5.3 \pm 8.2^\circ\text{C}$ (Table D.3, Fig. 2.5) for soil carbonates at high elevation. Further, W0628-2 and W0628-3 are identical in $\delta^{18}\text{O}_w$ within uncertainty regardless of the high apparent $T(\Delta_{47})$ retained by W0628-2. This suggests that the isotopic composition of the Nianbo Formation in the Oiyug Basin also reflect a rock-buffered system. As such, samples collected from this section likely maintain oxygen isotopic fidelity even under higher diagenetic temperatures.

Multi-proxy assessment of diagenesis and maximum carbonate temperatures

At sufficiently high temperatures, solid-state bond reordering can occur in the carbonate lattice without the aid of water (Passey and Henkes, 2012). Carbonate that experiences temperatures $>100^\circ\text{C}$ for 10^8 years are subject to reordering of ^{13}C - ^{18}O bonds to a more stochastic distribution (Henkes et al., 2014; Stolper and Eiler, 2015), or a lower Δ_{47} . A high degree of ^{13}C - ^{18}O clumping preserved in the carbonate lattice is thought to be diagnostic of primary carbonate because no known mechanisms have been described to alter a carbonate to a higher Δ_{47} value. However, recent measurements of latest Paleocene marine carbonates (Jialazi Formation) buried to at least 150 to 180°C (Orme, 2015) strongly suggest that ^{13}C - ^{18}O bonds in the carbonate lattice can increase in relative abundance (increasing Δ_{47}) during alteration (see Chapter 5; Ingalls et al. (2016a)). The mechanism by which bond ordering can increase during alteration has yet to be adequately modeled and attributed to a geological process during burial and exhumation. Therefore, it is exceedingly important to provide multiple assessments of alteration and isotopic resetting/reordering when interpreting clumped isotope and traditional stable isotope data.

The detection of diagenetic alteration and isotopic resetting requires careful characterization of carbonate mineralogy, inspection for recrystallization and alteration textures using

petrography and microscopy, and sub-sampling of $\delta^{18}\text{O}_c$ of clasts, veins and matrix material (DeCelles et al., 2007; Saylor et al., 2009) to detect possible diagenesis and isotopic resetting. Unfortunately, micron-scale recrystallization in the matrix and on mineral edges may go unnoticed using only these techniques (Garzzone et al., 2004; Leier et al., 2009). We therefore complement petrographic observations with further geochemical analyses to constrain thermal history and therefore the potential for alteration.

The extent of solid-state bond reordering in a carbonate is dependent on the time-temperature history (e.g., Passey and Henkes (2012)). Thermal maturation is estimated from a Nianbo Formation shale (645A) in the Penbo basin based on the lack of typical petroleum biomarkers (i.e., sterane and hopane) and long-chain n-alkanes indicative of deep burial. Vitrinite reflectance suggests these strata reached temperatures in excess of 110°C . Preliminary analyses of methylphenanthrenes (biomarkers) derived from this shale yield equivalent vitrinite reflectance values of $1.4\pm 0.4\%$, suggesting that these strata reached temperatures in excess of 135°C at some point in their burial history.

Apatite U-Th/He ages from two samples of the Eocene Qianggeren granite (51.9 ± 1.8 Ma; He et al. (2007)) collected ~ 1.5 km apart approximately 5 km north of the Penbo basin section provide some constraints on the upper bound of the duration of increased burial temperatures in the Penbo basin (L0706-2 and L0706-3; Table D.6). U-Th/He ages from these two granites suggest that the Penbo basin region exhumed to temperatures $< 70^\circ\text{C}$ by ~ 12.7 to 14.9 Ma. Given that the uppermost preserved Pana are ~ 50 Ma (Ding et al., 2014) and exhumation by ~ 15 Ma the maximum burial time scale is < 35 million years.

Although the organic thermal alteration estimates would permit temperatures in excess of 150°C for millions of years, such high, sustained temperatures would likely have led to wholesale solid-state reordering and shifts to high $T(\Delta_{47})$ values (Henkes et al., 2014; Stolper and Eiler, 2015). Our petrographically least altered samples record low $T(\Delta_{47})$ values, thereby suggesting these strata were not heated to high enough temperatures long enough to result in significant solid-state bond reordering. There could be slight reordering at the

lower bound temperatures from the organic thermal maturation estimates, perhaps boosting $T(\Delta_{47})$ estimates on the order of 10°C (Stolper and Eiler, 2015). If primary temperatures were cooler than those we estimate directly, then this would result in higher paleoaltimetry estimates. We do not make any correction for this potential slight reordering, thus our altimetric estimates remain conservative.

Testing the predictive capability of petrographic observations in assessing carbonate diagenesis

A subset of nodular, groundwater, lacustrine marl, pedogenic, and vein calcite samples from Penbo and Oiyug were selected for Δ_{47} analyses based on sedimentary and petrographic textures seen in thin section (Tables D.1 and D.2) in order to (1) sufficiently sample primary isotopic compositions to derive paleo-temperatures of each time slice throughout the Cenozoic, and (2) provide a comparison between microscopic assessment of primary carbonate textures and direct measurements of $T(\Delta_{47})$. This enabled a check on our ability to correctly assess diagenetic alteration in thin section. Based on visual observations in petrographic section, each sample was binned as “primary” (lacking evidence of recrystallization), “minor alteration” (heterogeneous, macroscopic and could be potentially avoided by careful sample drilling), or “diagenetic” (extensive recrystallization present).

Temperatures derived from clumped isotope measurements generally corresponded with the petrographic interpretations for six of the seven Oiyug basin samples. One sample, W0628-3 from the Nianbo Formation, was predicted to be diagenetic and yield a high $T(\Delta_{47})$ (low Δ_{47}) because of extensive cross-cutting of secondary calcite veins. Contrary to this assessment, triplicate measurements of micrite from this sample yielded a $T(\Delta_{47})$ of $5.3 \pm 8.2^\circ\text{C}$ (s.e.m.). This combination of petrographic observation and isotopic measurement suggests two possible interactions: (1) alteration occurred very early in the rocks history while the rock was at high elevation prior to burial, so the altered carbonate yields a cool signal, or (2) most of the sample mass is non-altered micrite. In the second scenario, even if the cal-

citic veins have modestly warm temperatures, they do not significantly shift the bulk Δ_{47} values. An alternative possibility that should be entertained is that there is a mechanism of carbonate diagenesis that cryptically recrystallizes pedogenic carbonate on a finer scale than observable by traditional petrographic screening practices (see Chapter 5). However, given the agreement between thermochronometric data, petrography, and the Δ_{47} -derived temperatures ($T(\Delta_{47})$) that sediments and paleosols from the Oiyug and Penbo basins have not reached burial temperatures that would likely alter the original Δ_{47} composition of carbonates via solid-state alteration. Therefore, we consider our low $T(\Delta_{47})$ carbonates from both sedimentary basins to represent primary depositional conditions throughout the Cenozoic.

2.4.3 Paleocene to Pliocene stable isotope paleoaltimetry of the Lhasa Terrane

Numerous investigations have reconstructed the elevation history of the Himalayas and Tibetan Plateau using the oxygen isotopic composition of nonmarine carbonates (Garzione et al., 2000; Rowley et al., 2001; Currie et al., 2005; Rowley and Currie, 2006; DeCelles et al., 2007; Quade et al., 2007; Saylor et al., 2009; Ding et al., 2014; Huntington et al., 2015). The isotopic composition of the carbonate minerals relates to that of the water from which they precipitated, which in turn depends upon the composition of meteoric water falling in the drainage basin. Paleo-elevation estimates then derive from the sensitive relationship between elevation and the isotopic value of precipitation in low-latitude ($<35^\circ\text{N}$) orographic systems (Rowley and Garzione, 2007; Rowley, 2007). This connection is predicted based on atmospheric thermodynamic modeling of the expected isotopic lapse rate for water vapor and precipitation and is verified by modern observations (Rowley et al., 2001; Rowley and Garzione, 2007). The primary determinants of this relationship are the temperature (T) and relative humidity (RH) of the starting air mass. Rowley et al. (2001) used National Centers for Environmental Prediction (NCEP) reanalysis output (Kalnay et al., 1996) of modern global monthly mean data over entirely oceanic, low latitude ($<35^\circ\text{N}$) regions to

compute the probability density function of T and RH. Each starting T and RH populates a unique vertical trajectory through isotopic composition and elevation space. The set of these vertical trajectories define the expected isotopic compositions of low-latitude atmospheric vapor and use empirical fitting to the frequency distribution of isotopic composition of precipitation as a function of elevation. Model elevations are calculated using a quartic function that describes the relationship between elevation and $\Delta(\delta^{18}\text{O}_p)$, where $\Delta(\delta^{18}\text{O}_p)$ is the difference between the oxygen isotopic composition of precipitation at sea level and at high altitude. This function is the condensation-weighted mean polynomial fit to a ~ 33000 iteration regression of 40 years of monthly global mean T and RH data:

$$\text{Elevation (m)} = -0.0155\Delta\delta^{18}\text{O}_p^4 - 1.1302\Delta\delta^{18}\text{O}_p^3 - 33.939\Delta\delta^{18}\text{O}_p^2 - 642.71\Delta\delta^{18}\text{O}_p \quad (2.2)$$

This model has been tested by sampling modern stream waters in the Himalaya to central Tibet, calculating $\Delta(\delta^{18}\text{O}_p)$, and comparing their predicted elevations with the actual modern elevations. This isotopic method yields reasonable fits to these datasets (Rowley et al., 2001; Currie et al., 2005; Rowley and Currie, 2006; Rowley and Garzzone, 2007; Hren et al., 2009). There is some tendency of the model to underestimate elevations rather than overestimate, suggesting that it is likely a conservative proxy for past elevations. Further discussion of the paleoaltimetry model parameters can be found in the Appendix (Section B).

The Siwalik Group has been a favored archive for low-latitude sea level climate conditions in the Neogene, as both carbon and oxygen isotopic compositions are interpreted to be primary (Quade et al., 1995; Quade and Cerling, 1995), and there exists excellent control on depositional age and burial history. We calculate $\Delta(\delta^{18}\text{O}_p)$ using the mean low elevation $\delta^{18}\text{O}_w$ value determined from 2.5 to 12 Ma paleosol carbonates (1 to 5 cm diameter) of the Siwalik Group in Pakistan and Nepal (Quade and Cerling, 1995; Quade et al., 2013). These carbonates are presumed to precipitate in near isotopic equilibrium from soil water, which

is closely related to meteoric water, and the oxygen isotopic fractionation between mineral and water is a function of temperature. We calculate $\delta^{18}\text{O}$ of water in the mineralizing solutions using the $T(\Delta_{47})$ determinations, $\delta^{18}\text{O}_c$ measurements, and the mineral-specific temperature dependent water-carbonate oxygen isotope fractionation as determined by Kim and O'Neil (1997) (calicte), Vasconcelos et al. (2005) (dolomite), and Zhang et al. (2001) (siderite).

$T(\Delta_{47})$ for paleosols from the upper 2.5 km (<5.5 Ma) of the Siwalik Group at Surai Khola in Nepal were $<34^\circ\text{C}$ (Quade et al., 2013). Although the deposits >5.5 Ma experienced greater burial depths and yielded higher $T(\Delta_{47})$, Quade et al. (2013) argues that the Surai Khola sedimentary package is rock-buffered and has undergone little recrystallization, and therefore the primary $\delta^{18}\text{O}_c$ value is preserved. The average $\delta^{18}\text{O}_c$ of the Neogene Siwaliks is -7.4‰ VPDB (Quade et al., 2013). Due to the extent of Δ_{47} alteration during burial in Surai Khola, we do not use the clumped isotope-derived temperatures from deposits older than 5.5 Ma for the calculation of $\delta^{18}\text{O}_w$ from $\delta^{18}\text{O}_c$. Instead, we use low elevation warm month mean temperatures (WMMT) of $28.1\pm 3.4^\circ\text{C}$ derived from a CLAMP (Climate Leaf Analysis Multivariate Program) analysis of two lower Siwalik mid-Miocene fossil flora (Khan et al., 2014). We assign a $\delta^{18}\text{O}_w$ of $-6.6\pm 2.8\text{‰}$ as our low elevation precipitation isotopic value in the Miocene and older sediments and $-4.6\pm 1.4\text{‰}$ to the Pliocene sediments to account for climate change during the Cenozoic. Error is propagated through the paleo-elevation model using the sum in quadrature of the uncertainties associated with calculating mean $\delta^{18}\text{O}_w$ values for each sample, as well as the 2σ Δ_{47} uncertainty.

Carbonate stable isotope paleoaltimetry depends critically on the preservation of a primary $\delta^{18}\text{O}_c$ signal in the variably altered rocks preserved in collisional zones. Primary carbonate isotopic compositions are prone to alteration and diagenetic resetting by deep burial (Leier et al., 2009), which can result in a falsely depleted oxygen isotopic composition, eliminating the possibility of constraining elevation history using the stable isotope record (Garzzone et al., 2004; Leier et al., 2009). Such a depletion of $\delta^{18}\text{O}_c$ would result in an

incorrectly high paleo-elevation interpretation (Garzzone et al., 2004). Our assessment of carbonate diagenesis, discussed in the previous section, employs petrography, vitrinite reflectance, thermochronometric data, and clumped isotope thermometry to rule out the use of isotopic data from thermally mature samples in paleo-elevation reconstructions.

We determine $\delta^{18}\text{O}_c$ - $\delta^{18}\text{O}_w$ fractionation factors ($\alpha_{\text{CO}_3\text{-H}_2\text{O}}$) for calcite (Kim and O’Neil, 1997), dolomite (Vasconcelos et al., 2005), and siderite (Zhang et al., 2001) applying the average Δ_{47} -derived temperature for each unit. Mineralogy-specific fractionation factors are used to derive paleo-surface or groundwater composition ($\delta^{18}\text{O}_w$, Tables D.1 and D.2) from carbonate isotopic values. The dominant controls on $\delta^{18}\text{O}_c$ values of unaltered to minimally altered carbonate are extent of Rayleigh distillation of water vapor in the air masses that deliver precipitation to the region (scales with elevation, Dansgaard (1954)) and extent of evaporative isotopic re-enrichment. An assessment of evaporative enrichment, particularly in the lacustrine dolomites in the Gazhacun Group, is incorporated into our presentation of the isotopic data.

Penbo Basin

All clumped isotope samples from the Penbo Basin are derived from the Nianbo Formation. As such, we use the average of the three Δ_{47} -derived “primary” paleo-temperatures ($8.9\pm 5.0^\circ\text{C}$) coupled with measured $\delta^{18}\text{O}_c$ to calculate the isotopic composition of the water with which calcite equilibrated (Kim and O’Neil, 1997). Paleo-water $\delta^{18}\text{O}_w$ values of the Nianbo Formation (ranging -11.8 to -22.6‰ VSMOW) are used to estimate elevation ($\Delta(\delta^{18}\text{O}_p)$). We report both individual elevation estimates and the mean elevation of each dominant lithology within a geologic formation (Table D.1; Fig. 2.7).

The best estimate of the paleo-elevation of the Nianbo Formation preserved in the Penbo basin is $4.4^{+1.3}_{-1.7}$ km, comparable to modern elevation of this basin (Table D.1; Fig. 2.7). We view this estimate to be conservative because we employ the modern isotopic lapse rate, which is likely significantly steeper than the true lapse rate in the Early Eocene (Rowley and

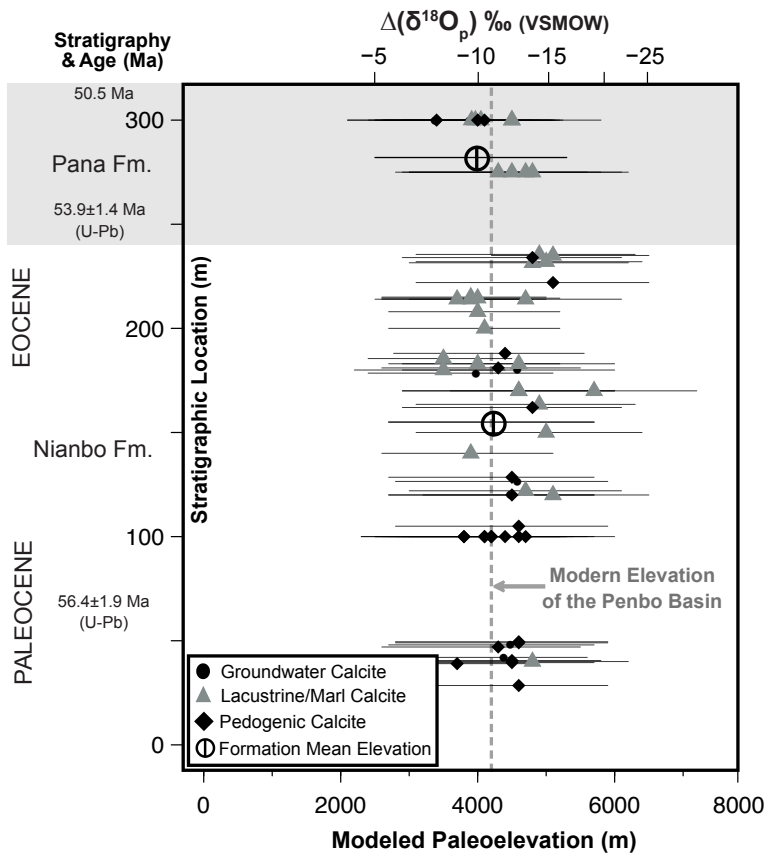


Figure 2.7 **Paleocene-Eocene elevation reconstruction of the Penbo basin.** We use equation 2.2 to convert $\Delta(\delta^{18}\text{O})$ to elevation. The average of the "primary" Δ_{47} -derived temperatures for lacustrine and pedogenic was used for the $\delta^{18}\text{O}_c$ to $\delta^{18}\text{O}_w$ fractionation factors for carbonates of like lithology. Symbols are indicative of lithology. Error bars represent propagation of analytical (s.e.m.) and model error in quadrature. The mean elevation for each formation is indicated by the black circle with vertical line. The vertical dashed line marks the modern hypsometric mean elevation of the Penbo basin.

Garzione, 2007). Further, the Siwalik value for low-latitude ($\sim 19.6 \pm 3.9^\circ\text{N}$) (Quade et al., 1989), low elevation precipitation is likely isotopically lighter than actual precipitation in the Early Eocene source region for moisture advecting to higher altitudes. The use of an isotopically more negative low elevation precipitation source contributes to making our paleoelevation calculations conservative, i.e., underestimates of the true elevation.

We apply the mean $T(\Delta_{47})$ derived from the underlying Nianbo Formation to calculate $\delta^{18}\text{O}_w$ of the overlying upper Pana Formation sediments. This succession yields paleo-surface water isotopic compositions of -16.9‰ to -13.4‰ VSMOW. These paleo-precipitation values correspond with an estimated paleo-elevation of the Pana Formation of $4.1^{+1.2}_{-1.6}$ km, identical to the underlying Nianbo Formation within error.

Oiyug Basin

The Nianbo, Rigongla, and Lower Gazhacun Formations are dominated by a common lithology (pedogenic calcite), which allows for a straightforward characterization of the Paleocene to Miocene elevation history (Table D.2). For samples on which clumped isotope measurements were made, the sample specific $T(\Delta_{47})$ was applied to calculate calcite-water isotopic fractionation. An average $T(\Delta_{47})$ for each geologic formation was applied for samples on which only $\delta^{18}\text{O}_c$ was measured. Employing $T(\Delta_{47})$ values of $3.0^{+8.2}_{-3.0}$ °C for the Nianbo Formation, 9.8 ± 4.3 °C for the Rigongla Formation, and 18.9 ± 8.2 °C for the Lower Gazhacun member, we calculate $\Delta(\delta^{18}\text{O}_p)$ of -18.5 ± 3.1 ‰, -10.7 ± 3.5 ‰, and -13.8 ± 1.9 ‰ VSMOW (1σ), respectively. These formations yield mean elevation estimates of $5.6^{+1.5}_{-2.1}$ km, $4.1^{+1.3}_{-1.6}$ km, and $4.5^{+1.5}_{-1.7}$ km, respectively. The elevation estimate for the Paleocene-Eocene Nianbo Fm suggests that the Oiyug region was 0.5 to 1.5 kilometers higher at the onset of India-Asia collision than it is today.

Early and Middle Miocene Gazhacun carbonate oxygen compositions span a broad range -5.5 to -21.1‰ VPDB. All marl calcite, mudstones, and dolomite deposited in the middle member of the Gazhacun Group are isotopically enriched in ^{18}O relative to other units. The high $\delta^{18}\text{O}_c$ values in the middle Gazhacun member are probably the result of evaporative enrichment because calcites from stratigraphically proximal horizons yielded low $T(\Delta_{47})$ values (3.9 to 19.7°C) with low $\delta^{18}\text{O}$ values. Therefore we can confidently say these low temperature samples host a primary record of paleo-water and have not been driven low $\delta^{18}\text{O}$ values by alteration at high temperature. This evaporative enrichment is not present in lacustrine calcite and siderite in the older Nianbo Formation or the younger Oiyug Formation. The mean elevation derived from the two clumped isotope samples in the Oiyug Formation is $6.5^{+1.8}_{-2.3}$ km using an average $\Delta(\delta^{18}\text{O}_p)$ of -25.4 ± 1.5 ‰ (2σ) (Table D.2). As a comparison, the elevation estimate of siderite nodule 618A from the upper Gazhacun is $4.4^{+1.3}_{-1.8}$ km ($\Delta(\delta^{18}\text{O}_p)$ of -11.7 ‰). We accept the elevations provided by the calcites in the Gazhacun and Oiyug Fms because of the preservation of primary Δ_{47} values (Fig. 2.6) and

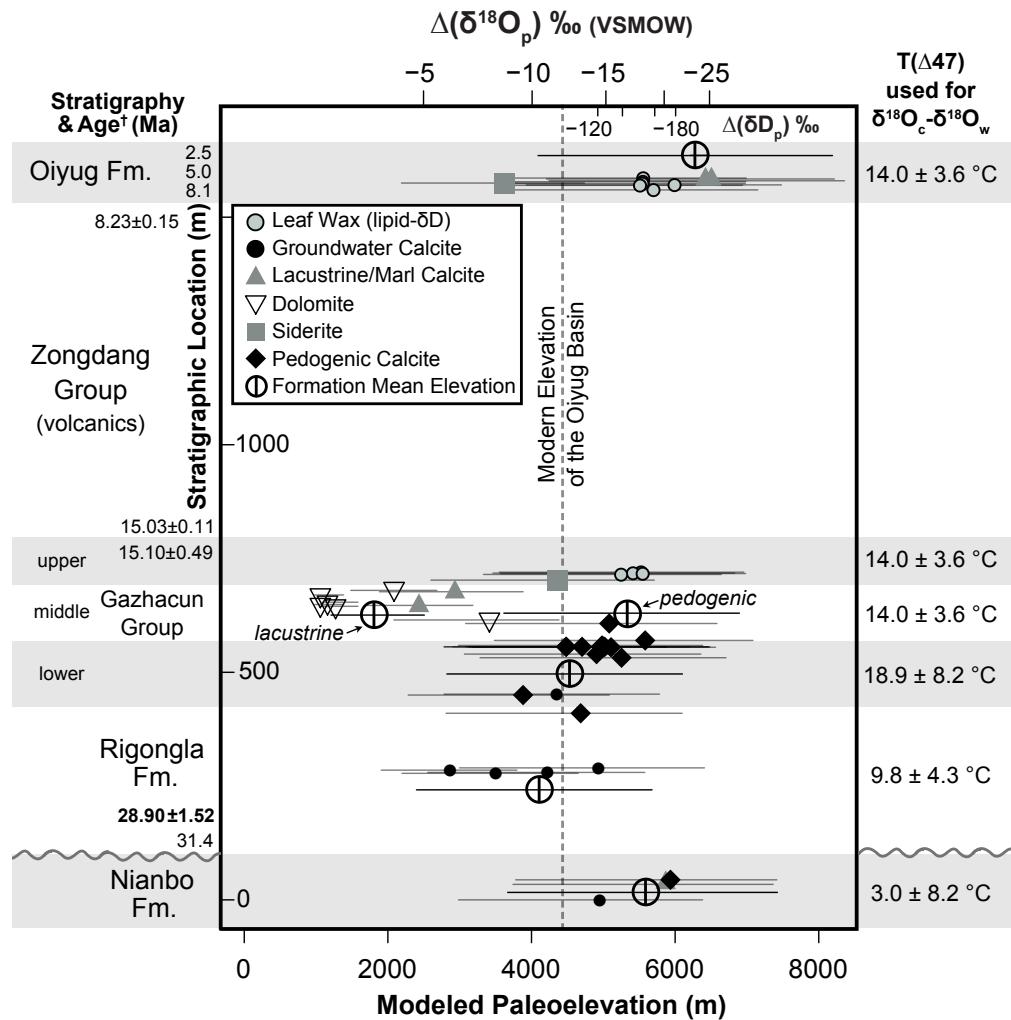


Figure 2.8 Cenozoic elevation reconstruction of the Oiyug basin, southern Tibet. Calculated paleo-elevations and oxygen isotopic compositions of pedogenic, lacustrine/marl, and groundwater calcite, and nodular siderite and dolomite are plotted relative to sample location in stratigraphic section and age. Symbols are indicative of lithology. Ages are taken from paleomagnetic (Chen et al., 2008) and radiometric data (Zhou et al., 2010), as well as one $^{40}\text{Ar}/^{39}\text{Ar}$ age from this study. Error bars represent propagation of analytical (s.e.m.) and model error in quadrature. The mean elevation for each formation is indicated by the black circle with vertical line. The mean elevation derived from lacustrine and pedogenic calcites in the Gazhacun Formation are plotted separately to visualize the isotopic enrichment of lacustrine dolomites and calcites. The vertical dashed line marks the modern hypsometric mean elevation of the Oiyug basin.

the evaporative trend demonstrated by plotting $\delta^{18}\text{O}$ of the two siderite samples relative to $\delta\text{D}_{\text{leaf wax}}$ and $\delta^{18}\text{O}_{\text{calcite}}$ from the same sedimentary horizon (see discussion and Fig. 2.9).

Comparing isotopic and temperature lapse rates

There can be a correlation between degree of depletion of oxygen in meteoric water and formation temperature as both are controlled by atmospheric lapse rates. Estimates of tropical sea surface temperature for times bracketing the age of the Nianbo Formation imply temperatures $>30^\circ\text{C}$ (Pearson et al., 2001) and thus a temperature gradient from sea level to the Penbo Basin of $\geq 20 \pm 5^\circ\text{C}$. Using a typical $6^\circ\text{C}/\text{km}$ atmospheric lapse rate implies elevations in excess of 3 km. Ground surface temperatures are typically warmer than the atmosphere at the same height, and pedogenic and lake carbonates appear to record this with a summer seasonal bias (Huntington et al., 2010). Thus our paleo-temperatures are also consistent with an elevation of ~ 4 km.

2.5 High elevation southern margin of Eurasia

Using $T(\Delta_{47})$ and $\delta^{18}\text{O}$ of pedogenic and lacustrine carbonates from the Paleocene-Eocene Nianbo Formation, we are able to extend the elevation record of the sediments within southern Lhasa block an additional ~ 20 My compared with the oldest prior records (Currie et al., 2016). Our oldest paleo-elevations support a pre-existing ‘high’ topography on the southern margin of Eurasia prior to the onset of India-Asia collision (Ding et al., 2014), with elevations potentially ~ 1 km higher than today in some areas. However, the sediments of the Nianbo Formation could have been deposited at an even higher altitude. The Paleocene-Eocene elevation estimate presented here is conservative because the isotopic lapse rate model is constructed using global mean T and RH data for the modern low-latitude ocean surface. The warmer temperatures of the Eocene would shift the $\Delta(\delta^{18}\text{O}_p)$ -elevation relationship to higher elevation changes for a given offset in precipitation isotopic compositions (see Rowley

(2007) for an in depth discussion). We accept the modern calibration as a conservative representation of past environmental conditions because we are data-limited in our knowledge of the frequency distribution of low-latitude ocean surface T and RH in the Paleocene-Eocene.

The Paleocene-Eocene Nianbo Fm sits unconformably below the Rigongla in the Oiyug Basin, so the elevation history between the two units is unconstrained. However, the similarity of estimated T(Δ_{47}) and $\delta^{18}\text{O}$ of the Nianbo and Rigongla imply little variability during this interval. The Rigongla and lower Gazhacun Fms yield elevation estimates close to the modern mean elevation of the Oiyug Basin. A face value assessment of model elevations from the middle and upper Gazhacun Formations, when interpreted based on $\Delta(\delta^{18}\text{O}_p)$ alone, would suggest that the southern Lhasa block experienced an interval of topographic deflation to 2.5 km in the early-mid Miocene. However, it is unlikely that the hypsometric mean elevation of the Oiyug Basin experienced subsidence from 4.5 km to 2.5 km in the Miocene, followed by an uplift to >6 km in the Pliocene, and subsidence to \sim 4.6 km by present day. It is more likely that the enriched oxygen values of the Gazhacun Formation are an evaporative overprint of the original precipitation signal.

However, the potential low in Miocene elevation temporally corresponds with the formation of the Kailas Basin (26 to 18 Ma, DeCelles et al. (2011); Leary et al. (2016)). The Kailas Formation, named after its type locality at Mt. Kailas, extends \sim 1400 km along strike and is <1 to 4 km thick where exposed (Leary et al., 2016). The Kailas basin is interpreted as a continental rift basin resulting from <5 to 10 km horizontal extension, which has been attributed to rollback of the subducting Indian slab beneath Tibet (DeCelles et al., 2011). The shearing and subsequent breakoff of the Indian slab would have caused a southward and downward pull on the overlying Indian continent, resulting in enough extension to drive the subsidence necessary to form the Kailas basin in southern Tibet (Leary et al., 2016). Due to the temporal overlap of the extension associated with the formation of the Kailas basin and the deposition of the isotopically enriched sediments of the middle Gazhacun member in the Oiyug Basin, we entertain the possibility that the marl calcites and dolomites in this

study preserve a primary isotopic signature representative of mid-Miocene precipitation.

Further work to the west along the southern Lhasa Block could determine whether the apparent lower elevations are actually a local evaporative overprint as interpreted here or are seen in the coeval carbonate record in the southern Lhasa block, and whether there is evidence elsewhere of ~ 6 km elevations five million years ago.

2.5.1 Prior work on pre-collisional topography

A prior study suggested that the Lhasa Block was already high prior to the onset of collision (Ding et al., 2014). They first hypothesized that the Penbo Basin was located >4 km above sea level applying traditional $\delta^{18}\text{O}$ stable isotope paleoaltimetry on lacustrine and pedogenic carbonates. Diagenetic alteration with isotopically light meteoric water or at elevated temperature can cause large wholesale shifts to lighter values in carbonate $\delta^{18}\text{O}$, and the traditional measurements did not distinguish between whether the isotopically light carbonates were primary compositions or reflected alteration. Ding et al. (2014) therefore took an intriguing approach using NanoSIMS $\delta^{18}\text{O}_c$ from a traverse across the width of an ostracod fossil to show what they interpreted as seasonal variations, which they presented as their strongest evidence that the $\delta^{18}\text{O}_c$ values represented primary compositions.

While this is an interesting approach and result, their interpretation is far from resolved for several reasons. The spread in their compositions (1 s.d. = 1.0‰) is not different from typical analytical precision of NanoSIMS oxygen isotope measurements on carbonates at this spatial scale (Hoppe et al., 2013; Bojanowski et al., 2015). Their traverse included only five measurements, which limits the ability to resolve oscillations. To the best of our knowledge, there are no modern studies on ostracod carapaces to demonstrate variation in original $\delta^{18}\text{O}$ at this spatial scale. If one were to accept that the Ding et al. (2014) NanoSIMS data show true variation in fossil ostracod $\delta^{18}\text{O}$, then we return to the question of whether or not the variation is primary, e.g. the asserted seasonal variation.

Ostracod carapaces are quite thin – commonly tens of microns thick – with a structure

that includes chitin and calcite. These carapaces are shed and regrown as the inhabitant micro-crustaceans outgrow their old carapaces. The length of time required to grow and mineralize a carapace is short (e.g., hours to days), and can vary by species (e.g., Roca and Wansard (1997); Ito et al. (2003)). These intervals are thought to be longer at lower temperatures, but are still generally rapid (often hours to days, at most) as survival rates are poor with slow mineralization (e.g., Roca and Wansard (1997)). Although some ostracods may have total life spans of a few years, many are much shorter. The time between molting of their carapaces is typically a few months (e.g., Cohen and Morin (1990)). Again, given that calcification is completed rapidly when the carapace initially forms, a carapace does not record seasonal variation in temperature or composition, so the variation observed in Ding et al. (2014) cannot have been seasonal.

Patterns of ostracod mineralization are complex and can result in different textures across a carapace (Decrouy et al., 2011). These spatial variations in mineralization and chitin content can lead to spatial variation in development of post-mortem porosity and permeability. Void space within the ostracod carapaces are filled with early cementing sparry calcite. It is not at all clear how much primary variation in isotopic composition exists within ostracod shells, nor the extent to which early infilling cements might mimic or contrast with the biomineralized calcite.

Later diagenetic alteration could act to eliminate isotopic variation through thorough overprinting, or it could partially preserve original variation, attenuating this variation through roughly a constant extent of alteration towards equilibrium with a later diagenetic fluid at elevated temperature, or it could impart isotopic variation through heterogeneous diagenetic alteration. The NanoSims analyses do not demonstrate analytically resolvable variation in oxygen isotope composition within the ostracod fossil. If such variation could be shown, it is unclear whether that would reflect primary variation, either fully preserved or attenuated, or heterogeneous diagenesis. Given these uncertainties, our results supercede the Ding et al. (2014) results by presenting a more robust assessment of secondary alteration

and by demonstrating that any alteration that did take place occurred within a rock-buffered system.

2.5.2 Past models of the regional tectonic history of the Lhasa Block

The tectonic development of Earth's quintessential active continent-continent collision zone has been extensively studied for the past three decades, with particular attention paid to the development and persistence of extreme high elevations. However, the majority of previous work on the uplift history invoke models of en masse (England and Houseman, 1986; Harrison et al., 1992; Molnar et al., 1993; Harrison et al., 1995) or local (Wang et al., 2006) plateau uplift in the Neogene. The paleoaltimetry work presented in this paper provides geochemical evidence that counters models involving late Cenozoic uplift.

Late Cretaceous to Early Cenozoic

Contrary to earlier models of Neogene uplift, Kapp et al. (2007) presented tectonic evidence that the Lhasa Block must have undergone extensive crustal thickening by the early Paleogene, if not in the Cretaceous. Kapp et al. (2007) utilized kinematic models to demonstrate that a pre-collisional northward-vergent retroarc thrust belt could have accommodated >250 km of north-south shortening. They attribute an additional >160 km of shortening to the emplacement of the Lhasa-Damxung thrust sheet, which is associated with a magmatic flare-up ~69 Ma that they suggest was due to removal of thickened mantle lithosphere. Kapp et al. (2007) coin their tectonic evolution model for the Lhasa terrane the “Lhasaplano” – a Cretaceous-early Tertiary Cordilleran-style (contractional) orogen associated with the Gangdese magmatic arc. Our >4 km Paleocene-Eocene elevation reconstruction largely agrees with the Lhasaplano model.

Late Cenozoic

Harrison et al. (1992) and Molnar et al. (1993) assert that the southern Tibetan Plateau reached its maximum elevation by 8 ± 1 Ma. Harrison et al. (1992, 1995) suggest that the initiation of slip on the Nyainqentanghla detachment fault is the result of the Tibetan Plateau attaining its maximum potential crustal thickness for the lithospheric temperature distribution and convergence rate. Their logic draws from the earlier work of England and McKenzie (1982) and England and Houseman (1986) on the response of the continental lithosphere to deformation. Continental deformation depends on the rheological stress state of the lithosphere, the Argand number, and distribution of heat-producing elements, and thus temperature, within the crust (England and McKenzie, 1982). The Argand number is the vertically averaged strength of the lithosphere (England and McKenzie, 1982). The vertical stresses in the lithosphere are more than the horizontal stresses, such as those related to convergence, then the lithosphere reaches its yield strength and either a plateau forms or extensional collapse ensues.

Harrison et al. (1992, 1995) reason that slip on the northeast-southwest striking Yangbajian graben northwest of Lhasa and other north-south striking rifts are indicative of extensional orogenic collapse due to over-thickening of the continental crust during shortening (England and Houseman, 1986). Potassium feldspar and biotite $^{40}\text{Ar}/^{39}\text{Ar}$ thermochronological data from an uplifted footwall of the graben-defining Nyainqentanghla detachment fault are indicative of fault and shear zone initiation at 8 ± 1 Ma. They use the numerically modeled temperature history and slip rate (3 mm/yr) to predict that the southern Tibetan Plateau reached its elevation and crustal thickness threshold at this time, and collapsed under its over-thickened crustal mass by way of graben formation.

However, Kapp et al. (2007) suggests that northward-vergent retroarc thrusting and ramp anticline formation, terminating at the same Nyainqentanghla range that bounds the northwestern edge of the Yangbajian graben from Harrison et al. (1995)s thermochronology transects, accommodated >250 km of convergence from 105 to 53 Ma. Growth of this

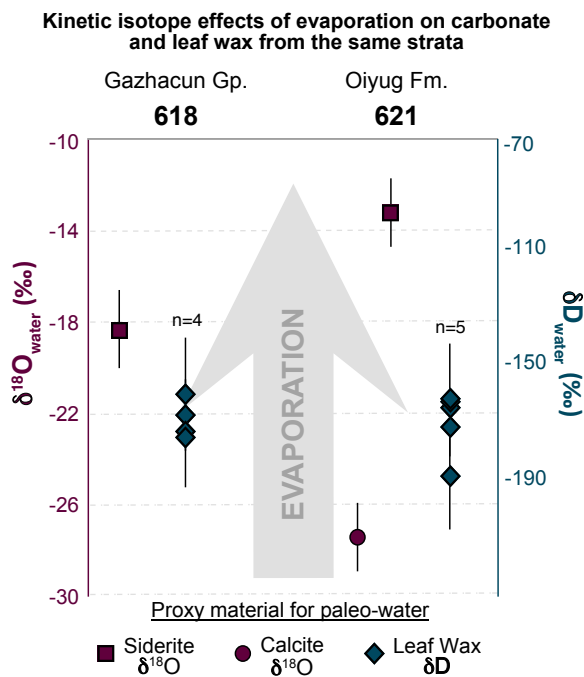


Figure 2.9 **Effects of evaporation on siderites (dark red square), calcites (dark red circles) and leaf wax (blue-green diamonds) from the same sedimentary horizon.** Inferred paleo-lake and soil water hydrogen and oxygen isotope compositions are plotted for sedimentary horizons 621 (Oiyug Formation) and 618 (Gazhacun Group). The $\delta^{18}\text{O}_{\text{w}}$ values are calculated from $\delta^{18}\text{O}_{\text{c}}$ measurements on carbonate minerals, and $\delta\text{D}_{\text{w}}$ values are calculated from leaf waxes, as described in the main text. The $\delta\text{D}_{\text{w}}$ and $\delta^{18}\text{O}_{\text{w}}$ axes are aligned using the Rozanski et al. (1993) Global Meteoric Water Line equation ($\delta\text{D}=8.13* \delta^{18}\text{O}+10.8$).

anticline is coeval with the oldest Linzizhong volcanic rocks (ca. 69 Ma). Our paleoaltimetry results imply that the region north of Lhasa near Nyainqentanghla reached near-modern elevations by the early Cenozoic, concomitant with the northward-vergent ramp anticline system.

2.6 The impact of evaporative enrichment of surface waters on paleo-elevation estimates

Elevations derived from two siderite samples (621F and 618A of the Oiyug Basin) are apparently offset by up to 2 km from the bulk of the data in their sampled sections. Here we present an assessment of evaporative overprinting of primary water signatures in these siderites. We interpret the siderites as evaporatively enriched, and report the mean elevation estimates of each formation focusing on preserved primary oxygen values.

Evaporative re-enrichment of $\delta^{18}\text{O}_{\text{w}}$ as recorded by $\delta^{18}\text{O}_{\text{c}}$ is particularly prevalent in car-

bonates formed in closed lakes and some groundwater systems (Steinman et al., 2013). The covariance of oxygen and hydrogen isotopes of meteoric water usually follow the established Global Meteoric Water Line (GMWL, Friedman (1953); Rozanski et al. (1993)). However, fast evaporation causes a kinetic isotope effect that disturbs this trend with a greater effect on the oxygen isotopes (Craig, 1961). The “evaporative slope”, or trajectory off the GMWL, is determined by local relative humidity and temperature (Clark and Fritz, 1997) and wind speed over the surface (Craig and Gordon, 1965). Polissar et al. (2009), using combined $\delta^{18}\text{O}$ and δD of samples from the Lunpola Basin, were able to corroborate the interpretation of (Rowley and Currie, 2006) that variable evaporative enrichment was the primary control on the isotopic composition of their samples. Polissar et al. (2009) thereby provided independent support for the use of the more negative oxygen isotopic compositions for the purposes of paleoaltimetry.

Oiyug Basin localities 618 (Upper Gazhacun Fm) and 621 (Oiyug Fm) provide both $\delta^{18}\text{O}$ and δD (from carbonates and organics, respectively), allowing us to plot these samples relative to the GMWL ($\delta\text{D}=8.13* \delta^{18}\text{O}+10.8$, Rozanski et al. (1993)). It is worth noting that the governing equation for the GMWL is determined primarily by the ratio of deuterium and oxygen vapor-water fractionation factors (Dansgaard, 1964; Craig and Gordon, 1965). In Figure 2.9, we have correlated $\delta^{18}\text{O}_w$ and δD_w using the GMWL in order to compare relative isotopic enrichment of different materials within the same sedimentary horizons (618 or 621). This alignment means that if the paleo-water isotopic composition lay on the modern Global Meteoric Water line, the corresponding carbonate and leaf wax samples would yield inferred $\delta^{18}\text{O}_w$ and δD_w values in the same vertical position. Calcite-derived surface water oxygen isotope compositions from the 621 horizon are isotopically lighter than their corresponding δD values, calculated from coeval leaf waxes. Very low $\delta^{18}\text{O}_w$ could indicate diagenesis, but because both calcites retain primary Δ_{47} -derived temperatures, we can rule out the possibility of excessive alteration.

However, the two siderites from the 618 and 621 localities yield $\delta^{18}\text{O}_w$ estimates that

are ~ 4 to 10% higher than expected from δD of coeval leaf waxes. Lacustrine siderite 621F has experienced much greater evaporative enrichment than pedogenic calcites 621H and 621I from the same strata. This could be indicative of a period of greater aridity or deposition in a closed playa lake rather than an open system, or a change in atmospheric circulation over the Lhasa Block in the late Cenozoic. The difference between the isotopic compositions of leaf waxes and siderite in the Miocene Gazhacun Formation is negligible within uncertainty.

Based on the observation that the calcites from these localities appear to preserve primary depleted $\delta^{18}O_w$ values, we interpret the enriched $\delta^{18}O$ siderites to be the product of groundwater evaporation. This suggests that any estimated water $\delta^{18}O$ compositions from this section $> -20\%$ are likely evaporatively enriched. We follow this approach by stressing elevation estimates based on the more depleted compositions under the assumption that more enriched values reflect more extensive evaporative re-enrichment relative to precipitation (Clark and Fritz, 1997).

2.7 Cenozoic climate

Reported $T(\Delta_{47})$ values (Table D.3) are likely warmer than mean annual air temperature (MAAT) due to the nature of increased carbonate precipitation in the warm months in both soils and lake settings (Quade et al., 2013; Huntington et al., 2010). $T(\Delta_{47})$ therefore likely correlates with a warm month, June-July-August (JJA), temperature for lake-derived sediments and a peak summer temperature for paleosols (Quade et al., 2013). Soil carbonate formation (due to CO_2 outgassing during groundwater evaporation) is most prevalent in the summer due to incident sunlight warming the uppermost 25 centimeters of soil. Lacustrine carbonate formation occurs in warm, unmixed near-surface waters. Here, abundant sunlight supports photosynthetic carbon fixation, which in turn can drive calcite and aragonite supersaturation by increasing pH and providing carbonate nucleation sites (Stumm and Morgan, 1981). For the purpose of both isotopic and temperature lapse rates in calculating paleoelevations, reporting warmer temperatures than MAAT assures a conservative estimate of

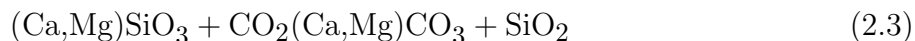
paleo-elevation.

The increased evaporative signal seen in the middle Gazhacun lake sediments could indicate a paleo-environmental change, such as shallower playa lakes in this region in the mid-Miocene, or a paleo-climatic change, such as warmer temperatures, decreased humidity, or changes in atmospheric circulation injecting drier air masses. The lacustrine dolomites from the Badamaqen section are stratigraphically closest to clumped isotope sample 555 with a $T(\Delta_{47})$ value of $19.7 \pm 4.2^\circ\text{C}$ (\pm s.e.m.). However, the lacustrine calcites, 551 and 553, are temporally bracketed by clumped isotope samples 554B and 548 with $T(\Delta_{47})$ values of $3.9 \pm 3.4^\circ\text{C}$ and $7.6 \pm 3.3^\circ\text{C}$, respectively. Khan et al. (2014) used the Climate Leaf Analysis Multivariate Program (CLAMP) on an ~ 15 Ma fossil flora to predict a WMMT of 8.8°C and cold month mean temperature (CMMT) of $-6 \pm 4^\circ\text{C}$ for the Oiyug Basin. Sample 555 does not provide enough evidence to suggest that the mean temperature of the Oiyug Basin was significantly warmer during the mid-Miocene. The preservation of evaporatively enriched $\delta^{18}\text{O}$ in lake sediments can potentially be attributed to shallow playa lake morphology, but changes in regional climate, orographic barriers, and atmospheric circulation should be considered.

2.7.1 Tectonic-weathering-climate feedbacks

Himalayan paleoaltimetry, or more specifically, the timing of the rise of the Himalaya, has figured prominently in attempts to connect global cooling during the Cenozoic with continental weathering rates and pCO_2 (Ruddiman and Kutzbach, 1989; Raymo and Ruddiman, 1992; Harrison et al., 1992; Kutzbach et al., 1989; Molnar et al., 1993). Cenozoic cooling has been documented most thoroughly in the $\delta^{18}\text{O}$ records of benthic forams (e.g., Zachos et al. (2001)). The potential for a connection between global climate and weathering is forged through the central role of CO_2 as both a greenhouse gas and chemical weathering agent (e.g., Kump et al. (2000)). The chemical weathering of silicate and aluminosilicate rocks consumes CO_2 as carbonic acid, exporting cations and carbonate alkalinity to the oceans

where both are removed as carbonate minerals with generic overall reactions (e.g., Ebelmen (1845); Urey (1952); Holland (1978); Berner and Maasch (1996)):



This type of chemical weathering serves as a net sink for atmospheric CO_2 . Raymo et al. (1988) and Raymo and Ruddiman (1992) suggested that uplift of the Himalaya could have enhanced chemical weathering rates by increasing the surface area of aluminosilicates available to weather. This surface area generation resulted from physical erosion processes that are accelerated by relief and glacial activity.

Evidence for the temporal link between the rise of the Himalaya and shifts in global weathering fluxes has relied heavily on the marine Sr isotope record. Sr has a long residence time in the oceans and is well mixed in terms of concentration and isotopic composition. Marine carbonates record the $^{87}\text{Sr}/^{86}\text{Sr}$ ratio of ambient seawater. The marine Sr isotope record is strongly influenced by the weathering flux of Sr to the oceans, and it has therefore been used as a weathering proxy (e.g., Richter et al. (1992); Edmonds (1992)). Shifts in the marine $^{87}\text{Sr}/^{86}\text{Sr}$ record over the Cenozoic appeared to coincide with earlier estimates for the timing of the uplift of the Himalaya (e.g., Raymo and Ruddiman (1992); Richter et al. (1992)). Furthermore, modern day weathering of highly radiogenic terrains in the Himalaya provides a large flux of radiogenic Sr to the ocean, contributing to the continuing rise in the $^{87}\text{Sr}/^{86}\text{Sr}$ ratio of sea water and consistent with overall Neogene trends (Palmer and Edmond, 1989, 1992; Galy et al., 1999).

Large changes in the Sr isotopic composition of the oceans from the Eocene through present have long been interpreted to signify the onset and importance of weathering of the Himalaya and Tibet. By extension, this curve is often cited as an indication that significant topography first developed within the India-Eurasia collisional domain at roughly 38 Ma (e.g., Raymo and Ruddiman (1992); Misra and Froelich (2012)). However, the cited inflection

in the Sr isotope curve could only reasonably be interpreted as the time at which sediment flux from the Himalaya-Tibet orogeny was sufficiently large to perturb the Sr composition of seawater, and is not a direct reflection or measure of topography or uplift. It has also been argued that other proxies for chemical weathering rates and intensity of weathering fit within this paradigm of the onset of Tibetan weathering in the late Eocene (e.g., Li isotopes in Misra and Froelich (2012)).

Our results provide strong evidence for high topography at the Tibetan margin dating to 56 Ma. This is well before the marine $^{87}\text{Sr}/^{86}\text{Sr}$ record begins its approximately monotonic climb towards more radiogenic values. Paleoelevations in the Linzizhong arc had reached modern Tibetan elevations prior to the Paleocene-Eocene Thermal Maximum and overlapped with Early Eocene equable climate states for the Earth (Fig. 2.10). These high elevations were achieved at low latitudes (arc position roughly $19\pm 4^\circ\text{N}$, van Hinsbergen et al. (2012)) in which conditions should have been warm and wet, i.e., favorable for intensive chemical weathering. All told, our paleoaltimetric findings suggest that enhanced chemical weathering of the high Linzizhong arc was insufficient to provide significant climatic forcing, at least during the early and middle Eocene.

This does not rule out the possibility for enhanced weathering related to high topography at the Tibetan margin. The Linzizhong arc would have been a source of highly reactive volcanic glasses and lithologies, i.e., andesite, dacite, and rhyolite with some trachy-andesite and basaltic trachy-andesite (Mo et al., 2008). Weathering of the Linzizhong arc would have delivered rather nonradiogenic Sr to the oceans. The $^{87}\text{Sr}/^{86}\text{Sr}$ of relict volcanic arc dating to that interval is generally between 0.7045 and 0.7075 (Mo et al., 2008). If the Linzizhong Arc became globally significant in terms of supplying weathered Sr to the oceans, the resultant Sr flux would not have shifted marine $^{87}\text{Sr}/^{86}\text{Sr}$ appreciably from its value of 0.7078 in the early Eocene.

Even if there were enhanced chemical weathering associated with the early development of high elevation in the Linzizhong, the overall carbon cycle dynamics associated with tectonism

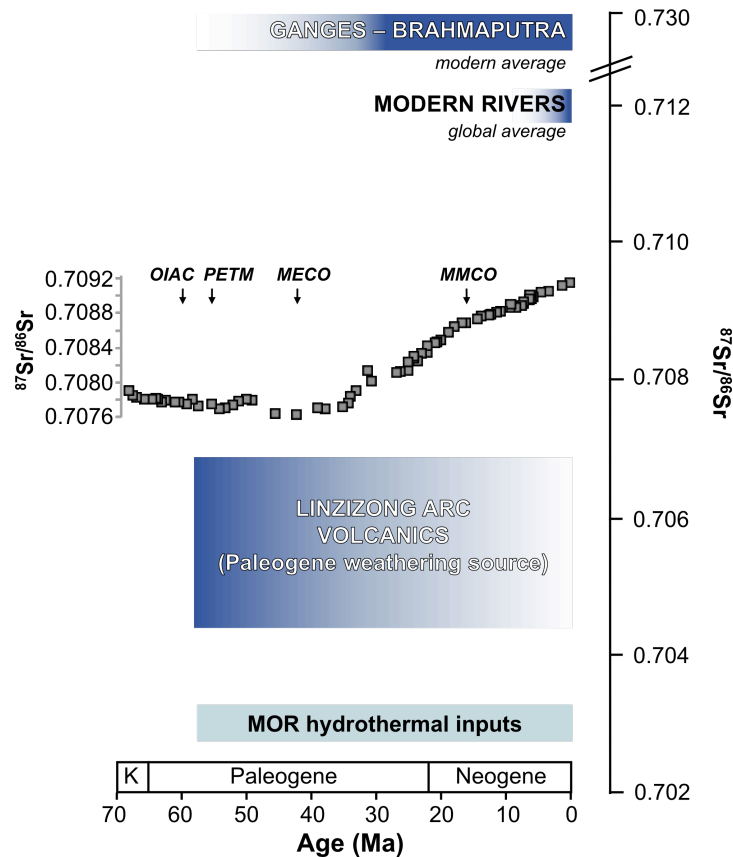


Figure 2.10 **The Cenozoic marine Sr isotope record in relation to source flux compositions.** The major feature of the Cenozoic record of seawater $^{87}\text{Sr}/^{86}\text{Sr}$ (plotted here using measured values on planktonic forams (Misra and Froelich, 2012)) is the steep climb in ratios from roughly 36 to 38 Ma to present. This has conventionally been interpreted as reflecting the onset of uplift in the India-Eurasia collision system with chemical weathering of radiogenic terrains (e.g., Raymo and Ruddiman (1992); Richter et al. (1992)). The modern day isotopic composition of the Ganges-Brahmaputra dissolved Sr flux is sufficiently high (e.g., Palmer and Edmond (1992); Galy et al. (1999), indicated on schematic) and sufficiently large that it shifts the modern global average river input flux to high $^{87}\text{Sr}/^{86}\text{Sr}$ ratios (e.g., Edmonds (1992)). This sustains the marine $^{87}\text{Sr}/^{86}\text{Sr}$ ratio at elevated values relative to the Paleogene. Our results indicate that the Linzizhong Arc was already at modern elevations in the late Paleocene and early Eocene. If chemical weathering rates were accelerated in these early stages of India-Eurasia collision, they likely would not have exerted significant influence on the marine Sr isotope record, because the arc lithologies had relatively nonradiogenic isotopic compositions (Mo et al., 2008). Major Cenozoic climate and tectonic events are marked with arrows: Onset of India-Asia Collision (OIAC), Paleocene-Eocene Thermal Maximum (PETM), Mid-Eocene Climatic Optimum (MECO), Mid-Miocene Climatic Optimum (MMCO).

are complicated. Uplift and arc volcanism can be associated with enhanced outgassing of metamorphic and volcanic CO₂ (e.g., Kerrick and Caldeira (1993)), which could counteract or even reverse the carbon balance in such a setting. If organic-rich marine sediments were also exposed, then oxidative weathering of the organics would have served as an additional CO₂ source to the atmosphere (e.g., Beck et al. (1995)). On the other hand, carbon sinks linked to tectonism include the potential for enhanced organic carbon burial efficiency through rapid burial rates in submarine fans and the high flux of fine grained sediments to the oceans with subsequent mineral surface area control on organic matter burial (e.g., Hedges and Keil (1995); France-Lanord and Derry (1997); Galy et al. (2007)). Organic carbon burial rates could also be influenced by changes in nutrient fluxes to the ocean as the rates and relative importance of different weathering domains and marine depositional environments change (Compton and Mallinson, 1996; Colman and Holland, 2000). Finally, the overall carbon mass balance for the atmosphere-ocean system likewise links to carbon release from mid-ocean ridge (MOR) spreading centers, and thus to global tectonism, which may or may not be coupled to regional processes (Richter et al., 1992).

Our results provide strong evidence that the marine Sr isotope record is not a sensitive indicator for the early rise of the Tibetan margin nor for the impact that the development of this topography had on global chemical weathering rates. The fact that this topography developed during a time of globally warm climates suggests that any enhancement in chemical weathering rates, which would have tended to lower atmospheric CO₂, was offset by other and feedbacks in the global carbon cycle.

2.8 Conclusions

We reconstruct an elevation history from the Tibetan Plateau spanning nearly the entire Cenozoic, from the onset of India-Asia collision to the present. This study provides multiple lines of geochemical evidence that the southern margin of the Lhasa Block was at modern elevation or higher (4 to >5km) around the onset of collision. We find that both temperature

lapse rates, informed by our clumped isotope measurements, and traditional stable isotopic lapse rates of paleo-precipitation, informed by oxygen isotopic compositions of lacustrine and pedogenic carbonates, agree that the sediments associated with the Linzizhong volcanic arc follow the “Lhasaplano” model of tectonic evolution. Further work on the central and northern plateau is necessary in order to differentiate between a pre-existing Andean-type volcanic arc or more extensive high terrain such as a proto-plateau in the early Cenozoic. Additionally, our data indicate high topography at low latitude dating to before the Eocene Climatic Optimum, suggesting a more complicated linkage between the Himalayan orogeny, proxies for chemical weathering, and the linkage between tectonics, weathering, and climate.

CHAPTER 3

**NORTH, SOUTH, EAST AND WEST: CLUMPED ISOTOPE
PALEOTHERMOMETRY AND STABLE ISOTOPE
PALEOALTIMETRY OF THE LHASA BLOCK**

3.1 Abstract

The elevation history of the Tibetan Plateau promises insight into the mechanisms and dynamics that develop and sustain high topography over tens of millions of years. Here we present the reconstructed Eocene to Miocene elevations of the Lunpola and Amu Xun regions of the Lhasa terrane, the southernmost crustal block of the Tibetan Plateau. This work expands our spatial resolution of the elevation history of the Tibetan Plateau and the latest Cretaceous to Eocene Gangdese arc immediately north of the Indus Yarlung Suture Zone. Paleo-elevation estimates of the Paleocene-Eocene Nianbo Formation in the Amu Xun, ~450 km west of Penbo and Lhasa, are 4.5 to 5 km. Paleo-elevation estimates for the Lunpola basin (~4.4 to 5 kilometers) support previous evidence (Rowley and Currie, 2006; Polissar et al., 2009) that the northern edge of the Lhasa Block attained high elevation by at least the late Eocene. This allows for the possibility that the entire Lhasa Block was composed of extremely thick continental crust early in the India-Asia collisional history, rather than restricting the extent of thick crust to the Linzizhong volcanic arc (“Lhasaplano” model) or Gangdese Mountains (Ding et al., 2014). However, better constraints on depositional ages in the Lunpola basin are needed to make a robust assessment of early Cenozoic elevations along the Bangong-Nujiang suture zone. In considering our expanded spatial resolution of Tibetan elevations through time, we review the current knowledge of stable isotope paleoaltimetry from on the plateau and its eastern margin.

3.2 Introduction

The Cenozoic elevation record provided by our work in the Oiyug and Penbo basins supports the hypothesis that the entire Linzizhong arc was likely >4 km above sea level >56 Ma, based on zircon U-Pb ages in the Nianbo Formation (He et al., 2007). However, the extent to which we can extrapolate our pre-collisional high elevation domain to the balance of the Lhasa terrane relies on the assumption that these two relatively proximal basins are representative of the whole. The Lunpola basin and Amu Xun sedimentary record enhance what we know of the Lhasa block's elevation history from the Paleocene to Miocene by providing additional tie points on the northern margin and the farthest west to date. We add a nominally Paleocene-Eocene stable isotope record from lacustrine carbonate in the Amu Xun, representing the farthest west paleo-elevation study from on Tibetan Plateau proper. The evidence presented here from these catchments and their associated sediments strengthens the argument for an early syn-collisional “high” Lhasa Block, ~ 270 km northwest and ~ 450 km west of the elevation record in the Penbo basin (Ingalls et al., 2017).

Tremendous effort from the tectonics community has been devoted to creating a spatially and temporally complete elevation history of Tibet (Quade et al., 2011; Huntington et al., 2015; Rowley and Currie, 2006; Currie et al., 2005, 2016; DeCelles et al., 2007; Ingalls et al., 2017) and the Himalaya (Saylor et al., 2009; Garzzone et al., 2000; Rowley et al., 2001) from before India-Asia collision to modern day. Here we synthesize all regional stable isotope paleoaltimetry studies on the Lhasa Block and eastern margin of Tibet (Hoke et al., 2014; Li et al., 2015), including our new paleo-elevation data >400 km west of Oiyug and supporting evidence for a high northern margin (Figure 3.1). We use the composite elevation record to reconsider past models of Tibetan uplift and crustal response to the India-Asia collision, which motivates our thinking about convergent orogens in the past and globally.

Since the Indian and Eurasian continents first made contact $\sim 56 \pm 2$ million years ago, there has been relative northward motion of these plates on the order of ~ 3500 km in the west and ~ 4500 km in the east. As such, we know there was a northern continuation of

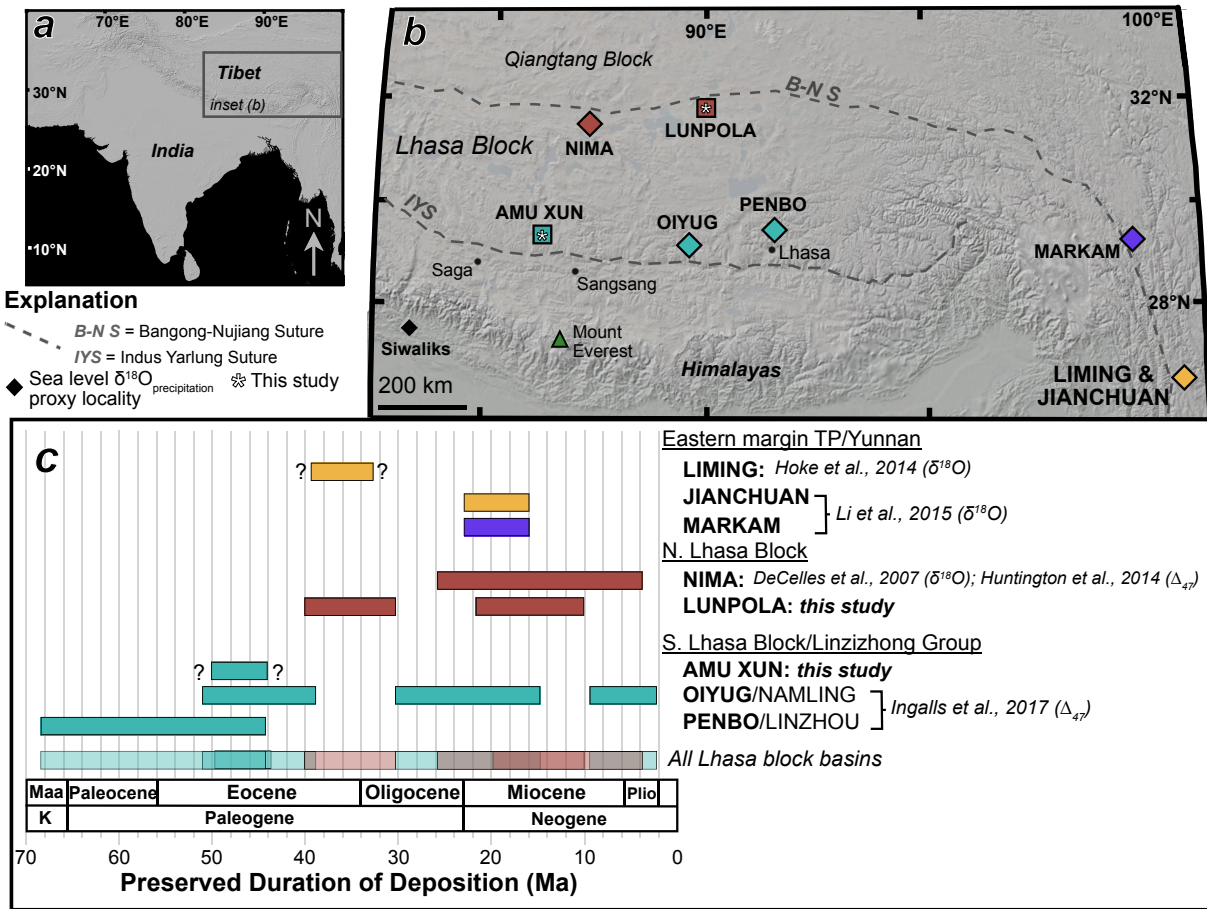


Figure 3.1 Map of paleoaltimetry studies and sampling localities. **a.** Modern topography of the India and the Tibetan Plateau. **b.** Stable- and clumped-isotope sampling localities on the Lhasa Block (Lunpola and Amu Xun basins [this study, maroon squares], Nima basin (DeCelles et al., 2007; Huntington et al., 2015), Oiyug and Penbo basins (Ingalls et al., 2017)) and the eastern margin of the Tibetan Plateau (Liming Basin (Hoke et al., 2014) and Markam Basin (Li et al., 2015)). **c.** Duration of preserved strata in each of the basins marked on the inset map (b) and discussed in the text. Question marks denote loosely constrained stratigraphic ages.

the modern Indian subcontinent—Greater India—and possibly a southern continuation of Eurasia, referred to as “Greater Tibet”. Recent accounting of currently reconstructable syn-collisional mass in the Himalayan orogenic system found that $49_{-33}^{+37}\%$ (2σ) of the total syn-collisional mass (Greater India and Greater Tibet) is missing from the crustal reservoir at the surface of the Earth today. Our previous calculations called for a “thick” Linzizhong Arc (61 ± 6 km) on the southern margin of Tibet at the start of collision, with the remainder of Tibet (“Deformed Asia”) relatively thin (38 ± 4 km, which corresponds to a mean elevation of 500 ± 500 m) (see Figure 4.2 and Figure 4.1). The thickness of the pre-collisional Linzizhong Arc was assigned in Ingalls et al. (2016b) extrapolating stable isotope paleoaltimetry results from Oiyug and Penbo basins (Ingalls et al., 2017; Ding et al., 2014) to potentially encompass the entire Linzizhong Arc. In this chapter, I present calculated paleo-elevations from the Nianbo Formation in the Amu Xun to strengthen our assessment of a >4 km elevation pre-collisional southern margin of Eurasia, and its contributions to the magnitude of continental recycling during the India-Asia collision.

3.2.1 Geologic Setting

Lunpola Basin

The Lunpola sedimentary basin formed largely in the Cenozoic, and is positioned on the northern edge of the Lhasa Block adjacent to the Bangong-Nujiang suture zone. The latest Jurassic to Early Cretaceous Bangong-Nujiang suture zone between the Lhasa and Qiangtang terranes (Dewey et al., 1988) has been reactivated as a 200–300 km wide and 1500–1800 km long zone of conjugate strike-slip faults accommodating east-west extension and north-south contraction (Taylor, 2003) (Fig. 3.1). The axis of the Lunpola basin strikes roughly east-west, parallel to the bounding thrust faults and folds associated with north-south shortening during India-Asia convergence.

More than four kilometers of deposition are recorded in the Paleocene to Pliocene age

stratigraphy of the Lunpola basin (Bureau of Geology and Mineral Resources Xizang Autonomous Region). The strata are most commonly divided into two units: the Paleocene to Oligocene Niubao Formation and the Miocene to Pliocene Dingqing (or Dingqinghu) Formation (Rowley and Currie, 2006). Age constraints are derived primarily from biostratigraphy (ostracods and palynological assemblages) from the efforts of regional geologic mapping and petroleum exploration campaigns (Bureau of Geology and Mineral Resources Xizang Autonomous Region; Xia, 1983; Xu, 1980; Xu et al., 1985). He et al. (2011) provides a zircon U-Pb age of 23.5 ± 0.2 Ma (2σ , MSWD = 1.1) from a bentonite layer in the middle to lower Dingqing Formation. This places an upper bound on our Niubao Formation samples of late Oligocene. More likely, our Niubao samples are late Eocene to Oligocene in age. Correlating our Dingqing samples to the stratigraphy of He et al. (2011) is not straightforward because they sampled from the westernmost reach of the Lunpola basin, and our Dingqing samples are from the south–central basin. However, we can assign a loose age of early Miocene or younger to our Dingqing section (Wu et al., 2008) (Fig. 3.2).

The lithology of the Middle Niubao member is dominated by lacustrine sediments. In the sampled strata of Rowley and Currie (2006) and this work, the Middle Niubao is composed of lacustrine mudstones, micritic and marl limestones, algal dolostones and dolomitic marls, and kerogenous shale.

The Upper Niubao member is dominated by more than 400 meters of fluvial/alluvial mudstones, sandstones, and conglomerates with intercalated calcic paleosol horizons. Peds are typically wedge-shaped, angular-blocky, or prismatic. Pedogenic carbonate nodules and rhizcretions were sampled for stable isotopes.

The Dingqing Formation is composed of lacustrine marls and limestones. Rowley and Currie (2006) sampled from the Middle Dingqing member in the south–central part of the basin where there is 19 meters of exposure. The base of the section is lacustrine marl with a few interbeds of oolitic limestone, rooted mudstone, and conglomerates. The upper part of the Dingqing section is mostly mudstone, sandy limestone, and sandstone.

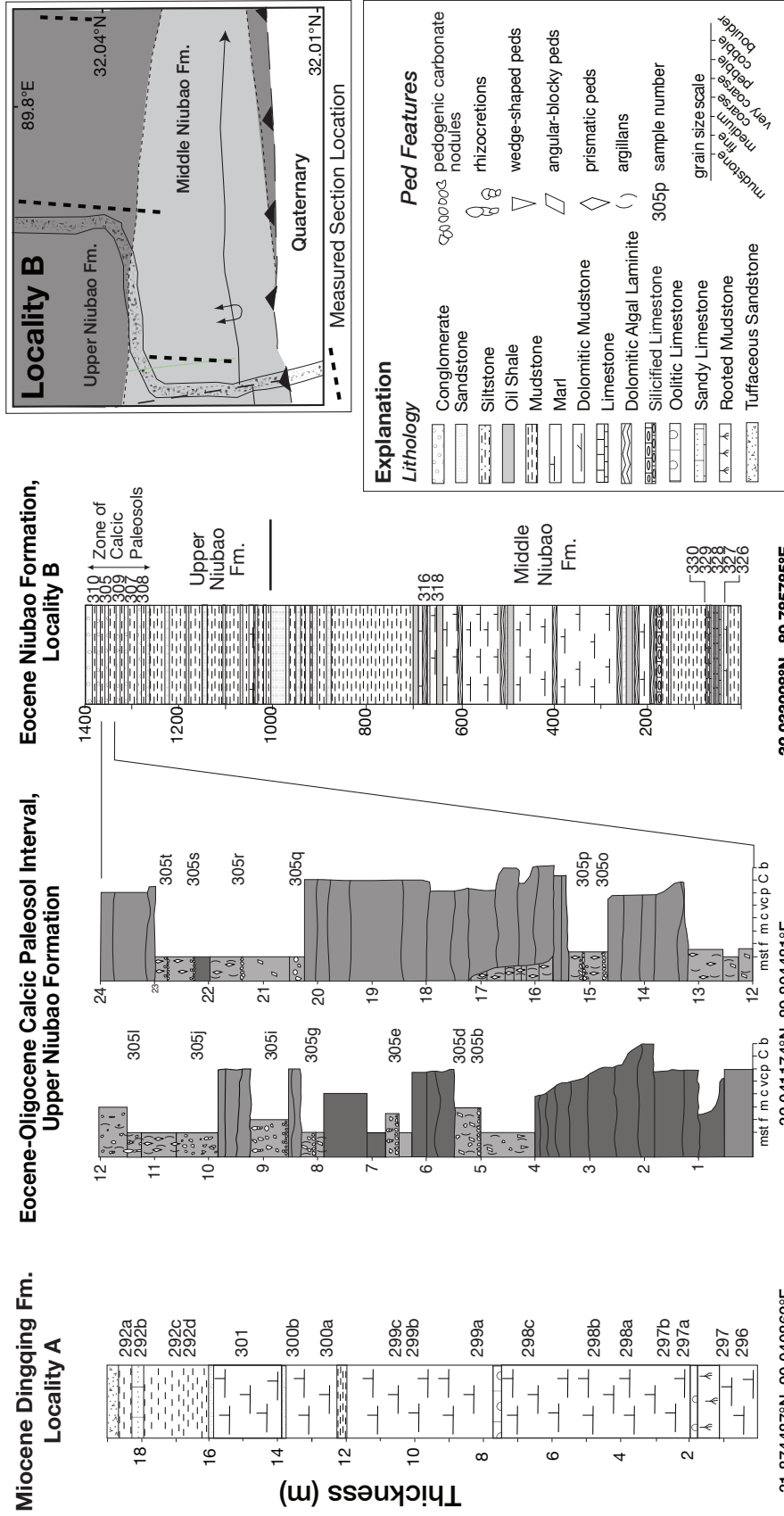


Figure 3.2 Stratigraphy and sample localities for the Lunpola basin. The inset geologic map shows three correlated sections measured and described through the Niubao Formation at Locality B. The Dingqing Formation was measured and sampled at Locality A.

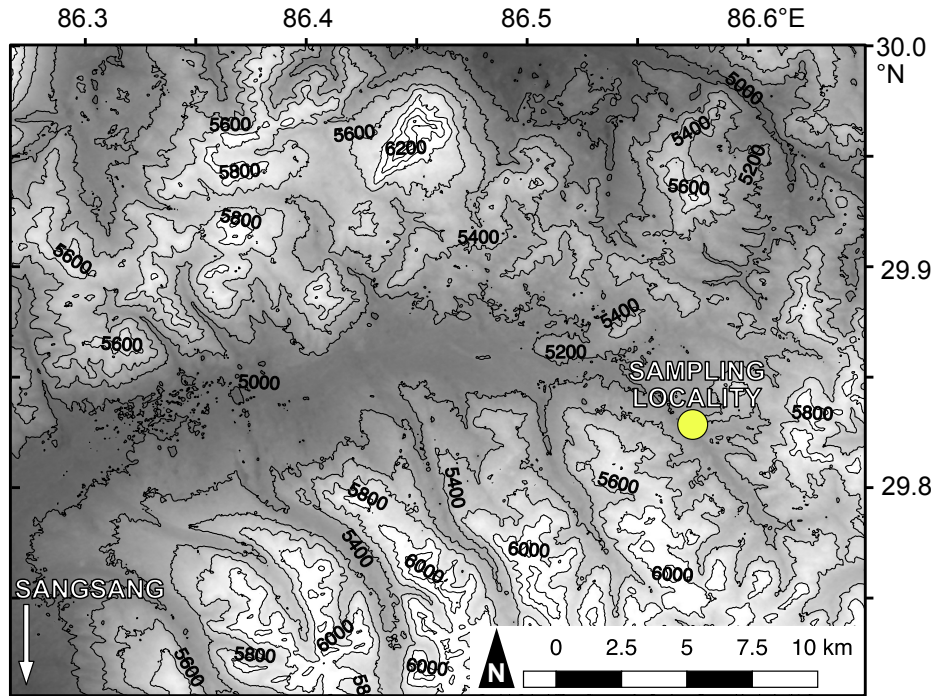


Figure 3.3 **Modern Amu Xun basin topography and sampling locality.** Elevation data is sourced from ASTER GDEM 2, a product of METI and NASA.

Amu Xun

The Amu Xun is located north of Sangsang, ~300 km west of the Oiyug basin and ~450 km west of Lhasa and the Penbo basin (Figure 3.3). The geologic unit from which we sampled is mapped as a Nianbo Formation equivalent (NGA, 2017). To the best of our knowledge, constraints on the depositional age of the Nianbo Formation in the Amu Xun region is limited to stratigraphic correlation to Nianbo Formation in the east near Lhasa. As such, our samples are considered Paleocene to Eocene in age (Ingalls et al., 2017).

We collected limestones for stable isotope analyses and rhyolitic ash for additional age constraints. The total thickness of the sampled section (Fig. 3.4) is 80 meters, with ~50 meters covered. The lower Nianbo is dominated by shale with interbedded mixed clastic and limestone rock with micritic cement. The section coarsens upward from finely laminated shale and mudstone to coarse mixed clastic and limestone rock and finally ~1.5 m of fine

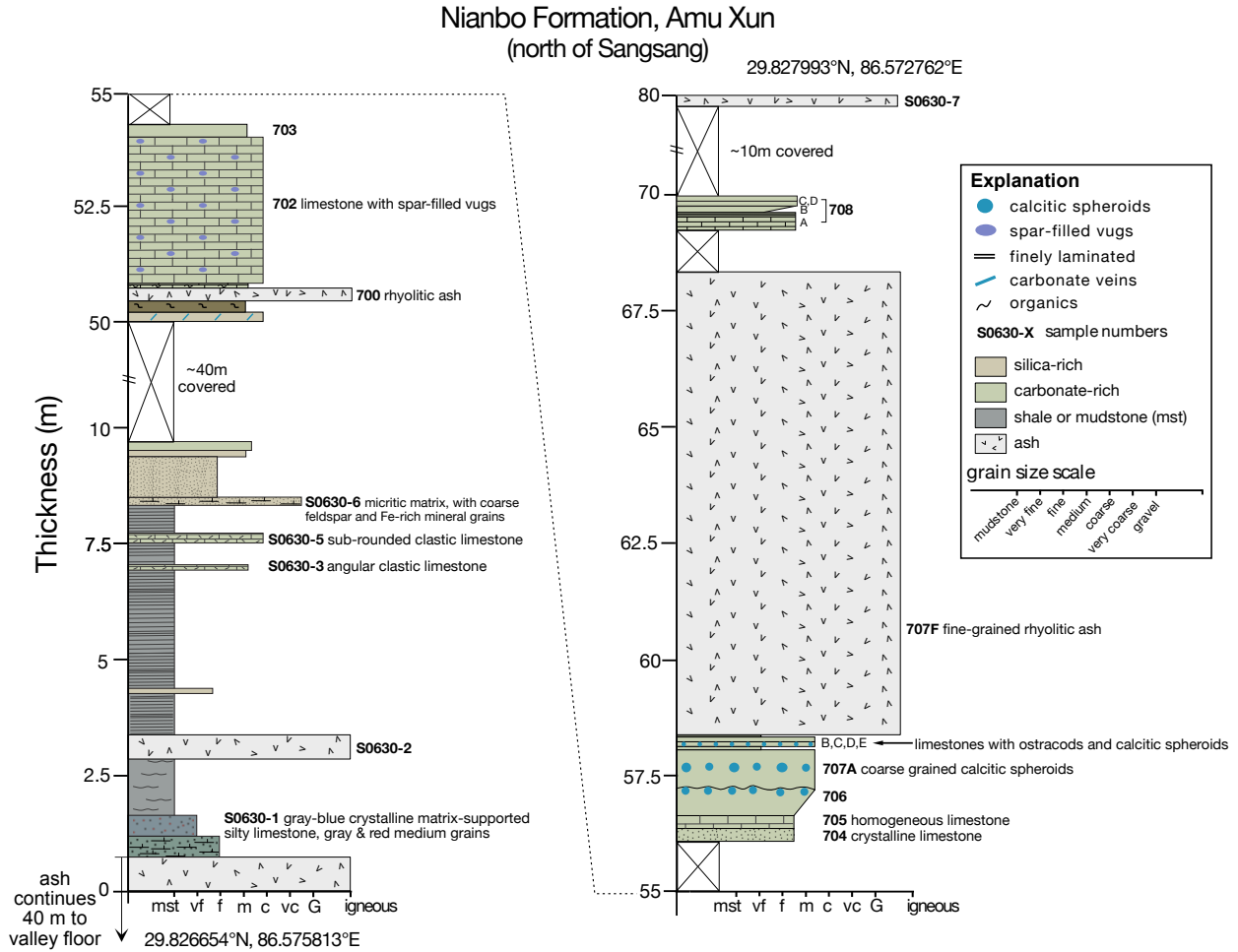


Figure 3.4 Measured and sampled stratigraphy in the Amu Xun, Tibet.

to very coarse calcarenite and sandstone. Clast mineralogy is predominantly intermediate volcanic. Clasts are sub-rounded to angular, suggesting they have not traveled far from their volcanic source and could have been deposited by air fall (Schnurrenberger et al., 2003). Evidence of active eruptions from the Linzizhong arc can be found throughout the Nianbo and Pana Formations. In this section, 1 to 40 meter thick ash beds mark large eruptions. The depositional environment following these eruptions are organic-rich alkaline lake systems with an increasingly large volcanoclastic input from the established arc. Further evidence for this volcanic sediment source is the increase in silica richness of the clastic material. The clasts are matrix-supported, which suggests syn-depositional cementation. The lithology in

the upper part of the Nianbo section is entirely limestone with spar-filled vugs, coarse-grained calcitic spheroids, and ostracods. A ~ 10 meter-thick rhyolitic ash deposit lies between two lacustrine limestone units.

3.3 Methods

In this study, we measured the $\delta^{18}\text{O}_c$ and $\delta^{13}\text{C}_c$ compositions of 22 carbonate samples collected from strata correlated to the Eocene in the Amu Xun basin and 41 carbonate samples from the Eocene to Miocene strata in the Lunpola basin. Carbonate sample preparation followed the methodology detailed in Ingalls et al. (2017). We performed clumped isotope analyses on 6 Amu Xun samples and 7 Lunpola samples. The subset of samples was chosen to optimize time and resources spent on Δ_{47} measurements while providing an accurate representation of the sampled strata. First, using traditional carbonate petrography, thin sections are screened for obvious signs of recrystallization or other fabrics indicative of thermal maturity. Second, of the samples that appear to retain primary micritic texture, at least one representative sample is chosen from each geologic unit to provide paleo-temperature measurements throughout the duration of deposition sampled. Additionally, where possible, each carbonate lithology (i.e. lacustrine versus pedogenic) found in the measured section is measured to account for isotopic and geochemical behavior specific to depositional environment (i.e. evaporation in lakes or incident solar heating of soils). The mean $T(\Delta_{47}) (\pm 2\sigma)$ of each formation was used to calculate oxygen isotopic values of ancient precipitation ($\delta^{18}\text{O}_w$) from carbonate rocks ($\delta^{18}\text{O}_c$) for all carbonates within the same formation.

Stable isotope and clumped isotope methods follow those detailed in Ingalls et al. (2017) and in Appendix Section A.1. Paleo-elevations are calculated using the equations of Ingalls et al. (2017) (Appendix Section B; Eq. 2.2), which fits a $\Delta(\delta^{18}\text{O}_w)$ -elevation lapse rate statistical regression to observed relative humidity and precipitation isotopic composition data.

3.4 Results

3.4.1 Oxygen and carbon isotopes

Carbon, oxygen, and deuterium stable isotope values for the Lunpola basin are reported in Rowley and Currie (2006) and Polissar et al. (2009).

While carbon isotope values are not directly used in stable isotope paleoaltimetry calculations, these values can be useful in screening for isotopic effects of secondary processes. For example, positive covariation of carbon and oxygen isotope values can signify an evaporative overprint (Polissar et al., 2009), which leaves an apparent enrichment of ^{18}O in carbonate-saturated waters. Figure 3.5 plots $\delta^{18}\text{O}_c$ against $\delta^{13}\text{C}$ to display trends likely attributable to evaporative enrichment. Polissar et al. (2009) directly screened for evaporative overprinting in a subset of our Lunpola samples by measuring deuterium and oxygen isotopes on the exact same samples. We use the measured $\delta^{18}\text{O}$ values for all samples in our paleo-elevation calculations, but focus our interpretations on the samples interpreted to reflect primary depositional conditions.

Additionally, we screen for diagenetic overprinting of primary isotopic signal which typically shifts carbonate oxygen isotope compositions to more negative values. When carbonate interacts with diagenetic water at high temperatures, the original carbonate exchanges oxygen with the water. This water-rock reaction is reflected in the recrystallized material by a $\delta^{18}\text{O}$ value shifted towards the composition of the diagenetic water (more negative). However, in highly rock-buffered systems (low water-rock ratio), carbonate minerals can retain a nearly primary $\delta^{18}\text{O}$ composition at elevated temperatures because there is little to no water to facilitate oxygen exchange. In our samples, we screen for potential water-rock diagenesis using optical petrography, scanning electron microscopy, and cathodoluminescence.

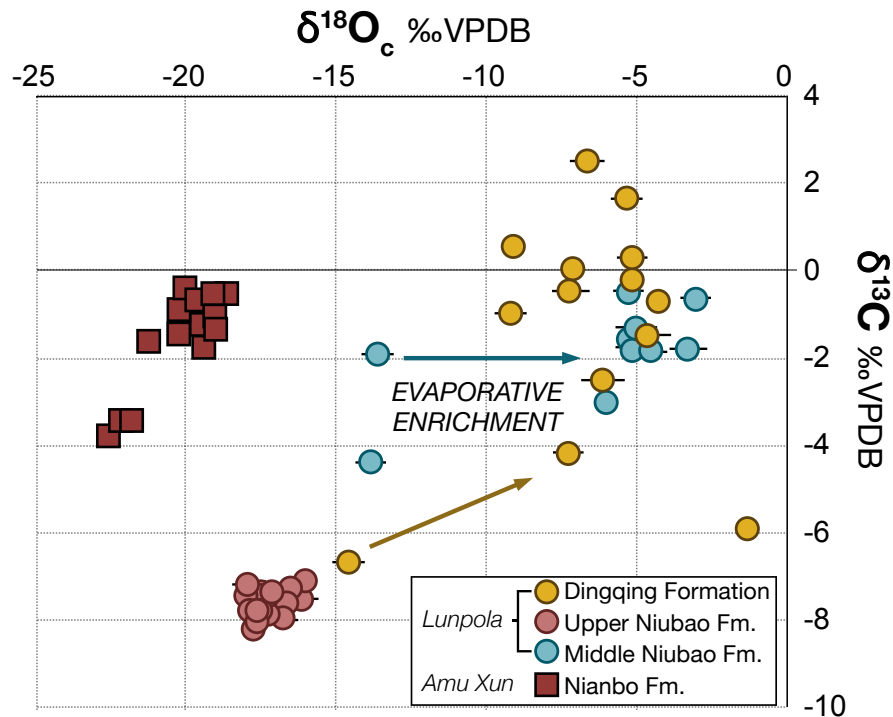


Figure 3.5 **Carbonate oxygen and carbon stable isotope data from the Amu Xun and Lunpola basins.** Arrows indicate direction of data scatter for the Middle Niubao and Dingqing Formation samples, likely due to evaporative enrichment.

3.4.2 Clumped isotope thermometry

All seven clumped isotope samples from the Lunpola basin yielded high Δ_{47} values on the Carbon Dioxide Equilibrium Scale (CDES; Dennis et al. (2011)) which correlate to plausible Earth surface temperatures using the Zaarur et al. (2013) thermometer. A sample from the Dingqing Formation yielded a $5.3 \pm 4.2^\circ\text{C}$ $T(\Delta_{47})$ value. The average of three samples (with 3 to 4 separate digestions) from each of the Upper and Middle Niubao Members yielded $T(\Delta_{47})$ values of $8.5 \pm 4.2^\circ\text{C}$ and $6.8 \pm 8.5^\circ\text{C}$, respectively. The average value for Carrera Marble, a common clumped isotope standard, was 0.458 ± 0.024 for 8 separate digestions.

Clumped isotope analyses for ten samples from the Amu Xun region have significantly lower Δ_{47} compositions than the Lunpola samples. Additionally, the Amu Xun carbonates are more heterogeneous in Δ_{47} space than the Lunpola samples. Carbonate powders were drilled from separate sections of several Amu Xun samples (henceforth referred to as

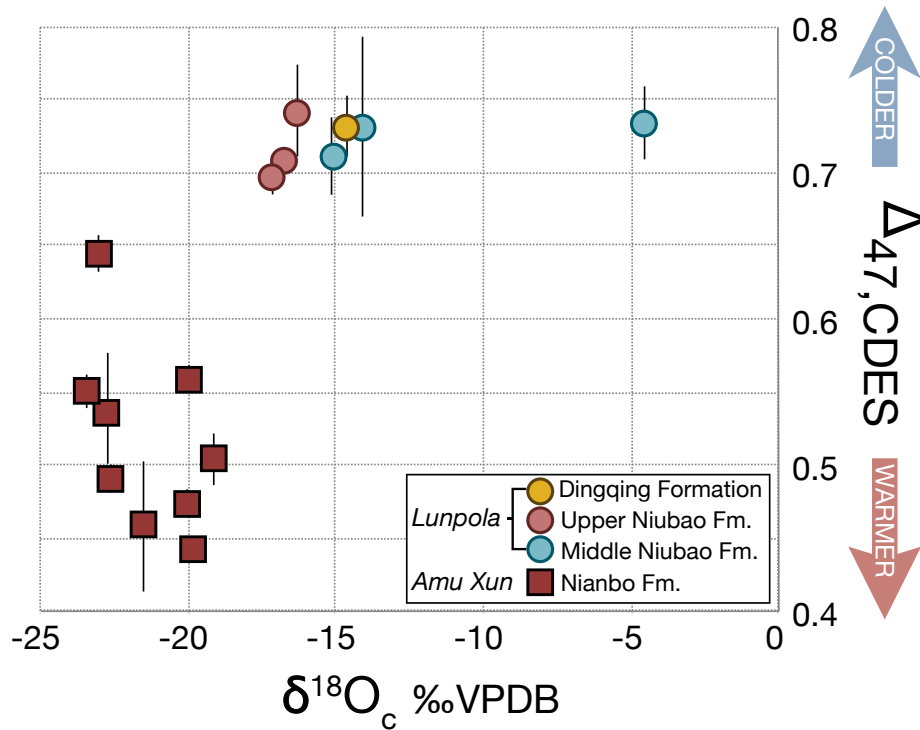


Figure 3.6 Carbonate oxygen and Δ_{47} data from the Amu Xun and Lunpola basins.

“sub-samples”), and analyzed separately for Δ_{47} , $\delta^{18}\text{O}$, and $\delta^{13}\text{C}$. For example, two powders from sample S0630-3 were measured. Sub-sample S0630-3a yields a Δ_{47} composition of 0.644 ± 0.012 , or a clumped isotope-derived temperature of $25 \pm 3^\circ\text{C}$ ($n=3$). Sub-sample S0630-3b yields a Δ_{47} composition of 0.551 ± 0.012 , or $T(\Delta_{47})$ of $52 \pm 4^\circ\text{C}$ ($n=2$). However, $\delta^{13}\text{C}$, $\delta^{18}\text{O}$, and CO_2 digestion yields were comparable between the two sub-samples. Similar $\% \text{CO}_3^{2-}$ suggests that the bulk material is the same and has not been replaced by purer secondary calcite precipitation. Consistent stable isotope values suggest that any secondary recrystallization, for which there is minimal petrographic evidence, exchanged oxygen to the same extent and in the same direction within the entire sample. Therefore, the within-sample variability of Δ_{47} compositions suggests that bond reordering kinetics were heterogeneous within this sample.

3.4.3 Elevations

Lunpola basin

A number of samples from the Miocene and Late Eocene-Oligocene units (Dingqing and Middle Niubao Formations) of the Lunpola basin have experienced extensive evaporative enrichment (Figs. 3.5 and 3.8). It is incredibly unlikely that the magnitude of variation in the carbon and oxygen isotopic compositions of carbonates from these formations is representative of precipitation compositions over the watershed. The scatter in these values suggests that each sample experienced a variable amount of evaporation and ^{18}O enrichment. In contrast, the $\delta^{13}\text{C}$ and $\delta^{18}\text{O}$ values from the Eocene Amu Xun section and Oligocene Upper Niubao are tightly clustered, and therefore more likely to represent isotopic compositions of minerals in equilibrium with primary (unevaporated) meteoric water. Additionally, as described in the previous section, we use the evaporation-corrected $\delta^{18}\text{O}_w$ values for the three Dingqing Formation samples to calculate $\Delta(\delta^{18}\text{O}_w)$ and elevation for the Miocene. The evaporation-corrected value for a Middle Niubao sample yields an elevation in excellent agreement with the most ^{18}O -depleted sample: 4530^{+1286}_{-1943} meters. The evaporation-corrected Dingqing Formation samples yield elevations from 4.4 to 5 km. The elevation from the most depleted Upper Niubao sample is 4496^{+1276}_{-1933} meters. Overall, clumped isotope-derived temperatures suggest that primary depositional conditions are recorded by the Lunpola sediments, and strengthen past assessments of pre-existing high elevation on the northern Lhasa Block as far back as the Eocene.

Amu Xun

Clumped isotope analyses from the Amu Xun basin provided evidence for high-temperature burial alteration of primary C-O bond ordering. At temperatures above $\sim 120^\circ\text{C}$, neighboring carbonate groups can experience rapid exchange of carbon and oxygen atoms to a more stochastic distribution of the rare isotopes without the facilitation of water (Passey and

Henkes, 2012; Henkes et al., 2014; Stolper and Eiler, 2015). There is little to no evidence of water-rock recrystallization, and therefore we assume the rock-buffered system preserved primary $\delta^{18}\text{O}_c$ compositions. Sub-sample S0630-3a yields a Δ_{47} -derived temperature of $25\pm 3^\circ\text{C}$ ($n=3$). As this is the most plausible lacustrine carbonate formation temperature in the Amu Xun data set, we use this temperature for calculating $\alpha_{\text{CaCO}_3\text{-H}_2\text{O}}$ and $\delta^{18}\text{O}_w$ for all Amu Xun carbonates.

$\Delta\delta^{18}\text{O}_p$ calculations range from -9.7 to -13.6‰ VSMOW, corresponding to model elevations of 4248 to 5041 meters above sea level, respectively. The average hypsometric mean elevation of the Amu Xun basin calculated from our stable isotope data is 4551 ± 413 meters. This paleo-elevation of the Nianbo Formation in the Amu Xun stratigraphically correlates to the Nianbo Formation in the Oiyug and Penbo basins, which yield equally high elevations using the same stable isotope paleoaltimetry methods (Ingalls et al., 2017).

3.5 Discussion

3.5.1 $\delta^{18}\text{O}$ versus δD : Multi-proxy approach to reconstructing ancient rainwater in arid climates

The Global Meteoric Water Line (GMWL; Rozanski et al. (1993)) describes the relationship between D/H and $\delta^{18}\text{O}$ compositions of global meteoric waters. There can be local deviations from global due to local climate and atmospheric circulation. The local meteoric water line in Lhasa, constructed from isotopic data from the CHNIP (Chinese Network of Isotopes in Precipitation) station there, is very close to the GMWL: $8.04\delta^{18}\text{O}+10.06$ (Liu et al., 2014). A study of $\delta^{18}\text{O}$ and δD compositions of modern lakewater from open and closed lake systems across the Tibetan Plateau yielded a slope of $5.2\text{‰ } \delta\text{D}/\text{‰ } \delta^{18}\text{O}$ (Yuan et al., 2011), suggesting a stronger influence of evaporation on lakewaters than other surface waters. Evaporation due to aridity shifts hydrogen and oxygen isotopes towards more enriched values, or to the right of the GMWL.

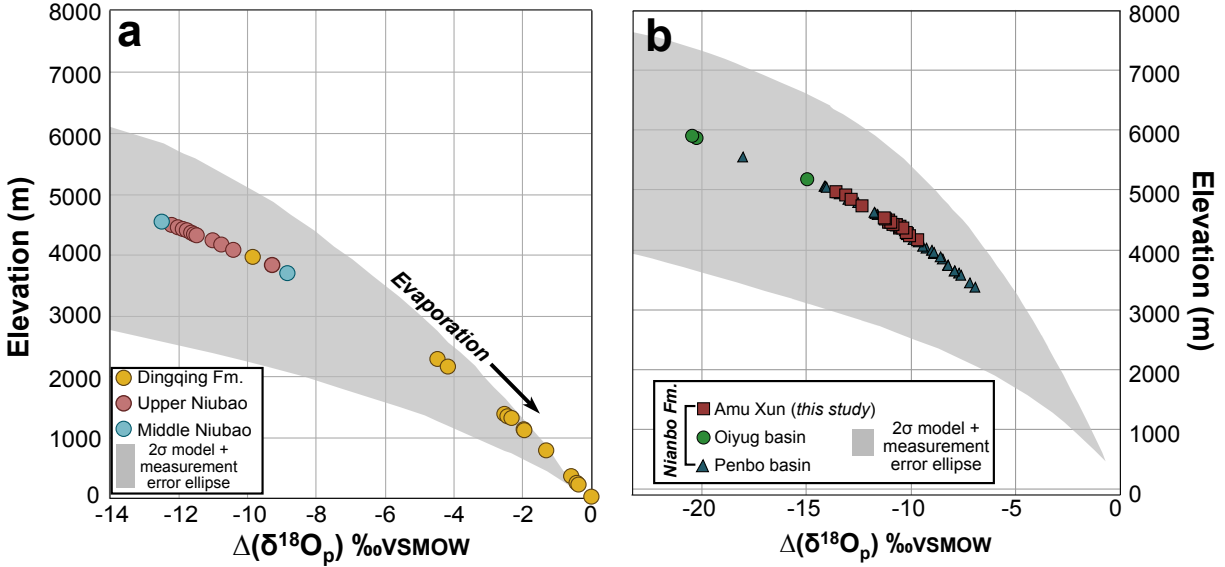


Figure 3.7 **Elevation reconstruction of the Lunpola basin and Nianbo Formation in the Amu Xun, Penbo, and Oiyug basins.** **a.** Paleo-elevations of the Lunpola basin stratigraphy. The Dingqing Formation $\delta^{18}\text{O}_c$ values are evaporatively enriched, leading to more positive $\Delta\delta^{18}\text{O}_p$ values. The Eo-Oligocene Niubao Formation preserves the isotopic composition of high elevation precipitation within carbonate samples. **b.** Along-strike variability in reconstructed paleo-elevations within the Paleocene-Eocene Nianbo Formation from Amu Xun (this study) and the Oiyug and Penbo basins (Ingalls et al., 2017). The gray shaded region is the 2σ error ellipse including model uncertainty and analytical error.

The extent of evaporative kinetic isotope effects is largely dependent on atmospheric relative humidity and the isotopic composition of atmospheric moisture (Polissar and Freeman, 2010). The trajectory of evaporated water off the meteoric water line (MWL) defines a local evaporation line (LEL) — a tie line between the unevaporated water on the MWL (Gonfiantini, 1986) and evaporatively enriched composition. Slopes for various vegetation ecosystems were empirically determined in Polissar and Freeman (2010) (e.g. a slope of ~ 1 for mixed forest-shrub vegetation representative of the Miocene Lunpola, as evidenced by pollen data).

In arid climates, the apparent fractionation (ϵ_a) of hydrogen isotopes between sedimentary plant-wax n-alkanes and local precipitation is less than that of carbonate- $\delta^{18}\text{O}$ (Polissar and Freeman, 2010). Paired lipid δD and carbonate- $\delta^{18}\text{O}$ measurements from lacustrine sed-

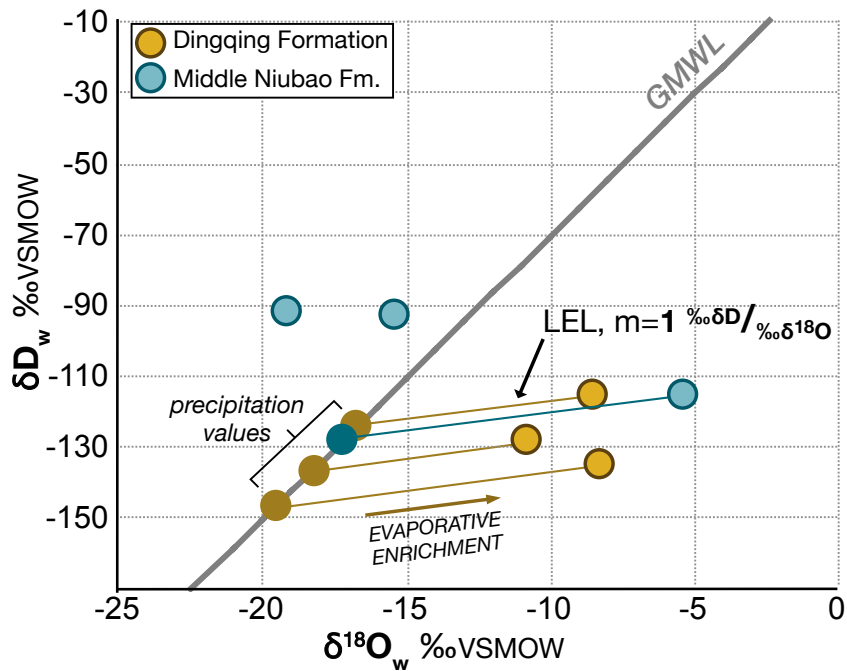


Figure 3.8 Leaf wax-derived δD_w versus carbonate-derived $\delta^{18}O_w$ for Lunpola samples relative to the GMWL. A conservative estimate of original precipitation compositions are calculated using a local evaporation line (LEL) with a slope of 1 (Polissar and Freeman, 2010; Polissar et al., 2009). Outlined circles mark measured values; solid circles mark back-calculated precipitation values. The isotopic compositions of two samples from the Middle Niubao Formation plot to the left of the GMWL, and therefore have not been impacted by lake water evaporation.

iments from the Lunpola basin were used in (Polissar et al., 2009) to estimate the isotopic composition of Miocene precipitation on the Tibetan Plateau (Figure 3.8). Water δD was calculated from plant-wax δD assuming an ϵ_a of $-121 \pm 10\%$. Our study slightly modifies the $\delta^{18}O_w$ calculation by using a direct temperature measurement for the Miocene carbonate sediments using clumped isotopes.

In an attempt to correct for the effect of aridity on isotope values, we estimate original precipitation isotope values by applying a leaf-water/lake-water evaporative slope of $1\% \delta D / \% \delta^{18}O$, empirically determined for mixed forest-shrub vegetation (Polissar and Freeman, 2010). The stated slope yields a conservative estimate of $\delta^{18}O$; any greater slope would imply more negative initial $\delta^{18}O$ compositions. Polissar and Freeman (2010) found

that the value of precipitation calculated using this approach was comparable to the most negative $\delta^{18}\text{O}_w$ values from carbonates at this locality, which are presumably the carbonates least effected by evaporative enrichment. Therefore, the use of multiple precipitation proxies in strongly evaporative systems—such as lakes in high-altitude, arid climates—provides a quantitative method of reversing apparent evaporative fractionation to reconstruct primary isotopic values. We use the evaporation slope to reconstruct primary compositions of the precipitation source to the catchment, which we use in our $\Delta\delta^{18}\text{O}_p$ paleo-elevation calculations in the Lunpola basin.

3.5.2 Near-modern elevations (>4 km) across the Lhasa terrane in the mid-Eocene

The stable isotope records from the latitudinal and longitudinal extent of sampled basins yield paleo-elevations consistently >4000 meters above sea level. However, our paleoaltitude record from each basin samples from different periods of sedimentation in the Cenozoic elevation history of the Lhasa block. The active tectonic state of the Lhasa Block, which has accommodated collision-related stress and strain for the last 56 ± 2 My, drives higher rates of sedimentation but also complicates preservation of primary sediments by diagenesis or wholesale elimination of strata by faulting and/or erosion. As such, our reconstructions are limited in time and space by location and stratigraphic exposure of Cenozoic depocentres and preservation of primary material within active Tibetan basins. Out of necessity, we must extrapolate from “postage stamp”-sized records to a much larger geologic terrane. The addition of each new paleoaltimetry record adds a tie point to this extrapolation and reduces the likelihood that a “high” paleo-elevation reconstruction reflects a local high (i.e. a peak), rather than a land surface more similar to today’s plateau.

Active faulting and subsidence consequent of India-Asia collision, and an earlier contractional thrust system related to the Gangdese arc, activated new basins to the immediate north and south of the IYS (Kapp et al., 2007; DeCelles et al., 2016). The Maqu angular

unconformity between the the extensively shortened Cretaceous marine strata and the less deformed uppermost Cretaceous to early Cenozoic Linzizhong Formation supports that the Gangdese magmatic arc may be associated with a contractional, Cordilleran-style orogen (Burg et al., 1983; England and Searle, 1986; Ratschbacher et al., 1992; Kapp et al., 2007). These fluvial-lacustrine depocentres have been the focus of extensive paleo-altitude reconstructions (DeCelles et al., 2016, 2011; Huntington et al., 2015; Ingalls et al., 2017; Currie et al., 2016; Ding et al., 2014; Quade et al., 2011). Here we consider the current knowledge of the development of high elevation across the Lhasa block and on the eastern margin of the Tibetan Plateau as recorded in basin sedimentation and the stable isotope proxy record.

Cretaceous to mid-Eocene

The stable and clumped isotopic record of the Nianbo Formation in the Penbo basin together with careful diagenetic screening provides the first explicit evidence that the southern margin of the Lhasa block was at near-modern elevations during pre- to early syn-collisional times (Ingalls et al., 2017). The Linzizhong Group in the Penbo basin has been carefully dated using zircon U-Pb geochronology (He et al., 2007). A rhyolite from the base of the Dianzhong Formation, the oldest unit of the Linzizhong Group, yields a U-Pb zircon age of 68.7 ± 2.4 Ma. A felsic lapilli tuff from the Pana Formation, the uppermost unit of the Linzizhong Group, yields a U-Pb zircon age of 47.1 ± 1.2 Ma. These ages place conservative bounds on the duration of high elevation sedimentation in the Linzizhong strata at Penbo, although the samples of Ingalls et al. (2017) are derived only from the late Paleocene to Eocene Nianbo and Eocene Pana Formations. The oldest zircon U-Pb age from near the base of the Nianbo Formation in Penbo is 53.9 ± 1.4 Ma (He et al., 2007). However, there is no geological evidence that the Dianzhong Formation was deposited at a significantly lower elevation than the Nianbo Formation volcanics and interbedded sediments.

The Dianzhong Formation sits in angular unconformity (Maqu Unconformity) above the late-Cretaceous Takena and Shexing Formations, and records deposition consistent with

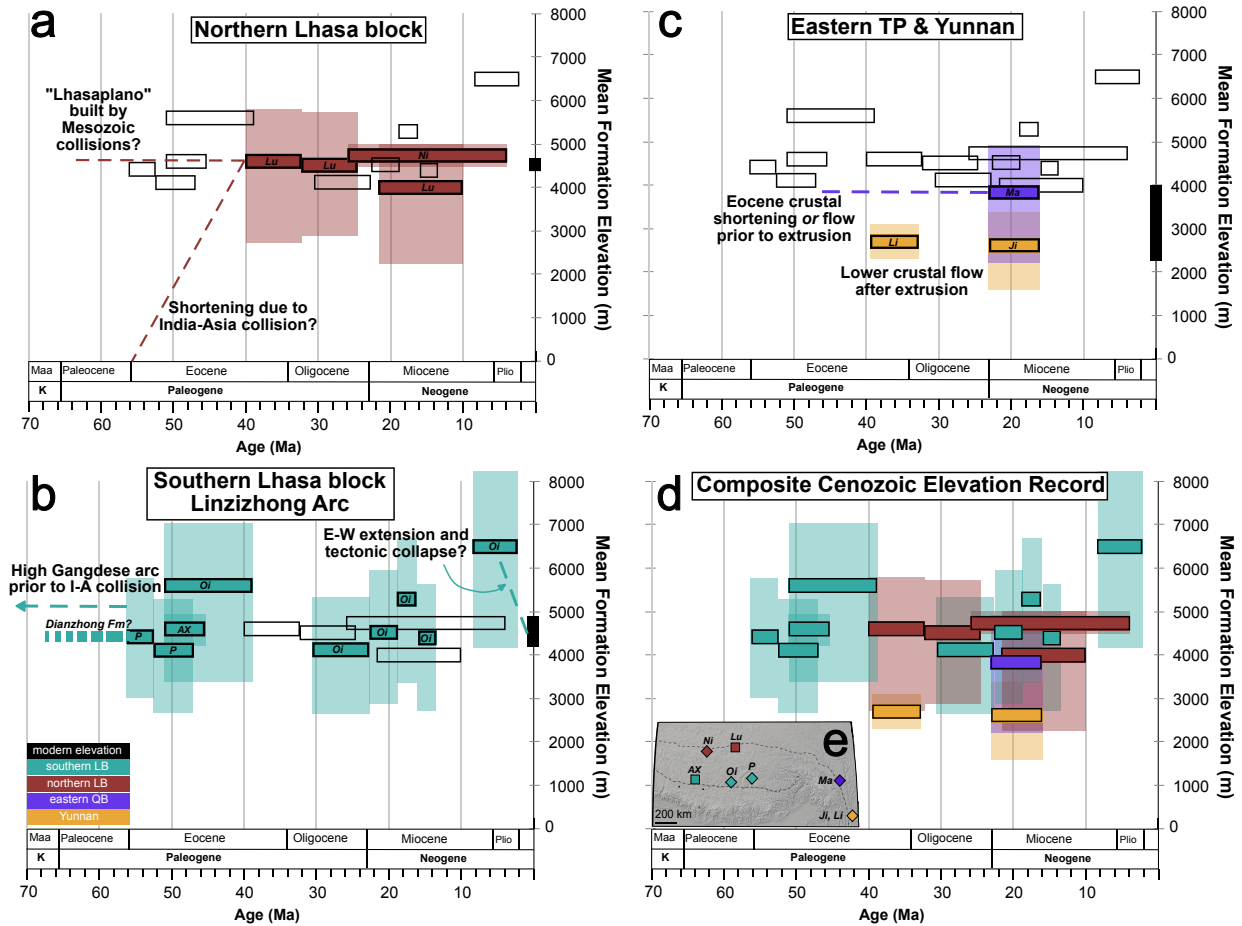


Figure 3.9 Cenozoic elevation reconstruction of northern and southern regions of the Lhasa block (LB) and the eastern Tibetan Plateau (TP). The length of each bar denotes duration of deposition preserved in the rock record, corresponding to Figure 3.1c. Translucent boxes represent elevation model uncertainty. Black boxes mark the modern watershed mean elevation for each set of sampling locations within a panel. **a.** Late Eocene to Pliocene stable isotope paleoaltimetry from the northern margin of the Lhasa block. The Lunpola (Lu) basin results are from this study and Rowley and Currie (2006). The Nima (Ni) basin results are originally from DeCelles et al. (2007), but they do not report precise errors for their calculated elevations. **b.** Paleoaltimetry from the southern Lhasa block, north of the Gangdese arc within the Linzizhong Group. Penbo (P) and Oiyug (Oi) elevations are derived from Ingalls et al. (2017), and Amu Xun, this study. **c.** A compilation of Eocene to Miocene paleo-elevations from the eastern Tibetan Plateau (Markam basin, Ma, Li et al. (2015)) and Yunnan province (Liming, Li, Hoke et al. (2014); Jianchuan, Ji, Li et al. (2015)). **d.** A composite record of Cenozoic elevation from stable isotope proxies across the southern TP. **e.** Regional map of the southern TP with locations of basins in panels a-d for reference.

a retro-arc foreland basin setting (Leier et al., 2007). The lower member of the Takena Formation is a ~250 m package of marine carbonate deposited in the Aptian-Albian shallow marine seaway, conformably overlain by ~100 m of stacked paleosol horizons and a 2 km-thick package of upward coarsening fluvial redbeds of the Shexing Fm (Leier et al., 2007; He et al., 2007). The Takena Formation is inundated by clastic sediment derived from the Early to early Late Cretaceous (~120 to 80 Ma) Gangdese arc. Takena facies are interpreted to record the shift from deposition in the forebulge to foredeep depozone (Leier et al., 2007). Sometime between deposition and ~70 Ma, the Takena Formation was incorporated into a retroarc fold-and-thrust belt (Leier et al., 2007; Kapp et al., 2007). The degree of folding within the Takena Formation is much more pronounced than in the less deformed Linzizhong Group (He et al., 2007; Kapp et al., 2007). Based on the difference in their deformation history and the dominance of marine facies in the Takena Formation, we know that there was a period of extensive folding, uplift, tilting, and erosion between Takena and Linzizhong deposition. Therefore, although we have no direct stable isotopic evidence, the regional geology supports that the Gangdese arc land surface was uplifted within a fold-and-thrust belt during Cordilleran-style contraction (Kapp et al., 2007) prior to or synchronous with the beveling of the land surface (Maqu unconformity) and Dianzhong deposition.

The Nianbo Formation in the Oiyug basin and Amu Xun (Fig. 3.1) are age-correlated to the Nianbo Formation in the Penbo basin. Using stratigraphic correlation, we can say that the Lhasa block within the northern parts of the Gangdese magmatic arc had a hypsometric mean elevation >4 km by 53.9 ± 1.4 Ma (He et al., 2007). We now have greater confidence that the entire Lhasa Block existed at high altitude by the Late Eocene (Rowley and Currie, 2006). Further, the volcanic and sedimentary succession of the Gangdese arc and Linzizhong Group just north of the IYS were at high altitude by at least the onset of India-Asia collision.

Late Eocene to Miocene

Paleoaltimetry results presented in this study from the Dingqing Formation in the Lunpola basin demonstrate that the central TP were already at elevations >4 km by at least 23.5 ± 0.2 Ma (He et al., 2011). However, the Middle and Upper Niubao Formation are older—probably mid to late Eocene in age—and also yield elevations in excess of 4 km. Stable isotope paleoaltimetry conducted in the Nima basin yields consistently negative $\delta^{18}\text{O}_c$ isotopic compositions and paleo-elevations comparable to those calculated in the Lunpola basin (DeCelles et al., 2007; Huntington et al., 2015). Huntington et al. (2015) urges caution in interpreting these oxygen isotopic results as primary high elevations because the same lacustrine samples yielded $T(\Delta_{47})$ measurements in the range of ~ 75 to 90°C . However, there is little to no visible evidence of recrystallization, and thus any burial heating and diagenesis is interpreted to have occurred in a rock-buffered environment; as such, the Nima basin carbonates are interpreted to preserve oxygen isotopic compositions similar to primary precipitation values, and can reasonably be used for traditional stable isotope paleoaltimetry under this cautionary advisement. Therefore, both the Nima and Lunpola basins reflect the existence of high elevations on the northern margin of the Lhasa block by conservatively the latest Oligocene, but more likely, the late Eocene. We have no existing sedimentary records from the northern Lhasa block that extend beyond the mid-Eocene, so thus far there have been no paleo-elevation estimates for the northern Lhasa block in the pre- to early syn-collisional timeframe such as those related to the Linzizhong. Such a record is necessary to test whether high elevations in the Lunpola and Nima basins are relict of Mesozoic collisions, and whether the Lhasaplano extended as far north as the Bangong-Nujiang Suture prior to onset of India-Asia collision. However, the southern half of the Qiangtang block and the middle of the Lhasa block are covered in marine late Early to Late Cretaceous marine clastics deposited in littoral to inner shelf environments (Zhang, 2000)—not early Cenozoic strata comparable in age to the Nianbo Formation.

The Oligo-Miocene Gazhacun Group and Mio-Pliocene Oiyug Formation in the Oiyug

basin record stable isotope-based paleo-elevations in excess of the modern watershed mean elevation (~ 4600 m), and potentially, though cautiously, up to ~ 6500 m in the latest Miocene to Pliocene (Ingalls et al., 2017). The Oiyug Formation yields the highest paleo-elevation estimate from any of the basins from the Lhasa block due to the most ^{18}O -depleted carbonate compositions. However, we would expect carbonate formation at elevations up to 2 km higher than the Oiyug basin throughout the Eocene to Miocene to yield $\sim 10^\circ\text{C}$ lower $T(\Delta_{47})$. The Δ_{47} compositions of the Oiyug Fm samples are comparable to the remainder of the Oiyug basin samples. As such, we are tentative in the youngest paleo-elevations derived from the Oiyug basin.

While we largely dismiss the past tectonic models of Tibetan uplift in support of Tibetan crustal thickness being entirely the result of India-Asia collision, the 1-2 km increase in Oiyug elevation coincides with models of rapid uplift ~ 8 Ma due to the loss of a mantle lithosphere root (Molnar et al., 1993), or could reflect a delayed response to an inferred rapid Miocene exhumation due to the initiation of normal faulting in the Miocene, also attributed to the loss of a mantle lithospheric root (Harrison et al., 1992). Houseman et al. (1981) first argued that the shortening that led to crustal thickening beneath Tibet should yield a convective instability that removes the lower part of the lithosphere, which would detach and sink into the mantle. However, regional maps of $V_s(z)$ (shear wave velocities as a function of depth) and inferred lithospheric thickness are incompatible with Houseman et al. (1981)—the Tibetan Plateau is underlain by ~ 260 km of lithosphere today (McKenzie and Priestley, 2008). The thick lithosphere that extends beneath the entire plateau does not allow for detachment of mantle lithosphere in the Miocene, and thus is not a valid explanation for Tibetan uplift or onset of normal faulting and development of topography. Whether or not the tectonic mechanism for late Miocene uplift can be explained by past models weighing on detachment of the lithospheric root, the difference between Mio-Pliocene elevations in Oiyug and the hypsometric mean elevation today requires ~ 2 km of subsidence in the past ~ 5 Ma. This depression in surface elevation can likely be attributed to east-west extension

and tectonic collapse.

Recent evidence suggests that there may have been a period of low elevation along the Indus-Yarlung suture in the late Oligocene to early Miocene (26-21 Ma) (DeCelles et al., 2016). The >1300 km long Kailas basin formed within the collisional suture zone >35 Ma after the onset of India-Asia collision (DeCelles et al., 2016). Paleontological (large cyprinid fish fossils), organic geochemical, and sedimentological data led DeCelles et al. (2016) to interpret the Kailas basin as a deep, biotically productive meromictic lake with fringing coal-forming swamps and water temperatures exceeding 25°C. The Great Counter Thrust deeply buried the lacustrine units of the Kailas basin, and thus traditional stable isotope paleoaltimetry of Kailas deposition has proven unsuccessful (Quade et al., 2011). These deposits are currently exposed at an elevation of ~5 km, implying rapid and dramatic uplift of the IYS in the intervening ~20 million years. Additionally, paleosol carbonate oxygen isotope data from the uppermost red-bed member of the Kailas Fm are consistent with >4.5km elevations by the early Miocene (DeCelles et al., 2011), shortening the interval in which significant uplift must have occurred. Finally, pedogenic calcite-based stable isotope paleoaltimetry from the lower Gazhacun Group, coeval with Kailas basin deposition, yields consistent elevations of ~4.5 km <100 km north of the IYS in present day tectonic configuration (Ingalls et al., 2017).

The elevation history of the eastern edge of the Tibetan Plateau and the “escaped” continental crust of the southeast Asian microplates provides means for evaluating the contribution of lower crustal flow to the development of low relief high elevation within and on the fringes of the Tibetan Plateau (Hoke et al., 2014; Clark and Royden, 2000). The modern elevation of southeastern Tibet and western Yunnan reflects a protracted history of surface uplift: Eocene crustal thickening occurring within the Qiangtang block (Hoke et al., 2014), uplift related to tectonic extrusion of present day southeast Asia along the Ailao Shan-Red River shear zone (Tapponnier et al., 1982; Wang et al., 2014), and initiation of lower crustal flow beneath southeast Asia by at least the middle Miocene (Clark and Royden, 2000; Clift,

2006; Li et al., 2015).

Li et al. (2015) presented lacustrine-derived stable isotope paleoaltimetry from three sedimentary basins: the Markam basin (Fig. 3.1) on the very southeastern margin of the Tibetan Plateau on the margin of the Qiangtang and Lhasa blocks, and two from the northwestern Yunnan-Guizhou Plateau, Jianchuan and Xiaolongtan basins. After accounting for Rayleigh fractionation of oxygen isotopes in precipitation due to continentality, the hypsometric mean elevations for the inland drainage systems feeding the Markam, Jianchuan, and Xiaolongtan lacustrine basins are $3.8^{+1.1}/_{-1.6}$ km, 1.2 ± 1.2 km, and $1.7^{+0.5}/_{-0.8}$ km, respectively (Li et al., 2015; Gourbet et al., 2017). The Markam basin strata record deposition ~ 23 to 16 Ma, Jianchuan basin records deposition in the latest Eocene >34 Ma (Gourbet et al., 2017), and Xiaolongtan basin records deposition 12.7 to 10 Ma.

Li et al. (2015) proposed two tectonic mechanisms by which the Markam basin may have reached its near-modern elevation of ~ 2.6 km by the latest middle Eocene (~ 40 Ma): (i) The Markam basin may be relict of the southeastern edge of the Qiangtang block in Eocene geographic configuration, and thickened to its current elevation by persistent crustal shortening from the India-Asia collision, or (ii) by lower crustal flow within the Lhasa and Qiangtang blocks during the Paleocene-Eocene. The Xiaolongtan basin of SE Yunnan was near sea level in the Eocene (Hoke et al., 2014), and thus its modern elevation is likely resultant of lower crustal flow since the Oligo-Miocene. Based on earlier stratigraphy, it was thought that the Jianchuan basin reached an elevation of ~ 2.7 km above sea level by the late Eocene (Hoke et al., 2014), maintained that elevation ± 600 meters through the entire Miocene (Li et al., 2015), and subsided to its modern day elevation of ~ 2300 m since the late Miocene. However, updated biostratigraphy and geochronology from the Jianchuan basin requires consideration of paleogeography and basin configuration in the late Eocene to correctly account for the $\delta^{18}\text{O}_p$ continentality effect. Gourbet et al. (2017) uses the ~ 40 Ma plate reconstruction of Replumaz and Tapponnier (2003) to correct for continentality using the Eocene moisture path of Licht et al. (2014). The corrected paleo-elevation for the

Jianchuan basin is then 1200 ± 1200 m (Gourbet et al., 2017). The Eocene eastern edge of the Tibetan Plateau was thus likely located near-north of the Jianchuan basin retro-rotated to its Eocene plate configuration.

3.6 Conclusions

The Oiyug basin provides the only complete record of sedimentation spanning nearly the entire Cenozoic, and demonstrates that the Linzizhong persisted as a low relief, high elevation surface similar to today's landscape. Earliest Eocene elevations of Nianbo Formation equivalent in the Amu Xun agree with the Oiyug and Penbo paleo-elevation reconstruction. Further work should be done on the carbonate sedimentary record within the IYS from 26 to 21 Ma to investigate the likelihood of dramatic subsidence and uplift within this short span of geologic time.

In considering all of these data together with the present study, we can confidently conclude that just prior to collision, the land surface elevation immediately north of the Indus Yarlung Suture and Linzizhong arc was >4500 - 5000 meters above sea level. By at least 26 Ma, the Nima and Lunpola basins were ≥ 4500 meters a.s.l. on the northern margin of the Lhasa terrane, but very likely by the mid-Eocene (~ 40 Ma). The modern elevations of a series of Cenozoic sedimentary basins that span the eastern flank of the Qiangtang block seem to reflect a summation of collision-related lower crustal flow and lithosphere-scale tectonic extrusion.

CHAPTER 4

BALANCING CRUSTAL MASS VIA SUBDUCTION DURING CONTINENTAL COLLISIONS

This work is published as: Ingalls, M., Rowley, D.B., Currie, B.S., and Colman, A.S. (2016) "Large-scale subduction of continental crust implied by India-Asia mass-balance calculation." *Nature Geoscience*, 9(11), 848-853.

4.1 Abstract

Crustal mass balance is estimated in the India-Asia collisional system using the pre-collisional crustal thickness and convergence history derived from plate kinematics. Here, current best estimates of the diachronous onset of collision between India and Eurasia are detailed. We find that $\sim 50\%$ of the pre-collisional crustal mass in the collisional domain cannot be accounted for in the crustal reservoir today, represented by the mass preserved in excess crustal thickness (in Himalaya, Tibet, and adjacent Asia), southeast Asian tectonic escape, and exported eroded sediments. This implies large-scale subduction of continental crust during this continent-continent collision with a mass equivalent to $\sim 15\%$ of the total oceanic crustal subduction flux since 56 Ma. We suggest that similar contamination of the mantle by direct input of radiogenic continental crustal materials during past continent-continent collisions is reflected in some ocean crust and ocean island basalt geochemistry and that subduction of continental crust contributes significantly to the evolution of continental crust and mantle geochemistry.

4.2 Introduction

Collision-related crustal mass balance is critical to understanding how continental crust behaves in large-scale collision systems, how continental crustal composition evolves over

time, and the degree to which direct input of continental crustal materials into the mantle may impact mantle geochemistry. It has long been assumed that crustal mass balance is maintained during collisions (Dewey and Bird, 1970; McKenzie, 1969) because continental crust is too buoyant to be subducted. Previous analyses of collision-related mass balance in the India-Asia system have yielded results that range from balanced (Richter et al., 1992), to unbalanced (van Hinsbergen et al., 2011), to potentially balanced (Yakovlev and Clark, 2014) reflecting differing approaches, ages of initial collision, and masses/volumes of contributing components. We re-assess the India-Asia collisional mass balance by integrating the most recent estimates of collision age, plate kinematic constraints on India-Asia convergence, and the correlation of paleo-elevation and crustal thickness distribution, all with associated uncertainties. We compare these to estimates of the present crustal mass within the collision system: integrated crustal thickness within the collision domain, escaped crustal mass, and detrital and dissolved sediment fluxes. We review and justify each aspect of the mass balance calculation below.

4.2.1 *Mass balance in an active collision zone*

Crustal mass balance in the Himalaya-Tibet system integrates the mass at the onset of the collision relative to crustal mass measured today (England and Houseman, 1986). If continental crustal mass is conserved at the Earth's surface, the continental crustal mass at the onset of collision ($M_{convergence}$) must balance the net mass reflected in crustal thickening and exported from the system:

$$M_{convergence} = M_{thicken} + M_{erode} + M_{escape} \quad (4.1)$$

In equation 4.1, $M_{convergence}$ is the mass of Greater Indian and Greater Tibetan continental crust (Fig. 4.1) reconstructed at the onset of collision, $M_{thicken}$ is the mass added to the Himalaya-Tibet system by collision-related crustal thickening integrated over the defor-

mation domain (Fig. 4.1B), M_{erode} is the eroded sediment flux (Richter et al., 1992; Clift, 2006; Métiévier et al., 2002) (including dissolved sediment), and M_{escape} is lateral tectonic escape (Tapponnier et al., 1982).

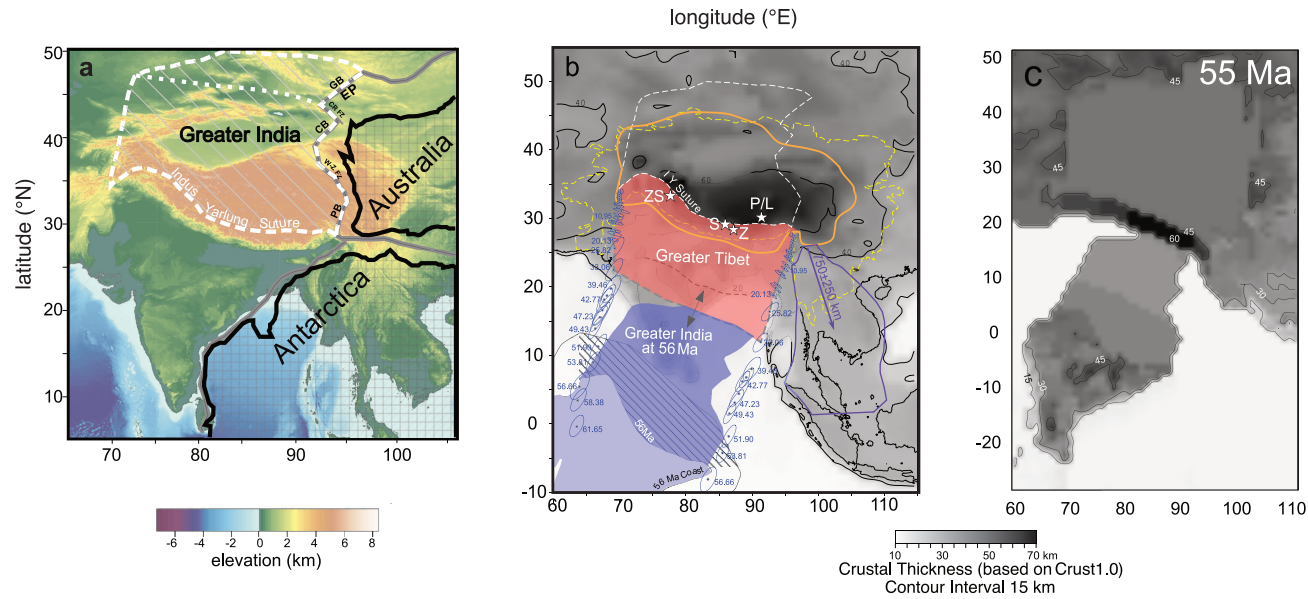


Figure 4.1 **Paleogeographic and paleothickness reconstructions of the Himalaya-Tibet orogen.** **A. Gondwanan reconstruction on modern Etopo1 topography** West Australian geologic structures: the Perth Basin (PB), Wallaby-Zenith Fracture Zone (WZFZ), Cuvier Basin (CB), Cape Range Fracture Zone (CRFZ, dotted white), Gascoyne Basin (GB), and Exmouth Plateau (EP, dashed white). **B. Reconstructed geometry at age of collision.** Modern geography and crustal thickness are indicated by dark grey outlines and grey-scale shading. Color is used to indicate colliding plates and collisional domains. Paleo-positions of the western and eastern syntaxes (ages in Ma are indicated in blue text) relative to fixed Eurasia are shown with 95% confidence ellipses. The double-ended arrow marks the potential leading edge of Greater India when assigned collisional ages of 58 and 54 Ma. Yakovlev and Clark's (2014) Greater India (slanted lines) and retrodeformed Asian margin (gray dashed line across modern India); present positions of the Penbo/Linzhou Basin (P/L), Sangdanlin (S), Zanskar Shelf (ZS), and Zhepure Shan (Z). The orange and yellow dashed polygons outline the excess crustal mass domains of this study and Yakovlev and Clark (2014), respectively. Purple outline marks the region of tectonic escape relative to the orange polygon outline. **C. Reconstruction at 55 Ma of CRUST1.0 (Laske et al., 2013) crustal thicknesses** with inferences regarding pre-collisional thicknesses of Greater India and Tibet, and a thick Linzizong arc margin.

We have compiled the most complete set to date of tectonic and geochronologic constraints on the pre-collisional geography of India and Eurasia. Additionally, recent paleoaltimetry results from the Linzizong Arc along the southern margin of Eurasia provide an explicit estimate of the crustal thickness beneath the arc at ~ 55 Ma (Ingalls et al., 2017).

The crustal mass at the onset of collision can be constrained by the initial crustal thickness distribution and the integrated amount of Indian and Eurasian plate convergence since collision onset, assuming a constant mean crustal density. Dating the age of onset of the collision of India with Asia has been a particularly difficult geological exercise. Recent estimates are greatly improved and imply a fairly complex and diachronous history from west to east along sutures separating India from Eurasia.

4.3 Paleogeography of the India-Asia Collision

4.3.1 *Age of initiation of the India-Asia continent-continent collision*

The following discussion summarizes the age of onset of the India-Asia collision starting along the western margin and proceeding eastwards along the suture. In the west in the late Paleocene, oceanic arcs and the Bela, Quetta, and Muslimbagh ophiolites collided with the northwestern Indian passive margin (Beck et al., 1995). In the mid-Eocene, a passive-type margin was re-established unconformably above these obducted ophiolites. This was followed by collision with the Makran-related accretionary prism along this margin in the late Eocene to Pliocene (Rowley, 1996). Farther north in the Kohistan-Ladakh Arc (KLA), Ypresian ($\sim 51 \pm 1.5$ Ma) collision of the KLA with the Indian passive margin is well constrained by stratigraphic relations (Gaetani and Garzanti, 1991; Green et al., 2008), isotopic dating of ultra high pressure (UHP) metamorphism from the Kaghan (Wilke et al., 2010) and Tso Morari (Leech et al., 2005; St-Onge et al., 2013), and transition from mantle-derived to contaminated magmatism in the southern KLA at 50 Ma (Bouilhol et al., 2013). However, the age of the Shyok suture between Kohistan-Ladakh and Eurasia is less certain. Recent

data (Bouilhol et al., 2013) imply that India+KLA-Asia related collision began at $\sim 40.4 \pm 1.3$ Ma. However, syn-collisional provenance data stratigraphically overlying Indian passive margin sequences imply proximity to Asian sources north of the KLA and Shyok suture at 51 Ma (Roddaz et al., 2011). We accept these data and assign a likely age of India-Eurasia collision along the ~ 1000 km long western segment at 51 ± 1.5 Ma.

Detrital zircon data from Sangdanlin and Zhepure Shan provide constraints on the onset of collision farther east (Fig. 4.1). Onset is marked by first arrival of Gangdese-derived sediments in the Asian fore-arc basin (Orme et al., 2014) overtop the Xigaze fore-arc basin and deep-water, off-shelf Indian passive margin. A minimum date of ~ 58 Ma is provided by interbedded ash near the top of the section (DeCelles et al., 2014), updating previous work that dates the initial arrival of Gangdese-derived sediments on the shallower water Indian passive margin at $\sim 51 \pm 1$ Ma (Najman et al., 2010; Zhu et al., 2005). Unlike farther west, there is no evidence for an oceanic arc intervening between the Xigaze forearc (derives its sediments from the Gangdese arc on the Lhasa block to the north) and the Indian passive margin (derives its Asian margin sediments also from the Gangdese margin) at ~ 58 Ma. We assign the age of initial collision of thicker continental crust of India with Asia at 56 ± 2 Ma, acknowledging the high mean convergence rate of ≥ 150 km/my during this interval. This requires that the younger suturing along the KLA-India suture terminate west of the Xigaze forearc (84.8°E), limiting the younger 51 ± 1.5 Ma suture length to ≤ 1000 km.

There are no data that directly constrain the age of the India-Asia collision east of the Zhepure Shan (Rowley, 1996) adjacent to the suture zone. Indirect evidence comes from dating the minimum age of Eo-Himalayan metamorphism in the eastern Tethyan Himalaya at ≥ 44 Ma (Aikman et al., 2008). For the purposes of modeling, we use an age of suturing in the vicinity of the eastern syntaxis at 54 ± 4 Ma. We infer a younger, $\sim 40 \pm 4$ Ma age for suturing along the east-facing passive-margin corresponding to the Gascoyne, Cuvier, and Perth Basin conjugates of Greater India.

4.3.2 *Geometry of Greater India constrained by Gondwanan reconstructions*

Greater India, a pre-collisional northern continuation of the modern Indian continent, has long been discussed (Argand, 1924) as an explanation for the double thickness of Tibetan continental crust. We use the rifting relations of eastern Gondwana between East Antarctica, India, and the western Australian margin to define the geometry of eastern Greater India (Fig. 4.1A).

Greater India must fit against the Australian margin from the Perth Basin (Ali and Aitchison, 2005) to some distance northward. Ali and Aitchison (2005) prefer a northern edge coincident with the Wallaby-Zenith Fracture Zone and thus limit it to fitting the Perth Basin. A northward limit of Greater India matching to the Cuiver Basin at the Cape Range Fracture Zone has also been proposed (Powell et al., 1988). Finally, we and others extend Greater India to the northeastern boundary of the Exmouth Plateau to match the Gascoyne Basin (Matte et al., 1997; Hall, 2012). Greater India as postulated here extends approximately 2400 km north-south. This is compatible with the existing Late Cretaceous paleomagnetic data from the Tethyan Himalayas (van Hinsbergen et al., 2012).

The fit adopted here only explicitly constrains the geometry of the eastern passive margin of Greater India with the western margin drawn to match the timing of collisions from Sangdanlin (Fig. 4.1) and farther west. Greater India occupies an area of $\sim 4.2 \times 10^6$ km² in our reconstruction.

4.4 **Bootstrap estimate of areal, volume and mass convergence since onset of collision**

We estimate area, volume and mass convergence associated with the diachronous India-Asia collision. We incorporate plate kinematic constraints on the convergence history and their uncertainties in our calculations (Tables C.1, C.2). The effective convergence zone length

(CL) as a function of time (Table C.3) is defined as the difference ($D_1 - D_2$) between the suture zone end points (EP_1 and EP_2) measured relative to each of the stage rotations (P_t) times the radius of the Earth (R_{Earth}).

$$D_1 = P_t \times EP_1 \quad (4.2)$$

$$D_2 = P_t \times EP_2 \quad (4.3)$$

$$CL_{12} = (D_1 - D_2) \times R_{Earth} \quad (4.4)$$

The areal convergence, A_{12} , over time ($t - \Delta t$) is given by:

$$A_{12} = | \cos(D_2) - \cos(D_1) | \times \Omega \times G \quad (4.5)$$

where $G = \pi/180R_{Earth}^2$, and Ω is the rotation angle about P_t . The length-weighted mean convergence rate is then

$$R_{12} = A_{12}/CL_{12}/\Delta t \quad (4.6)$$

where Δt is the time interval between constraining rotations. The cumulative area ($C(t)$), volume ($V(t)$), and mass ($m(t)$) convergence as a function of age (t) are

$$C(t) = \Sigma_0^t A_{12} dt \quad (4.7)$$

$$V(t) = \Sigma_0^t A_{12} dt \times \bar{z} \quad (4.8)$$

$$m(t) = \Sigma_0^t A_{12} dt \times \bar{z} \times \bar{\rho} \quad (4.9)$$

where z is the area-weighted mean crustal thickness and ρ is density (using 2800 kg/m³ as a mean crustal density). We treat these integral quantities as summations to reflect the discrete nature of the rotation data. The only inputs required are the convergence zone end point locations (EP_1 and EP_2) as a function of age (Table C.3) and corresponding

Table 4.1 **Local convergence length of continental crust along the Indus Yarlung Suture since the onset of India-Asia collision.**

Region	Time Interval (Ma)	Length Convergence (km) ($\pm 2\sigma$)
Western Indus Suture	51.0 ± 1.5	2440 +350/-320
Central Indus-Yarlung Suture	56.0 ± 2.0	3800 +530/-510
Eastern Syntaxis	40.0 ± 4.0	2580 +580/-550
Eastern Himalayas	52.0 ± 4.0	3440 +890/-720

rotations. Because both the end points and rotations have associated uncertainties, we use a bootstrap to estimate uncertainties resulting from these quantities (see below). We treat the age of collision and interval rotation uncertainties as Gaussian distributed estimates. We allow suture and convergence zone lengths to vary up to their maximum length. Plate convergence data between India and Eurasia are based on a compilation of global rotations with associated 95% confidences (Tables C.1, C.2, C.3). Random lengths of the Asia+KLA to India suture (up to 1000 km) and eastern syntaxis sutures are subtracted from the total length of the suture zone such that suture zone length grows to its total length by the age of elimination of intervening oceanic lithosphere at the end of suturing. This end is defined by the Gaussian distributed age specified at the start of each iteration. For ages younger than this, the end points are maintained at the full convergence zone length.

To summarize, the mass balance calculations use collision ages of 51 ± 1.5 Ma (1σ) along the ≤ 1000 km western end of the suture (Gaetani and Garzanti, 1991; Green et al., 2008), 56 ± 2 Ma along the main Indus-Yarlung Suture (DeCelles et al., 2014; Orme et al., 2014) (IYS) from $\sim 79^\circ\text{E}$ to $\sim 95^\circ\text{E}$, and 40 ± 4 Ma along the ≤ 500 km suture in the far east (Aikman et al., 2008).

Total converged area is constrained in our reconstruction, as is the trajectory of motion and associated rotation-related uncertainties (Fig. 4.1). We use a 50,000 iteration bootstrap approach to integrate area flux along the IYS, incorporating uncertainty in the age of suturing, length of sutures and rotations as a function of age.

The resulting best estimate of the total areal convergence of continental crust since

continent-continent collision began is $9.1^{+2.4}/_{-2.0} \times 10^6 \text{ km}^2$ (2σ) using plate reconstructions and the timing of juxtaposition of Greater Indian and Greater Tibetan crust (Fig. 4.2). Figure 4.2B and 4.2C summarize local and areal convergence, incorporating both age and rotation-related uncertainties.

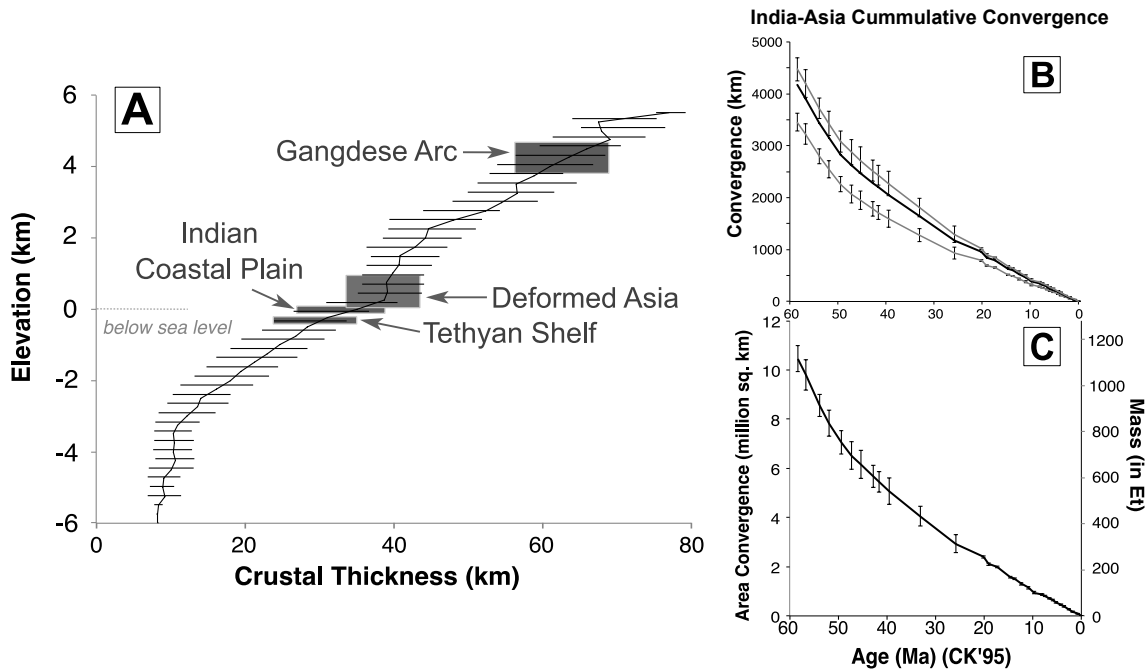


Figure 4.2 **Continental thickness and mass convergence.** **A.** Relationship of continental crustal thickness to elevation derived from CRUST1.0(Laske et al., 2013) with 1σ thickness standard deviations. **B.** Mean (dark line) cumulative India-Asia convergence (1σ) as a function of time together with the east (upper grey line) and west (lower grey line) ends of the Indus-Yarlung suture. **C.** Areal convergence with 1σ uncertainties and equivalent mass convergence (without uncertainties) associated with India-Eurasia relative motions incorporating only rotation and age-related uncertainties.

4.4.1 Assignment of crustal thickness

We employ a second bootstrap to estimate the corresponding volume and mass convergence. We input the total area convergence with associated uncertainty. We apportion the colli-

sional area into four crustal thickness domains: Indian coastal plain, Tethyan shelf, Linzizong Arc, and remaining deformed Asia. We use Crust1.0s (Laske et al., 2013) relationship between crustal thickness and elevation, averaged at the same spatial resolution as the crustal thickness grid, to assign crustal thicknesses and associated standard deviations to each of the elements in this analysis (Fig. 4.2). We exclude areas where the current crustal thickness is less than the estimated pre-collisional average crustal thickness.

Greater India represents $\sim 50\%$ of the total convergence. We therefore assign $25 \pm 5\%$ (1σ) of the converged area to each the Indian coastal plain and Tethyan shelf, which comprise Greater India (Fig. 4.1C). There is no preserved evidence of a Cretaceous or early Cenozoic northern source of sediments in the Lesser Himalaya prior to the Eocene Subathu and Bhainskati, and clear evidence for a southern Indian cratonic source in the early Paleocene Jidula Formation of the Tethyan Himalayas (DeCelles et al., 2014; Zhu et al., 2005). We therefore assign a crustal thickness of 35 ± 5 km (1σ) to the Indian coastal plain assuming an average elevation of 0 m, and 31 ± 5 (1σ) km to the Tethyan shelf assuming an average elevation of ~ 250 m. These are conservative elevation estimates and therefore conservative crustal thicknesses.

We use recent paleo-elevation estimates of 4100 ± 550 m (Ding et al., 2014; Ingalls et al., 2017) and the areal extent of Gangdese granitoids and Linzizong volcanics at ~ 55 Ma to assign a crustal thickness of 61 ± 6 km to the Linzizong Arc. The present Linzizong arc occupies $\sim 4 \pm 2\%$ (1σ). The bootstrap allows the areal extent of high elevations in the Linzizong Arc to be (1) all, (2) a small fraction (but $\geq 0.5\%$), or (3) a much broader area than implied by preserved outcrop of the Linzizong magmatism. The remaining $\sim 3.85 \times 10^6$ km², which we refer to as Deformed Asia, presumably had a broad distribution of elevations reflecting the complex prior tectonic history. We ascribe a mean elevation of 500 ± 500 m to Deformed Asia with a crustal thickness of 38 ± 4 km (Fig. 4.2A) because significant areas had been at or below sea level in the Cretaceous (Zhang, 2000). This elevation and crustal thickness range encompasses the mean elevation of areas above sea level and mean crustal thickness of the

continental crust as a whole.

We assume Gaussian fractional area and crustal thickness uncertainties in this bootstrap. We then solve for volume and mass by summing the crustal thickness (\pm uncertainty) multiplied by fractional area (\pm uncertainty) multiplied by area convergence (\pm uncertainty). The resultant total volume and mass convergences are $3.3_{-0.8}^{+1.0} \times 10^8 \text{ km}^3$ ($\pm 2\sigma$) and $915_{-237}^{+290} \times 10^3 \text{ Gt}$ ($\pm 2\sigma$), respectively. These correspond with a mean pre-collisional crustal thickness over the entire domain of $\sim 36 \text{ km}$, $\sim 21 \text{ km}$ less than currently within the deformed region.

4.4.2 Contributions of the components of the mass balance equation

Excess crustal thickness

We assess the current excess crustal mass of the India-Asia system using two data sets of crustal thickness, Crust1.0 (Laske et al., 2013) (Fig. 4.2) and that used by Yakovlev and Clark (2014), applied to two different area domains of potentially thickened crust during India-Asia convergence and the area of southeast Asia that may have been transported laterally via tectonic escape (Fig. 4.1). We perform all of the calculations using both domains and crustal thickness data sets in order to ensure that our results are insensitive to both domain size of potential crustal thickening and the crustal thickness distribution. We incorporate a $\pm 5 \text{ km}$ uncertainty in estimates of the present crustal thickness (Ding et al., 2014).

Excess crustal mass is defined as:

$$M_{excess} = \rho_c \int_A (z_{today} - z_{CollisionOnset}) dA \quad (4.10)$$

where z is crustal thickness, A is the area of potential crustal thickening (Fig. 4.1B), and ρ_c is mean crustal density. The estimate of excess crustal mass represented by the current distribution of crustal thickness, independent of the crustal thickness source and definition of the domain, is $\sim 280 \pm 100 \times 10^3 \text{ Gt}$ or about $30 \pm 10\%$ of the mean pre-collisional crustal

mass.

Erosional mass flux

We use a volume of $5.0 \pm 1.0 \times 10^7 \text{ km}^3$ ($\pm 1\sigma$) for the erosional mass transported out of the collision domain, or a mass of $\sim 140 \pm 28 \times 10^3 \text{ Gt}$ ($\pm 1\sigma$). This volume is comparable to two previous estimates of the erosional rock equivalent volume flux. Richter et al. (1992) estimated erosional loss to be $\sim 5 \times 10^7 \text{ km}^3$. Métiévier et al. (2002) estimated removal of $\sim 3 \pm 1 \times 10^7 \text{ km}^3$ rock equivalent volume, but their estimate did not include the Makran ($\geq 1.1 \times 10^7 \text{ km}^3$), Indo-Burman-Andaman-Sumatran accretionary complex ($\sim 2.5 \times 10^6 \text{ km}^3$), or the associated dissolved flux ($\sim 1.0 \times 10^7 \text{ km}^3$). Our erosional mass flux is nearly three times greater than that assumed by Yakovlev and Clark (2014).

Tectonic escape

We define escape as the transport of the entire crustal column from within the Deformed Asia domain to a location outside that domain (Richter et al., 1992). We use the boundaries shown in Figure 4.1B of both the deformed region and the region of potentially escaped crust. We compute the volume and mass of the potentially escaped region as a function of latitude because the mass transport is largely north to south. We calculate displacement along the bounding faults using both CRUST1.0 (Laske et al., 2013) and crustal thickness from Yakovlev and Clark (2014), separately. We use the estimated $750 \pm 250 \text{ km}$ displacement (Leloup et al., 1995) to derive an escaped volume and mass of $\sim 1.55 \pm 0.85 \times 10^7 \text{ km}^3$ and $54 \pm 27 \times 10^3 \text{ Gt}$ ($\pm 1\sigma$), respectively.

4.5 Discussion and Conclusions

4.5.1 *Half of pre-collisional continental crust absent from the surface of the Earth*

By this accounting, the currently reconstructable excess mass of the Himalayan orogenic system is $465_{-176}^{+192} \times 10^3$ Gt or $\sim 51\%$ of the syn-collisional mass. This leaves $\sim 450_{-308}^{+338} \times 10^3$ Gt, or essentially $49_{-33}^{+37}\%$ (2σ) of the total syn-collisional mass of Greater India and Greater Tibet unaccounted for. Previous attempts to make this calculation have relied on shortening estimates derived from surface structures relative to convergence (van Hinsbergen et al., 2011), area (Yakovlev and Clark, 2014), and volume (Richter et al., 1992). We have improved this body of work by using rigorous tectonic constraints on the collisional system and uncertainties, the most recent age estimates for collision along the IYS, and recent estimates of pre-collisional paleo-elevation and corresponding crustal thickness along Eurasias southern margin. We conclude that the system is not in mass balance and that essentially half of the collisional crustal mass is missing. Wholesale subduction of continental crust into the mantle appears to be the only reasonable explanation for this missing mass.

4.5.2 *Subduction of continental crust*

These results imply large-scale subduction of continental crust into the mantle. This is expected where the lower continental crust is largely transformed to eclogite during underthrusting (Fig. 4.33). Detailed tomography (Li et al., 2008) implies the existence of ongoing subduction of seismically fast material into the upper mantle today. Eclogitized lower crust beneath southern Tibet has been inferred both seismically (Nabelek et al., 2009; Wittlinger et al., 2009) and from fitting of gravity anomalies (Hetenyi et al., 2007), and it is expected from petrological modeling (Hetenyi et al., 2007; Bollinger et al., 2006). Current estimates of eclogitized lower crust extends ~ 150 to 200 km in a north-south direction and is ~ 19 km thick (Nabelek et al., 2009; Wittlinger et al., 2009) in the HiCLIMB section. This material

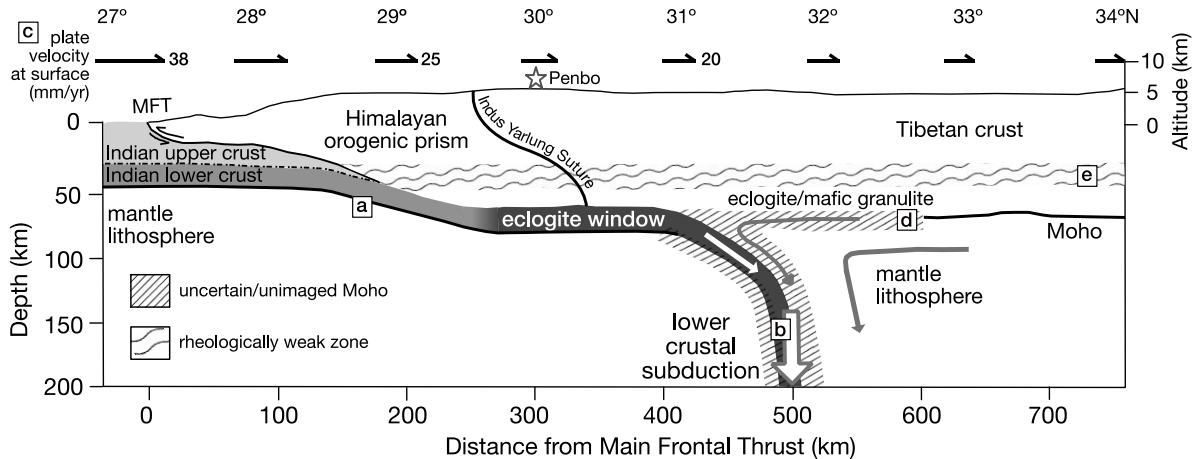


Figure 4.3 **Schematic tectonic cross-section of India, the Himalayan orogenic prism, and southern Tibet during lower crustal subduction.** **A.** Placement of the dipping and flattening Indian lower crust and Moho are based on receiver functions (Nabelek et al., 2009). Seismic doublet represents the seismic Moho and the eclogite transition zone (“eclogite window”). **B.** Li et al. (2008) image a steeply dipping channel of seismically fast material (interpreted as subducting mantle lithosphere and eclogitized lower crust) in the upper mantle beneath southern Tibet. **C.** The relative length of arrows represent plate velocity using surface GPS data from an 85°E transect (Zhang et al., 2004). **D.** Crust-mantle boundary in the subduction zone $+2^\circ$ north is poorly resolved (hashed area). **E.** A mid-crustal, rheologically weak zone (wavy pattern) allows northward motion of upper crust while the eclogite/mafic granulite Tibetan lower crust remains stationary relative to fixed Eurasia.

would represent 4 to 5 My of residence time at modern convergence rates of ~ 40 km/My. When combined with both shallow and deeper mantle tomographic evidence for subduction of mantle lithosphere, we surmise that this eclogitized lower crust is being recycled into the mantle. We infer that this has been a general process that has subducted lower crust into the mantle throughout this collision.

Existing images (Li et al., 2008) imply a discontinuous “deblobbing” of lithospheric mantle and eclogitic crust rather than a continuous tabular structure typical of subduction zones. Existing interpretations map most of the eclogite to Indian lower crust (Wittlinger et al., 2009), but we note that approximately half of the present India-Eurasia convergence is accommodated north of 32° (Zhang et al., 2004) (Fig. 4.3) requiring detachment of Tibetan

mid- and upper-crust from underlying mantle lithosphere and likely eclogitic lower crust. Subduction of the lower Tibetan crust likely contributes to crustal mass loss (Fig. 4.33).

We infer that loss of eclogitized crust has been ongoing since the beginning of collision and is responsible for the missing crustal mass. The presence of seismically fast material below India attributed to the “Tethyan” slab (Hafkenscheid et al., 2006; van der Voo et al., 1999), and particularly with depths shallower than 1300 km, could well represent eclogitized crust and mantle lithosphere derived from both India and Tibet, assuming a mean radial sinking rate of ~ 30 km/My and ~ 3900 km of post-56 Ma convergence. The eastward continuation of these seismically fast anomalies extending beneath southeast Asia³⁶ would represent the along-strike oceanic lithosphere continuation of this material.

To gain some appreciation for the magnitude of the missing crustal mass, we compare it with the total mass flux of subducted oceanic crust over the same 56 Ma history. The annual oceanic crustal volume flux is about ~ 20.1 km³/yr at the current oceanic subduction rate of ~ 3.1 km²/yr and with a mean oceanic crustal thickness of ~ 6.5 km. This flux corresponds to ~ 56 Gt/yr. If we assume a constant rate of collision-related mass loss from the India-Asia collision, the resulting annual rate of continental mass subduction would be about 7.6 Gt/yr, or $\sim 14\%$ of the total ocean crust subduction mass flux.

4.5.3 *Crustal mass loss*

Lee (2014) discusses the petrological consequences of lower crustal subduction with small scale examples relative to what we present here. Although not derived from the India-Asia collision, geochemical signatures of lower crustal eclogite have been recognized in mid-ocean ridge basalts along the Southeast Indian ridge south of Australia (Hanan et al., 2013), and possibly in ocean island basalts (Hofmann, 2014), as well. Previous large scale collisions, such as the Variscan of central Europe (O’Brien, 2000), the Pan-African (Fritz et al., 2013), and the Grenville (Dewey and Burke, 1973), may have been responsible for subduction of lower crust and associated mantle contamination, as seen in various radiogenic systems (Hofmann,

2014). The scale of this phenomenon in the Himalaya-Tibet orogen is compatible with two-stage models for continental crustal evolution, that include significant loss of a more mafic lower crust (Li et al., 2008). We propose that subduction of lower continental crust and mantle lithosphere during collision-related convergence may serve as a more general model for crustal recycling during continent-continent collisions throughout Earth history, producing radiogenic isotope anomalies in mantle-derived magmas, and influencing the long-term evolution of the continental crust.

4.5.4 Comparison of our mass balance calculations with those of Yakovlev and Clark

Yakovlev and Clark (2014) recently published an assessment of the India-Eurasia collision related mass balance. Their approach focused on using current estimates of surface shortening within Himalaya-Tibet together with some paleogeographic data to reconstruct the pre-collisional margins of India and Eurasia. Plate kinematic and direct dating of the age of onset of the India-Asia collision was not incorporated in their final mass balance assessment. They derive estimates of potential mass loss into the mantle that overlap as a percentage those that we compute but are based on analyses that are largely inconsistent with those arrived at in our analysis. Their major contention is that mass balance can be reconciled if the average crustal thickness over the entire collision domain was 26 ± 3 km, and thus that subduction of continental crust into the mantle associated with this collision is unnecessary. I review aspects of their analysis here.

Greater Indian continental crust directly in contact with Greater Tibetan crust demarcates the initiation of collision. As shown in (Fig. 4.1B), Greater India and Greater Tibet, as determined by Dupont-Nivet et al. (2010) and used by Yakovlev and Clark (2014) would have been separated by ~ 2000 km at 56 Ma, the current best estimate of the age of initiation of collision. This represents $\sim 4.2 \times 10^6$ km², equivalent to the entire area of Greater India, or $\sim 46\%$ of the integrated converged area that is missing from their initial set up. Yakovlev

and Clark (2014) indicated that they preferred a smaller estimate of Asian shortening that reduces the area of Greater Tibet to about one third this size and so would accentuate the gap to ≥ 2500 km at 56 Ma. This is $\sim 5.4 \times 10^6$ km² of missing crustal area from their initial set up. An alternative way of quantifying this is to compute the ages of initiation of collision compatible with these area reductions relative to the plate kinematically constrained convergence history. Using their crustal shortening estimates collision should have begun between ~ 36 Ma and ~ 28 Ma. Thus the area estimates used in the Yakovlev and Clark (2014) calculation are incompatible with current best estimates of the age of onset of the collision by about a factor of two or more.

The area of Greater India derived from the fit of India within Gondwana (Fig. 4.1A) that extends as far north as matching the northern edge of the Exmouth Plateau is $\sim 4.2 \times 10^6$ km². Coincidentally, this is the same areal extent derived by Yakovlev and Clark (2014), even though the boundaries defining the area of Greater India are entirely different (Fig. 4.1). YYakovlev and Clark (2014) limit the northern edge to match the Wallaby-Zenith Fracture Zone (WZFFZ), but draw an extensive eastward and southward prolongation that incorrectly and extensively overlaps with the western margin of Australia and East Antarctica in Gondwanan reconstructed coordinates (Fig. 4.1). This eastward projection encompasses an additional $\sim 0.8 \times 10^6$ km² of crust that cannot be part of Greater India. If Yakovlev and Clark (2014) had rigorously considered the Gondwanan crustal geometry, they would have determined a Greater India considerably smaller ($\sim 2.7 \times 10^6$ km²) than that estimated in our work. This reduction would have significantly impacted their overall estimate of crustal mass balance.

Yakovlev and Clark (2014) cite paleoaltimetry studies from various parts of the Tibetan Plateau that mostly constrain the age of high elevations to Late Eocene (38 Ma) or younger (Bershaw et al., 2012; Hoke et al., 2014; Quade et al., 2011; Rowley and Currie, 2006). On the basis of these results they include in some of their calculations areas of thickened crust extending over all of the Lhasa block and potentially Qiangtang block. However, only two

more recent studies (Ding et al., 2014; Ingalls et al., 2017) constrain the pre- to syn-56 Ma paleo-topography. These newer data are restricted to a segment of the Linzizong arc that dates from the age of onset of collision. The studies reporting results related to younger paleo-elevations are therefore not relevant to the mass balance calculations and result in a larger mass deficit than current paleoaltimetry data support.

As noted in the main text, another component for which we use a significantly different value is for the exported eroded sediments. Yakovlev and Clark (2014) use a volume of $1.7 \times 10^6 \text{ km}^3$ and we use a volume of $5.0 \times 10^6 \text{ km}^3$, almost a factor of 3 larger. Their value derives from Métivier et al. (2002) but include only the post-40 Ma sediments, while our volume takes the entire Cenozoic record of Métivier et al. (2002) but adds the Makran, Indo-Burman-Andaman Flysch, and dissolved fraction to it.

Finally, Yakovlev and Clark (2014) conclude that a reasonable solution to achieve crustal mass balance in this collisional system is for the mean crustal thickness of the entire converged crustal domain to have been $\sim 26 \pm 3 \text{ km}$ thick, or about 2/3 normal continental crustal thickness. Based on Fig. 4.2A globally the mean elevation for a crustal thickness of 26 km is $\sim -460 \text{ m}$, leading to the expectation that the vast majority of the pre-collisional paleogeography would have been characterized by deep shelf to off-shelf facies marine sediments, in stark contrast to the observed largely non-marine to at most intermittent shallow marine facies sedimentary rocks of Cretaceous (Zhang, 2000) to early Cenozoic age (Bureau of Geology and Mineral Resources Xizang Autonomous Region) on the Plateau north of the suture. Non-marine to shallow marine shelf facies sedimentary rocks dominate the Late Cretaceous to Early Cenozoic of Lesser (DeCelles et al., 2001) and Tethyan (Green et al., 2008; Willems and Zhang, 1993) Himalaya south of suture zone. Their preferred solution thus appears incompatible with the preserved geology and the relationship between crustal thickness and elevation.

CHAPTER 5

CRYPTIC CARBONATE DIAGENESIS AND

Δ_{47} THERMOMETRY: INFORMING COMPLEX THERMAL

HISTORIES WITH A VARIABLY ALTERED PROXY RECORD

5.1 Introduction

The clumped isotope thermometer ($T(\Delta_{47})$) is arguably one of the most important tools introduced to the field of paleoclimatology in the past decade (Keating-Bitonti et al., 2011; VanDeVelde et al., 2013; Snell et al., 2013), with additional uses for tectonics (Ghosh et al., 2006b; Snell et al., 2014; Huntington et al., 2015; Ingalls et al., 2017), environmental reconstructions (Passey et al., 2010; Zaarur et al., 2011), and paleo-ecology (Eagle et al., 2010; Henkes et al., 2013). This thermometer relies on the homogeneous isotopic equilibrium among carbonate ions, enabling us to derive past mineral formation temperatures without independent knowledge of the meteoric water compositions.

There is a greater degree of bond ordering between the rare isotopes of carbon and oxygen (^{13}C and ^{18}O) at relatively cool carbonate (CO_3^{2-}) formation temperatures (Eiler, 2007). However, we measure clumped isotope abundances in natural materials collected from sedimentary basins that have experienced their own complex thermal histories after original mineral formation. The degree of isotopic ‘clumping’ can be altered in two ways (Fig. 5.1): (i) by water-facilitated recrystallization at a range of temperatures, and (ii) solid-state reordering of C-O bonds within the minerals crystal lattice at temperatures $>120 - 150^\circ\text{C}$ for tens of millions of years (Passey and Henkes, 2012; Henkes et al., 2014; Stolper and Eiler, 2015). It is conventionally thought that on relevant geologic timescales, carbonate that forms at Earth surface temperatures (high Δ_{47}) and is buried to the solid-state reordering temperature regime (decrease Δ_{47}) cannot create greater bond ordering. As such, a high Δ_{47} value is consistently assumed to reflect primary (low-T) carbonate formation conditions. However,

the isotopic results presented in this chapter require a mechanism for apparently increasing bond ordering during burial diagenesis and/or exhumation in the absence of recrystallization.

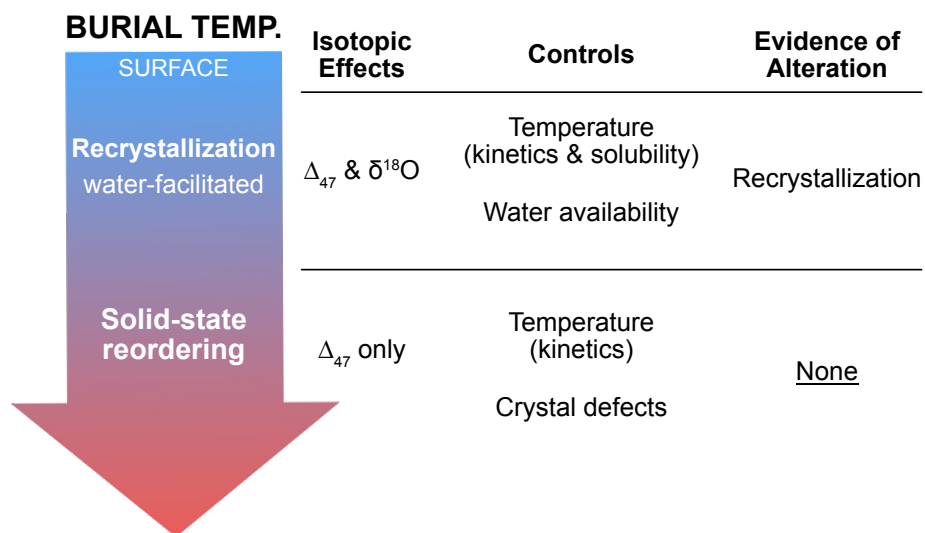


Figure 5.1 **Two modes of isotopic alteration during carbonate diagenesis.** At any temperature and in the presence of water, carbonate may recrystallize to form new carbonate. Recrystallization alters Δ_{47} and $\delta^{18}\text{O}$ signatures, and should be able to be identified petrographically. Internal isotopic exchange by means of diffusive bond reordering only happens at sufficiently elevated temperatures, and only strictly alters Δ_{47} . There are no visible signs of this form of alteration. We presume low water:rock ratio during deep burial within the Tso Jiangding, and thus the dominant alteration mechanism would be SSR. However, there was likely a limited amount of water-facilitated isotopic exchange at depth.

The upper Paleocene to Eocene Jialazi Formation (southern Tibet) records a facies transition from shallow marine to terrestrial during the early stages of India-Asia collision (Orme et al., 2014). The marine samples presented in this chapter are geologically and isotopically ideal for investigating mechanisms and isotopic effects of burial diagenesis on carbonate because (1) the initial isotopic values are constrained by known marine compositions and low-latitude sea surface temperatures in the Paleocene, and (2) zircon fission track and U-Th/He thermochronometry has provided constraints on the burial history of these strata. Late Paleocene-early Eocene, low-latitude marine carbonate should yield $\delta^{18}\text{O}_c$ values of ~ -2 to -3 ‰ VPDB (Kobashi et al., 2001) and temperatures of ~ 25 to 30°C . Paleocene marine siltstones and mudstones with carbonate cement, limestone, shells, and forams, collected

in the Tso Jiangding region of the southern Tibetan Plateau, record unequivocal isotopic evidence of pervasive alteration, but have very little evidence of optically identifiable recrystallization. Additionally, Δ_{47} -derived temperatures from within individual hand samples are highly variable (< 10 to $>80^\circ\text{C}$), requiring either differential aqueous alteration at different stages of burial-exhumation, or differential reordering.

Here I present evidence that a high Δ_{47} (low $T(\Delta_{47})$) does not unequivocally reflect primary mineral formation conditions. In this chapter, I use theoretical water-rock isotopic exchange and solid-state reordering results to reconstruct possible alteration pathways that could explain the shift in isotopic values from marine oxygen compositions and temperatures to the measured values. The isotopic values cannot be simply or completely explained by known solid-state reordering mechanisms or water-rock reactions. There are shortcomings to each modeling effort. For example, certain caveats such as how meteoric water could be introduced to the rock package at a late stage falls short when petrography and shell morphology (Fig. 5.2) demonstrate early void filling removing any available pore space for later waters. However, the data stand, and there must be a means to introducing water to the system during the alteration history in order to facilitate pervasive oxygen exchange. Mechanisms that introduce ^{18}O -depleted water to compacted limestones with negligible porosity may leave geochemical and/or textural fingerprints at very small spatial scales that hopefully can be identified with micro-analytical tools beyond normal petrography.

Shell morphology and internal morphology retained

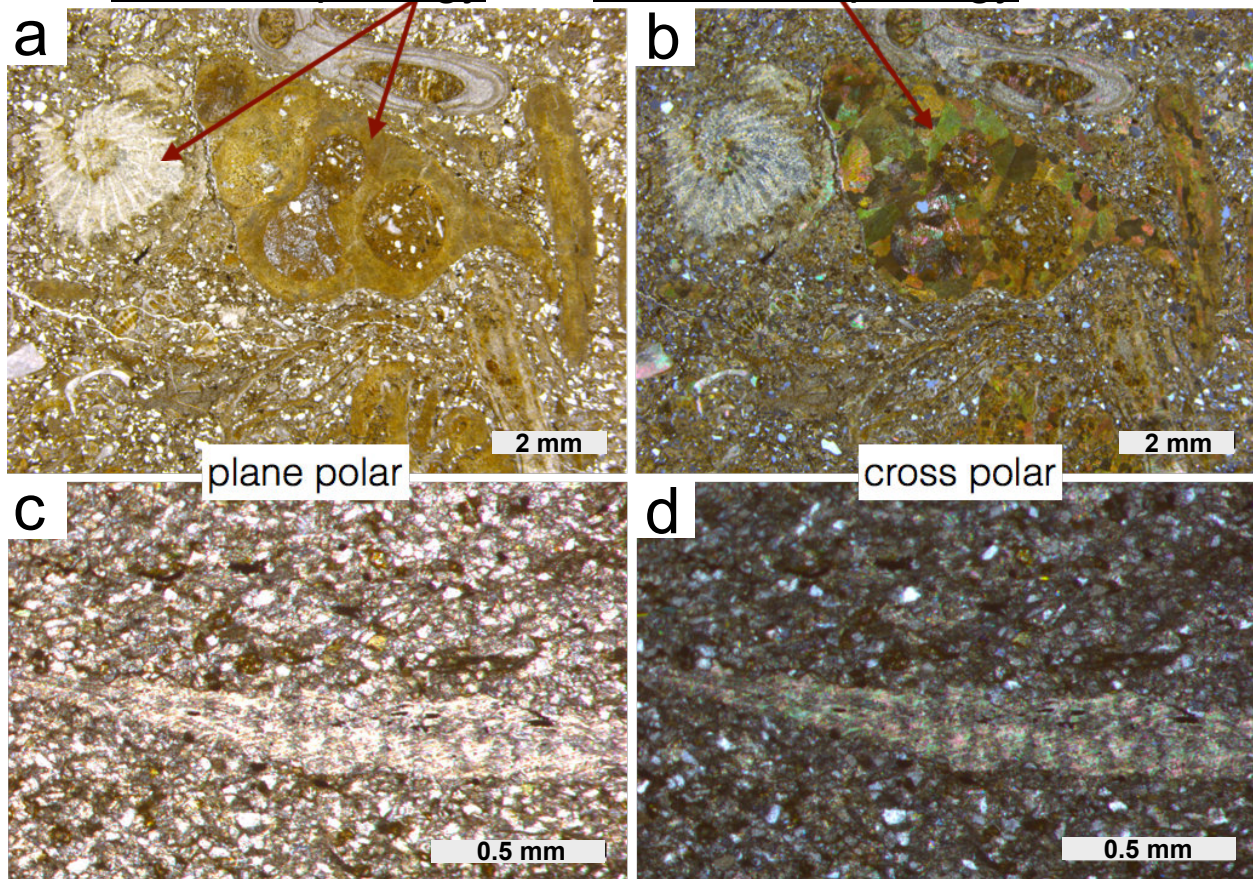


Figure 5.2 **Petrographic screening of fossiliferous limestones of the Tso Jiangding Group.** The external shell and foraminifera morphologies are retained throughout the burial history of these samples, as seen in plane polar light (a, c). The internal morphology of shells is also retained, as seen in cross polar light (b, d).

5.2 Geologic Setting

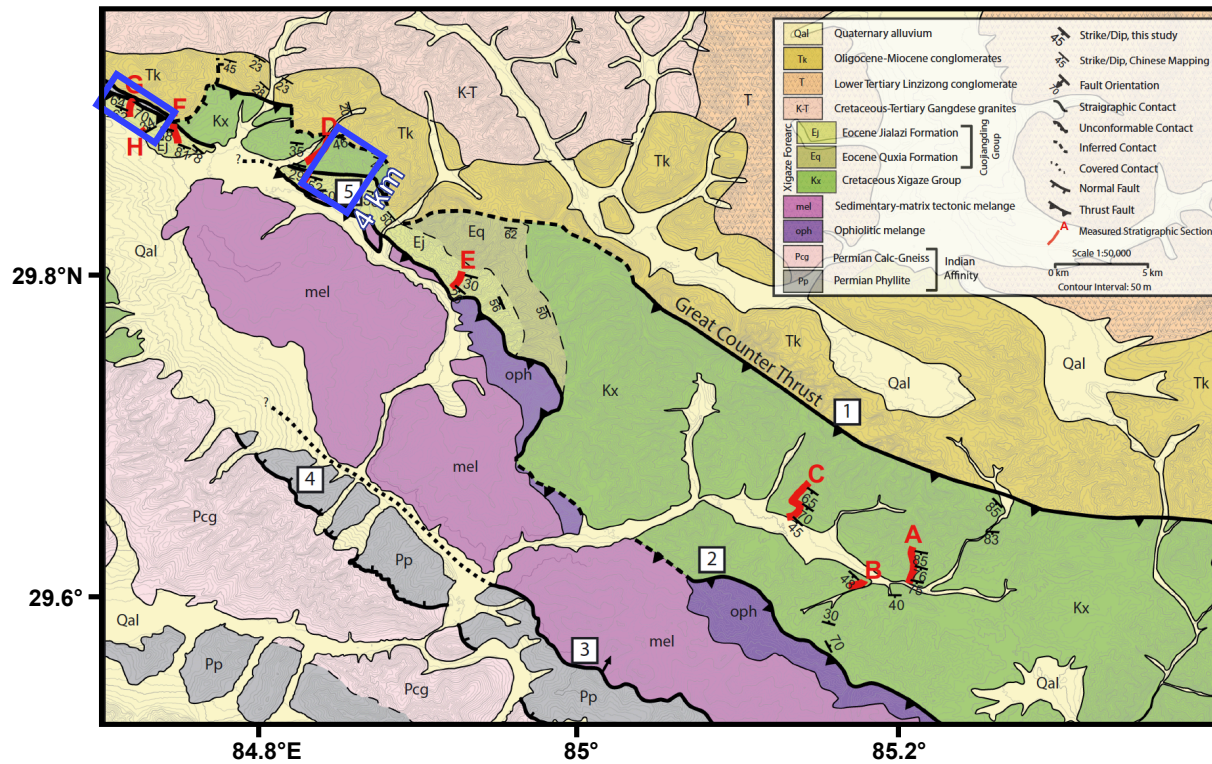


Figure 5.3 Map of Xigaze Forearc strata in study area adapted from Orme et al. (2014). Xigaze Forearc strata are bounded by northvergent thrust faults. The red lines indicate measured stratigraphic sections from Orme et al. (2014); the blue boxes indicate measured and sampled sections from this study.

5.2.1 Xigaze forearc basin

The stratigraphy of the Xigaze forearc basin records Cretaceous to lower Eocene sedimentation along southern Tibet. The preserved Xigaze forearc basin stratigraphy, which sits today at an average elevation of 5000 meters, is 5 to 8 km thick and extends east-west for roughly 550 km (Orme et al., 2014). This basin provides an exceptional opportunity to study the evolving geology of Asia's southern margin prior to and through the earliest stage of collision. The Xigaze strata record facies transitions from deep to shallow to marginal marine, and finally to non-marine fluvial facies. Additionally, along-strike facies variability

has enabled reconstructions of basin geometry and paleogeography of the southern margin of Tibet (Orme et al., 2014; Carrapa et al., 2014; Leary et al., 2016; Orme and Laskowski, 2016; Hu et al., 2015, 2016; Bouilhol et al., 2013; Wang et al., 2011, 2012; Ding et al., 2005; Einsele et al., 1994; Wan et al., 1998; An et al., 2014).

The Tethyan Himalayan passive margin of northern India made first contact with Eurasian continental crust 58 ± 2 Ma (DeCelles et al., 2014). At this time, the last of the intervening Neo-Tethyan oceanic lithosphere subducted beneath the Lhasa terrane or obducted onto the accretionary margin by frontal scraping (Ding et al., 2005), contributing to Xigaze forearc sedimentation (Orme and Laskowski, 2016). Due to the asymmetric topography of the Indian and Eurasian plates—a marine shelf and a high elevation magmatic arc, respectively—at the time of collision, the detrital sedimentary record of collisional onset is located on the lower, Indian plate. The initial collision is marked by the arrival of Asian sediments overlying and interbedded with Indian sediments. Each continent has a unique lithological composition, which leaves a traceable signature in the rock record. In the Sangdanlin area south of the Indus-Yarlung Suture, there is an abrupt change from quartz-arenitic to feldspatholithic sandstone in the upper Paleocene strata (DeCelles et al., 2014). This facies change marks a transition from Indian to Asian sediment provenance on the Indian continental slope and rise, with the Asian sediments largely derived from the Gangdese arc, active at this time on the southern Lhasa terrane.

Wang et al. (2012) divides the stratigraphy of the Xigaze forearc basin into two groups: lower to upper Cretaceous Xigaze Group and the upper Cretaceous to lower Eocene Tso Jiangding Group. We focus on the latter group in this study. An absence of forearc strata $< \sim 51$ Ma suggests sedimentation in the forearc basin ceased at this time, or has been subsequently eroded, possibly due to local uplift of the suture zone related to continental collision.

5.2.2 *Tso Jiangding Group*

The Tso Jiangding Group (S. Tibet) records a general shoaling upward trend coincident with the closing Tethys (Orme et al., 2014). This group can be divided into four units whose facies associations trace the change from deep to shallow marine environments: the Padana, Qubeiya, Quxia, and Jialazi Formations. The latter three formations are only found at our sampling locality in the westernmost end of the Xigaze forearc basin northwest of Saga (see Fig. 5.3). The abundantly fossiliferous marine limestones analyzed in this study belong to the youngest unit, the Jialazi Formation. This unit consists of 145-400 meters of fossiliferous limestone interbedded with 25-50 meter thick sandstone and conglomerate sequences and thin lenses of pale gray shale. The age of the Jialazi is constrained as 62 to 51 Ma by biostratigraphy (Eocene *Nummulites-Discocyclus*), Ypresian-age zircons in sandstones near the top of the section, and a tuff in the lower part of the stratigraphy (Orme et al., 2014; Ding et al., 2005; Hu et al., 2015; Aitchison et al., 2011; Wan et al., 1998).

5.3 Methods

5.3.1 *Sample collection*

Five shales, thirty carbonates, and three ash beds were collected from Jialazi Formation sections described in Orme et al. (2014) and adjacent sections (Fig. 5.3). Section labels in this chapter correlate with those in Orme et al. (2014). The first sampled section is most proximal to Section D, but stratigraphically correlated with lower Cenozoic Section E. These samples are dominantly fossiliferous, shallow marine limestones with variable quartz sand content. Stable and clumped isotope samples range from carbonaceous mudstone to sandy limestone. Late Paleocene to early Eocene Sections F-H record the transition from shallow marine to on shore deposition. Marine calcareous mudstone was collected from Section F. Foraminifera *Nummulites-Discocyclus* are abundant in limestones in this section. Sparse paleosols were sampled from the upper 72m of Section F. The facies interpretation of the

red-green paleosol beds are periods of low to no flow in overbank channel deposits formed during progradation of the coastal plain fluvial system (Orme et al., 2014). The conformable transition from marine to fluvial deposition seen in the Jialazi Formation correlates to high-flux magmatism of the Gangdese arc in the Eocene (Chung et al., 2005; Lee et al., 2009). The remainder of the samples collected in sections G and H are paleosol carbonate, shales, and ashes.

5.3.2 *Micro-sampling*

Samples were powdered using a Foredom TX low speed drill with a Brasseler US#2 HP Round bit at low speed to avoid significant frictional heating and the potential for carbonate C-O bond reordering. Additional “sub-samples” (fossil shells, forams, veins, and micrite within individual 1-inch by 2-inch thin section billets) were powdered using a micromill (Fig. 5.4).

5.3.3 *Stable isotope and clumped-isotope measurements*

Stable isotope measurements ($\delta^{18}\text{O}$ and $\delta^{13}\text{C}$) were made on both the MAT253 and DeltaV IRMS at the University of Chicago. MAT253 $\delta^{18}\text{O}_{\text{CO}_2}$ measurements are converted to $\delta^{18}\text{O}_{\text{carbonate}}$ compositions using a calcite- CO_2 fractionation factor ($\alpha_{\text{CO}_2-\text{CO}_3}$) associated with phosphoric acid digestion (Guo et al., 2009). Stable and clumped isotope analyses follow the methodology of Ingalls et al. (2017) and can be found in the Appendix (section A.1).

5.3.4 *Traditional screening tools for carbonate diagenesis*

Petrography and Scanning Electron Microscopy (SEM)

~30 μm -thick geological thin sections were made from the corresponding billets mentioned in section 5.3.2. Thin sections were optically screened for potential alteration fabrics following

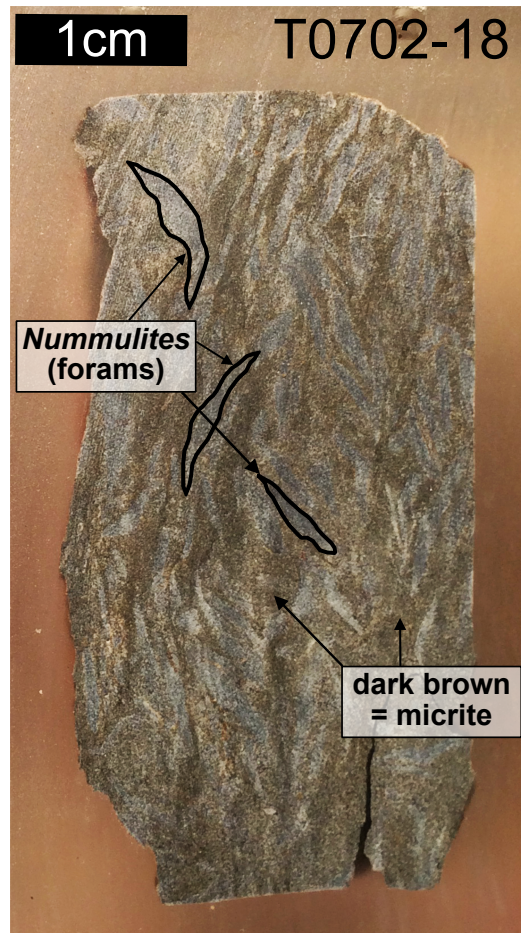
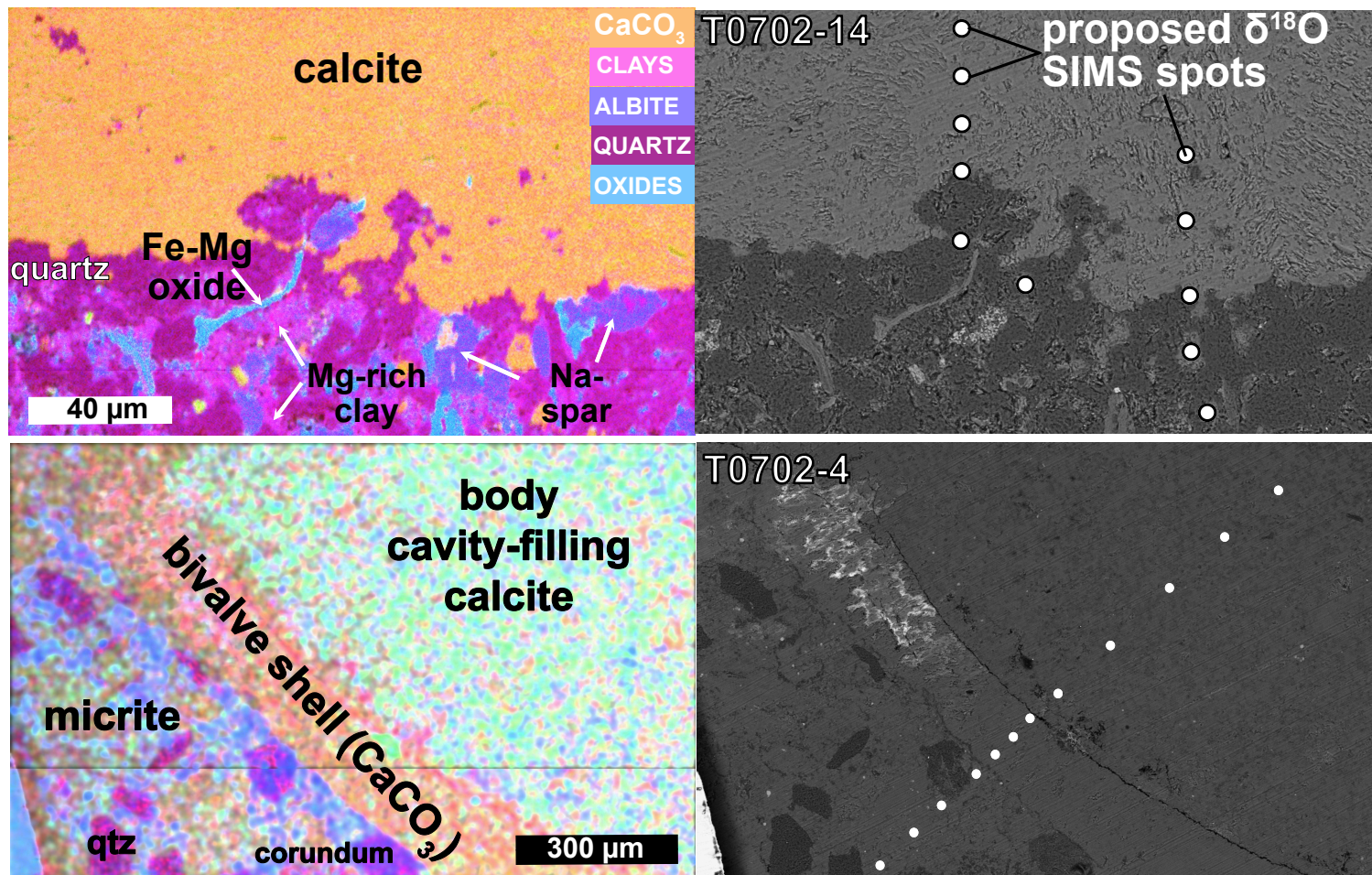


Figure 5.4 **Cross sectional cut of Tethyan marine carbonate sample T0702-18.** 2.5 cm by 4 cm thin section billet of an abundantly Nummulitic shallow marine limestone with three forams outlined.

a similar protocol as for the terrestrial carbonates in section 2.3.1 of this dissertation.

SEM imaging was conducted on the Zeiss Supra 35 VP FEG SEM at the Center for Advanced Microscopy and Imaging at Miami University (Oxford, OH). SEM peripherals provide a variety of analytical techniques for assessing carbonate diagenesis. We have used preliminary back-scattered electron detector (BSE) images in parallel with energy-dispersive X-ray spectroscopy (EDS or EDX) to make quantitative compositional interpretations of our marine samples (Fig. 5.5) while simultaneously assessing alteration textures. Mineralogical assignments were made using elemental abundance EDS spectra of individual points matched to zones of like-composition within EDS maps.

Figure 5.5 Scanning electron microscopy (SEM) images of Tethyan marine carbonates. EDS chemical maps (left) are paired with BSE images (right) to identify mineral phases and fabrics. White dots mark proposed sites for $\delta^{18}\text{O}$ micro-analyses on a secondary ionization mass spectrometer (SIMS).



Cold-cathode cathodoluminescence microscopy (CL)

We use optical and CL petrography to identify attributes of samples that are consistent with primary, unaltered carbonate versus diagenetically altered or secondary carbonate (Snell et al., 2013, 2014; Huntington et al., 2011; VanDeVelde et al., 2013). CL is used to reconstruct relative timing of crystallization and alteration/post-depositional events. The cold-cathode luminescope at Miami University is mounted directly onto the stage of a petrographic microscope. The benefit of using a cold-cathode cathodoluminescope, rather than microprobe, is the capability to directly compare optical and CL petrography of the exact same site in real-time (Fig. 5.6). The images were taken at a vacuum of ~ 90 mTorr with a beam strength of 0.8-0.83 mV. Each petrographic slide has approximately 20 CL images of 2mm width.

CL intensity reflects the relative abundances of the reduced forms of elemental iron, Fe^{2+} (dominant activator of carbonate luminescence), and manganese, Mn^{2+} (dominant quencher, Budd et al. (2002); Marshall (1988)). Variation in CL is thought to reflect the redox conditions of the depositional and post-depositional environments in which calcite forms. Oxidizing environments such as unsaturated soil produces dull or nonluminescence because Fe^{2+} and Mn^{2+} are not readily available for incorporation into carbonate minerals. However, carbonate formed during deeper burial will produce brighter luminescence (Boggs and Krinsley, 2006). Luminescence zonation is indicative of chemical heterogeneity in calcite formation conditions (Budd et al., 2002), and thus multiple calcite generations. Here we map CL distribution patterns and variation in micrite, foraminifera (Fig. 5.6), bivalve and gastropod shells, and calcite cements in shell body cavities. In the results section, we make initial interpretations of depositional and post-depositional events and crystallization environments based on luminescence. The goal is to provide supporting evidence to isotopic and modeling results to constrain when in the samples burial history the oxygen isotope composition altered away from marine composition. In future work, I will further correlate these events with existing and additional isotopic measurements to identify linkages between CL distribution, isotopic variation, and diagenesis.

5.4 The motivating samples

5.4.1 *Thermal history of the Jialazi Fm precludes a potential sea level precipitation proxy (δD_p) for syn-collisional Tibetan paleoaltimetry*

Shallow marine carbonates and shales of the Tso Jiangding Group were sampled for lipid biomarkers of Asian origin, transported off the late Cretaceous to Paleocene Gangdese Arc into the shallow marine Xigaze forearc basin, for lipid- δD (D/H) analyses. The isotopic composition of paleo-rainwater ($\delta D_{\text{precipitation}}$) can be calculated from lipid- δD values by a standard fractionation (Polissar et al., 2009). The original intent was to provide a new low-elevation precipitation proxy of a similar age (pre- to syn-collisional) as the majority of our samples used in $\Delta(\delta^{18}\text{O}_p)$ or $\Delta(\delta D_p)$ paleoaltimetry calculations. Studies using traditional stable isotope paleoaltimetry on the Tibetan Plateau must rely on $\delta^{18}\text{O}_c$ values from the Miocene to Pliocene Siwalik sediments of Pakistan and Nepal as the low-elevation end member of the isotopic lapse rate simply because no older sediments have been found that preserve a primary isotopic signal. Preliminary organic geochemical analyses indicated that the Tso Jiangding rocks experienced temperatures in excess of those necessary to retain a primary deuterium isotopic value.

Additionally, zircon U-Th/He data from the Jialazi Formation of the Tso Jiangding Group require that this sedimentary package experienced temperatures >110 and $<200^\circ\text{C}$ at some interval after deposition and before exhumation $\sim 20\text{-}30$ Ma (Orme, 2015). The upper bound on burial temperature is derived from multiple lines of evidence from zircon fission track (ZFT) and U-Th/He (ZHe) data. ZFT on two samples from the Jialazi Fm yield ages syndepositional and older (~ 60 Ma; Orme, in review). ZHe ages from the lower section of these strata are partially reset and range from 10-30 Ma (Orme, 2015). If the Jialazi Fm zircons were heated $\gg 200^\circ\text{C}$, one would expect partial resetting of ZFT to post-depositional dates and less variability in ZHe dates. Additionally, best-fit paths from thermal modeling of a tuff from the base of the Jialazi Fm produce the observed age variability with a maximum

temperature $<200^{\circ}\text{C}$ (Orme, in review). The best-fit thermal model of the tuff suggests the rock package experienced maximum burial temperature ~ 150 to 200°C ~ 30 to 20 Ma, and exhumed at a fairly constant rate to present conditions (Orme, in review).

5.4.2 Field and hand sample observations as related to water:rock ratios

It is important to consider the isotopic data within the framework of our geologic observations. One of our diagenetic scenarios requires water-facilitated recrystallization and isotopic exchange during deep burial at temperatures $>150^{\circ}\text{C}$ and late-stage exhumation at near-surface temperatures. This diagenetic history requires a mechanism or pathway to introduce water to the strata both at 5-6 km depth and during the final stages of exhumation. The preservation of primary external and internal shell morphology within the marine limestones (Fig. 5.2) suggests that pore-filling microspar cementation is either syngenetic with the carbonaceous mud (Munnecke et al., 1997) or occurred early in the burial history (“eogenetic”; Choquette and Pray (1970)). This early cementation allowed shells to maintain their structural integrity during burial compaction, which reduces porosity and permeability by both physical and chemical processes (Choquette and Pray, 1970). For these reasons, we assume a modest water:rock ratio during oxygen isotopic exchange at depth. During tectonic unroofing, decompression fractures can provide pathways for groundwater to interact with the exhuming strata. However, evidence one would expect to see in the field and in hand sample of such fractures are absent. Additionally, micro-scale fractures were only observed in one sample in thin section.

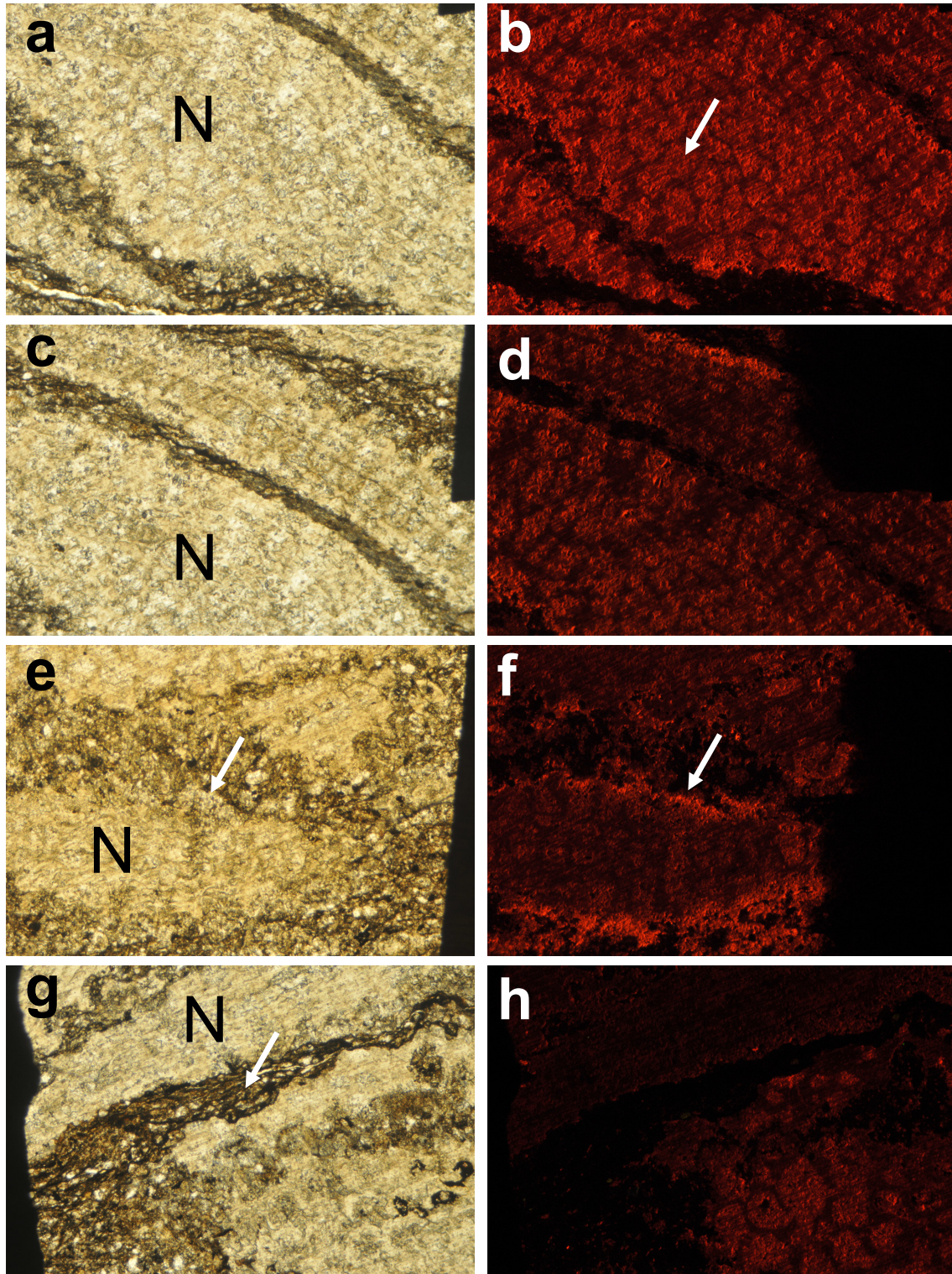


Figure 5.6 Paired plane polar light (PPL) and cathodoluminescent (CL) petrographic images. Slides a, c, e, and g are PPL and b, d, f, and h are CL. All images are from sample T0702-18. *Nummulites-Discocyclus* foraminifera are labeled with an “N”. White arrows point to areas described in the text. The width of each image is 2mm.

5.4.3 Cathodoluminescence

Here I present initial observations and interpretations of cold-cathode CL images, with a focus on sample T0702-18 (Fig. 5.6). Sample T0702-18 varies in CL from nonluminescent to bright red-orange. Typically both biogenic and inorganic marine carbonates either do not luminesce or exhibit dull luminescence (Boggs and Krinsley, 2006). Bright luminescence is characteristic of carbonate formation under deep burial conditions (Boggs and Krinsley, 2006). In sample T0702-18, we observe dull to non-luminescence within the cement binding the silt between foraminifera (see Fig.5.6g). Additionally, dissolution surfaces are seen much more clearly in CL than PPL (Solomon and Walkden, 1985). The boundary between the foraminifera and silt groundmass in Fig. 5.6e-f has evidence of secondary dissolution-precipitation. The edges of the foram in Fig. 5.6f display bright red-orange luminescence. The dissolution rim around this foram could be a pressure solution seam formed with water with a higher concentration of the primary calcite luminescence activator, Mn^{2+} (Marshall, 1988), than the primary marine water. Regions of bright luminescence could point to physical evidence of the wholesale oxygen exchange required by the $\delta^{18}O_c$ compositions of our samples.

Fig. 5.6a-b display the preservation of the septa and chamber framework of the *Nummulites-Discocyclusina*. The structural carbonate material (septa) has brighter luminescence than the marine cement surrounding the lenticular fossils. This does not necessarily indicate that marine cementation occurred under different conditions than foraminifera formation; marine cements are known to more precisely record primary marine water chemistry than biogenic minerals susceptible to vital effects (Carpenter and Lohmann, 1997). The infilling microspar displays the brightest luminescence, indicating more luminescence activators (Mn^{2+}) within the infill (Janssen et al., 2016). This may indicate a change in the water chemistry between cementation of the silt groundmass and infilling of shell void space (Marshall, 1988). Alternatively, the void-fill microspar may have experienced a greater degree of recrystallization during the later wholesale oxygen exchange event and reflect this advanced interaction with

water in a deeper burial setting with a greater supply of Mn^{2+} and Fe^{2+} cations (Marshall, 1988; Huntington et al., 2011).

5.4.4 *Isotopic results*

All carbonate material in this section is ^{18}O -depleted (-12 to -21‰ ; Fig. 5.8) relative to typical marine values. Figure 5.7 displays the carbon and oxygen stable isotopic values of the Jialazi Formation relative to approximate Paleogene marine mollusk $\delta^{18}\text{O}_c$ values (Kobashi et al., 2001). The full set of $\delta^{18}\text{O}$ and $\delta^{13}\text{C}$ data for shallow marine, marine cements, and groundwater and paleosol (fluvial-deltaic system) carbonates of the Jialazi Formation can be found in the Appendix (Table D.8). In Figure 5.7, the orange and blue arrows indicate two end member water-rock interactions that could alter Paleogene marine limestone isotopic compositions to the measured values for the Jialazi Formation. These alteration pathways are discussed further in section 5.7.

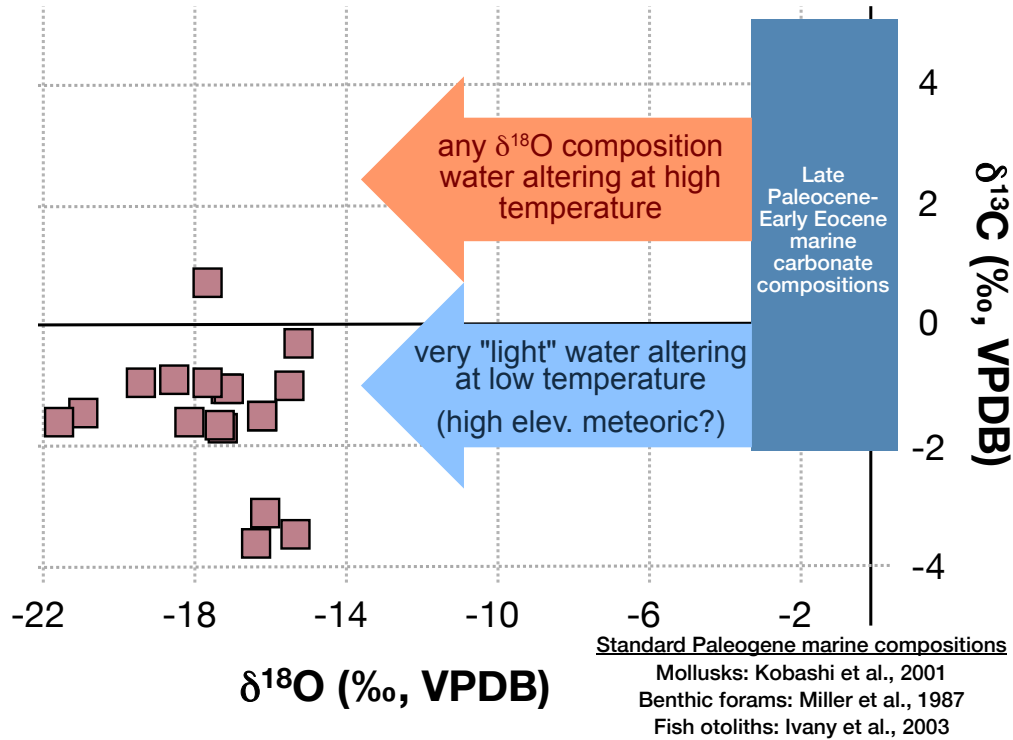


Figure 5.7 **Stable isotope values of Jialazi Formation marine carbonates compared to expected values.** Light red squares indicate shallow marine carbonates (fluvial-deltaic carbonates from the upper Jialazi Formation have been excluded from this figure). The two arrows are labeled with possible composition-temperature regimes of altering waters to drive marine values to depleted compositions. Late Paleocene-Early Eocene marine carbonate compositions represent low-latitude mollusks (Kobashi et al., 2001), benthic forams (Miller et al., 1987), and fish otoliths (Ivany et al., 2003).

Δ_{47} measurements from the shallow marine Jialazi Formation samples range 0.456 to 0.721. Quality control checks on clumped isotope measurements are outlined in detail in the Appendix. Using the Zaarur et al. (2013) Δ_{47} thermometer for low temperature carbonate digestions, these Δ_{47} compositions equate to temperatures as high as 87.8°C and as low as 7.4°C. In Table D.9, I have calculated the oxygen isotopic composition of water if these clumped isotope temperatures and oxygen isotopic compositions reflect carbonate precipitation under equilibrium conditions. The oxygen isotope calcite-water fractionation factor (Kim and O'Neil, 1997) is calculated using the measured $T(\Delta_{47})$, and $\delta^{18}\text{O}_w$ is calculated assuming equilibrium carbonate precipitation at $T(\Delta_{47})$. The apparent equilibrium compo-

sition of the formation water has a greater dependency on temperature than the carbonate oxygen composition. The $\delta^{18}\text{O}_c$ compositions range from -12 to -21‰ VPDB, but $\delta^{18}\text{O}_w$ ranges -2.5 to -21‰ VSMOW. However, it is quite possible that the clumped isotope values do not represent equilibrium carbonate precipitation, but rather variable degrees of solid-state reordering, and therefore should not be used directly to calculate the water oxygen isotopic composition.

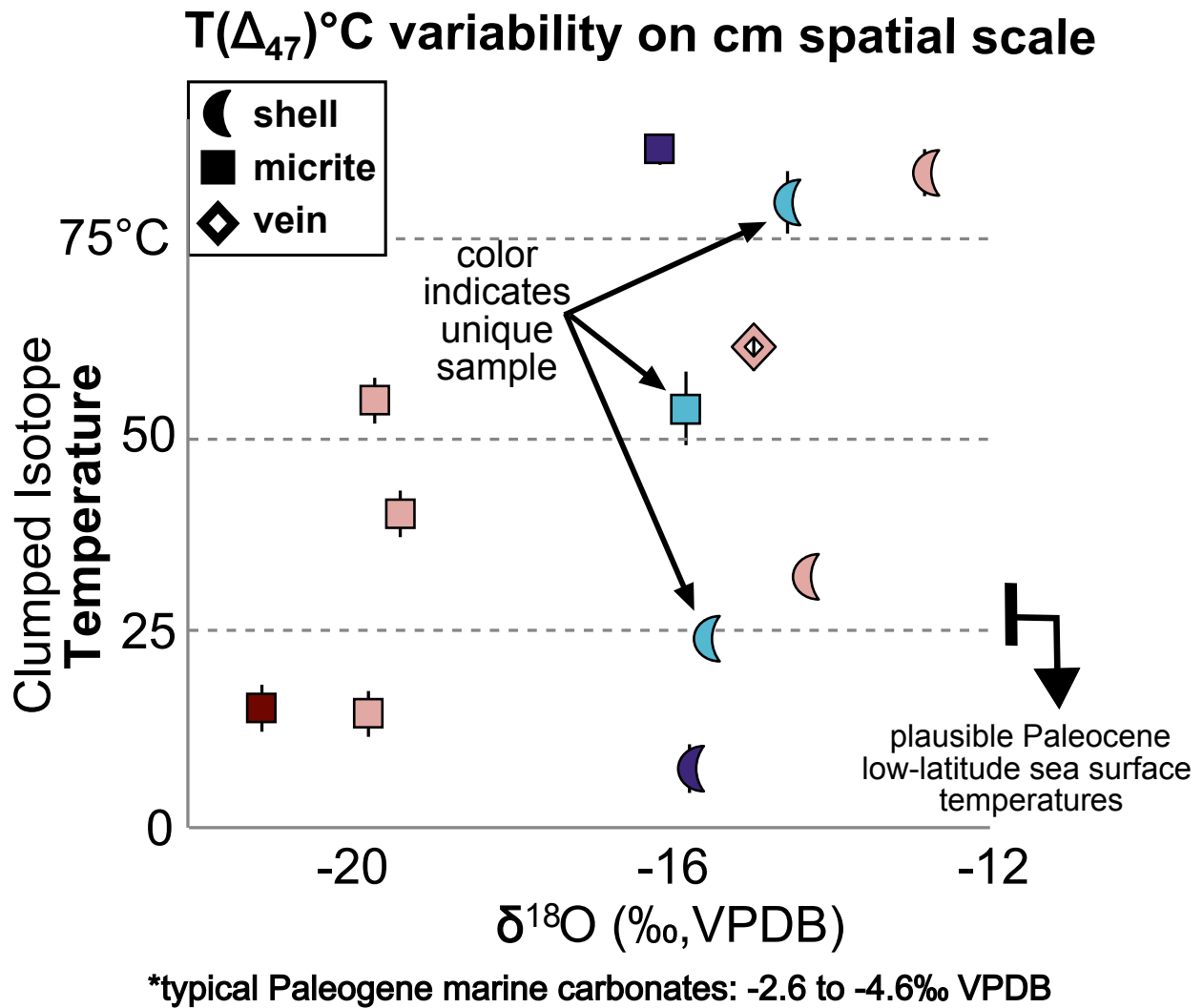


Figure 5.8 **Within-sample Δ_{47} and stable isotopic variability.** Arrows point to two forams and micrite from sample T0702-18 (5.4), that yield $>50^{\circ}\text{C}$ variability in $T(\Delta_{47})$. Each color is a unique sample from the Jialazi Fm. The error bars represent analytical uncertainty and the standard error of all replicate analyses. Typical Paleogene marine carbonate values are based on low-latitude mollusks (Kobashi et al., 2001), benthic forams (Miller et al., 1987), and fish otoliths (Ivany et al., 2003).

5.5 Isotopic theory

5.5.1 *Water-rock isotopic exchange during carbonate recrystallization*

Both $\delta^{18}\text{O}_c$ (carbonate oxygen isotopic composition) and Δ_{47} values can be altered during carbonate recrystallization. Water-rock oxygen exchange drives $\delta^{18}\text{O}_c$ towards the value of the water, and vice versa. The extent to which $\delta^{18}\text{O}_c$ shifts in isotopic space depends largely on the water-rock ratio, porosity, temperature, and open- versus closed-system behavior. The higher the fraction of water relative to rock, the more pervasive recrystallization will be until the two are in chemical equilibrium. When the water-rock ratio is very small, the system is considered “rock-buffered”. In a rock-buffered system, even under high temperature conditions, it is expected that the rock retains its primary $\delta^{18}\text{O}_c$ composition because there is little to no water available for oxygen exchange. Any isotopic exchange will be reflected in an ^{18}O isotopic enrichment in the water composition.

I derive mass balance equations and use them to model water-rock isotopic exchange under variable diagenetic conditions. In the modeling presented in this chapter, rather than using the traditional water-rock ratio to relate the relative contributions of water and rock to the total oxygen of the system, I use N which is defined as weight percent oxygen from carbonate relative to the system (i.e. $g \text{ O}_{\text{carbonate}} / (g \text{ O}_{\text{carbonate}} + g \text{ O}_{\text{H}_2\text{O}})$).

5.5.2 *Solid-state internal isotopic exchange*

Carbonate clumped-isotope thermometry is most typically used to measure mineral formation or (re)equilibration temperatures. The measured temperature of mineral growth reflects the temperature at which carbonate ions crystallized. However, at elevated temperatures, carbon-oxygen bonds may break and reorder between carbonate groups within a crystal lattice through internal isotope-exchange reactions (Stolper and Eiler, 2015; Ghosh et al., 2006a; Dennis and Schrag, 2010). This involves the breakage of C-O bonds formed during primary mineral formation, diffusive migration of C and/or O within the carbonate lattice,

and reforming of new bonds using C and O from neighboring carbonate groups (Passey and Henkes, 2012; Shenton et al., 2015). The internal isotope-exchange reactions (solid-state bond reordering) overprint the primary mineral formation Δ_{47} and $T(\Delta_{47})$, trending towards equilibrium with the elevated temperature regime (Passey and Henkes, 2012; Henkes et al., 2014).

In recent years, the kinetics of these closed-system isotope exchange reactions have been constrained by measurements of natural carbonatites (igneous rocks >50 wt.% carbonate) (Dennis and Schrag, 2010) and marbles (Ghosh et al., 2006a), laboratory heating experiments, and modeling efforts (Passey and Henkes, 2012; Henkes et al., 2014; Stolper and Eiler, 2015). These models have explored kinetic parameters related to material type (Passey and Henkes, 2012; Henkes et al., 2014), differing burial-exhumation histories (Shenton et al., 2015), diffusion of isotopes through the crystal lattice, and isotope-exchange reactions between adjacent carbonate groups (Stolper and Eiler, 2015).

Stolper and Eiler (2015) demonstrate that natural carbonate samples undergo Δ_{47} alteration in two temperature-dependent stages:

(1) **Rapid, “Low”-T:** Initially, there is rapid exchange between neighboring carbonate groups within the crystal lattice that each contain one rare isotope. Under this lower temperature (~ 75 to $<150^\circ\text{C}$) regime, the measured $T(\Delta_{47})$ never reaches the ambient temperature. For example, in their experiment, a sample held at 75°C for 100 million years will experience $<1^\circ\text{C}$ increase in $T(\Delta_{47})$, but the $T(\Delta_{47})$ of the same sample held at 120°C will increase by up to 40°C . However, $T(\Delta_{47})$ will always be lower than the ambient or environmental temperature at temperatures $<120^\circ\text{C}$. In this first step, neighboring carbonate groups rapidly exchange C and O, which creates concentrations within the crystal enriched in both ^{13}C and ^{18}O .

(2) **Slower, High-T:** The second stage requires a slower process of diffusion of ^{13}C and ^{18}O away from each other through the crystal lattice. This yields lower Δ_{47} values. At temperatures above 150°C , the $T(\Delta_{47})$ value can reach true ambient temperature (i.e. the

kinetics are sufficient for the apparent equilibrium temperature to catch up to the environmental temperature). On the retrograde cooling path, closed-system exchange proceeds reflecting the lowering temperature until the kinetics of exchange and diffusion slow sufficiently and “lock in” a final temperature (Fig. 5.9). This final recorded temperature is referred to as the “apparent equilibrium blocking temperature” (Stolper and Eiler, 2015).

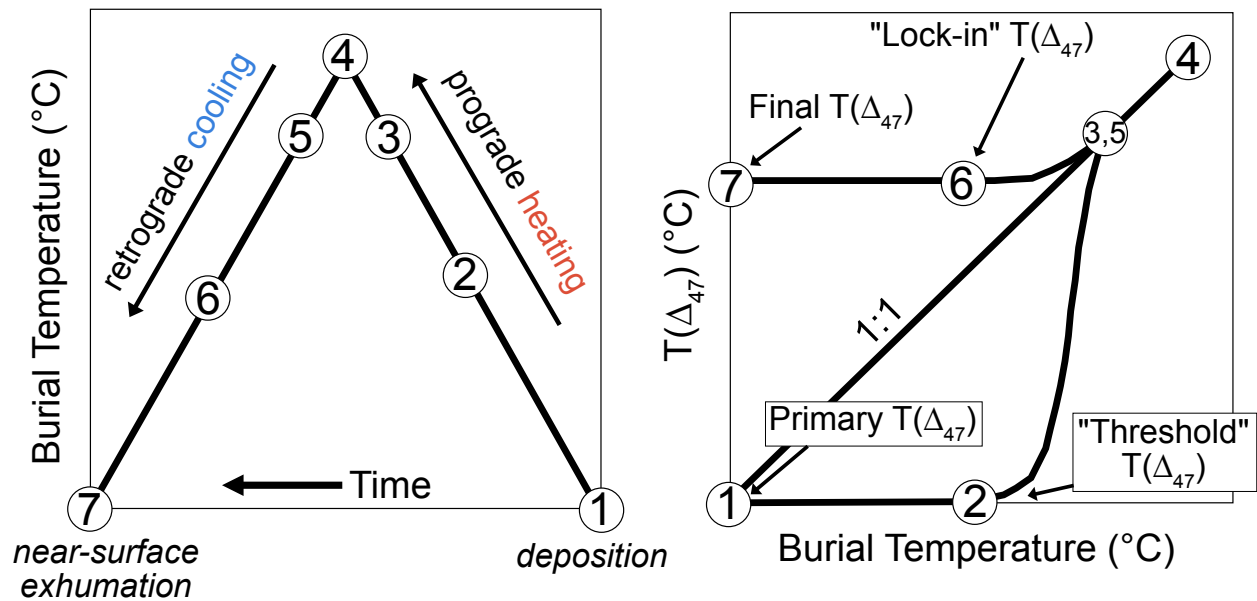


Figure 5.9 **Time-temperature schematic diagram of bond ordering behavior during burial and exhumation.** The lefthand panel represents a simple, symmetrical burial history: (1) deposition, (2, 3) burial heating, (4) maximum burial temperature, (5, 6) retrograde cooling, and (7) exhumation to surface conditions. The righthand panel displays the Δ_{47} response to each corresponding time step. Based on the hypothetical rock’s kinetic parameters and environmental conditions, the “threshold” temperature is reached at time (2) to initiate rapid stage 1 internal isotope exchange. The internal isotopic exchange rate slows at time (3) when reordering is dominated by slower intracrystalline diffusion processes. In this phase, there is a 1:1 relationship between recorded $T(\Delta_{47})$ and ambient temperature, on both the prograde and retrograde pathways. When the rock passes through the lower temperature zone at time (5), reordering slows further. At time (6), the carbonate crystal “locks in” a final $T(\Delta_{47})$ value. In the absence of water-facilitated recrystallization, the carbonate crystal will retain this $T(\Delta_{47})$ until surface exhumation at time(7). Diagram adapted from Henkes et al. (2014).

The experimental heating work of Passey and Henkes (2012); Henkes et al. (2014) yield

a different type of two-phase closed-system isotope exchange based on duration of heating. The apparent equilibrium temperature evolved rapidly (minutes to hours) but incompletely at the start of the experiment, followed by slower reordering kinetics (Henkes et al., 2014). They determined that their results could not be explained by first order kinetics for one chemical reaction, so they created a model to describe “non-pseudo-first-order behavior.” They attribute the initial, rapid change in Δ_{47} to fast annealing of ‘transient’ structural or point defects which act as ‘fast’ exchange pathways (Henkes et al., 2014). The slower internal isotope exchange reactions dominate once the defects have annealed.

Henkes et al. (2014) determined that when modeling solid state reordering reactions within geologic thermal histories above 150°C, there was no significant difference between a simpler model employing first order kinetics, or their model allowing for initial rapid annealing. The Jialazi Fm has experienced maximum burial temperatures in the range of 150 to 200°C, so we model solid-state reordering following the simpler model of Henkes et al. (2014) model. Stolper and Eiler (2015) demonstrated that their experimental results as well as the results from optical calcites from Passey and Henkes (2012) and brachiopods from Henkes et al. (2014) yield an indistinguishable relationship when fit to their two-phase model. As such, in this chapter I employ the Henkes et al. (2014) model and kinetic parameters determined therein to model hypothetical, yet plausible, time-temperature heating and cooling paths for our samples. I attempt to fit a time-temperature burial history to the “final” values ($\delta^{18}\text{O}_c$ and Δ_{47} measurements), constraints on the starting $\delta^{18}\text{O}$ composition of shallow marine carbonate and early Cenozoic low-latitude sea surface temperature (Kobashi et al., 2001), upper bounds on burial temperature (Orme, 2015), and solid-state reordering kinetics.

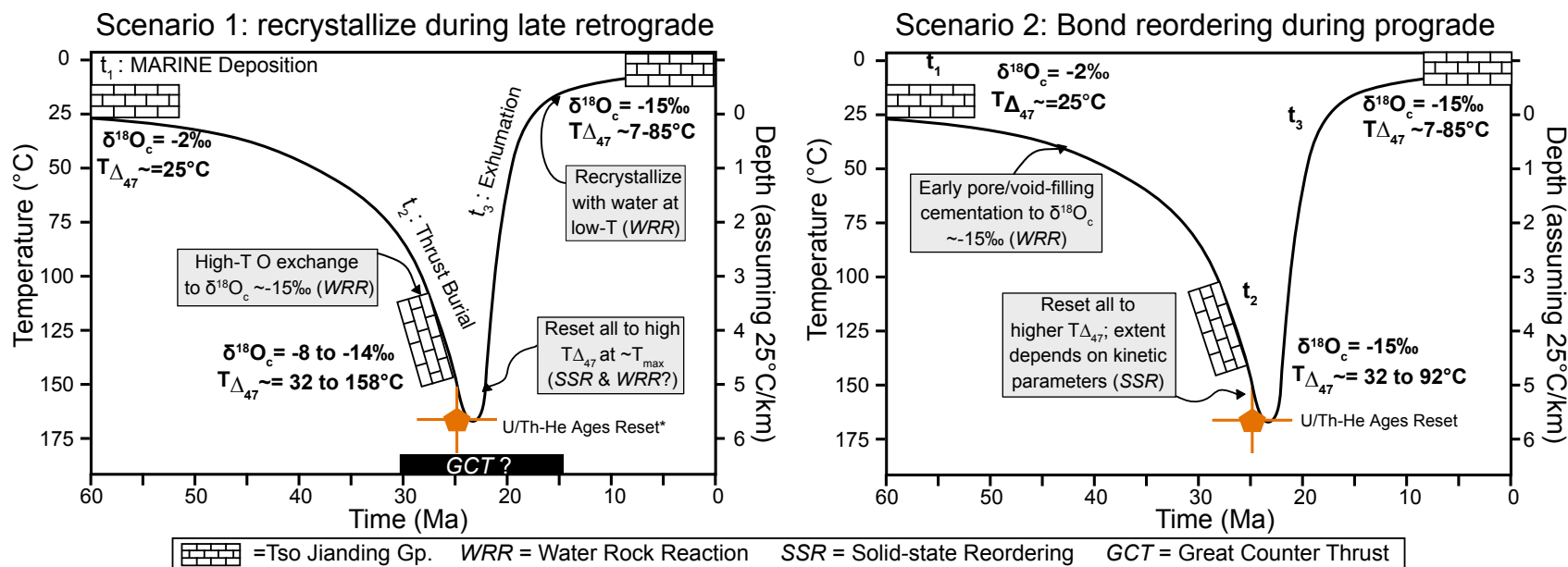
5.6 Using carbonate clumped isotope thermometry and solid-state reordering kinetics to constrain sedimentary basin thermal histories: Results & discussion

Thermodynamic modeling and geochemical tools are introduced to attempt to reconcile the data with what we presently know of isotopic and chemical fingerprints of carbonate diagenesis and bond ordering behavior at elevated temperature. I also suggest future work to expand our knowledge of the physical, chemical, and isotopic effects of cryptic carbonate diagenesis.

The specific diagenetic pathway the Tso Jiangding Group experienced, and when in that diagenetic history oxygen isotopic exchange occurred, is unknown. This sedimentary package experienced temperatures of $>110^{\circ}\text{C}$ and likely maximum burial temperatures of $150\text{-}200^{\circ}\text{C}$ based on thermokinematic modeling (see section 5.4.1), and exhumed to near-surface temperatures shortly following the initiation of the Great Counter Thrust 20-30 Ma (Orme, 2015). However, the precise duration of maximum burial temperature (T_{max}), which is important for modeling the extent of solid-state alteration, is presently unknown. An additional constraint is that carbonate oxygen exchanged with waters either within pore space and veins at depth (high-T) or with near-surface water (low-T). Two possible scenarios are outlined below, and in Figure 5.10:

(1) The carbonates are pristine until deeply buried, correlating to high temperatures. They experience high-temperature oxygen exchange with pore waters at depth to $\delta^{18}\text{O}_c$ values of $\sim -15\text{‰}$. All recrystallized calcite would record a new Δ_{47} at this recrystallization temperature or reflecting some temperature experienced during exhumation. Calcite could experience some amount of solid-state reordering during burial depending on the time spent at or above threshold reordering temperature. At ~ 25 Ma, the rocks exhume to near-surface conditions, now at high elevation. Here, some material recrystallizes with ^{18}O -depleted water to record low $T(\Delta_{47})$.

(2) Early cementation and diagenesis fills shell voids and pore space during shallow burial. This is supported by the preservation of original shell morphology, which should display compaction features if shell voids were vacant during deep burial (Fig. 5.2). However, low temperature diagenesis with either marine waters or low elevation meteoric water would be expected to leave the samples relatively ^{18}O -enriched compared with their observed compositions. Next, the rocks are buried to T_{max} for some length of time. Solid-state reordering kinetics are material-dependent, allowing for variability in Δ_{47} between samples that have experienced the same thermal history. However, in our samples, the same material type (forams) record very different temperatures (24 and 79°C), making this explanation unlikely. In this scenario, the rocks exhume retaining the early diagenetic $\delta^{18}\text{O}$ values and burial Δ_{47} .



133

Figure 5.10 **Schematic diagrams of potential diagenetic and isotopic alteration pathways.** The diagrams contain constraints on initial and final isotopic compositions as well as maximum recorded temperature from U-Th/He inversions (Orme, 2015) related to burial during the Great Counter Thrust (GCT). Isotopic compositions at depth represent the full range of isotopic model results for the two diagenetic scenarios, and SSR models. The initiation and duration of active deformation along the GCT is poorly constrained (Yin and Harrison, 2000), but the possible extent is represented by a black bar on the time axis. SSR = Solid-state Reordering; WRR = Water-Rock Reaction.

The following sections describe and model isotopic exchange under two regimes: (i) water-rock oxygen exchange by recrystallization, and (ii) solid-state C-O isotopic exchange by diffusion within the crystal lattice. Both sets of isotopic reactions attempt to reconcile our isotopic data set with the two possible diagenetic pathways described above, with the understanding that there are many other possible diagenetic pathways.

5.6.1 Water-rock reactions: Calculations of early- and late-stage oxygen isotopic exchange between H_2O and CO_3^{2-} during burial diagenesis

The Paleocene-Eocene Jialazi Formation of the Tso Jiangding Group started their geologic life cycle as shallow marine carbonates. As such, we can assume that their starting $\delta^{18}O_c$ composition was $\sim -2\text{‰}$ VPDB (Kobashi et al., 2001). The low-latitude shallow marine seawater from which they precipitated was likely 20 to 30°C, with a $\delta^{18}O_{\text{water}}$ composition of ~ 0 to -1‰ VSMOW (Kobashi et al., 2001). Today, these rocks record $\delta^{18}O_c$ values of -12 to -21‰ VPDB, requiring extensive replacement of primary marine calcite by secondary mineralization. It is uncertain when in our samples' post-depositional history they experienced pervasive oxygen exchange with environmental water. Based on preservation of internal shell morphology, we believe that void- and pore-filling by secondary micrite and spar happened early in our samples' burial history. However, the complicated $T(\Delta_{47})$ values preserved in these samples require post-oxygen exchange differential reordering of C-O bonds at some stage in the burial, but more likely exhumation, process. One possibility is that this reordering reflects late-stage, near-surface recrystallization. Therefore, I model water-rock reaction during both prograde and retrograde burial conditions to identify the time and conditions under which it is geologically and isotopically plausible for pervasive water-rock exchange to have occurred.

Equilibrium recrystallization on the prograde pathway: Early recrystallization at shallow depth or deeper burial?

In the prograde water-rock reaction model, I vary the water composition, N (fraction of oxygen from CO_3^{2-} by mass, a metric of water:rock proportion), and reaction temperature to constrain the conditions that would allow for alteration of marine carbonate to very light $\delta^{18}\text{O}$ values. The goal of the first set of models is to test how far along the diagenetic pathway—from marine to measured composition ($\sim -15\text{‰}$)—varying water compositions and values of N can alter the Tso Jiangding isotopic compositions during burial.

The fossils found in the limestones contain microspar infill, which facilitates the preservation of primary shell morphology during the entire burial history. Based on these optical observations, the microspar infill likely occurred at shallow depths (low- T) with water of approximately marine composition. The shallow marine siltstones and sandstones are bound by a carbonate cement. Carpenter and Lohmann (1997) found that modern marine cements record a relatively tight range of $\sim 0.6\text{‰}$ for $\delta^{13}\text{C}$ and $\delta^{18}\text{O}$, and are representative of abiotic precipitation in equilibrium with shallow marine water. Additionally, $\delta^{13}\text{C}$ and $\delta^{18}\text{O}$ of marine cements are less variable than that of co-occurring biogenic and micritic carbonate because they are relatively unaffected by vital effects (Keith and Weber, 1965; Gonzalez and Lohmann, 1985), and thus more likely to represent primary marine water chemistry (Carpenter et al., 1991). Can early, shallow water-rock reactions be responsible for the majority of prograde alteration? The calculations presented in this section tests whether the present oxygen isotopic compositions can be explained by early diagenesis of the marine cements and microspar infill at shallow depth with marine to nearly marine water, or if the present compositions can only be attained by wholesale oxygen exchange at higher temperatures.

I explore the parameter space in two ways: (i) varying all possible values of N (0 to 1), and a reasonable range of deep and shallow burial temperatures, and (ii) holding N constant (0.75) and allowing for burial at any depth from surface to 6km by varying reaction temperature continuously (30 to 180°C). I allow the water oxygen isotopic composition in

both models to vary from 0 to -30‰ VSMOW.

The oxygen isotopic compositions of water and carbonate in equilibrium can be related by considering their relative contributions to the equilibrium water-rock system, $\delta^{18}\text{O}_\Sigma$:

$$\delta^{18}\text{O}_\Sigma = N \times \delta^{18}\text{O}_c + (1 - N) \times \delta^{18}\text{O}_w \quad (5.1)$$

$$\delta^{18}\text{O}_\Sigma = N \times \delta^{18}\text{O}_c + (1 - N) \times (\delta^{18}\text{O}_c - \Delta) \quad (5.2)$$

where N is the mass fraction of oxygen derived from CO_3^{2-} :

$$N = \frac{g_{\text{O}_{\text{CO}_3}}}{g_{\text{O}_{\text{CO}_3}} + g_{\text{O}_{\text{H}_2\text{O}}}} \quad (5.3)$$

and Δ is the difference between $\delta^{18}\text{O}_c$ and $\delta^{18}\text{O}_w$, given by $1000\ln\alpha$. α is the temperature-dependent water-calcite fractionation factor of Kim and O'Neil (1997):

$$1000\ln(\alpha_{\text{water-calcite}}) = \frac{18.03 \times 10^3}{T} - 32.42. \quad (5.4)$$

Within a closed system, $\delta^{18}\text{O}_\Sigma$ is constant. Thus, initial and reacted isotopic compositions can be explicitly related through a manipulation of Eq. 5.2:

$$N \times \delta^{18}\text{O}_{c,t=0} + (1 - N) \times \delta^{18}\text{O}_{w,t=0} = N \times \delta^{18}\text{O}_c + (1 - N) \times (\delta^{18}\text{O}_c - \Delta) \quad (5.5)$$

$$\delta^{18}\text{O}_{w,0} = \frac{N}{1 - N} \times (\delta^{18}\text{O}_c - \delta^{18}\text{O}_{c,0}) + (\delta^{18}\text{O}_c - 1000\ln\alpha) \quad (5.6)$$

Using Eq. 5.6, I calculate the water oxygen isotopic composition in equilibrium with an initially marine carbonate oxygen composition at $T(\Delta_{47})$ and a given N, resulting in a range of final (“altered”) $\delta^{18}\text{O}_c$. Isotopic ratios with a 0 subscript represent initial conditions of water and rock either at deposition (prograde model) or maximum burial (retrograde model). $\delta^{18}\text{O}_c$ is the oxygen isotopic composition of the carbonate at the given burial temperature in equilibrium with the altering water ($\delta^{18}\text{O}_{w,0}$).

In the first set of calculations, I model early diagenesis at near-surface to shallow burial temperatures ranging 25° to 35°C, reflecting progressive early burial. The lines of Figure

5.11 mark the final $\delta^{18}\text{O}_c$ composition for calcite formed in equilibrium with water of varying composition (0 to -30‰ VSMOW) and N at the set temperatures. Early eogenetic $\delta^{18}\text{O}_c$ alteration at shallow depth could have occurred while N was still low (high water:rock ratio), prior to compaction. The shallow pore fluids likely would have had near marine compositions, but could have had low elevation meteoric water compositions comparable to those in the modern Himalayan foreland, \sim -4 to -8‰ VSMOW (Hren et al., 2009). Within these constraints, marked by the black box in Fig. 5.11, early diagenesis could have shifted marine carbonate oxygen isotopic compositions to -4 to -8‰ VPDB at 25° to 35°C. The greater the value of N (lower W:R ratio), the less alteration marine to low elevation waters can facilitate. Further, marine carbonate can only alter from -2‰ to -6 to -8‰ when N is <0.5 . This set of calculations demonstrates that water with marine to low elevation meteoric composition cannot alter marine carbonate to the measured $\delta^{18}\text{O}_c$ values of our samples.

In the water-rock alteration models at deeper burial conditions, maximum temperature varies 150 and 190°C based on thermochronometric data described in section 5.4.1. This temperature range corresponds to maximum burial depths of 6-8 km assuming an average geothermal gradient of 25°C/km. We assume the rock package was already compacted (high N) prior to reaching these depths and water is non-marine. These conditions can easily take a marine composition limestone to any of the “altered” $\delta^{18}\text{O}_c$ compositions calculated in this set of measurements even within a closed system.

The high-temperature water-rock equilibration can alter marine carbonate compositions to isotopically light enough values to finish the $\delta^{18}\text{O}_c$ alteration during retrograde cooling. However, low-temperature alteration with plausible low elevation waters cannot. These results suggest that the event in which wholesale oxygen exchange occurred was not syngenetic with marine cementation, infilling, and early diagenesis. However, if we had considered low temperature alteration at the full range of water compositions in Figure 5.11, marine carbonate could have altered to isotopic compositions comparable with the measured values. This set of model results demonstrates the necessity of placing the model results into their

geologic context to determine the probable realism of each model scenario. Further, it is likely that much of the oxygen exchange occurred under a high-temperature regime.

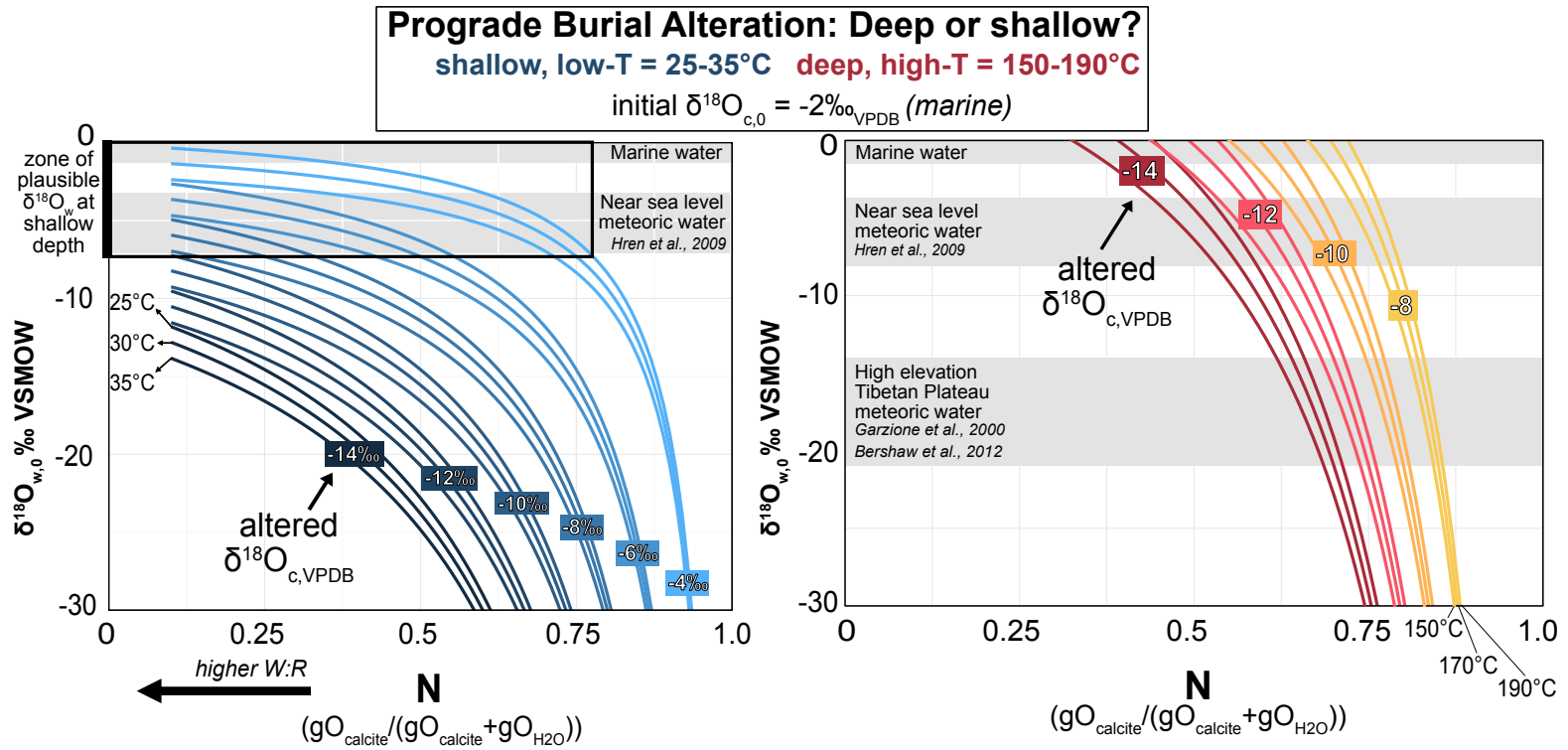


Figure 5.11 **Water-rock oxygen isotope exchange at shallow and deep burial conditions.** Final, "altered" $\delta^{18}\text{O}_{\text{c}}$ compositions are calculated using equations 5.3, 5.4, and 5.6, where N is the molar fraction of oxygen from calcite and $\delta^{18}\text{O}_{\text{w},0}$ is the composition of the altering water. Reactions are run at shallow (25° to 35°C) and deep (150 to 190°C) burial conditions. Gray boxes mark marine, low elevation meteoric, and high elevation meteoric water from this region (Hren et al., 2009; Garzione et al., 2000; Bershaw et al., 2012).

In the second set of prograde calculations, temperature varies from just warmer than Paleocene shallow marine temperature (Kobashi et al., 2001) to deep burial (30°C to 180°C). The starting isotopic composition is the same as in the first set of models ($\delta^{18}\text{O}_c = -2\text{‰}$). In the previous model, I restricted alteration to shallow and deep, but in this set the carbonate package is allowed to react with water at any burial depth and temperature. I hold N constant throughout each model run, and replicate the modeling experiment with N values of 0.5, 0.75, and 0.9. A constant N value is a reasonable parameterization for the prograde (and retrograde) water-rock reactions if we assume that pore space was either filled or compacted early in the burial history and remained constant. As previously mentioned, when considering N and water:rock ratios, one must also consider the duration over which oxygen partitioning between water and carbonate occurs. Even at high values of N and limited water flow rates, carbonate $\delta^{18}\text{O}$ can be pervasively altered on geologic timescales within an open system. In this set of calculations, we batch equilibrate marine composition carbonate with water within a closed system.

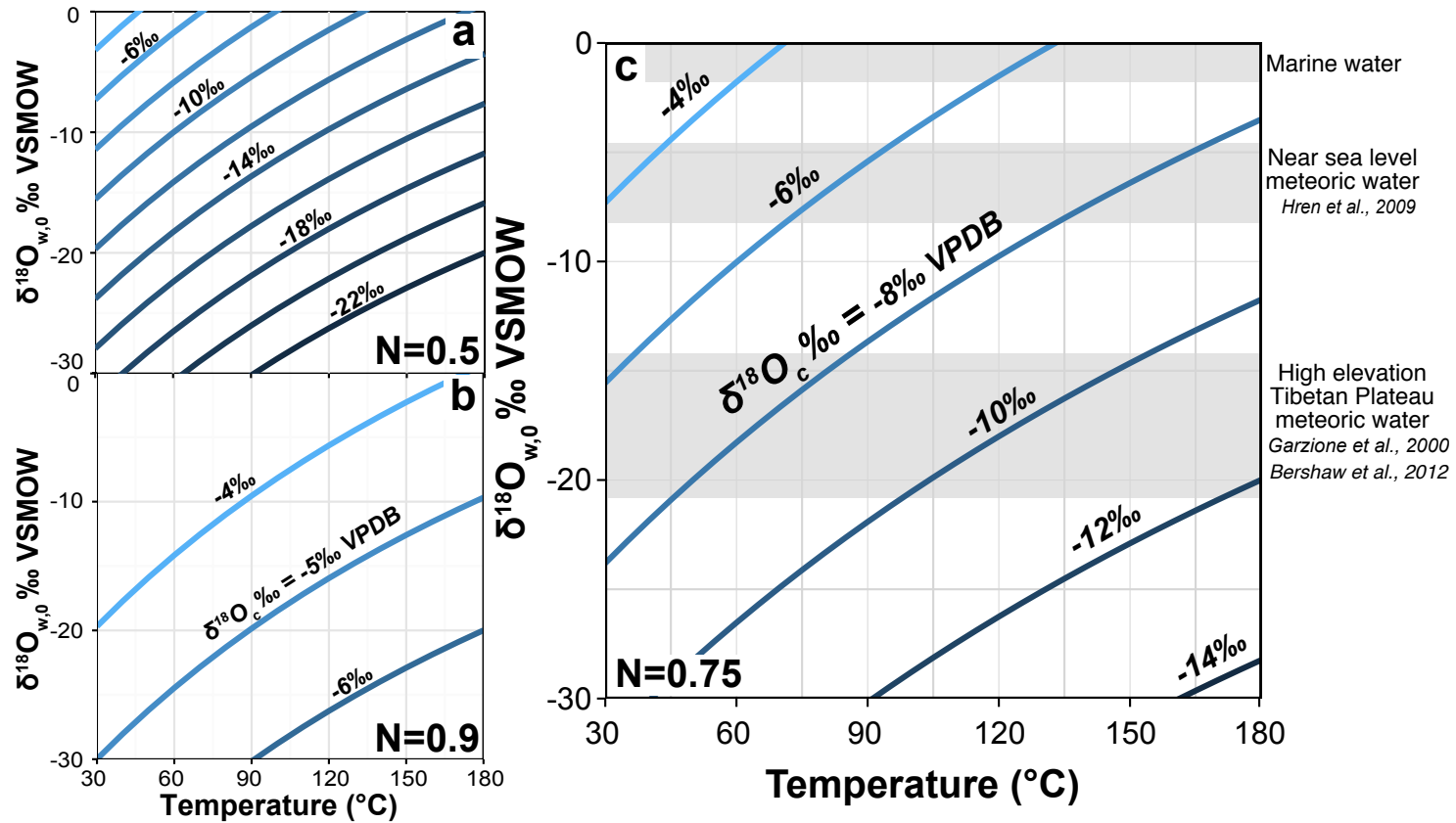


Figure 5.12 **Water-rock oxygen isotope exchange of marine carbonate at varying burial depths and temperatures.** The molar fraction of calcite (N) is set at 0.5 (panel a), 0.9 (panel b), and 0.75 (panel c). At higher temperatures, water of any composition precipitates equilibrium carbonate with lighter isotopic compositions than at cooler temperatures. The gray shaded regions represent the modern $\delta^{18}\text{O}_w$ values of meteoric or marine water in the Himalayan-Tibetan region at sea level, low elevation (Hren et al., 2009), and on the Tibetan Plateau (Garzione et al., 2000; Bershaw et al., 2012).

The carbonate oxygen mass fraction (N) is a rate limiting factor in water-rock oxygen exchange. Water:rock ratio and N in open systems can be considered time integrative characteristics because the same $\delta^{18}\text{O}_c$ can be produced through water-rock oxygen exchange with a very low water:rock ratio over a long period of time as with a very high water:rock ratio over a short period of time. Therefore, even though field, hand sample, and petrographic observations all but preclude the possibility of extensive water-rock exchange after initial carbonate infilling and cementation, a minimal amount of water within or introduced to the system during burial and exhumation could have facilitated recrystallization and isotopic exchange within the 62 to 51 Ma history of these strata. Figure 5.12 demonstrates that with an N of 0.9 ($\ll W:R$), the system is water-limited and can only facilitate minimal carbonate oxygen exchange on the order of 2‰ at temperatures $>90^\circ\text{C}$. However, when N is 0.5 (i.e. half of the oxygen is derived from water), the final $\delta^{18}\text{O}_c$ can vary from -4 to <-22 ‰ depending on the reaction temperature and starting isotopic composition of the water. To contrast, with a $\delta^{18}\text{O}_w$ of -20‰ VSMOW—some of the isotopically lightest water on the Tibetan Plateau today (Garzione et al., 2000; Bershaw et al., 2012)—and a reaction temperature on the “hot” end of the maximum burial temperature (180°C), the altered carbonate composition ranges from -22‰ to -6‰ VPDB with N values between 0.5 and 0.9, respectively. Thus, with limited constraints on the value of N for our samples during burial, we are limited in our ability to determine the conditions under which this sample set experienced pervasive oxygen exchange.

To yield the range of $\delta^{18}\text{O}_c$ measurements within this sample set, and considering the model results in Figure 5.12, oxygen partitioning between water and rock most likely occurred when the value of N was between 0.5 and 0.75. With an N of 0.75, the initial marine carbonate can recrystallize to very depleted (<-14 ‰) $\delta^{18}\text{O}_c$ compositions at T_{max} (Fig. 5.12). Under shallow burial conditions ($T < 40^\circ\text{C}$) and an N of 0.75, the initial marine carbonate package can only alter to modestly ^{18}O -depleted compositions (~ -4 ‰) within a closed system. It is worth noting that oxygen exchange could progress further within an open system.

If we assume an amount of available water and its composition, the final equilibrium carbonate composition will scale directly with the reaction temperature and, thus, burial depth. In the next section, I model water-rock reaction and isotopic alteration on the retrograde cooling pathway to constrain what the oxygen isotopic composition of the carbonate package could have been at maximum burial depth (start of exhumation) to reach its final, measured $\delta^{18}\text{O}_c$ value with the constraints of closed system behavior. Better constraints on retrograde cooling alteration could inform diagenesis on the prograde pathway and the composition of the initial altering water.

Equilibrium recrystallization on retrograde cooling pathway

In the retrograde models, I explore possible combinations of N , and water and carbonate oxygen compositions from maximum burial depth that could result in the final $\delta^{18}\text{O}_c$ values recorded by the Tso Jiangding samples. The retrograde cooling pathway represents the rock package during exhumation (see Fig. 5.10). I calculate water-rock oxygen isotope exchange under the assumption that Δ_{47} reflects carbonate (re)crystallization conditions, rather than an unconstrained combination of recrystallization and solid-state reordering during retrograde cooling.

Using Equation 5.6, I calculate the water oxygen isotopic composition in equilibrium with a set initial carbonate oxygen composition at $T(\Delta_{47})$ and a given N , resulting in the measured $\delta^{18}\text{O}_c$. In this set of models, we use measured $T(\Delta_{47})$ in calculations of calcite-water fractionation. N is the molar fraction of calcite in the water-calcite system. Isotopic ratios with a 0 subscript represent initial conditions of water and rock at maximum burial (retrograde model). $\delta^{18}\text{O}_c$ is the oxygen isotopic composition of the carbonate sample measured on the Gas Bench at the University of Chicago.

As with all of the modeling in this chapter, I use fossiliferous limestone T0702-18 as the modeled material. The measured $\delta^{18}\text{O}_c$ values for the matrix (T0702-18), and two forams (T0702-18N1,N2) are -15.1‰ , -15.5‰ , and -14.5‰ , respectively. The measured

$T(\Delta_{47})$ values are 55°C , 24°C , and 80°C , respectively, using the Zaarur et al. (2013) Δ_{47} -thermometer. I vary the initial carbonate oxygen composition from -2 (approximately marine) to -14‰ . The former composition would require the primary marine carbonate to have been buried to T_{max} without experiencing any oxygen isotope alteration from water-rock interaction, which we do not believe to be the case. The lighter composition represents material that experienced extensive water-rock diagenesis with ^{18}O -depleted waters on the prograde pathway, and begin their retrograde exchange reactions with isotopically “light” oxygen compositions. This model highlights the possible range of water compositions to produce the final $\delta^{18}\text{O}_{\text{c}}$ values from a range of $\delta^{18}\text{O}_{\text{c},0}$ compositions and calcite:water ratios (Fig. 5.13).

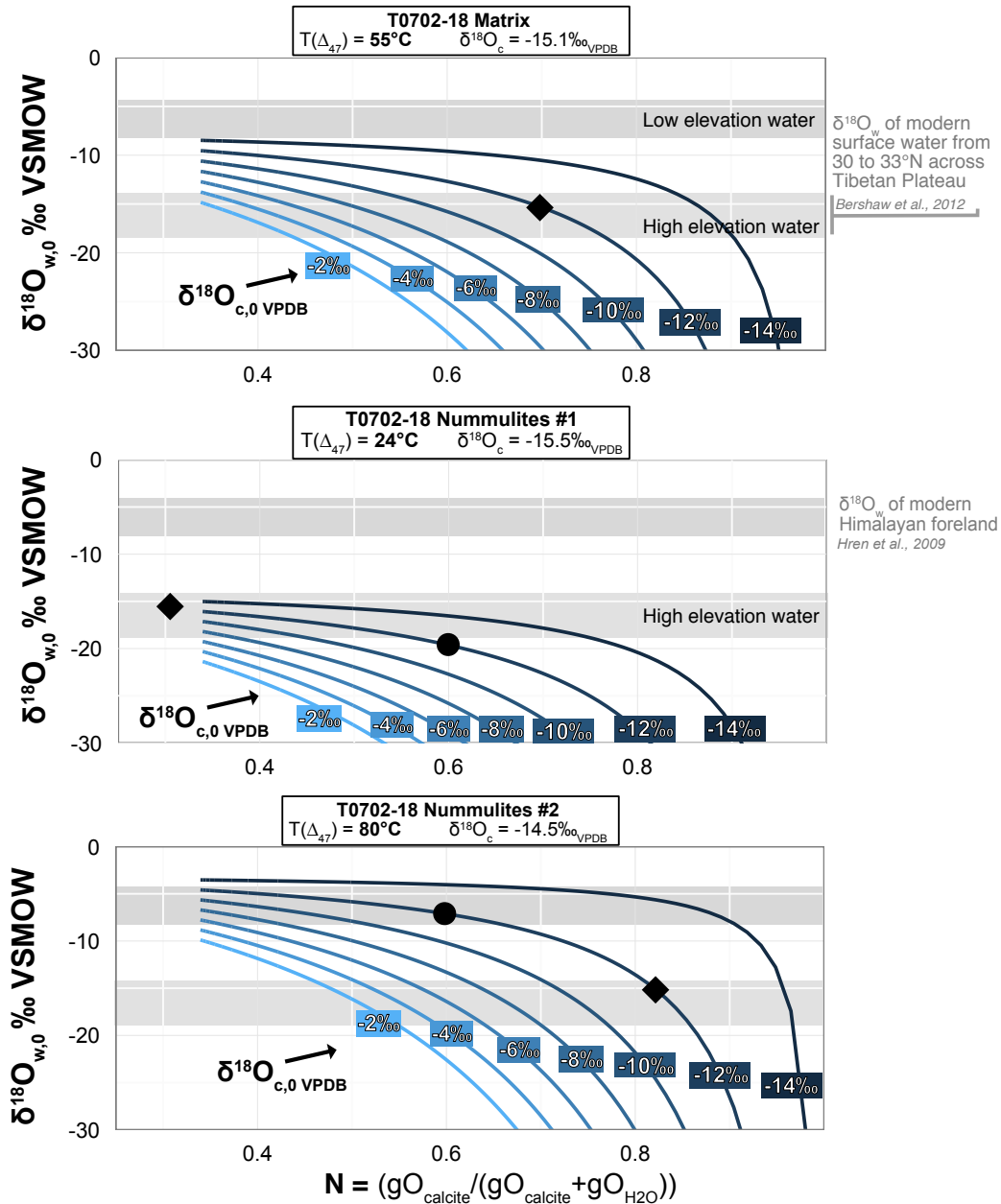


Figure 5.13 **Equilibrium oxygen isotopic composition of water and carbonate at varying values of N.** N is the calcite oxygen:total oxygen ratio by mass, where total oxygen is the sum of calcite and water in the system (decrease contribution of O from water from left to right). The measured $T(\Delta_{47})$ and carbon $\delta^{18}\text{O}$ compositions for each sub-sample of T0702-18 are listed above their respective plots. The gray shaded regions highlight modern surface water from on the Tibetan Plateau (Bershaw et al., 2012), and modern surface water of the Himalayan foreland (Hren et al., 2009). The lines represent possible carbonate oxygen compositions on the retrograde cooling pathway that could undergo isotopic exchange with water (y-axis) to produce the measured $\delta^{18}\text{O}_c$ composition at $T(\Delta_{47})$. Locations of diamonds mark the same starting isotopic carbonate (-12‰) and water (-15‰) compositions, yielding measured $\delta^{18}\text{O}_c$ at measured $T(\Delta_{47})$ with differential N.

The micrite and two forams sampled from limestone T0702-18 yield similar final $\delta^{18}\text{O}$ compositions. However, there is no clear set of solutions that can explain all three final compositions from one diagenetic event or N. First, it is worth noting that water-rock reactions facilitated by water with near sea level meteoric compositions (see panel 3 of Fig. 5.13) is only possible early in the diagenetic history. The only time in which the rocks of the Tso Jiangding Group interacted with sea level meteoric water was very soon after deposition. Based on geologic observations and evidence from modern marine cements (Carpenter and Lohmann, 1997), marine cements and shell infilling likely occurred with waters of sea level composition (see Section 5.4.2), but not on the retrograde cooling pathway, as modeled here. The retrograde models demonstrate that water with sea level isotopic composition could only precipitate carbonate with $\delta^{18}\text{O}_c$ compositions comparable to our samples (-14.5 to -15.5‰ VPDB) when interacting with carbonates with $\delta^{18}\text{O}_c$ compositions of -12 to -14‰ —clearly non-marine.

Sub-sample T0702-18N1, the “cold” T(Δ_{47}) *Nummulites* foraminifera of non-marine oxygen isotopic composition, is the most difficult sub-sample to logically explain. If 24°C is the reaction temperature, only high elevation water (-14 to -21‰ VSMOW) reacting with a previously altered carbonate could yield a final carbonate oxygen composition of -15.5‰ VPDB. Our model results suggest that the initial buried carbonate likely had an oxygen isotopic composition of -12 to -14‰ VPDB. A high value of N requires an even more ^{18}O -depleted initial carbonate composition, suggesting that T0702-18N1 experienced water-rock oxygen exchange during burial to shift its $\delta^{18}\text{O}_c$ from marine composition to -11 to -14‰ , and a second recrystallization event at low-T.

The micritic matrix could have reached its current carbonate oxygen composition reacting with high elevation water starting at modestly altered carbonate oxygen compositions (-4 to -10‰) over a wide range of values of N. If we assume a higher value of N as we did for T0702-18N1, the initial carbonate oxygen of the buried carbonate would have been -10 to -13‰ , comparable to our model result for T0702-18N1. Under the same restrictions,

the initial, buried T0702-18N2 could have started from a composition of -8 to -13‰ and exchanged with ^{18}O -depleted waters at a temperature of 80°C.

We assume $T(\Delta_{47})$ records the temperature of carbonate formation in this set of models. By nature of this assumption, these three sub-samples of one small piece of limestone record dissolution-precipitation at three very different temperatures, yet yield similar $\delta^{18}\text{O}_c$ compositions. In order for the three sub-samples to have altered to their measured $\delta^{18}\text{O}_c$ compositions with the same composition water, each sub-sample would need to have a different proportion of carbonate-derived oxygen than the other two sub-samples. I have represented this using water and carbonate oxygen compositions of -15‰ VSMOW and -12‰ VPDB, respectively, marked with diamonds on Fig. 5.13. In this scenario, T0702-18N1 would require an $N < 0.3$. Also, this example does not explain why each sub-sample records a different Δ_{47} composition. Within the constraints of our assumptions, each sub-sample must have recrystallized with water of similar compositions within three unique temperature regimes during exhumation. Here I will highlight that this requires differential aqueous alteration within small fragments of limestone. This sample has no signs of fracturing or other methods of introducing water to the system for late stage recrystallization, making this situation geologically implausible.

Next, I assigned the two forams the same value of N , because they are the same material type and may respond to burial diagenesis more similarly than the micrite, and the same $\delta^{18}\text{O}_{c,0}$ of -12‰ VPDB (black circles in Fig. 5.13). However, because in these calculations we are assuming $T(\Delta_{47})$ represents carbonate formation temperature, and thus the two forams formed at 24° and 80°C, the water with which the forams reacted would be $\sim 14\%$ different. This again can be explained by the fact that each sub-sample records a different Δ_{47} -derived temperature and yet $\delta^{18}\text{O}_c$ compositions within 1‰ of each other, and thus the Δ_{47} values could very possibly be unrelated to the water-rock exchange that resulted in very ^{18}O -depleted carbonate compositions. As such, in the following sections I model diffusive C-O bond reordering in an attempt to explain the differential Δ_{47} values recorded within

individual samples in the Jialazi Fm.

5.6.2 *Solid state reordering modeling*

Diffusive ^{13}C - ^{18}O bond reordering is likely for the Jialazi Fm samples in light of the elevated temperatures experienced during thrust burial. These strata exhumed from a T_{max} of $>150^\circ\text{C}$ (U-Th/He thermochronometry; Orme (2015)), above the threshold temperature for the second thermal phase of both Stolper and Eiler (2015) and Henkes et al. (2014) reordering behavior described by slow diffusion of ^{13}C and ^{18}O away from each other through the crystal lattice. In this phase the apparent equilibrium $T(\Delta_{47})$ can be equal to the true ambient temperature. Because the Jialazi Fm samples dwelled at or above the zircon He (ZHe) closure temperature ($\sim 150^\circ\text{C}$) long enough for total diffusive loss of ZHe (Dodson, 1973), all carbonate in this stratigraphic package theoretically should have experienced some degree of bond reordering to a more stochastic distribution of ^{13}C - ^{18}O clumps (i.e. lower Δ_{47} , higher $T(\Delta_{47})$). In this section, I model the effects of burial and exhumation (heating and cooling) on bond ordering. This work follows the work of Passey and Henkes (2012), Henkes et al. (2014), and Stolper and Eiler (2015) on the kinetics of solid-state reordering in the calcite lattice.

As represented in the schematic diagram Figure 5.9, there is no diffusive bond reordering below a “threshold” temperature. In the diagram, that temperature is at time 2. Between times 2 and 3, rapid reordering occurs either facilitated along easy exchange pathways in the form of lattice defects (Passey and Henkes, 2012; Henkes et al., 2014) or solid-state exchange of C and O between “neighboring” carbonate groups within the lattice (Stolper and Eiler, 2015). The duration that carbonate material experiences temperatures in excess of the threshold temperature determines how far along the prograde reordering pathway the carbonate’s Δ_{47} will record. If two carbonates with the same Arrhenius parameters experience different burial histories (i.e. one rock sits above the threshold temperature for 10 My longer than the other), the carbonate that dwells above the threshold temperature

for a longer period will have more time to undergo diffusive C-O bond reordering within the crystal lattice. The sample with the longer high-T burial history will record a lower apparent equilibrium Δ_{47} , or a higher apparent $T(\Delta_{47})$.

In Figure 5.14, I depict symmetrical burial histories (i.e. bury and exhume to and from T_{\max} at a constant rate) for three maximum burial temperatures: 150, 165, and 180°C. I set the “threshold” reordering temperature for this carbonate type to be 150°C. The burial history with a maximum temperature of 180°C allows the carbonate material to experience a thermal regime above the threshold reordering temperature for >10 My. This means diffusive C-O bond reordering took place within the crystal lattice for >10 My, producing a final $T(\Delta_{47})$ of 158°C. The burial history with a T_{\max} of 165°C only experienced reordering for ~ 7 My, and locks in a much lower apparent $T(\Delta_{47})$ of 64°C. The burial history that experiences nearly instantaneous exchange at the threshold temperature before beginning exhumation only sees a $T(\Delta_{47})$ increase of 7°C.

This final example demonstrates that in a rock-buffered system, $\delta^{18}\text{O}_c$ and Δ_{47} are robust to pervasive alteration under significant burial conditions up to $\sim 150^\circ\text{C}$ (i.e. 6 km burial depth assuming a geothermal gradient of $25^\circ\text{C}/\text{km}$). However, if the burial temperature is increased by 15°C —whether by increased burial depth or contact with hot fluids— $T(\Delta_{47})$ is significantly altered to 64°C. A common recurrence of moderately altered $T(\Delta_{47})$ values in the range of ~ 60 to 75°C is an unsolved problem in the clumped isotope community. It is unclear whether the commonality reflects a common shallow burial system geochemistry that favorably facilitates open system recrystallization, in which case the recurring $T(\Delta_{47})$ of 60°C reflects a crystallization temperature, or if there is an undescribed kinetic reason why reordering may reach a hitch within the reordering realm of a 60°C apparent lock-in temperature. An improved understanding of the mechanisms by which cryptic carbonate alteration is facilitated and metrics by which to identify it should improve our understanding of why we commonly measure secondary $T(\Delta_{47})$ in the range of 60° to 75°C .

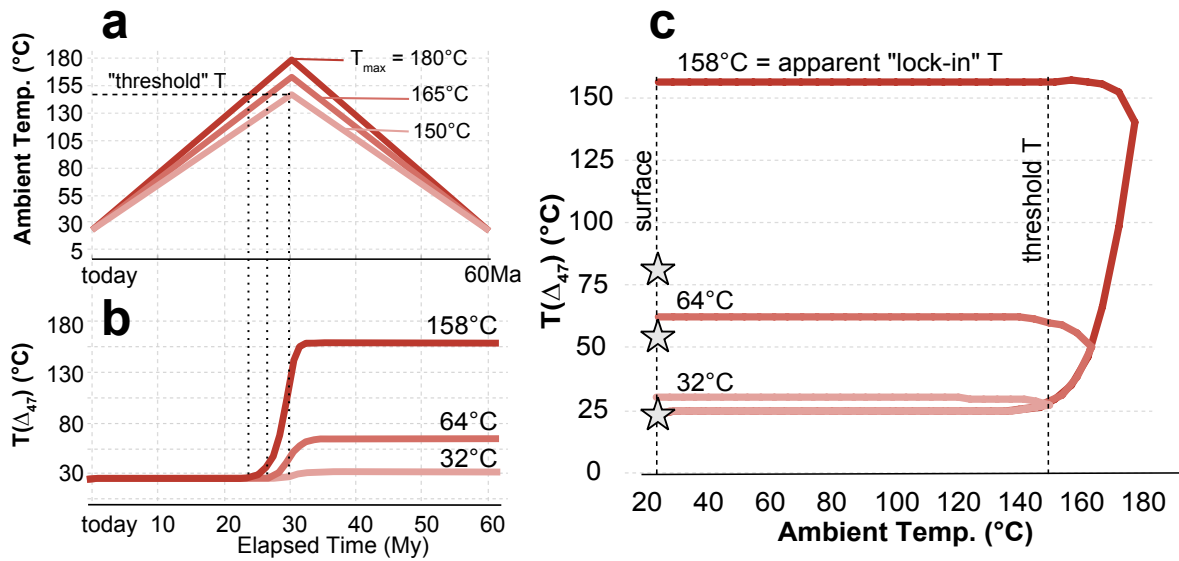


Figure 5.14 **Effect of maximum burial temperature and integrated time above “threshold” temperature on apparent “lock-in” $T(\Delta_{47})$.** **a.** Symmetric burial histories with three maximum temperatures. **b.** Final (“lock-in”) $T(\Delta_{47})$ depends on integrated time above threshold temperature. **c.** Ambient burial temperature versus recorded $T(\Delta_{47})$. Retrograde cooling begins at T_{\max} . Stars mark the measured $T(\Delta_{47})$ for the three subsamples of T0702-18. If T_{\max} is $<170^{\circ}\text{C}$, T0702-18 Δ_{47} values can be attained; however, this one small sample experienced one maximum temperature. Modeling based on the parameters outlined in Passey and Henkes (2012) and Henkes et al. (2014).

Figure 5.14C demonstrates that the burial histories with lower maximum temperature and shorter integrated time above the threshold temperature never allow the carbonate to move into the second, slower diffusive reordering stage described in Stolper and Eiler (2015) and Passey and Henkes (2012). The two cooler examples never move beyond stage 3 of Figure 5.9 where apparent equilibrium $T(\Delta_{47})$ can be equal to ambient temperature. The burial history with a T_{\max} of 180°C does not yield a $T(\Delta_{47})$ equal to T_{\max} , but is much more extensively reordered than the other two experiments. The stars in panel C denote the $T(\Delta_{47})$ measurements from micrite and forams of T0702-18. If considering an alteration history strictly based on solid-state reordering, this would suggest that the carbonate strata never reached a burial temperature $>170^{\circ}\text{C}$.

I also modeled reordering under a thermal history similar to the 165°C history, but with a plateau at 165°C for 10 My. In the symmetrical burial-exhumation scenario with a T_{\max} of 165°C, the final “lock-in” $T(\Delta_{47})$ is 64°C. In the scenario with a plateau at 165°C for 10 My, the final $T(\Delta_{47})$ is 132°C. This modeling exercise demonstrates the integrated time above the threshold reordering temperature is more important than the maximum temperature alone.

Passey and Henkes (2012) experimentally determined kinetic Arrhenius parameters for different calcite polymorphs common in natural carbonate samples. Here I use the Arrhenius parameters defined in Henkes et al. (2014) for optical calcite, labile spar, and refractory spar to determine whether calcite polymorph-dependent Arrhenius parameters could explain the variability in final apparent equilibrium temperatures seen in sample T0702-18 (Fig. 5.15).

Sample T0702-18 has been sub-sampled from one thick section (Fig. 5.4) for micrite and two *Nummulites-Discocyclusina*. 2-3 separate digestions and analyses have been completed for each of the three sub-samples. The micrite records a $T(\Delta_{47})$ of $\sim 55^\circ\text{C}$. The two *Nummulites-Discocyclusina* bracket this value at $T(\Delta_{47})$ of 24 and 80°C . However, the difference in recorded Δ_{47} in the two foraminifera cannot be explained by this logic (Fig. 5.15). Thus far we have not determined the diffusive property that could allow two sub-samples of the same origin and calcite polymorph that have experienced the same thermal history to have vastly disparate apparent “closure” temperatures.

The greatest conundrum in this data set is the apparent cool $T(\Delta_{47})$ of T0702-18N2. As previously stated, there is no evidence of macro-recrystallization in petrographic thin section of the shells or micritic matrix. We interpret this to mean burial occurred in a rock-buffered system, following the logic of deep burial and associated loss of formation water and fluid inclusions within the rocks. Also, any existing primary porosity in the *Nummulites-Discocyclusina* should have crystallized with shallow meteoric or marine water and filled with marine cements early on in burial, as the fossils have no obvious signs of compaction. Late-stage retrograde recrystallization at a temperature as cold as $\sim 25^\circ\text{C}$

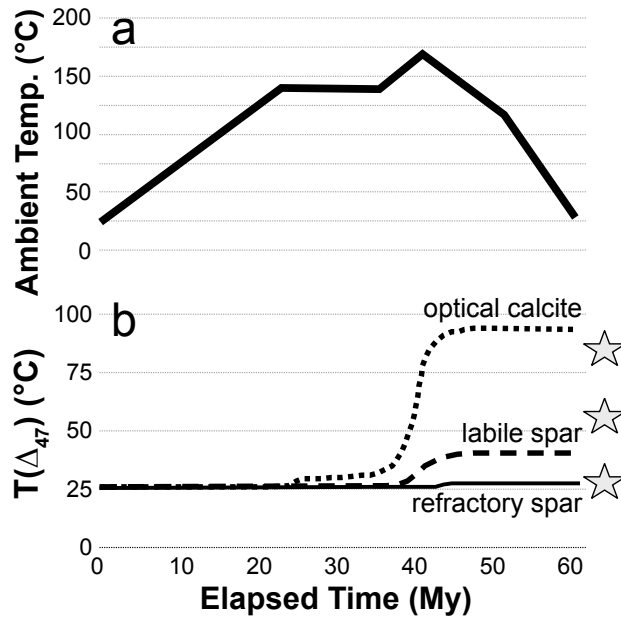


Figure 5.15 **One thermal history yields three unique apparent equilibrium $T(\Delta_{47})$ based on material-specific Arrhenius parameters.** **a.** Burial history with a prolonged plateau at 135°C and T_{\max} at 170°C. **b.** Different calcite polymorphs reach their “threshold” diffusive reordering temperature at different time points. Optical calcite has the longest duration above threshold- T , and thus the greatest period of reordering and highest apparent equilibrium T . Stars mark the measured $T(\Delta_{47})$ for the three sub-samples of T0702-18. Material-specific Arrhenius parameters for optical calcite, labile spar, and refractory spar were determined experimentally in Passey and Henkes (2012).

would require an exceptionally high water:rock ratio and very depleted waters. The depleted waters could easily be high altitude meteoric water representative of the Tibetan Plateau today. However, without pore space in the rocks during exhumation, where would water exist to drive the cooler $T(\Delta_{47})$ calcites to continue reacting during retrograde cooling for longer than the calcite that records a warmer burial T (80°C)? It is uncertain how water could have been introduced to the system upon exhumation to the near-surface without leaving geological evidence of pervasive fracturing, not seen in section. Further, these data require that some foraminifera recrystallized at cool temperatures while other foraminifera retained deep burial $T(\Delta_{47})$ values despite experiencing identical thermal histories.

5.7 Refining diagenetic pathways to constrain diagenetic history

The Tso Jiangding Group deposited in a shallow marine environment during the Paleocene. Presence of marine shells and *Nummulites* forams requires that the primary carbonates formed at sea level with starting isotopic compositions ($\delta^{13}\text{C}$, $\delta^{18}\text{O}_c$, and Δ_{47}) representing typical low-latitude late Paleocene-early Eocene marine carbonate (Kobashi et al., 2001). Oxygen exchange with secondary waters has shifted the stable isotopic compositions of these samples significantly away from marine values. The goal of the water-rock reaction modeling was to constrain when the Tso Jiangding carbonates experienced pervasive oxygen exchange with water during thrust burial and mid- to late-Cenozoic exhumation. However, the calculations presented here demonstrate that there are numerous scenarios in which limestone of marine composition could experience oxygen exchange during burial, *if* there is enough water present. The greatest constraints on the alteration history of these rocks are from traditional petrography and geological intuition. The limiting factor for isotopic exchange in the Tso Jiangding is introduction of water to the system after burial compaction and cementation. Typically water is introduced to a rock package exhumed from deep burial by fracturing, and we do not see evidence for fracturing or other means of water infiltration on the stratigraphic or micro-scale.

Finally, the kinetics of solid-state reordering do not allow for a late retrograde increase in clumping of multiply-substituted carbonate groups within the carbonate lattice given current constraints on Arrhenius parameters of calcites. I posit that there is an as of yet uncharacterized mechanism that cryptically alters carbonate isotopic compositions but is undetectable by traditional diagenesis screening tools.

5.8 Summary: Seemingly contradictory isotopic, thermal, and textural data require a cryptic alteration mechanism

The study samples experienced temperatures $>150^{\circ}\text{C}$ for longer than 10 My based on ages of partial resetting of zircon He (Orme, 2015). It is expected under this time-temperature regime (t-T) that solid-state reordering should drive Δ_{47} values unidirectionally to lower values (< 0.700) yet some of the material yields high Δ_{47} measurements (> 0.700) (Ingalls et al., 2016a). Carbonate powders sub-sampled from $\sim 12\text{cm}^2$ billets yield a range of clumped isotope-derived temperatures from plausible Paleocene sea surface temperature to above any Earth surface temperature. For example, from one fossiliferous limestone, micritic cement yields a $T(\Delta_{47})$ value of 52°C and two forams yield $T(\Delta_{47})$ of 24 and 79°C . The latter demonstrates that carbonate material type is not the dominating factor in Δ_{47} variation within these samples.

Additionally, very negative $\delta^{18}\text{O}_c$ values (demonstrably non-marine, -12 to -21‰ VPDB) require complete oxygen isotopic exchange either during high-temperature burial with water that could have a range of compositions and high N (low water:rock ratio), or late-stage recrystallization with ^{18}O -depleted water at low temperature, requiring a low N (high water:rock ratio). The lack of fabrics indicative of recrystallization are contradicted by both the burial diagenesis and late-stage secondary precipitation scenarios (Fig. 5.2).

Further, the range of oxygen and clumped isotope data recorded within these samples calls into question our ability to use $\delta^{18}\text{O}$ and Δ_{47} in studies of carbonate rocks having experienced modest burial and/or encountered meteoric water. If we accept that the four micrites and forams that yield low- $T(\Delta_{47})$ ($<25^{\circ}\text{C}$; Fig. D.9) record equilibrium carbonate formation temperatures, we must accept that this carbonate material exchanged oxygen with high elevation meteoric water either at shallow burial depths or at the surface. The $\delta^{18}\text{O}$ and Δ_{47} compositions of these low-T samples mimic the compositions and formation temperatures of modern lacustrine and pedogenic carbonates formed at >4 km elevation on

the Tibetan Plateau. This is highly troubling because if rocks of originally marine composition can be pervasively altered during burial and exhumation, yield low Δ_{47} -derived temperatures similar to modern Tibetan temperatures, and appear texturally pristine, we must question our ability to assess carbonate alteration within terrestrial rocks without a “ground truth” $\delta^{18}\text{O}_c$ composition. These results demonstrate that we do not have a sufficient understanding of the behavior of ^{13}C - ^{18}O bond ordering and/or all possible alteration pathways at elevated temperatures within the realm of shallow-to-deeply buried sediments. I posit that a careful study of the geochemical, textural, and isotopic signatures of deeply buried, cryptically altered marine carbonates will substantively impact the use of clumped isotopes in reconstructions of past terrestrial and marine temperatures in a wide range of Earth Science applications.

5.8.1 Next steps: Micro-analytical techniques for identifying cryptic carbonate alteration

Despite the fluid-facilitated bulk oxygen exchange, our Paleocene marine samples preserve primary micritic textures, which is a fabric typically interpreted as primary but can be a diagenetic product. Recently, studies have employed techniques in trace element mapping, electron backscatter diffraction (EBSD), cathodoluminescence (CL), and clumped isotope thermometry together to correlate individual results that would typically be used individually to diagnose secondary calcite or aragonite precipitation to provide a more robust assessment of diagenetic regime (e.g. Cummins et al. (2014); Moreno-Azanza et al. (2016); Snell et al. (2012)). The next phase of work on this project will be to explore micro-analytical techniques to identify the chemical, physical, and/or isotopic fingerprints of cryptic carbonate alteration to provide for more robust use of the carbonate proxy record in paleoclimate and paleoaltimetry applications.

Crystallography by Electron Backscatter Diffraction

EBSD, which identifies crystallographic orientation of individual calcite grains, will be used to characterize dissolution and secondary precipitation of primary calcite or overprinting by other carbonate mineralogies. EBSD provides a measure of degree and style of recrystallization typically within biogenic carbonate because micrite loses its primary fabric much more readily than shells and corals (Snell et al., 2012; Cummins et al., 2014). EBSD is also used to map preferred orientations of dynamically recrystallized grains in calcite mylonite to reconstruct diagenetic regime (Lefebvre et al., 2011; Almqvist et al., 2011).

Together, EBSD, BSE, and EDX images will form a more complete picture of generational calcite growth based on crystallographic orientation, dissolution-precipitation textures, and compositional differences, respectively. The suite of maps generated on the SEM will inform my sampling strategy for secondary ionization mass spectrometry (SIMS) and additional clumped isotope analyses (Fig. 5.5). These images facilitate observation of micromorphological structures and compositional variation not visible in hand sample and thin section.

Secondary Ionization Mass Spectrometry (SIMS)

The large-radius double-focusing CAMECA IMS 7f at Caltech achieves isotopic ratio analyses at the level of $\sim 0.1\%$ with a $10\ \mu\text{m}$ -diameter Cs^+ primary ion beam. I will make in situ $\delta^{18}\text{O}$, $\delta^{13}\text{C}$, and minor and trace element (Mn, Mg, K, Na, Sr) measurements across vein-matrix boundaries, shell microstructures, and body cavity infill (e.g. Fig. 5.5) to examine high-resolution isotopic and chemical variation or potential homogeneity due to alteration. $\delta^{13}\text{C}$ will be analyzed to investigate potential exchange with organic material during burial, and how organic constituents could affect solid-state bond reordering in the carbonate lattice. I will use changes in trace elemental concentrations to distinguish solid-state reordering (no change) from alteration in the presence of meteoric water (lower concentrations) (Snell et al., 2012). Each of these measurements can be used to distinguish pristine primary carbonate material from material that has undergone exchange with non-primary water. For example,

differential metal-to-calcium ratios (i.e. Mn/Ca) measured by SIMS across veins and shell-groundmass boundaries have been used to detect small diagenetic domains undetectable by petrography or CL (Gothmann et al., 2015). SIMS measurements will aid our understanding of how a material that appears petrographically pristine can have demonstrably altered stable isotope compositions.

I will observe whether shell material and shell body cavity-filling carbonate cement have homogenized during burial and alteration or maintained heterogeneity (Snell et al., 2012). This could address the extent of recrystallization not apparent in thin section. Further, I will compare $\delta^{18}\text{O}_c$ of calcite veins, micrite, and clay minerals to determine the extent of micrite matrix oxygen exchange with secondary calcite veins (likely cracks filled with altering waters) and clays weathered by altering waters from feldspars.

SIMS and nanoSIMS measurements will elucidate the extent of oxygen isotope exchange between different materials under a known thermal regime, which will inform future studies of where to be cautious in precise sub-sampling for clumped isotope and oxygen isotope measurements.

Informed clumped isotope sub-sampled measurements

The goal of additional Δ_{47} analyses is to correlate $T(\Delta_{47})$ variability in the study samples with:

- $\delta^{13}\text{C}$ and $\delta^{18}\text{O}$ (heterogeneity vs. homogeneity),
- physical and chemical evidence of alteration and secondary calcite precipitation, and
- major, minor, and trace element distribution.

How do the minor and trace element maps compare to variation in $T(\Delta_{47})$ and stable isotope compositions? Do carbonate generations with similar crystallographic orientation (EBSD) and/or CL correlate with similar temperatures, or can $T(\Delta_{47})$ vary across a generation suggesting variable high-temperature reordering?

The additional Δ_{47} analyses will be done in the Snell lab at the University of Colorado, Boulder. Portions of the marine samples will be strategically selected for further clumped isotope analyses at CU based on the results of CL identification of sequential calcite growth and SIMS analyses. Targets for Δ_{47} analyses will be extracted as carbonate powder using a micromill at CU for precise sampling. An individual clumped isotope analysis at CU requires 1-2 mg equivalent of pure carbonate. The mass required for each impure natural sample will be determined by calculating weight percent carbonate on a DeltaV isotope ratio mass spectrometer (IRMS) with a GasbenchII peripheral as a part of $\delta^{18}\text{O}$ and $\delta^{13}\text{C}$ analysis of each sample; these measurements will be done prior to clumped isotope analysis. Sample powders for clumped isotope analysis are digested in 105% phosphoric acid at 90°C in a common acid bath, and passed through a Poropak Q column on an automated vacuum line to remove water, non-condensables, and other gases that would cause isobaric interference.

Targeted Δ_{47} measurements paired with the micro-analytical techniques will more tightly constrain when a sample has experienced physical, chemical, and/or isotopic alteration during its complex geologic history (burial and exhumation). I will draw relationships between elemental distribution within carbonate samples (determined by SIMS) and solid-state re-ordering (lower Δ_{47}). Further, I will determine whether micro-fabrics indicative of secondary calcite observed during SEM analyses correlate with lower Δ_{47} to be used as a tool for diagenetic screening before clumped isotope analyses in future studies. Further, we will characterize how the extent of oxygen isotope exchange varies with Δ_{47} .

If $\delta^{18}\text{O}$, $\delta^{13}\text{C}$ and Δ_{47} are preserved within veins and/or pore space of the Tso Jiangding samples, these measurements in combination with the proposed micro-analytical techniques may allow us to reconstruct a more comprehensive burial history of Xigaze forearc basin and the Great Counter Thrust System, and other carbonate-rich sedimentary basins.

5.9 Conclusions

Carbonate rocks hold the details of past climate states, which in turn reflect the behavior of modern climate-tectonic feedbacks and dynamics. A complete understanding of how and when clumped isotopes reorder during burial is imperative for the robust use of Δ_{47} in earth science applications. In the Tso Jiangding marine samples, the extensively altered $\delta^{18}\text{O}$ and intrasample variability in Δ_{47} measurements cannot be explained by simple water-rock isotope exchange reactions or what we presently know of solid-state reordering behavior. A more complete understanding of how bonds break and reorder, and potentially increase order, within reasonable geologic conditions is essential for the robust use of this carbonate-derived proxy. Additionally, the reactions and mechanisms by which “cryptic” carbonate alteration affects carbonate $\delta^{13}\text{C}$, $\delta^{18}\text{O}$, and Δ_{47} should be characterized in future work. This work will directly improve accurate usage of Δ_{47} and $\delta^{18}\text{O}$ proxies necessary for understanding the history of climatic and tectonic dynamics.

CHAPTER 6

CONCLUSIONS

This chapter summarizes the major results from each preceding data chapter (Ch. 2-5) and provides a synthesis of how this work has contributed to the greater knowledge of Tibetan tectonics and the use of carbonate clumped isotope thermometry in tectonic sedimentary basins.

6.1 Major results and conclusions

Chapter 2 presents a nearly continuous Cenozoic record of reconstructed land surface elevations of the Linzizhong arc. In the Penbo basin, the hypsometric mean elevations of the Paleocene-Eocene Nianbo Formation and Eocene Pana Formation depocentres are $4.4_{-1.7}^{+1.3}$ km and $4.1_{-1.6}^{+1.2}$ km above sea level, respectively. A pre- to early syn-collisional Linzizong arc requires that some amount of the Tibetan Plateau thickened to > 4 km elevation prior to the onset of collision. This result agrees with the “Lhasaplano” model of an Andean-type continental margin system on the southern margin of Eurasia before the onset of collision 56 ± 2 Ma. In this model, a retroarc thrust belt associated with Gangdese magmatic arc propagation facilitates shortening and thickening of the Lhasa block in the late Cretaceous to early Cenozoic (Kapp et al., 2007). Paleoaltimetry results from the Oiyug basin, ~ 160 km west of Penbo, corroborate an early syn-collisional high elevation southern margin, and provide evidence that the southern margin maintained high altitude throughout most of the Cenozoic.

Chapter 3 provides new paleoaltimetric results from the Amu Xun basin, 500 km west of the Penbo basin, and more robust elevation estimates from the previously studied Lunpola basin (Rowley and Currie, 2006; Polissar et al., 2009) using clumped isotope paleothermometry. Carbonates within the Dingqing and Middle Niubao Formations of the Lunpola basin experienced significant evaporative ^{18}O enrichment, altering their $\delta^{18}\text{O}$ compositions to more

positive values. I correct for the isotopic effects of aridity by applying a local evaporation line with a slope of 1 ‰ $\delta\text{D}/\text{‰ } \delta^{18}\text{O}$ to the $\delta^{18}\text{O}_w$ compositions of samples with paired $\delta^{18}\text{O}$ and δD measurements (Polissar and Freeman, 2010; Polissar et al., 2009). The mean elevations of the three formations that record conformable sedimentation from the mid-Eocene to Miocene in Lunpola are all ~ 4500 m.

The measured section in Amu Xun is mapped as a western extension of the Nianbo Formation of the Linzizhong volcanic arc. As such, we accept the hypsometric mean elevation derived from the Amu Xun, 4551 ± 413 m (2σ), as the mean elevation of the Linzizhong arc ~ 300 to 500 km west of Oiyug and Penbo in pre- to early syn-collisional time. The majority of clumped isotope results from the Amu Xun yield hotter than Earth surface temperatures. There is little to no evidence of recrystallization within the Amu Xun samples, so alteration probably occurred within a rock-buffered system. We assume diffusive C-O exchange within the crystal lattice at temperatures $>120^\circ\text{C}$ partially reordered carbonate ‘clumps’ to more stochastic Δ_{47} compositions. Thus, although $T(\Delta_{47})$ measurements are ‘hot’, the primary meteoric water $\delta^{18}\text{O}$ composition is likely reflected in the carbonate mineral.

Chapter 4 integrates the total mass of continental crust within the India-Asia collision system just prior to the onset of collision and through the modern by considering the most up to date constraints on paleogeography and timing of diachronous continental collision, new paleo-thickness constraints on the pre-collisional Linzizhong arc, and all known reservoirs of Indian and Tibetan-derived continental material. The calculation allows the Indus Yarlung Suture—the boundary between the two plates—to vary in length to account for the diachroneity of collision and uncertainty in suture zone length in the past. I integrate crustal thickness (z) within the defined collision domain to calculate the difference between mass of continental crust within the domain at the onset of collision and at any point in the collisional history (M_{excess} , or crustal thickening). In addition to crustal thickening, I account for erosional sediment flux and tectonic escape. The currently reconstructable excess mass of the Himalayan orogenic system is $465_{-176}^{+192} \times 10^3 \text{Gt}$ or 51% of the earliest Cenozoic mass.

This requires that 49% of the earliest Cenozoic (just pre-collisional) continental mass within the collisional domain is not found at the Earth surface today. Therefore, the India-Asia continental crustal reservoir is not in mass balance. We suggest that wholesale subduction of lower continental crust and mantle lithosphere into the mantle is the most reasonable explanation for the ‘missing’ mass.

Chapter 5 explores our ability to reconstruct possible diagenetic pathways a carbonate rock may take from $\delta^{18}\text{O}$ and Δ_{47} measurements, and aims to refine our ability to assess carbonate diagenesis in the absence of optically detectable recrystallization. The Tso Jiangding marine carbonates provide a unique sample set for exploring the current state of knowledge of bond ordering behavior during burial diagenesis because existing constraints on Paleocene seawater compositions and low-latitude sea surface temperatures allow us to compare our measurements to ‘ground truth’ marine compositions. I consider the isotopic consequences of both water-rock reactions and intracrystalline solid-state bond reordering. I find that there is no geologically reasonable alteration mechanism that agrees with the water-rock reaction and/or solid-state reordering models, intra-sample Δ_{47} variability, and petrographic textural observations. I conclude that we do not understand all mechanisms by which C-O bonds reorder or recrystallize within rock-buffered systems, nor are we able to sufficiently identify alteration by traditional screening practices. An understanding of the geochemical, isotopic, and textural fingerprint of cryptic carbonate diagenesis is absolutely necessary for the robust use of carbonate stable isotope proxies in tectonic and paleoclimate applications.

6.2 Broad implications of this work

1. The combined results of Chapters 2 and 3 indicate that high relief at low latitude prevailed on the Asian margin prior to the Eocene Climatic Optimum. This result refutes earlier tectonic models in which the southern Tibetan Plateau attains high elevation in the late Cenozoic, and suggests a more complicated relationship between the Tibetan-Himalayan orogeny, chemical weathering, and tectonics-weathering-climate feedbacks.

2. Large-scale subduction of eclogitized lower continental crust could be a general model of continental recycling during past continent-continent collisions throughout Earth history, which would produce radiogenic isotope anomalies in mantle-derived magmas and influence the long-term evolution of the continental crust.
3. Careful and persistent geochemical, isotopic, and textural screening for diagenesis and other syngenetic to post-depositional isotopic processes is essential to the correct interpretation of carbonate stable isotopic proxies. Additionally, a more sophisticated understanding and explanation of cryptic carbonate alteration is required for the robust use of carbonate clumped isotopes, and perhaps even $\delta^{13}\text{C}$ and $\delta^{18}\text{O}$, within the variably altered sedimentary record for paleoclimate and tectonic reconstructions.

APPENDIX A

ANALYTICAL DETAILS

A.1 Tests on Δ_{47} clean up

Subambient and ambient (room) column temperatures were tested for optimal sample clean-up efficiency. Column performance was verified using 1000°C heated gases, CO₂ standard gases, and CO₂ derived from the acid digestion of clean (Carrara Marble) and dirty (modern non-living coral fragments; impure limestone) calcite (Table A.1). The column as configured above was found to clean samples effectively and provide throughput yields of CO₂ indistinguishable from 100% when processed at room temperature and allowing a 35 to 45 minute collection time, depending on sample size. Samples were analyzed isotopically within 24 hours of digestion and purification.

Table A.1: All clumped isotope measurements run on standard materials during the analytical period in which Oiyug and Penbo basin measurements were made.

Sample	$\delta^{13}\text{C}$	$\delta^{18}\text{O}_{\text{CO}_2}$	$\Delta_{47,SG-WG}$	δ_{47}	Δ_{48}	$\Delta_{47,CDES}$	Analysis Date
Carrera Marble	2.3	38.8	-0.432	19.0	0.632	0.445	5/28/14
	2.1	38.9	-0.451	18.9	0.671	0.422	5/28/14
	2.1	39.0	-0.430	19.1	0.787	0.447	5/29/14
	1.9	38.8	-0.431	18.7	0.480	0.445	6/3/14
	2.1	39.0	-0.437	19.0	-0.034	0.439	7/5/14
	2.1	39.1	-0.450	19.1	0.181	0.424	8/28/14
	2.1	39.0	-0.465	19.0	0.403	0.423	9/10/14
	2.0	38.9	-0.419	18.9	0.359	0.475	9/12/14
	2.1	39.0	-0.511	19.0	0.246	0.402	9/11/15
	2.0	38.9	-0.518	18.8	1.147	0.395	9/29/15
	2.1	38.9	-0.476	18.9	0.741	0.440	9/29/15
	1.9	38.6	-0.501	18.5	1.114	0.412	9/30/15
	2.0	39.0	-0.521	18.9	1.177	0.392	10/6/15
	2.0	39.1	-0.525	19.0	0.882	0.388	10/14/15
	2.1	39.1	-0.564	19.0	-0.119	0.380	12/17/15
	2.0	39.0	-0.506	18.9	-0.737	0.438	1/12/16
	1.9	38.7	-0.466	18.5	-0.718	0.477	1/14/16
	2.0	39.0	-0.503	18.9	-0.645	0.441	1/25/16
	2.0	38.9	-0.513	18.8	-0.769	0.431	1/27/16
	1.9	38.7	-0.463	18.5	-1.283	0.481	1/27/16
	2.1	39.0	-0.502	19.0	0.517	0.442	3/16/16
	2.1	39.0	-0.505	19.0	0.454	0.439	3/16/16
	2.0	39.0	-0.504	19.0	0.392	0.440	4/6/16
	2.1	39.1	-0.508	19.1	0.468	0.437	4/13/16
	2.1	39.1	-0.495	19.0	0.407	0.449	4/21/16
	2.1	39.1	-0.483	19.1	0.108	0.461	4/27/16

	2.2	39.4	-0.492	19.5	0.439	0.454	5/26/16
	2.2	39.2	-0.459	19.4	0.689	0.486	5/30/16
	2.1	39.1	-0.497	19.0	0.247	0.448	7/7/16
	2.0	38.9	-0.531	18.8	0.169	0.413	7/7/16
	2.1	39.1	-0.518	19.1	0.427	0.426	7/8/16
Average ± s.e.m.*	2.05±0.00	38.98±0.01	-0.486±0.001	18.96±0.01		0.435±0.001	
ETH-1	2.0	38.9	-0.513	18.8	0.361	0.368	9/4/14
	2.1	38.8	-0.571	18.8	-0.188	0.303	9/5/14
	2.1	39.0	-0.575	18.9	0.431	0.299	9/8/14
	2.1	39.1	-0.622	19.0	0.284	0.322	7/12/16
	2.0	39.0	-0.491	18.9	1.059	0.453	4/19/16
Average ± s.e.m.*	2.05±0.01	38.96±0.05	-0.554±0.023	18.88±0.04		0.349±0.029	
ETH-2	-10.1	21.8	-0.533	-9.9	0.207	0.312	9/4/14
	-10.1	21.9	-0.521	-9.8	0.273	0.326	9/4/14
Average ± s.e.m.*	-10.06±0.01	21.86±0.05	-0.527±0.009	-9.85±0.07		0.319±0.010	
ETH-3	1.8	39.5	-0.209	19.4	0.805	0.702	9/17/14
	1.8	39.5	-0.201	19.5	0.436	0.712	9/17/14
	1.6	39.3	-0.206	19.2	0.441	0.739	
	1.6	39.4	-0.203	19.2	0.198	0.743	
	1.6	39.4	-0.252	19.1	-0.070	0.693	10/5/15
	1.6	39.4	-0.188	19.3	0.417	0.758	3/16/16
Average ± s.e.m.*	1.68±0.02	39.40±0.01	-0.210±0.004	19.27±0.03		0.725±0.004	
ETH-4	-10.1	21.8	-0.322	-9.8	-0.006	0.551	9/17/14
	-10.2	21.7	-0.312	-9.9	0.136	0.562	9/18/14
	-10.2	21.7	-0.294	-9.9	0.827	0.596	7/11/16
	-10.2	21.7	-0.293	-9.9	0.590	0.596	7/12/16
	-10.1	21.9	-0.283	-9.6	1.444	0.607	
Average ± s.e.m.*	-10.17±0.03	21.78±0.02	-0.301±0.003	-9.80±0.03		0.582±0.005	
NBS-19	1.9	38.9	-0.494	18.8	-1.762	0.450	1/21/16

	1.9	39.0	-0.498	18.8	-1.544	0.446	1/21/16
	1.9	38.9	-0.467	18.8	-2.018	0.477	1/22/16
	2.0	39.1	-0.540	18.9	-0.908	0.404	1/22/16
Average ± s.e.m.*	1.95±0.01	38.99±0.03	-0.500±0.015	-18.85±0.03		0.444±0.015	

Note: *s.e.m. (Standard Error of the Mean) used to estimate analytical error for samples with more than 3 measurements.
For samples with <3 measurements, standard deviation is reported.

A.2 Corrections and Quality Control Checks on the MAT253

The analytical run structure employed a pressure baseline correction described previously. Our run was divided into 5 or 6 acquisitions with pressure balancing in between each acquisition to achieve a 16V signal on the m/z 44 detector. Cumulative on-peak signal integration time was generally 1000 to 1600 seconds for each of sample and reference gases, and instrumental uncertainty was at or near that calculated from counting statistics (around 10 ppm in Δ_{47}).

We performed a number of quality control checks on our analytical system. These included monitoring the Δ_{47} vs. cycle number for individual runs to ensure stable instrument performance. The m/z 48 signal was monitored for excess amplitude that would indicate inadequate cleaning of the sample gas. None of the samples used in the data chapters and models and interpretations therein gave anomalous Δ_{48} values. Nevertheless, we passed a subset of our samples through the chromatographic clean-up column a second time in order to ensure that isobaric interferences had been removed; analyses before and after the second column clean-up gave Δ_{47} values within uncertainty of each other (Table A.2). As a further test for isobaric interferences, we equilibrated splits of CO₂ from a few large samples at 26°C or 60°C with water, or roasted at 1000°C without water (Table A.3). These test equilibrations yielded Δ_{47} values that were on our equilibrated gas lines within uncertainty, indicating that sample gases were free of isobaric interferences.

Table A.2: **Once- and twice-cleaned sample analyses.** Saving leftover CO₂ gas post-analysis and “cleaning” the CO₂ by passing it through the chromatographic column a second time allows us to ensure isobaric interferences have been sufficiently removed and are not being introduced by the clean-up column. The values from the initial and re-cleaned analyses are differenced in the neighboring column, and the standard deviation (S.D.) of the two measurements is calculated in a third column. The date listed in the first column is the date of the initial sample analysis.

Date	Sample ID	$\delta^{13}\text{C}$	Diff.	S.D.	$\delta^{18}\text{O}$	Diff.	S.D.	$\Delta_{47,CDES}$	Diff.	S.D.	δ_{47} PBL-corr.	Diff.	S.D.	Δ_{48}	Diff.	S.D.
1/19/14	Carrera Marble (CM)	2.002	0.016	0.011	38.835	-0.031	0.022	0.470	0.009	0.006	18.863	-0.038	0.027	3.274	-0.031	0.022
	reclean	2.018			38.867			0.461			18.900			3.305		
1/27/14	48hr incubation with H ₃ PO ₄	-40.687	0.238	0.168	10.841	-0.120	0.085	0.056	0.011	0.008	-50.035	-0.331	0.234	-0.041	0.215	0.152
	reclean	-40.449			10.960			0.045			-49.704			-0.256		
2/2/14	CM-1	1.861		0.155	38.480		0.426	0.478		0.023	18.366		0.582	0.873		0.492
	CM-2	2.009			38.844			0.445			18.843			-0.111		
	CM-1+2 reclean	1.699			37.995			0.433			17.685			0.399		
2/2/14	House coral	-0.378	0.005	0.004	38.399	0.056	0.040	0.651	-0.057	0.040	16.298	0.065	0.046	-0.213	-0.307	0.217
	reclean	-0.383			38.343			0.708			16.233			0.094		
2/4/14	579	-5.731	0.061	0.043	21.486	-0.200	0.142	0.761	0.009	0.006	-5.649	0.264	0.186	0.574	-0.252	0.178
	reclean	-5.792			21.286			0.752			-5.913			0.826		
2/4/14	CM	1.957	0.066	0.046	38.464	-0.114	0.081	0.498	-0.026	0.018	18.461	0.156	0.110	0.614	0.244	0.172
	reclean	1.891			38.350			0.524			18.305			0.370		
2/4/14	CM	2.145	-0.028	0.020	38.958	0.056	0.040	0.498	0.042	0.030	19.137	-0.047	0.033	0.259	0.424	0.300
	reclean	2.173			39.014			0.456			19.184			-0.165		
2/24/14	CM-small volume	1.987	0.064	0.046	38.806	-0.185	0.131	0.502	0.009	0.006	18.836	0.255	0.181	0.070	-0.119	0.084
	reclean	1.923			38.621			0.493			18.580			0.189		
2/24/14	CM-medium volume	1.975	0.099	0.070	38.763	-0.269	0.190	0.419	-0.029	0.021	18.709	0.342	0.242	-0.062	0.199	0.141
	reclean	1.876			38.494			0.448			18.367			-0.261		
2/24/14	CM-large volume	1.999	0.012	0.009	38.858	-0.099	0.070	0.409	-0.014	0.010	18.817	0.096	0.068	-0.450	-0.475	0.336
	reclean	1.987			38.759			0.423			18.721			0.025		
3/3/14	576	-3.660	0.198	0.140	19.177	-0.406	0.287	0.601	-0.043	0.030	-6.085	0.556	0.393	0.273	0.043	0.030
	reclean	-3.858			18.771			0.644			-6.641			0.230		
3/3/14	579	-6.544	0.110	0.078	20.909	-0.245	0.173	0.645	-0.053	0.037	-7.102	0.304	0.215	-0.010	-0.111	0.079
	reclean	-6.654			20.664			0.698			-7.406			0.101		
6/12/14	6211	1.259	-0.114	0.081	12.162	0.849	0.600	0.749	0.034	0.024	-8.234	-0.927	0.655	0.833	0.346	0.244
	reclean	1.373			13.010			0.715			-7.307			0.488		
6/19/14	555	-5.974	-0.101	0.072	19.533	0.292	0.207	0.804	0.002	0.001	-7.782	-0.384	0.272	0.376	-0.106	0.075
	reclean	-5.873			19.825			0.802			-7.397			0.482		
12/5/14	DL104-3b HG	-2.253	0.038	0.027	26.538	-0.077	0.055	-0.013	0.012	0.008	1.962	0.125	0.088	-0.390	2.903	2.053
	reclean	-2.291			26.461			-0.025			1.837			-3.293		

4/15/15	704	-1.774	-0.023	0.016	20.303	0.075	0.053	0.438	-0.025	0.018	-3.366	-0.120	0.085	-3.213	-2.010	1.421
	reclean	-1.752			20.377			0.463			-3.246			-1.203		
1/12/16	W0628-3	-1.258	0.013	0.009	14.932	-0.021	0.015	0.643	-0.009	0.006	-7.995	0.025	0.017	-0.242	0.420	0.297
	reclean	-1.272			14.911			0.652			-8.020			-0.662		
1/12/16	CM	2.033	0.009	0.006	39.004	-0.017	0.012	0.438	0.021	0.015	18.945	0.046	0.033	-0.737	-0.135	0.096
	reclean	2.024			38.987			0.417			18.899			-0.602		
1/27/16	CM	1.952	0.013	0.009	38.881	-0.102	0.072	0.512	-0.009	0.006	18.820	0.104	0.074	-1.505	1.185	0.838
	reclean	1.939			38.779			0.521			18.716			-2.690		
5/22/16	EG-RT	-10.413	0.052	0.036	75.009	0.074	0.052	-0.045	-0.045	0.032	42.814	0.078	0.055	0.545	0.087	0.062
	reclean	-10.465			74.935			0.001			42.736			0.458		
7/7/16	546	-6.987	-0.001	0.001	19.575	-0.037	0.026	-0.284	-0.014	0.010	-8.911	-0.051	0.036	0.219	0.203	0.144
	reclean	-6.985			19.612			-0.270			-8.860			0.016		
7/14/16	T0702-8SH	1.294	0.017	0.012	26.493	0.010	0.007	0.617	-0.004	0.003	5.936	0.003	0.002	0.569	-0.159	0.112
	reclean	1.277			26.503			0.621			5.933			0.728		
7/27/16	CM	2.216	-0.005	0.004	39.310	0.012	0.008	-0.529	-0.072	0.051	19.408	-0.067	0.047	0.746	-0.201	0.142
	reclean	2.221			39.298			-0.457			19.475			0.947		
7/27/16	316	-4.530	-0.019	0.013	25.720	-0.015	0.010	-0.208	0.005	0.004	-0.373	-0.029	0.020	0.873	0.770	0.544
	reclean	-4.511			25.735			-0.214			-0.344			0.103		
2/6/17	S0630-3b	-4.077	0.012	0.008	16.976	-0.021	0.015	0.542	-0.017	0.012	-8.749	0.017	0.012	0.769	-0.155	0.110
	reclean	-4.089			16.955			0.559			-8.766			0.924		
2/8/17	703B	-1.211	0.006	0.004	21.600	-0.038	0.027	0.484	-0.033	0.023	-1.466	0.000	0.000	0.558	0.366	0.259
	reclean	-1.217			21.562			0.517			-1.466			0.192		

Table A.3: **Sample gases re-equilibrated at 26, 60, and 1000°C.** Re-equilibrating the saved gas from digested and analyzed carbonates with water at room temperature or 60°C, or roasting at 1000°C, allows for an additional check on possible isobaric interferences in the sample not detected during the initial analysis. $\delta^{13}\text{C}$ and $\delta^{18}\text{O}$ should not change during dry-roasting. $\delta^{18}\text{O}$ should alter during equilibration with a clean water of known composition, but $\delta^{13}\text{C}$ should not significantly alter. Analyses are separated by gas equilibration temperature. Equilibrated (EG) or heated gas (HG; i.e. roasted) analyses are italicized for ease of comparison. Δ_{47} is given in both standard gas minus working gas (SG-WG) and Carbon Dioxide Equilibrium Scale (CDES; Dennis et al. (2011)) reference frames.

Analysis Date	Sample	Equil. T (°C)	$\delta^{13}\text{C}$	$\delta^{18}\text{O}$	$\Delta_{47,SG-WG}$	δ_{47}	Δ_{48}	$\Delta_{47,CDES}$
9/30/15	CM		1.925	38.647	-0.501	18.487	1.114	0.412
<i>10/7/15</i>	<i>EG CM</i>	<i>26</i>	<i>2.054</i>	<i>18.009</i>	<i>0.113</i>	<i>-1.390</i>	<i>0.515</i>	<i>1.042</i>
5/18/16	706		-1.433	19.773	-0.384	-3.475	0.527	0.518
<i>5/22/16</i>	<i>EG 706</i>	<i>26</i>	<i>-1.368</i>	<i>16.989</i>	<i>0.148</i>	<i>-5.656</i>	<i>1.359</i>	<i>1.047</i>
5/18/16	708A		-0.580	19.847	-0.345	-2.543	1.863	0.559
<i>7/18/16</i>	<i>EG 708A</i>	<i>26</i>	<i>-0.668</i>	<i>16.977</i>	<i>0.129</i>	<i>-5.016</i>	<i>0.687</i>	<i>1.029</i>
10/28/14	446D		-2.983	23.574	-0.370	-1.172	-0.023	0.540
<i>11/6/14</i>	<i>EG 446D</i>	<i>60</i>	<i>-2.866</i>	<i>10.641</i>	<i>-0.180</i>	<i>-13.731</i>	<i>2.597</i>	<i>0.779</i>
11/20/14	MBMI-01A		0.785	31.646	-0.151	10.741	2.116	0.730
<i>10/4/15</i>	<i>EG MBMI-01A</i>	<i>60</i>	<i>0.743</i>	<i>10.203</i>	<i>-0.079</i>	<i>-10.629</i>	<i>0.005</i>	<i>0.828</i>
4/7/16	W0628-1		-3.099	22.282	-0.151	-2.350	0.275	0.753
<i>4/18/16</i>	<i>EG W0628-1</i>	<i>60</i>	<i>-10.224</i>	<i>13.145</i>	<i>-0.070</i>	<i>-18.161</i>	<i>3.929</i>	<i>0.804</i>
7/7/16	546		-7.003	19.536	-0.276	-8.957	0.277	0.616
<i>7/18/16</i>	<i>EG 546</i>	<i>60</i>	<i>-6.888</i>	<i>10.845</i>	<i>-0.103</i>	<i>-17.295</i>	<i>0.018</i>	<i>0.773</i>

7/7/16	CM-1		2.058	39.057	-0.497	19.033	0.247	0.448
7/18/16	<i>EG CM</i>	60	2.190	11.049	0.002	-8.324	0.612	0.895
7/21/16	T0702-8V		0.221	25.827	-0.393	4.143	0.588	0.524
8/19/16	<i>EG T0702-8V</i>	60	0.247	70.161	-0.120	48.698	0.838	0.882
7/26/16	330C		-1.128	36.723	-0.236	13.852	0.565	0.699
11/21/16	<i>EG60-330C</i>	60	-0.946	70.875	-0.476	47.828	8.899	0.501
7/26/16	T0702-18 matrix		-0.585	24.735	-0.372	2.296	0.493	0.540
8/18/16	<i>EG T0702-18</i>	60	-0.625	16.861	-0.061	-5.279	0.215	0.838
2/6/17	ETH4		-10.271	21.699	-0.305	-9.991	0.426	0.571
2/16/17	<i>EG ETH4</i>	60	-9.833	10.554	-0.031	-20.307	2.562	0.831
2/8/17	707D		-0.665	20.565	-0.450	-2.014	0.312	0.438
2/16/17	<i>EG 707D</i>	60	-0.671	11.109	-0.082	-11.076	0.258	0.795
9/17/14	ETH3-a		1.747	39.479	-0.209	19.442	0.805	0.702
9/19/14	<i>HG ETH3</i>	1000	1.755	34.970	-0.790	14.358	2.787	0.009
9/17/14	ETH4-a		-10.133	21.804	-0.322	-9.773	-0.006	0.522
9/19/14	<i>HG ETH4</i>	1000	-10.086	20.159	-0.804	-11.826	1.264	-0.050
12/4/14	DL104-3b		-2.325	28.746	-0.273	4.706	5.310	0.622
12/5/14	<i>HG DL104-3b</i>	1000	-2.253	26.538	-0.887	1.962	-0.390	-0.013
8/19/16	299B		-2.254	40.619	-0.216	16.650	0.777	0.725
11/16/16	<i>HG 299B</i>	1000	-1.879	31.318	-0.854	7.113	0.263	0.044
8/24/16	CM		2.017	39.048	-0.491	18.989	0.687	0.453

11/16/16

HG CM

1000

2.352

29.061

-0.873

8.951

0.584

0.028

A.3 Equilibrated gases and calcite standards

Tibetan samples were weighed out to yield roughly 100-200 μg CaCO_3 equivalent. Comparable size ranges of the isotopic standards NBS-18 ($\delta^{13}\text{C} = -5.01\text{‰}$ VPDB scale; $\delta^{18}\text{O} = -23.20\text{‰}$ VPDB), NBS-19 ($\delta^{13}\text{C} = 1.95\text{‰}$ VPDB; $\delta^{18}\text{O} = -2.19\text{‰}$ VPDB), and periodically LSVEC ($\delta^{13}\text{C} = -46.6\text{‰}$ VPDB) were interspersed with the Tibetan samples.

We measure Δ_{47} , Δ_{47} , $\delta^{13}\text{C}$, and $\delta^{18}\text{O}$ relative to an Oztech (Oztech Trading Co., Safford, AZ, USA) isotopic standard gas (UOC 1766, $\delta^{13}\text{C} = -3.61$ VPDB; $\delta^{18}\text{O} = 24.99$ VSMOW; VSMOW used in Δ_{47} calculations) used as the working reference gas. The Δ_{47} values measured relative to the working gas were corrected to an acid digestion temperature of 25°C using the temperature dependent acid fractionation factor for calcite computed by Guo et al. (2009). These Δ_{47} results are then converted from the working gas reference frame to the carbon dioxide equilibrium scale (Dennis et al., 2011) (CDES) using results from routine analyses of CO_2 heated to 1000°C and CO_2 equilibrated through reaction with water at 4°C , 25°C , and 60°C (Table A.4).

The empirical transfer functions (ETF) and heated (HG) and equilibrated (EG) gas analyses for each analytical period can be found in Figure A.1. Arrays of HG and EG analyses are used to generate an ETF, following the steps detailed in He et al. (2012) and the approach of Dennis et al. (2011). The top row of plots contain the HG and EG data corresponding to analytical intervals (P8-10) during which the Tibetan samples and carbonate reference materials were analyzed. All data are pressure baseline (PBL) corrected (He et al., 2012). In contrast to the negative slopes encountered with PBL-corrected HG and EG lines in He et al. (2012), we observed small positive slopes in P8 ($-3.092\text{e-}03$), a period in which Oiyug and Penbo samples were measured, signifying a slight undercorrection of the pressure baseline. Nevertheless, the HG and EG slopes were reduced by a factor of 4 and there is no evidence for a change in the PBL-corrected HG and EG line slopes over the P8 measurement interval. The bottom row of plots show the resultant ETF for each interval, with the ETF enumerated below each plot. The ETF permits the conversion of Δ_{47} measurements relative to the

working gas in the reference bellows ($\Delta_{47,SG-WG}$) into Δ_{47} measurements in the absolute reference frame (Dennis et al., 2011), also referred to as the “carbon dioxide equilibrium scale”, and symbolized by $\Delta_{47,CDES}$. The term $\Delta_{47SG-WG,0}$ in the lower panels refers to the projection of a $\Delta_{47SG-WG}$ value to $\Delta_{47,SG-WG} = 0$, using the composite best-fit slope from the HG and EG lines. The points plotted in the lower panels are the y-intercepts for the HG and EG lines in the left plot.

Table A.4: **Equilibrated gases.** CO₂ gases equilibrated with water of known isotopic composition at 4, 26, or 60°C, or equilibrated at 1000°C without water. The δ_{47} and Δ_{47} values are used to populate “equilibrated gas curves” and calculate an empirical transfer function for defined analytical periods.

Equilibrium Temperature (C°)	Analysis Date	$\Delta_{47SG-WG}$ (PBL-corrected)	δ_{47}	Period
4	5/12/14	0.078	16.187	7
4	9/22/14	0.082	43.239	7
4	9/24/14	0.050	29.523	7
4	11/24/14	0.223	42.450	8
26	1/28/14	0.062	1.183	7
26	4/30/14	0.036	-1.131	7
26	9/26/14	0.004	12.577	7
26	10/13/14	0.139	40.345	7
26	10/13/14	0.139	40.345	8
26	10/21/14	0.229	50.368	8
26	10/21/14	0.208	53.618	8
26	11/24/14	-0.055	-13.870	8
26	10/7/15	0.113	-1.390	9
26	10/18/15	0.042	-28.445	9
26	10/18/15	0.016	-9.744	9
26	11/3/15	0.118	-75.429	9
26	11/3/15	0.043	-20.855	9

26	11/3/15	0.094	-47.978	9
26	11/3/15	-0.034	9.142	9
26	11/4/15	0.090	-47.323	9
26	11/4/15	0.054	-18.986	9
26	11/9/15	0.072	-47.925	10
26	11/9/15	0.041	-18.613	10
26	11/9/15	0.044	-20.749	10
26	11/9/15	0.061	-47.187	10
26	11/10/15	-0.029	8.965	10
26	5/22/16	-0.045	42.814	10
<hr/>				
60	1/28/14	-0.174	33.100	7
60	1/29/14	-0.100	-19.862	7
60	3/7/14	-0.099	-5.024	7
60	3/14/14	-0.152	32.958	7
60	4/2/14	-0.199	32.872	7
60	4/9/14	-0.194	19.121	7
60	4/17/14	-0.194	19.121	7
60	4/17/14	-0.124	-6.672	7
60	9/22/14	-0.178	33.030	7
60	9/22/14	-0.178	33.160	7
60	10/21/14	-0.063	33.387	8
60	10/26/14	-0.018	33.344	8
60	10/26/14	-0.002	33.159	8
60	11/25/14	0.000	36.699	8
60	12/4/14	0.071	-20.600	8
60	1/18/15	-0.087	19.130	8
60	1/18/15	0.039	36.418	8
60	2/26/15	0.072	46.240	8
60	9/8/15	-0.095	-50.030	9

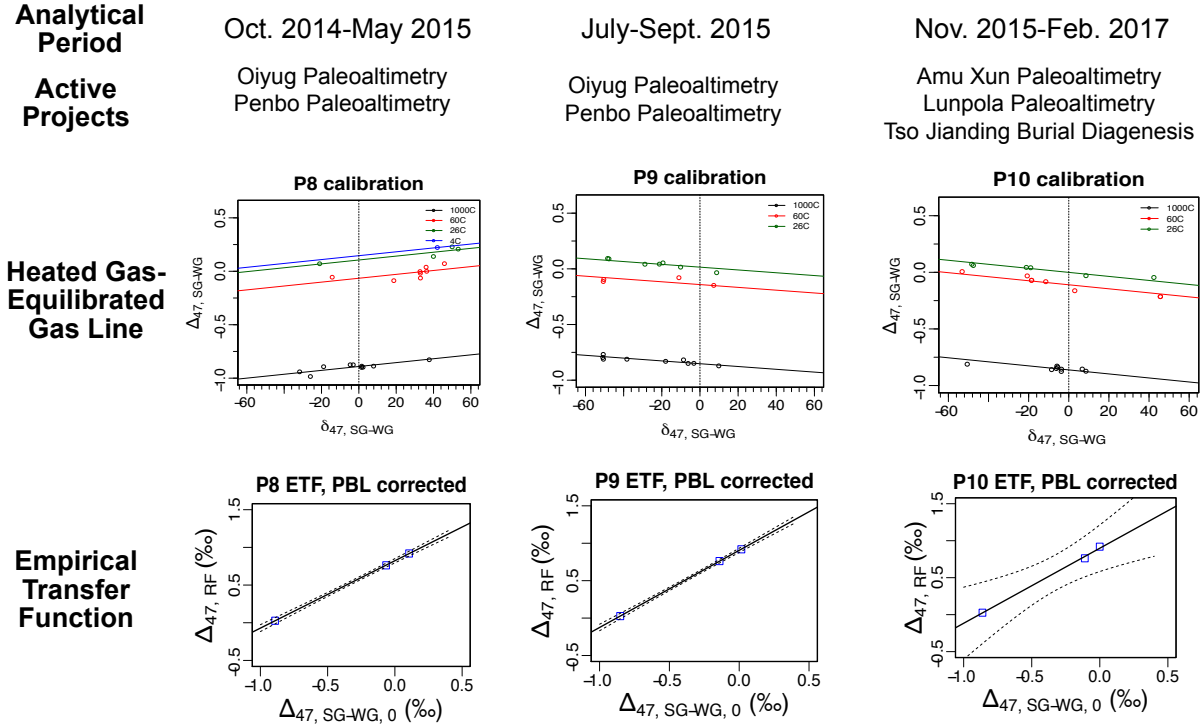
60	9/8/15	-0.148	7.626	9
60	9/9/15	-0.113	-50.274	9
60	10/4/15	-0.079	-10.629	9
60	12/5/15	-0.162	3.375	10
60	12/5/15	0.007	-52.761	10
60	4/19/16	-0.070	-18.161	10
60	4/19/16	-0.214	46.043	10
60	4/19/16	-0.070	-18.161	10
60	4/19/16	-0.214	46.043	10
60	2/16/17	-0.031	-20.307	10
60	2/16/17	-0.082	-11.076	10
<hr/>				
1000	3/11/13	-0.760	-2.938	7
1000	3/12/13	-0.747	-2.204	7
1000	3/12/13	-0.744	-2.967	7
1000	1/16/14	-0.784	9.110	7
1000	1/16/14	-0.769	9.124	7
1000	1/17/14	-0.712	-50.151	7
1000	1/22/14	-0.717	-50.301	7
1000	2/2/14	-0.675	-45.079	7
1000	3/31/14	-0.744	-1.911	7
1000	3/31/14	-0.759	-3.565	7
1000	4/1/14	-0.758	-14.219	7
1000	4/21/14	-0.697	-44.675	7
1000	7/16/14	-0.714	-49.174	7
1000	7/17/14	-0.712	-48.744	7
1000	8/5/14	-0.806	7.327	7
1000	8/5/14	-0.771	-4.971	7
1000	8/13/14	-0.806	-7.615	7
1000	9/19/14	-0.790	14.358	7

1000	9/19/14	-0.804	-11.826	7
1000	9/19/14	-0.819	22.247	7
1000	9/22/14	-0.764	-38.045	7
1000	9/25/14	-0.805	-5.868	7
1000	9/26/14	-0.828	12.283	7
1000	10/13/14	-0.827	38.116	7
1000	10/13/14	-0.887	8.296	7
1000	10/13/14	-0.827	38.116	8
1000	10/14/14	-0.887	8.296	8
1000	10/30/14	-0.892	-18.473	8
1000	10/30/14	-0.940	-31.320	8
1000	10/31/14	-0.984	-25.554	8
1000	11/25/14	-0.874	-2.617	8
1000	12/5/14	-0.887	1.962	8
1000	12/5/14	-0.899	1.837	8
1000	1/19/15	-0.874	-4.228	8
1000	2/2/15	-0.897	2.626	8
1000	7/14/15	-0.830	-17.602	9
1000	7/15/15	-0.871	10.266	9
1000	7/16/15	-0.817	-8.218	9
1000	7/20/15	-0.811	-37.891	9
1000	8/21/15	-0.768	-50.296	9
1000	8/24/15	-0.848	-2.777	9
1000	8/25/15	-0.795	-50.512	9
1000	12/8/15	-0.811	-50.210	9
1000	12/8/15	-0.849	-5.804	9
1000	12/8/15	-0.811	-50.210	10
1000	12/8/15	-0.849	-5.804	10
1000	3/11/16	-0.828	-5.482	10

1000	5/2/16	-0.875	-3.317	10
1000	5/16/16	-0.855	-3.271	10
1000	5/20/16	-0.859	-8.156	10
1000	11/16/16	-0.837	-5.144	10
1000	11/16/16	-0.854	7.113	10
1000	11/16/16	-0.873	8.951	10

We interspersed sample runs with digestions and analyses of reference carbonates (Table A.1). These included Carrara Marble (our own sample and CM-2 from D. Schrag, Harvard University) and the suite of ETH-1, ETH-2, ETH-3, and ETH-4 (S. Bernasconi, ETH Zurich). Carrara Marble analyses, using both our sample and CM-2, are generally ca. 20-30 ppm higher in Δ_{47} than those results reported in Dennis et al. (2011), but fall within the range measured by other labs. Our ETH results are within uncertainty of the mean results from a preliminary interlaboratory comparison reported by S. Bernasconi at the 4th and 5th International Clumped Isotope Workshops, held in August 2014, Zurich, Switzerland, and January 2016, St. Petersburg, Florida. We include the ETH standards because we expect that they will become widely used as international standards for clumped isotope analysis in the coming years.

Figure A.1 **Empirical transfer functions for each analytical period.** Δ_{47} measurements from each project are corrected using the ETF from the active analytical period. Some projects (Ex: Oiyug and Penbo Paleothermometry) span two analytical periods, but unique measurements from each period are corrected with their respective period's ETF. ETFs are calculated by analyzing CO_2 gas equilibrated at 4 known temperatures, with Δ_{47} compositions representative of the sample space.



P8: $\Delta_{47, \text{CDES}} = (\Delta_{47, \text{SG-WG}} - 1.815\text{e-}03 \cdot \delta_{47}) \cdot 0.89418 + 0.822703$

P9: $\Delta_{47, \text{CDES}} = (\Delta_{47, \text{SG-WG}} + 1.257\text{e-}03 \cdot \delta_{47}) \cdot 1.03088 + 0.905297$

P10: $\Delta_{47, \text{CDES}} = (\Delta_{47, \text{SG-WG}} + 1.780\text{e-}03 \cdot \delta_{47}) \cdot 1.01490 + 0.89824$

APPENDIX B

PALEOALTIMETRY MODEL PARAMETERS

Paleo-elevation estimates are calculated using a modified version of the Rowley (2007) isotopic lapse rate model. We first use the Δ_{47} temperature estimate coupled with measured $\delta^{18}\text{O}_c$ in order to calculate the $\delta^{18}\text{O}_w$ of the water with which the carbonate equilibrated (Kim and O’Neil, 1997):

$$\delta^{18}\text{O}_{\text{water}} = \delta^{18}\text{O}_{\text{calcite}} - 18.03(10^3/T(\Delta_{47})) + 32.42$$

with all $\delta^{18}\text{O}$ values on VSMOW scale (converting the carbonate data using $\delta^{18}\text{O}(\text{VSMOW}) = 1.03086 \times \delta^{18}\text{O}(\text{VPDB}) + 30.86\text{‰}$) (Friedman and O’Neil, 1977). The paleowater $\delta^{18}\text{O}_w$ was then used to estimate model elevation, Z :

$$Z \text{ (m)} = -0.0129(\Delta(\delta^{18}\text{O}_p))^4 - 1.1213(\Delta(\delta^{18}\text{O}_p))^3 - 38.214(\Delta(\delta^{18}\text{O}_p))^2 - 715.22(\Delta(\delta^{18}\text{O}_p))$$

where $\Delta(\delta^{18}\text{O}_p)$, a model parameter, is the difference between the oxygen isotopic composition of precipitation at elevation and that near sea level along the same mean storm trajectory.

Licht et al. (2014) recently reported fresh water gastropod carbonate and tooth enamel phosphate oxygen isotopic compositions and corresponding reconstructed surface waters in late Eocene (~ 40 Ma) strata from the central Burma basin with values of $\sim -7.2\text{‰}$ to -8.4‰ , respectively. Although they discount a high elevation contribution, it would only require the precipitation-weighted hypsometric mean elevation to be between ~ 500 and ~ 1500 m assuming the -6.6‰ normalization value adopted here to account for these slightly more depleted values. Given the detrital zircon data (Robinson et al., 2014) from this same area and our conclusion regarding the paleo-elevation of the Linzizong arc (Ingalls et al., 2017), we view it likely that their (Licht et al., 2014) estimates are not sea level values.

Using the modern isotopic composition of low-latitude, near sea level precipitation ($-3.6 \pm 1.6 \text{‰}$ (Rowley and Currie, 2006)), our calculated mean elevation is boosted to 4.3 ± 0.4

km or 4.8 ± 0.4 km, using the Dennis et al. (2011) or Zaarur et al. (2013) thermometers, respectively. The Zaarur et al. (2013) paleothermometer (derived from analysis of inorganic CaCO_3 and supported by biogenic CaCO_3 analyses, conducted in individual phosphoric acid reactors at 25°C) is more appropriate for our sample digestion conditions and has been applied to other recent clumped isotope paleoaltimetry in Tibet (Huntington et al., 2015). Even if we were to use the warm endmember Δ_{47} paleothermometer from Dennis et al. (2011) (derived from analysis of inorganic CaCO_3 precipitates processed in a 90°C common phosphoric acid bath), the calculated paleotemperatures would be 25 to 29°C . The conservative elevation calculation, using these warmer temperatures and the oldest Siwaliks to constrain lowland $\delta^{18}\text{O}_p$, still implies that the Penbo Basin would have been in excess of 3 km at the onset of the Indo-Eurasian collision. We emphasize that our first-order conclusion regarding high topography is independent of the paleothermometer calibration and/or near-sea level $\delta^{18}\text{O}_p$ used.

The $\pm 2\sigma$ error envelope for the elevations uses the equations that characterize the 2σ error on the empirically determined modern precipitation-elevation relationship updated from Rowley (Rowley and Garzzone, 2007). The $T(\Delta_{47})$ errors are propagated through the equation for the calcite-water fractionation factor to determine $\Delta(\delta^{18}\text{O}_w)$ 2σ error.

APPENDIX C

PALEOGEOGRAPHY AND CRUSTAL GEOMETRY OF THE INDIAN AND EURASIAN CONTINENTAL CRUST

C.1 Age of Initiation of the Continent-Continent Collision in the India Asia System

The following discussion summarizes the current state of knowledge regarding the age of onset of the India-Asia collision. This discussion starts along the western margin and proceeds eastwards along the suture. In the west, oceanic arcs and the Bela, Quetta, and Muslimbagh ophiolites collided with the western margin of the Indian passive margin in the late Paleocene (Beck et al., 1995), followed by re-establishment of a passive-type margin unconformably above these obducted ophiolites by mid-Eocene and subsequent collision with Eurasian elements in late Eocene to Pliocene times from north to south along this margin (Rowley, 1996). Farther north, in the Kohistan-Ladakh Arc (KLA) segment of the margin, Ypresian ($\sim 52 \pm 1$ Ma) collision of the KLA with the Indian passive margin is well-constrained by a wide range of stratigraphic relations (Gaetani and Garzanti, 1991; Green et al., 2008), isotopic dating of ultra-high pressure (UHP) metamorphism from the Kaghan (Wilke et al., 2010) and Tso Moriri (Leech et al., 2005; St-Onge et al., 2013), and the transition from mantle-derived to contaminated magmatism in the southern KLA arc at ~ 50 Ma (Bouilhol et al., 2013). However, the age of suturing between Kohistan-Ladakh and Eurasia along the Shyok suture is less certain. The data of Bouilhol et al. (2013) imply that India-Asia related collision begins at $\sim 40.4 \pm 1.3$ Ma.

Farther east, data constraining age of onset of the India-Asia collision derive primarily from the vicinity of Sangdanlin Ding and Lai (2003); Ding et al. (2005); Wang et al. (2011); Orme et al. (2014); DeCelles et al. (2014) and Zhepure Shan (Rowley, 1996; Najman et al., 2010; Rowley, 1998; Zhu et al., 2005). Orme et al. (2014) and DeCelles et al. (2014) provide

provenance and detrital zircon data from both the Asian fore-arc basin and Indian passive margin of the Indus-Yarlung Tsangpo suture that date the initial age at which Gangdese-derived sediments overtop the Xigaze fore-arc basin and overlie Indian-passive margin sediments in the vicinity of Sangdanlin at ~ 58 Ma, based on an interbedded ash near the top of the section (DeCelles et al., 2014). This updates the previous work, particularly in the Zhepure Shan, that dates the initial arrival of Gangdese-derived sediments on the shallower water Indian passive margin at $\sim 51 \pm 1$ Ma (Najman et al., 2010; Zhu et al., 2005). It is important to emphasize here that unlike farther west there is no evidence for an oceanic arc intervening between the Xigaze forearc, that derives its sediments from the Gangdese arc on the Lhasa block to the north, and the Indian passive margin that derives its Asian margin sediments also from the Gangdese margin at $\sim > 58$ Ma. This requires that the Shyok suture terminate west of the Tso Jiangding region ($\sim 84.8^\circ\text{E}$; see Fig. 5.3) at the western end of the Xigaze forearc as per scenario 2 of Bouilhol et al. (2013).

There are no data that directly constrain the age of onset of the India-Asia collision east of the Zhepure Shan (Rowley, 1996) adjacent to the suture zone. Indirect evidence comes from dating the minimum age of Eo-Himalayan metamorphism in the eastern Tethyan Himalaya at > 44 Ma (Aikman et al., 2008). Stratigraphic data from the south (east prior to rotation of SE Asia (Kornfeld et al., 2014)) of the eastern syntaxis in Burma and farther east support derivation of sediments in the Inner Burman Basin (Bender, 1983) from the Gangdese belt by no later than ~ 40 Ma (Rowley, 1996; Robinson et al., 2014). For the purposes of modeling, we use an age of suturing in the vicinity of the eastern syntaxis at 54 ± 4 Ma.

C.2 Greater Indian Basin

Recently van Hinsbergen et al. (2012) postulated the existence of an oceanic lithosphere founded “Greater Indian Basin” that would have separated the Tethyan and Greater Himalayan regions from the Lesser Himalaya and Indian subcontinent regions farther south to as young as ~ 25 Ma. They hypothesize that this basin grew in post-Aptian times to

about ~ 2400 km wide based on combining three paleomagnetic studies of the southernmost Tethyan Himalayan. According to their analysis Aptian paleomagnetic data from Thakhola (Klootwijk and Bingham, 1980) overlap Indian apparent polar wander paths (APWP) but Late Cretaceous and Paleocene units near Gamba and Duela, when compared relative to a global APWP estimate of Indias paleo-latitude, are discordant by $16.6 \pm 2.9^\circ$ and $13.6 \pm 4.4^\circ$ latitude, respectively (van Hinsbergen et al., 2012). Wang et al. (2014) correctly points out that the Aptian data are misleading because present north was much closer to Aptian east and therefore these paleomagnetic data do not constrain the relative positions of the Tethyan Himalayas to India proper and thus do not contribute to the establishment of this basin.

There are no geological data that support the Greater Indian Basin hypothesis and much that argues against it. For example, there are no ophiolitic sequences associated with this ocean, nor preserved shallow or deep passive margin sedimentary sequences, nor evidence of arc-related magmatism or subduction-related metamorphism within the Tethyan Himalayan or Greater Himalayan sequences or southern Lhasa block associated with the subduction of ~ 2500 km of oceanic crust and lithosphere beneath these already sutured terranes. Sedimentary provenance data from early foreland basin sediments south of the Higher Himalayan sequence provide the clearest data against the existence of the Greater Himalayan Basin. Marine, fossil-dated Eocene ($\sim 45 \pm 5$ Ma) Subathu (Jain et al., 2009; Najman et al., 2005; Najman and Garzanti, 2000) and Bhainskati Formations (DeCelles et al., 2014, 2004) in the upper Lesser Himalayan sequence contain detrital zircons and chromites with sources restricted to regions along or north of the Indus Yarlung Tsangpo suture zone. Jain et al. (2009) report detrital fission track ages of ~ 50 Ma in the Subathu that require rapid exhumation from depths with temperatures above the zircon fission track partial annealing zone. These data imply continuity from south of the Main Central Thrust foreland basin north to Indus-Yarlung Tsangpo suture zone at 45 Ma, precluding the existence of an intervening ocean basin at this time (DeCelles et al., 2014). We therefore do not incorporate this basin into our calculations and instead treat the collisional domain as underlain by continental

crust. We discuss implications of various assumptions of the pre-collisional distribution of elevations across the Himalayan-Tibet collisional domain.

C.3 Greater India constrained by Gondwanan reconstructions

Greater India, a northern continuation of India has been discussed since Argand⁴⁷ hypothesized it as an explanation for the double thickness of continental crust in the Tibetan Plateau. We follow the approach of Powell et al.⁴⁸ and use the rifting relations of eastern Gondwana between western Australia, East Antarctica, and India (Fig. 4), and particularly the preserved western Australian margin to place constraints on the geometry of eastern Greater India that must fit against the Australian margin from the Perth Basin to some distance northward. As reviewed by Ali and Aitchison⁴⁹, there are a remarkable range of interpretations of the shape and extent of Greater India. Ali and Aitchison⁴⁹ prefer a northern edge coincident with the Wallaby-Zenith Fracture zone and thus limit it to fitting the Perth Basin. Powell et al.⁴⁸ preferred a northward limit at the Cape Range Fracture Zone thus matching north to the Cuvier Basin. Finally Matte et al.⁵⁰ and Hall et al.⁵¹ extend Greater India up to the northeastern boundary of the Exmouth Plateau to match the Gascoyne Basin. Seafloor spreading along the entire western Australian margin is well dated as beginning at ~ 130 Ma⁵² without any clear evidence of significant differences in opening history from the Gascoyne Basin south to the Perth Basin. This suggests that a single continental block rifted from this margin in the late Valanginian (~ 130 Ma). This supports the interpretation^{50,51} that we adopt in our analysis. This fit only explicitly constrains the geometry of the eastern passive margin of Greater India with the remainder sketched in to match the timing of collisions from Sangdanlin (S - Fig. 4) and farther west. Greater India in this mapping occupies an area of $\sim 4.2 \times 10^6 \text{ km}^2$.

C.4 Bootstrap estimate of uncertainties of areal convergence since onset of collision

Our bootstrap takes as input the age of initiation of India and KLA-Eurasia collision to be 40.4 ± 1.3 Ma in the west along a suture zone segment that may be up to ~ 1000 km long, 56 ± 1.5 Ma along the main segment of the Indus-Yarlung Tsangpo suture, and farther east, a younger 40 ± 4 Ma collision within ~ 500 km of the eastern syntaxis corresponding to promontories matching the Cuvier and Perth basins. The above quoted uncertainties in age of onset of collision along each segment represent $\pm 1\sigma$ values. To model the cumulative continent-continent convergence between India and Asia, we treat the age range of collision onset as Gaussian-distributed estimates and suture zone lengths as random variables up to their maximum length. Plate convergence data between India and Eurasia is based on a compilation of global rotations with associated 95% uncertainties rescaled to $\pm 1\sigma$ values. Constraints on the length and age of the suturing between India and Eurasia as a function of age do not exist, so we use the bootstrap to estimate the range of possible cumulative convergence of area underlain by continental crust.

C.5 Collisional crustal volume

We use Crust1.0 (Laske et al., 2013) to derive the average relationship between crustal thickness as a function of elevation averaged at the same spatial resolution of the crustal thickness grid to assign crustal thicknesses and associated standard deviations to each of the elements in this analysis. We assume Greater India was near sea level across the entire domain because there is no evidence preserved of a northern source of sediments in the Lesser Himalaya prior to the Subathu and Bhainskati. We therefore assign this domain a crustal thickness of 38 ± 4 (1σ) km in the south and 36 ± 3 (1σ) km in the north where shelfal conditions dominate in the Late Cretaceous to Early Eocene. We use our paleoaltimetry estimate of 4000 ± 500 m as an inference that the Gangdese Arc domain had a crustal thickness

of $\sim 61 \pm 5$ km. This thickness is assigned over an area of $\sim 3.5 \pm 1.0 \times 10^5$ km² of potentially high (>4 km) elevations at ~ 54 Ma. The remaining $\sim 3.85^{+1.5}/_{-1.1} \times 10^6$ km² of “Deformed Asia” presumably had a broad distribution of elevations reflecting the complex prior tectonic history, with significant areas at or below sea level in the Early and early Late Cretaceous (Zhang, 2000). We ascribe a mean elevation of 250m to this broad region, equivalent to $\sim 38 \pm 4$ (1σ) km mean crustal thickness. Given this crustal thickness distribution, respective areas, and uncertainties, we use a bootstrap to assess the net crustal volume of the system at the time of collision to be $3.3^{+1.6}/_{-1.1} \times 10^8$ km³, corresponding to $930^{+450}/_{-290}$ Zg (i.e. Zg= 10^{21} g).

C.6 Erosional mass flux

Our value of $5.0 \pm 1.0 \times 10^7$ km³ is comparable to two previous estimates of the erosional rock equivalent volume flux. Richter et al. (1992) estimated erosional loss to be $\sim 5 \times 10^7$ km³. Métivier et al. (1999) estimated that erosion removed $\sim 3 \pm 1 \times 10^7$ km³ rock equivalent volume, but this estimate did not include either the Makran ($>1.1 \times 10^7$ km³), Indo-Burman-Andaman-Sumatran accretionary complex ($\sim 2.5 \times 10^6$ km³) (Curray, 1991), or the associated dissolved flux ($\sim 1.0 \times 10^7$ km³) (Richter et al., 1992).

Richter et al. (1992) argued that Himalaya-Tibet was in mass balance with the implication that crustal mass was conserved. Richter et al. (1992) dated the collision based on the marked slow down in convergence velocity at ~ 50 Ma that corresponds with ~ 47 Ma using a more recent time scale. In the intervening 25 years, improved plate kinematic constraints, and most importantly, direct estimates of the age of initial collision between India and Tibet that dates this at closer to 56 ± 2 Ma, 9 ± 2 Ma older than Richter et al. (1992) estimate, are responsible for the majority of the difference in conclusions.

One way to bring the system closer into balance is to significantly reduce initial crustal thickness over the non-Gangdese portions of the Himalaya-Tibet region. Clark (2012) argues for an average initial crustal thickness of ≤ 27 km for the entire region. However, Crust1.0-

based global average crustal thickness at an elevation of 250m, the height Clark (2012) assigned to the pre-collisional mean topography, is 38.4 ± 8.6 km (2σ). Thus, it seems unreasonable to assume that all of pre-collisional Greater India and Greater Tibet crust deviated from the global mean by more than two standard deviations. We are thereby left with the conclusion that significant mass is unaccounted for in this orogenic system.

C.7 Tables related to plate rotations

Table C.1: **Pairwise plate rotations.** Reconstruction code has Doubrovine routines embedded that inverts rotations and covariances and interpolates between rotations where necessary. References for plate rotation data: (1) Bull, J. M., DeMets, C., Krishna, K. S., Sanderson, D. J. & Merkouriev, S. Reconciling plate kinematic and seismic estimates of lithospheric convergence in the central Indian Ocean. *Geology* 38, 307-310, doi:10.1130/g30521.1 (2010). (2) Cande, S. C., Patriat, P. & Dymant, J. Motion between the Indian, Antarctic and African plates in the early Cenozoic. *Geophysical Journal International* 183, 127-149, doi:10.1111/j.1365-246X.2010.04737.x (2010). (3) Horner-Johnson, B. C., Gordon, R. G., Cowles, S. M. & Argus, D. F. The angular velocity of Nubia relative to Somalia and the location of the Nubia-Somalia-Antarctica triple junction. *Geophysical Journal International* 162, 221-238 (2005). (4) Merkouriev, S. & DeMets, C. High-resolution estimates of Nubia-North America plate motion: 20 Ma to present. *Geophysical Journal International* 196, 1281-1298, doi:10.1093/gji/ggt463 (2013). (5) Mller, R., Royer, J., Cande, S., Roest, W. & Maschenkov, S. New Constraints on Caribbean Plate Tectonic Evolution. *IGCP Project 433 Caribbean Plate*, 49 (1999). (6) Merkouriev, S. & DeMets, C. High-resolution Neogene reconstructions of Eurasia-North America Plate motion. *Geophysical Journal International* 198, 366-384, doi:10.1093/gji/ggu142 (2014). (7) Gaina, C., Roest, W. & Mller, R. Late Cretaceous Cenozoic deformation of northeast Asia. *Earth And Planetary Science Letters* 197, 273-286 (2002).

190	Moving Plate	Fixed Plate	Age (CK 95)	Rot Lat. °	Rot. Long. °	Rot Angle °	kappa	a	b	c	d	e	f	Source
	India	Capricorn	0	1.12	77.56	0	1	0.00E+00	0.00E+00	0.00E+00	0.00E+00	0.00E+00	0.00E+00	
	India	Capricorn	0.78	1.12	77.56	0.248	1	3.03E-07	4.61E-07	-8.67E-08	9.04E-07	-4.98E-08	1.22E-07	1
	India	Capricorn	1.86	5.36	71.7	0.533	1	2.81E-07	2.63E-07	-1.81E-07	4.46E-07	-1.46E-07	1.58E-07	1
	India	Capricorn	2.581	5.55	71.18	0.768	1	4.28E-07	5.95E-07	-1.65E-07	1.06E-06	-1.27E-07	1.73E-07	1
	India	Capricorn	3.58	1.02	79.64	0.772	1	6.49E-07	9.06E-07	-2.08E-07	1.72E-06	-6.75E-08	2.60E-07	1
	India	Capricorn	5.23	6.73	72.06	1.541	1	5.15E-07	7.05E-07	-2.56E-07	1.31E-06	-2.50E-07	2.42E-07	1
	India	Capricorn	5.894	2.45	74.34	1.752	1	1.22E-06	1.77E-06	-5.64E-07	3.22E-06	-5.10E-07	5.47E-07	1
	India	Capricorn	6.567	2.97	74.59	1.854	1	1.11E-06	1.46E-06	-6.72E-07	2.26E-06	-7.34E-07	5.80E-07	1
	India	Capricorn	8.072	3.77	74.87	2.348	1	8.85E-07	1.19E-06	-4.65E-07	2.08E-06	-3.91E-07	4.41E-07	1
	India	Capricorn	9.025	2.51	76.88	2.139	1	8.27E-07	1.09E-06	-5.70E-07	1.91E-06	-6.51E-07	5.19E-07	1
	India	Capricorn	9.74	6.2	73.46	2.486	1	2.21E-06	3.50E-06	-1.23E-06	6.30E-06	-1.76E-06	9.55E-07	1
	India	Capricorn	10.949	3.3	74.72	2.594	1	1.26E-06	1.72E-06	-5.77E-07	3.65E-06	-5.00E-07	5.71E-07	1
	India	Capricorn	12.401	3.61	73.63	2.793	1	9.56E-07	1.37E-06	-4.65E-07	3.19E-06	-4.91E-07	4.43E-07	1
	India	Capricorn	14.612	2.76	74.62	2.837	1	1.72E-06	3.43E-06	-8.72E-07	7.81E-06	-1.64E-06	6.75E-07	1

India	Capricorn	16.014	3.9	73.47	3.411	1	7.79E-07	1.28E-06	-4.45E-07	2.79E-06	-6.16E-07	3.61E-07	1
India	Capricorn	17.227	3.68	73.46	3.245	1	8.77E-07	1.76E-06	-4.23E-07	4.12E-06	-7.58E-07	3.34E-07	1
India	Capricorn	18.281	3.75	74.61	3.507	1	1.03E-06	1.96E-06	-4.24E-07	4.44E-06	-6.70E-07	3.60E-07	1
India	Capricorn	20.131	4.02	74.69	3.395	1	3.68E-06	4.83E-06	-1.97E-06	9.00E-06	-1.37E-06	2.04E-06	1
India	Capricorn	83	4.02	74.69	3.395	1	3.68E-06	4.83E-06	-1.97E-06	9.00E-06	-1.37E-06	2.04E-06	1
Capricorn	Somalia	0	11.66	51.22	0	1	0.00E+00	0.00E+00	0.00E+00	0.00E+00	0.00E+00	0.00E+00	
Capricorn	Somalia	0.78	10.24	52.04	-0.527	1	1.03E-06	1.20E-06	-8.65E-07	2.22E-06	-1.11E-06	7.65E-07	1
Capricorn	Somalia	1.86	10.28	49.54	-1.17	1	2.35E-06	1.97E-06	-1.76E-06	3.15E-06	-1.65E-06	1.39E-06	1
Capricorn	Somalia	2.581	10.84	48.97	-1.675	1	1.28E-06	1.59E-06	-9.74E-07	2.85E-06	-1.28E-06	7.87E-07	1
Capricorn	Somalia	3.58	13.39	49.81	-2.228	1	1.94E-06	1.73E-06	-1.55E-06	3.02E-06	-1.40E-06	1.28E-06	1
Capricorn	Somalia	5.23	10.27	49.16	-3.39	1	2.80E-06	3.42E-06	-2.22E-06	6.27E-06	-2.75E-06	1.87E-06	1
Capricorn	Somalia	5.894	12.45	48.94	-3.676	1	4.93E-06	5.97E-06	-3.93E-06	9.46E-06	-4.91E-06	3.25E-06	1
Capricorn	Somalia	6.567	11.81	49.21	-4.193	1	8.17E-06	9.65E-06	-6.73E-06	1.31E-05	-8.05E-06	5.63E-06	1
Capricorn	Somalia	8.072	11.48	49.82	-5.104	1	3.84E-06	3.70E-06	-3.47E-06	5.19E-06	-3.38E-06	3.21E-06	1
Capricorn	Somalia	9.025	13.81	48.29	-5.279	1	6.41E-06	8.79E-06	-5.03E-06	1.54E-05	-7.08E-06	4.11E-06	1
Capricorn	Somalia	9.74	12.21	47.78	-5.767	1	1.77E-05	2.91E-05	-1.20E-05	5.37E-05	-1.97E-05	8.45E-06	1
Capricorn	Somalia	10.949	13.88	46.91	-6.247	1	7.52E-06	9.54E-06	-5.65E-06	2.10E-05	-7.27E-06	4.47E-06	1
Capricorn	Somalia	12.401	14.13	45.87	-6.967	1	5.64E-06	7.96E-06	-4.08E-06	2.17E-05	-5.56E-06	3.22E-06	1
Capricorn	Somalia	14.612	15.98	44.53	-7.823	1	1.33E-05	2.72E-05	-9.14E-06	6.47E-05	-1.83E-05	6.82E-06	1
Capricorn	Somalia	16.014	15.14	44.92	-8.915	1	5.89E-06	1.01E-05	-4.25E-06	2.26E-05	-6.94E-06	3.36E-06	1
Capricorn	Somalia	16.726	15.66	44.48	-9.528	1	3.71E-06	7.21E-06	-2.54E-06	1.78E-05	-4.76E-06	1.95E-06	1
Capricorn	Somalia	17.227	16.24	43.92	-9.54	1	6.40E-06	1.41E-05	-3.99E-06	3.50E-05	-8.49E-06	2.79E-06	1
Capricorn	Somalia	18.281	16.08	44.33	-10.19	1	7.02E-06	1.35E-05	-4.63E-06	3.16E-05	-8.56E-06	3.35E-06	1
Capricorn	Somalia	19.048	17.38	43.37	-10.178	1	1.43E-05	2.44E-05	-9.70E-06	5.31E-05	-1.61E-05	7.03E-06	1
Capricorn	Somalia	20.131	17.29	43.29	-10.883	1	5.15E-06	1.10E-05	-3.47E-06	2.94E-05	-7.10E-06	2.56E-06	1
Capricorn	Somalia	33.738	-16.32	-132.31	18.93	0.59	8.90E-07	2.66E-06	-8.66E-07	8.79E-06	-2.80E-06	9.62E-07	2
Capricorn	Somalia	39.464	-16.76	-131.58	22.22	0.63	2.11E-06	7.20E-06	-2.05E-06	2.60E-05	-7.29E-06	2.14E-06	2
Capricorn	Somalia	41.59	-17.24	-132.14	23.12	0.93	4.95E-07	1.42E-06	-4.11E-07	4.52E-06	-1.30E-06	4.85E-07	2
Capricorn	Somalia	42.774	-17.71	-132.64	23.5	0.78	3.31E-07	1.08E-06	-3.59E-07	3.94E-06	-1.20E-06	5.34E-07	2
Capricorn	Somalia	45.346	-17.06	-133.3	24.69	0.55	2.38E-07	5.98E-07	-1.82E-07	1.82E-06	-4.83E-07	2.74E-07	2

Capricorn	Somalia	47.235	-17.03	-134.13	25.74	1.86	2.51E-07	7.17E-07	-2.26E-07	2.35E-06	-6.63E-07	3.59E-07	2
Capricorn	Somalia	49.427	-17.22	-136.65	26.87	1.4	4.87E-07	1.64E-06	-4.45E-07	5.99E-06	-1.58E-06	5.81E-07	2
Capricorn	Somalia	51.901	-15.72	-138.5	29.55	0.74	7.87E-07	2.96E-06	-7.36E-07	1.16E-05	-2.85E-06	8.46E-07	2
Capricorn	Somalia	53.808	-15.65	-141.06	31.4	0.72	1.12E-06	4.30E-06	-9.77E-07	1.72E-05	-3.81E-06	1.03E-06	2
Capricorn	Somalia	56.665	-15.71	-144.32	34.05	0.52	2.10E-06	8.13E-06	-1.53E-06	3.27E-05	-6.04E-06	1.33E-06	2
Capricorn	Somalia	58.379	-14.95	-145.15	36.37	1.35	2.80E-06	1.14E-05	-2.02E-06	4.82E-05	-8.52E-06	1.71E-06	2
Capricorn	Somalia	61.65	-13.35	-146.15	40.64	1.15	2.98E-06	1.21E-05	-1.78E-06	5.08E-05	-7.44E-06	1.32E-06	2
Capricorn	Somalia	63.104	-12.86	-146.6	42.71	0.66	7.50E-06	3.00E-05	-3.91E-06	1.22E-04	-1.59E-05	2.28E-06	2
Capricorn	Somalia	65.118	-13.72	-149.94	44.76	0.53	1.15E-06	4.89E-06	-4.85E-07	2.24E-05	-2.17E-06	3.81E-07	2
Somalia	Nubia	0	-27.395	43.277	0	1	1.00E-10	1.00E-10	1.00E-10	1.00E-10	1.00E-10	1.00E-10	
Somalia	Nubia	3.22	-44.462	2.277	0.27	1	4.45E-08	4.92E-08	1.90E-08	6.05E-08	2.65E-08	1.79E-08	3
Somalia	Nubia	10.949	-27.395	43.277	0.4	1	1.00E-10	1.00E-10	1.00E-10	1.00E-10	1.00E-10	1.00E-10	
Somalia	Nubia	20.131	-27.395	43.277	0.8	1	1.00E-10	1.00E-10	1.00E-10	1.00E-10	1.00E-10	1.00E-10	
Somalia	Nubia	25.009	-27.395	43.277	0.999	1	1.00E-10	1.00E-10	1.00E-10	1.00E-10	1.00E-10	1.00E-10	
Somalia	Nubia	85	-27.395	43.277	0.999	1	1.00E-10	1.00E-10	1.00E-10	1.00E-10	1.00E-10	1.00E-10	
N. America	Nubia	0	80.98	22.82	0	1	0.00E+00	0.00E+00	0.00E+00	0.00E+00	0.00E+00	0.00E+00	
N. America	Nubia	0.78	-77.86	207.09	-0.182	1	4.99E-11	-1.99E-11	-1.94E-11	1.21E-10	3.21E-10	1.54E-09	4
N. America	Nubia	1.77	-77.79	208.99	-0.408	1	9.23E-09	6.80E-10	1.28E-09	3.12E-09	-3.80E-10	2.22E-09	4
N. America	Nubia	2.581	-78.32	211.01	-0.601	1	4.07E-09	-1.58E-09	8.28E-10	3.28E-09	-1.57E-09	3.03E-09	4
N. America	Nubia	3.58	-78.74	237.97	-0.782	1	2.33E-08	3.45E-09	-1.14E-09	4.56E-09	-1.72E-09	2.99E-09	4
N. America	Nubia	4.18	-78.65	224.07	-0.964	1	3.77E-08	1.23E-08	-7.85E-09	9.15E-09	-4.85E-09	4.92E-09	4
N. America	Nubia	5.23	-79.29	224.81	-1.176	1	5.56E-08	1.26E-08	-7.62E-09	9.09E-09	-4.50E-09	4.43E-09	4
N. America	Nubia	5.894	-79.74	227.43	-1.343	1	3.62E-08	-6.15E-09	5.23E-09	7.15E-09	-4.93E-09	6.56E-09	4
N. America	Nubia	6.567	-79.85	228.27	-1.504	1	3.81E-08	-7.10E-09	5.85E-09	6.79E-09	-3.61E-09	7.27E-09	4
N. America	Nubia	7.432	-80.39	225.37	-1.724	1	5.56E-08	3.23E-09	-9.96E-10	8.23E-09	-2.61E-09	3.68E-09	4
N. America	Nubia	8.072	-80.48	232.45	-1.858	1	1.52E-08	-7.78E-09	4.57E-09	1.13E-08	-6.21E-09	7.68E-09	4
N. America	Nubia	9.025	-80.93	225.32	-2.172	1	3.52E-08	-2.15E-09	2.03E-09	1.19E-08	-6.86E-09	7.87E-09	4
N. America	Nubia	9.74	-79.12	259.79	-2.268	1	8.92E-08	1.14E-08	-1.25E-08	2.58E-08	-1.54E-08	1.69E-08	4
N. America	Nubia	10.949	-80.97	232.83	-2.664	1	3.20E-08	7.18E-09	-6.79E-09	2.60E-08	-1.73E-08	1.73E-08	4
N. America	Nubia	12.401	-80.69	238.24	-3.059	1	1.04E-08	-7.07E-09	4.34E-09	8.43E-09	-4.48E-09	8.81E-09	4

N. America	Nubia	13.703	-80.36	237.11	-3.415	1	2.42E-08	-1.27E-08	1.15E-08	1.34E-08	-4.10E-09	1.64E-08	4
N. America	Nubia	14.612	-79.86	241.65	-3.716	1	2.35E-08	-2.93E-10	4.72E-09	2.13E-08	-2.55E-09	1.07E-08	4
N. America	Nubia	16.014	-80.14	222.31	-4.21	1	1.86E-08	5.09E-09	-6.08E-10	2.70E-08	-1.14E-08	1.27E-08	4
N. America	Nubia	17.277	-79.9	217.71	-4.63	1	6.52E-08	-1.19E-09	9.41E-09	2.27E-08	-7.99E-09	1.34E-08	4
N. America	Nubia	18.281	-79.66	215.06	-4.916	1	2.83E-08	1.17E-08	-7.88E-09	3.23E-08	-1.41E-08	1.44E-08	4
N. America	Nubia	19.048	-79.69	217.76	-5.135	1	2.20E-08	1.14E-08	-9.21E-09	4.33E-08	-2.18E-08	2.68E-08	4
N. America	Nubia	20.131	-78.4	198.84	-5.591	1	1.45E-07	-1.17E-09	-4.92E-08	4.21E-08	2.20E-08	7.27E-08	4
N. America	Nubia	25.823	79.34	28.56	7.042	2.53	1.71E-04	-1.71E-04	1.24E-04	1.96E-04	-1.41E-04	1.04E-04	5
N. America	Nubia	33.058	75.99	5.98	9.767	1.19	8.32E-05	-8.47E-05	5.97E-05	1.03E-04	-7.14E-05	5.21E-05	5
N. America	Nubia	38.426	74.54	0.19	11.918	1.65	1.98E-04	-2.08E-04	1.43E-04	2.41E-04	-1.64E-04	1.16E-04	5
N. America	Nubia	46.264	74.23	-5.01	15.106	1.19	1.80E-04	-2.03E-04	1.36E-04	2.68E-04	-1.80E-04	1.26E-04	5
N. America	Nubia	52.364	77.34	-1.61	16.963	3.08	2.65E-04	-3.13E-04	2.07E-04	4.05E-04	-2.67E-04	1.80E-04	5
N. America	Nubia	55.904	80.64	6.57	17.895	1.26	1.19E-04	-1.36E-04	8.64E-05	1.87E-04	-1.18E-04	7.87E-05	5
N. America	Nubia	65.578	82.74	2.93	20.84	1.07	9.12E-05	-1.07E-04	6.64E-05	1.58E-04	-9.83E-05	6.45E-05	5
Eurasia	N. America	0	70.21	135.71	0	1	0.00E+00	0.00E+00	0.00E+00	0.00E+00	0.00E+00	0.00E+00	
Eurasia	N. America	0.78	-60.32	320.4	0.158	1	1.14E-09	-1.80E-10	7.50E-10	3.90E-10	0.00E+00	4.40E-09	6
Eurasia	N. America	1.77	-63.65	315.8	0.363	1	4.37E-09	2.25E-09	1.19E-09	3.87E-09	-1.89E-09	6.02E-09	6
Eurasia	N. America	2.581	-63.81	318.16	0.538	1	3.84E-09	7.00E-10	2.02E-09	2.79E-09	-3.67E-09	1.13E-08	6
Eurasia	N. America	3.58	-62.94	319.02	0.744	1	7.50E-09	2.93E-09	2.84E-09	6.66E-09	-4.47E-09	1.10E-08	6
Eurasia	N. America	4.18	-62.38	317.91	0.858	1	1.60E-08	2.25E-09	7.95E-09	3.87E-09	-2.29E-09	1.08E-08	6
Eurasia	N. America	5.23	-62.1	318.19	1.076	1	5.68E-09	2.91E-09	2.36E-09	7.03E-09	-3.38E-09	9.13E-09	6
Eurasia	N. America	5.894	-62.68	315.93	1.222	1	6.92E-09	1.53E-09	2.87E-09	5.16E-09	-5.16E-09	1.06E-08	6
Eurasia	N. America	6.567	-63.59	315.57	1.393	1	1.08E-08	3.36E-09	5.95E-09	6.58E-09	-2.90E-09	1.29E-08	6
Eurasia	N. America	7.432	-63.56	317.83	1.574	1	1.20E-08	4.18E-09	4.89E-09	6.63E-09	-4.32E-09	1.85E-08	6
Eurasia	N. America	8.072	-64.25	317.09	1.752	1	9.15E-09	1.72E-09	3.20E-09	4.50E-09	-5.93E-09	1.65E-08	6
Eurasia	N. America	9.025	-64.64	315.91	2.017	1	1.32E-08	1.63E-09	7.18E-09	5.64E-09	-3.87E-09	1.39E-08	6
Eurasia	N. America	9.74	-67.44	314.9	2.273	1	2.16E-08	4.07E-09	1.17E-08	9.29E-09	-7.07E-09	3.96E-08	6
Eurasia	N. America	10.949	-68.18	313.9	2.613	1	1.10E-08	2.92E-09	5.32E-09	9.44E-09	-1.09E-08	3.08E-08	6
Eurasia	N. America	12.401	-67.22	316.07	2.972	1	2.23E-08	8.80E-09	8.50E-09	1.32E-08	-6.09E-09	2.87E-08	6
Eurasia	N. America	13.703	-64.35	316.69	3.215	1	4.14E-08	1.35E-08	1.87E-08	1.47E-08	-7.23E-09	4.20E-08	6

Eurasia	N. America	14.612	-65.98	315.58	3.522	1	7.58E-08	2.86E-08	2.15E-08	3.56E-08	-2.40E-08	8.54E-08	6
Eurasia	N. America	16.014	-68.06	315.87	4.011	1	7.77E-08	5.20E-08	-3.54E-09	5.89E-08	-1.85E-08	3.39E-08	6
Eurasia	N. America	17.277	-68.2	314.84	4.327	1	1.17E-07	8.74E-08	8.61E-09	9.86E-08	-1.44E-08	4.19E-08	6
Eurasia	N. America	18.281	-69.05	313.69	4.623	1	9.39E-08	5.02E-08	1.06E-08	4.65E-08	-1.14E-08	4.04E-08	6
Eurasia	N. America	19.048	-70.71	311.3	4.927	1	2.07E-08	-4.63E-09	2.23E-08	2.94E-08	-4.42E-08	1.11E-07	6
Eurasia	N. America	20.131	-69.38	312.94	5.069	1	2.71E-08	7.64E-09	1.14E-08	1.37E-08	-1.16E-08	5.00E-08	6
Eurasia	N. America	33.058	68.22	131.53	-7.65	1.56	8.37E-08	1.86E-08	7.39E-08	5.78E-08	-7.52E-08	3.29E-07	7
Eurasia	N. America	39.552	67.72	133.91	-9.25	2.52	1.37E-07	1.75E-07	5.48E-08	4.41E-07	-1.00E-07	3.76E-07	7
Eurasia	N. America	47.906	65.38	138.44	-10.96	0.74	9.44E-08	2.47E-08	1.03E-07	9.24E-08	-2.67E-08	2.70E-07	7
Eurasia	N. America	49.714	64.52	138.18	-11.5	1.06	1.36E-07	1.26E-07	9.91E-08	3.24E-07	-3.32E-08	3.11E-07	7
Eurasia	N. America	53.347	63.07	144.26	-12.82	0.84	1.45E-07	9.93E-08	1.97E-07	3.44E-07	1.02E-07	4.30E-07	7
Eurasia	N. America	55.904	56.17	145.06	-13.24	0.89	5.23E-06	-2.39E-06	6.58E-06	1.27E-06	-3.02E-06	8.38E-06	7
Eurasia	N. America	68.737	54.45	147.06	-15.86	1.04	6.56E-06	-2.64E-06	7.97E-06	1.32E-06	-3.20E-06	9.78E-06	7

Table C.2: **Rotations of India with respect to Eurasia.** Covariance matrix structure is $\begin{bmatrix} a & b & c \\ b & d & e \\ c & e & f \end{bmatrix}$.

Age (Ma)	Rotation Latitude	Rotation Longitude	Rotation Angle	kappa	a	b	c	d	e	f
0.78	-27.31	-157.08	0.383	1	1.35E-06	1.66E-06	-9.50E-07	3.12E-06	-1.15E-06	8.89E-07
1.77	-25.41	-156.34	0.773	1	2.27E-06	1.91E-06	-1.63E-06	3.05E-06	-1.50E-06	1.30E-06
2.581	-25.56	-156.60	1.161	1	1.77E-06	2.23E-06	-1.13E-06	3.94E-06	-1.39E-06	9.73E-07
3.58	-26.48	-150.71	1.795	1	2.70E-06	2.71E-06	-1.73E-06	4.80E-06	-1.43E-06	1.54E-06
4.18	-24.95	-154.55	2.023	1	1.61E-06	1.68E-06	-1.02E-06	2.97E-06	-9.64E-07	9.09E-07
5.23	-20.66	-158.09	2.342	1	3.53E-06	4.23E-06	-2.49E-06	7.55E-06	-2.94E-06	2.07E-06
5.894	-26.22	-162.06	2.616	1	6.47E-06	7.87E-06	-4.48E-06	1.26E-05	-5.29E-06	3.67E-06
6.567	-23.42	-159.20	3.015	1	9.79E-06	1.13E-05	-7.39E-06	1.52E-05	-8.53E-06	5.95E-06
7.432	-22.93	-160.02	3.382	1	3.49E-06	3.71E-06	-2.63E-06	5.15E-06	-2.74E-06	2.23E-06
8.072	-21.76	-159.98	3.581	1	5.05E-06	4.99E-06	-3.94E-06	7.21E-06	-3.64E-06	3.47E-06
9.74	-18.88	-158.16	4.011	1	2.13E-05	3.35E-05	-1.33E-05	5.93E-05	-2.08E-05	8.93E-06
10.949	-22.23	-161.93	4.684	1	9.37E-06	1.15E-05	-6.21E-06	2.44E-05	-7.56E-06	4.77E-06
12.401	-22.54	-161.79	5.36	1	7.06E-06	9.58E-06	-4.53E-06	2.48E-05	-5.93E-06	3.47E-06
13.703	-24.69	-162.84	6.12	1	6.84E-06	1.26E-05	-4.26E-06	2.91E-05	-7.75E-06	3.12E-06
14.612	-25.14	-161.93	6.482	1	1.61E-05	3.16E-05	-1.00E-05	7.19E-05	-1.94E-05	7.18E-06
17.277	-24.38	-162.03	8.125	1	7.28E-06	1.49E-05	-4.03E-06	3.54E-05	-8.17E-06	2.74E-06

19.048	-24.79	-162.73	8.603	1	1.67E-05	2.68E-05	-1.01E-05	5.56E-05	-1.59E-05	7.00E-06
20.131	-24.96	-163.27	9.75	1	9.48E-06	1.63E-05	-5.52E-06	3.81E-05	-8.24E-06	4.55E-06
25.823	-24.61	-155.03	13.012	1	1.12E-04	-6.71E-05	3.61E-05	8.39E-05	-3.64E-05	2.05E-05
33.058	-23.94	-153.02	18.441	1	1.30E-04	-7.35E-05	2.83E-05	8.76E-05	-3.01E-05	1.45E-05
39.464	-23.54	-152.19	23.296	1	1.90E-04	-9.21E-05	2.34E-05	1.23E-04	-3.22E-05	1.21E-05
41.59	-24.05	-153.05	24.792	1	1.42E-04	-7.57E-05	1.74E-05	6.96E-05	-1.64E-05	7.14E-06
42.774	-24.53	-153.79	25.557	1	1.53E-04	-8.25E-05	1.84E-05	7.51E-05	-1.76E-05	7.63E-06
45.346	-23.93	-154.58	27.407	1	2.68E-04	-1.51E-04	2.86E-05	1.22E-04	-2.49E-05	9.76E-06
47.235	-23.88	-155.02	28.872	1	2.48E-04	-1.38E-04	2.21E-05	1.08E-04	-1.94E-05	7.83E-06
49.427	-23.79	-156.94	30.527	1	1.38E-04	-7.01E-05	8.74E-06	6.32E-05	-1.01E-05	4.76E-06
51.901	-21.45	-157.08	33.729	1	1.82E-04	-8.90E-05	2.71E-06	8.48E-05	-9.18E-06	4.55E-06
53.808	-21.05	-158.47	36.233	1	1.16E-04	-4.82E-05	-2.54E-06	6.94E-05	-7.48E-06	4.74E-06
56.665	-21.38	-161.36	40.241	1	2.14E-04	-8.34E-05	-6.70E-06	1.37E-04	-1.29E-05	9.17E-06
58.379	-20.46	-161.50	42.791	1	1.55E-04	-6.12E-05	-9.81E-06	9.12E-05	-4.92E-06	6.91E-06
61.65	-18.64	-161.53	47.414	1	1.28E-04	-4.31E-05	-1.69E-05	9.00E-05	-1.34E-06	7.11E-06

Table C.3: **India-Eurasia convergence and rotation data.** Area convergence here includes rotation uncertainties, diachroneity, and uncertainty in suture zone length and therefore differs from what would be derived from the integrated area represented by the end points listed in columns 2 and 5. Note: Et = 10^{18} tons = 10^9 Gt.

Age (Ma)	W. Suture	W. Suture	E. Suture	E. Suture	Effective Suture Length (km)	Cummulative Converged Area (km ²)	Converged Mass (Et)	W. Suture Convergence (km)	Mean Convergence (km)	E. Suture Convergence (km)
	Long. & Paleo-Long. Rel. to Eurasia (°E)	Lat. & Paleo-Lat. Rel. to Eurasia (°N)	Long. & Paleo-Long. Rel. to Eurasia (°E)	Lat. & Paleo-Lat. Rel. to Eurasia (°N)						
0.78	69.98	33.75	96.37	27.17	2617.8	87783.0	9.34	27.8	35.1	38.4
1.77	69.99	33.50	96.28	26.83	2606.3	176545.9	18.78	56.2	70.9	77.4
2.581	69.98	33.24	96.16	26.50	2607.9	265898.1	28.29	84.6	106.7	116.4
3.58	70.01	32.95	96.02	26.02	2600.0	379435.1	40.37	116.5	153.8	171.3
4.18	70.01	32.71	95.95	25.77	2598.3	452311.8	48.13	143.1	182.4	200.2
5.23	70.13	32.37	95.97	25.39	2572.2	550803.0	58.61	181.9	222.6	240.5
5.894	69.79	32.15	95.58	25.20	2620.1	634749.4	67.54	206.5	252.4	271.2
6.567	69.97	31.91	95.65	24.82	2600.1	715049.0	76.08	232.9	286.5	309.5
7.432	69.97	31.61	95.55	24.48	2598.9	810065.7	86.19	265.4	324.3	349.3
8.072	70.05	31.45	95.56	24.27	2589.8	859123.2	91.41	283.4	344.7	370.9
9.74	70.32	31.17	95.70	23.85	2553.1	945543.5	100.61	316.6	384.2	414.1
10.949	69.92	30.59	95.16	23.26	2599.5	1146099.1	121.94	379.5	457.6	489.9
12.401	69.87	30.11	94.95	22.67	2601.3	1308905.2	139.27	432.5	522.4	559.8
13.703	69.54	29.58	94.46	22.06	2615.4	1502701.0	159.89	493.3	597.2	639.4
14.612	69.49	29.40	94.33	21.78	2615.9	1575577.9	167.64	514.3	626.8	673.2
17.277	69.41	28.19	93.87	20.28	2612.5	1980828.7	210.76	649.0	788.4	845.8
19.048	69.25	27.81	93.61	19.87	2615.7	2109717.7	224.47	691.9	838.4	898.1
20.131	69.03	26.95	93.16	18.85	2617.2	2402183.8	255.59	788.9	953.7	1020.3
25.823	69.40	25.66	92.73	16.41	2597.0	2929413.2	311.69	929.7	1180.2	1293.2
33.058	69.18	22.53	91.35	11.98	2584.4	4048126.7	430.72	1277.5	1639.2	1807.1

39.464	68.77	19.72	89.97	8.05	2577.0	5058875.3	538.26	1593.1	2052.8	2268.9
41.59	68.18	18.68	89.15	6.81	2585.6	5443753.6	579.22	1713.1	2200.8	2427.3
42.774	67.72	18.11	88.60	6.18	2592.5	5662498.6	602.49	1781.3	2282.7	2513.0
45.346	67.46	16.65	88.06	4.44	2589.8	6142590.2	653.57	1945.9	2474.3	2715.8
47.235	67.09	15.61	87.47	3.17	2590.9	6508769.4	692.53	2065.4	2618.7	2870.6
49.427	66.38	13.99	86.63	1.49	2596.2	7047894.4	749.90	2254.9	2824.3	3077.7
51.901	66.77	11.32	86.53	-1.77	2575.7	7830715.6	833.19	2543.6	3152.1	3425.5
53.808	66.05	9.11	85.60	-4.22	2577.7	8555603.9	910.32	2797.1	3434.8	3716.5
56.665	64.05	5.54	83.42	-8.03	2591.5	9803334.0	1043.07	3224.2	3905.7	4194.3
58.379	63.80	3.47	82.91	-10.50	2584.3	10452164.9	1112.11	3454.6	4169.3	4472.3

APPENDIX D
ADDITIONAL TABLES

Figure D.1 Petrography of Penbo basin carbonates.

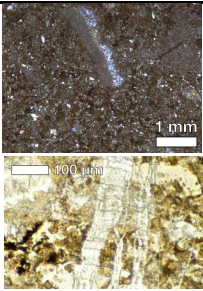
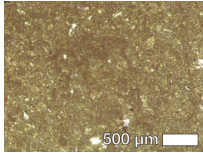
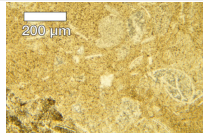
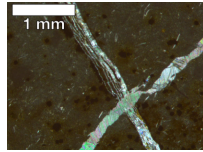
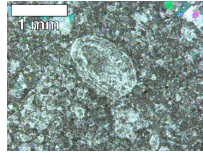
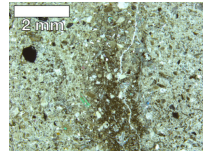
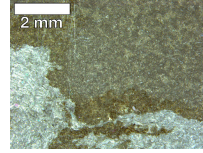
Sample	Petrographic Image	Textural Description	Petrographic Interpretation	T(Δ_{47}) (°C)
446D		Abundant sparry calcite filling voids and veins; silicification	Diagenetic/High T	49.9 ± 2.9
DL104-3b		Micro-spar and small amount of dense micrite; recrystallized ostracodes; minor vuggy calcite spar	Primary/Low T	8.5 ± 5.0
P0929-c		Micro-spar with patchy dense micrite; sparry vuggy calcite; some silicification	Primary/Low T	11.9 ± 5.6
448D		Dense micrite to micro-spar; ostracodes; vein calcite and pyrite	Diagenetic/High T	40.9 ± 2.4
440D		Micro-spar/sparry calcite; silicification; ostracode fossils	Minor Alteration	55.2 ± 1.5
440C		Sparry calcite; calcite veins; silicification	Diagenetic/High T	---
446H		Coarse micro-spar/sparry calcite; fibrous calcite	Diagenetic/High T	---

Figure D.2 Petrography of Oiyug basin carbonates.

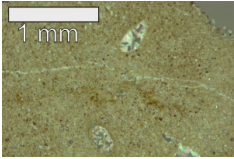
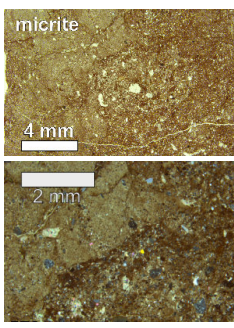
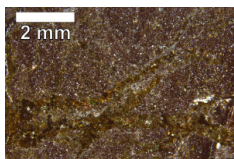
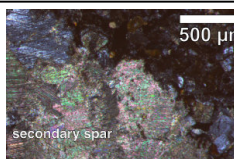
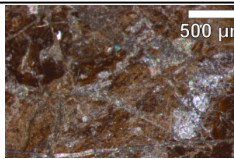
Sample	Petrographic Image	Textural Description	Petrographic Interpretation	T(Δ_{47}) (°C)
554B		Matrix-supported limestone Very fine grain micritic matrix Numerous microfossils <1mm	Primary/Low T	3.9 ± 3.4
555		Red-brown matrix with gray, micritic, cm-sized regions (labeled) No visible recrystallization or iron rims between calcite and oxidized siliciclastics	Primary/Low T	19.7 ± 4.2
579		Fissures traverse the slide from left to right (likely micron-scale veins) Abundant ~1mm rounded quartz crystals (sand clasts) Mud matrix Hematite rim on micritic region?	Minor alteration	9.8 ± 4.3
6211		Slightly recrystallized sparry calcite matrix mixed with micrite Finely laminated	Primary/Low T	15.0 ± 3.5
W0628-1		Clast-supported and loosely lithified Birefringent vein with an iron-stained rim of a different texture	Primary/Low T	0.7 ± 2.3
W0628-2		Clast-supported Extensive crosscutting of veins Pervasive infill of sparry calcite in fissures	Diagenetic/High T	45.7 ± 8.3
W0628-3		Matrix appears to have been micritic but has been extensively cross-cut by sparry veins	Diagenetic/High T	5.3 ± 8.2

Table D.1: **Stable isotope data for all carbonates and calculated paleo-elevations of the Penbo Basin.** Calcite-water fractionation factors are calculated using the average primary $T(\Delta_{47}) \pm 5^\circ\text{C}$. Samples are organized by carbonate type (ped. = paleosol carbonate nodule, g.w. = groundwater carbonate nodule, lake = lacustrine limestone) and approximate location in stratigraphic section by correlating laterally extensive units between measured sections. Error estimates for mean elevations are reported as the quadrature of the model error for each elevation estimate.

<div style="display: flex; justify-content: space-between;"> <div style="width: 30%;"> <p><i>Lacustrine Carbonate</i></p> <p>$T(\Delta_{47})^\circ\text{C}$ ($\pm 5^\circ\text{C}$):</p> <p>$\alpha_{\text{calcite-H}_2\text{O}}$: 1.03170 1.03057 1.03288</p> </div> <div style="width: 30%;"> <p>10.2°C 15.2°C 5.2°C</p> </div> <div style="width: 30%;"> <p><i>Pedogenic Carbonate</i></p> <p>$T(\Delta_{47})^\circ\text{C}$ ($\pm 5^\circ\text{C}$):</p> <p>$\alpha_{\text{calcite-H}_2\text{O}}$: 1.03262 1.03219 1.03305</p> </div> <div style="width: 30%;"> <p>6.3°C 8.1°C 4.5°C</p> </div> </div>										
Sample	Carbonate Type	Location in Section (m)	$\delta^{13}\text{C}$ ‰ $VPDB$	$\delta^{18}\text{O}_c$ ‰ $VPDB$	$\delta^{18}\text{O}_w$ ‰ $VSMOW$	mean $\delta^{18}\text{O}_w$ $\pm 2.2\%$	$\Delta\delta^{18}\text{O}_w$ ‰	Model Elevation (km, $\pm 2\pm$)		
<u>Pana Fm.</u>										
483C	lake	300	-7.6	-13.9	-14.7	-13.6	-15.8	-14.7 ± 2.2	-10.1	$3.9^{+1.1}_{-1.3}$
484A	lake	300	-7.2	-14.0	-14.9	-13.8	-16.0	-14.9 ± 2.2	-10.3	$4.0^{+1.1}_{-1.3}$
483D	lake	300	-6.3	-14.3	-15.2	-14.1	-16.3	-15.2 ± 2.2	-10.6	$4.0^{+1.2}_{-1.3}$
483B	lake	300	-7.5	-14.7	-15.5	-14.4	-16.6	-15.5 ± 2.2	-10.9	$4.5^{+1.3}_{-1.6}$
483A	lake	300	-7.3	-14.8	-15.6	-14.5	-16.7	-15.6 ± 2.2	-11.0	$4.5^{+1.3}_{-1.7}$
491B	g.w.	300	-6.6	-13.1	-14.8	-14.4	-15.2	-14.8 ± 0.8	-8.2	$3.9^{+1.0}_{-1.5}$
491C	g.w.	300	-5.8	-11.7	-13.4	-13.0	-13.8	-13.4 ± 0.8	-6.8	$3.4^{+0.8}_{-1.3}$
490A	ped.	300	-7.6	-14.1	-15.8	-15.4	-16.2	-15.8 ± 0.8	-9.2	$4.1^{+1.1}_{-1.6}$
490B	ped.	300	-7.2	-13.6	-15.2	-14.8	-15.7	-15.2 ± 0.8	-8.6	$4.0^{+1.1}_{-1.5}$
491A	ped.	300	-6.1	-11.7	-13.4	-13.0	-13.8	-13.4 ± 0.8	-6.8	$3.4^{+0.8}_{-1.3}$
475B	lake	275	-3.2	-13.7	-14.5	-13.5	-15.7	-14.6 ± 2.2	-10.0	$4.3^{+1.3}_{-1.5}$
475C	lake	275	-3.8	-14.4	-15.2	-14.2	-16.4	-15.3 ± 2.2	-10.7	$4.5^{+1.3}_{-1.6}$
475D	lake	275	-4.5	-15.4	-16.2	-15.1	-17.3	-16.2 ± 2.2	-11.6	$4.7^{+1.4}_{-1.7}$
475A	lake	275	-4.1	-16.1	-16.9	-15.8	-18.0	-16.9 ± 2.2	-12.3	$4.8^{+1.4}_{-1.8}$

											Mean	4.1 ^{+1.2} _{-1.6} km
<u>Nianbo Fm</u>												
446C	lake	236	-2.7	-16.7	-17.5	-16.5	-18.7	-17.6 ± 2.2	-13.0	4.9 ^{+1.4} _{-1.8}		
446H	lake	235	-2.2	-17.9	-18.7	-17.7	-19.9	-18.7 ± 2.2	-14.1	5.1 ^{+1.4} _{-1.9}		
446D	ped.	234	-4.6	-17.3	-18.9	-18.5	-19.4	-18.9 ± 0.8	-12.3	4.8 ^{+1.3} _{-1.9}		
446F	lake	232	-3.5	-16.1	-16.9	-15.8	-18.0	-16.9 ± 2.2	-12.3	4.8 ^{+1.4} _{-1.8}		
446E	lake	232	-3.2	-17.3	-18.1	-17.0	-19.2	-18.1 ± 2.2	-13.5	5.0 ^{+1.4} _{-1.9}		
447A	ped.	222	-3.8	-19.0	-20.7	-20.3	-21.1	-20.7 ± 0.8	-14.1	5.1 ^{+1.4} _{-2.0}		
448C	lake	215	-3.8	-12.7	-13.5	-12.4	-14.6	-13.5 ± 2.2	-8.9	4.0 ^{+1.2} _{-1.4}		
448A	lake	215	-3.9	-12.0	-12.8	-11.7	-13.9	-12.8 ± 2.2	-8.2	3.9 ^{+1.1} _{-1.3}		
448E	lake	214	-4.8	-11.4	-12.2	-11.1	-13.3	-12.2 ± 2.2	-7.6	3.7 ^{+1.1} _{-1.2}		
448D	lake	214	-4.0	-12.0	-12.8	-11.7	-13.9	-12.8 ± 2.2	-8.2	3.9 ^{+1.1} _{-1.3}		
448	lake	214	-3.5	-15.3	-16.2	-15.1	-17.3	-16.2 ± 2.2	-11.6	4.7 ^{+1.4} _{-1.7}		
P0929-c	lake	208	-3.3	-12.7	-13.1	-11.9	-14.4	-13.1 ± 2.5	-8.6	4.0^{+1.2}_{-1.3}		
DL104-3b	lake	200	-2.5	-12.4	-13.6	-12.5	-14.7	-13.6 ± 2.2	-9.0	4.1^{+1.2}_{-1.4}		
451B	ped.	188	-2.7	-15.3	-17.0	-16.6	-17.4	-17.0 ± 0.8	-10.4	4.4 ^{+1.2} _{-1.7}		
452A	lake	186	-4.0	-10.9	-11.7	-10.7	-12.9	-11.8 ± 2.2	-7.2	3.5 ^{+1.0} _{-1.1}		
452B	lake	183	-3.7	-12.3	-13.1	-12.0	-14.3	-13.1 ± 2.2	-8.6	4.0 ^{+1.2} _{-1.3}		
452D	lake	183	-3.5	-15.0	-15.8	-14.8	-17.0	-15.9 ± 2.2	-11.3	4.6 ^{+1.4} _{-1.7}		
452C	ped.	181	-3.2	-14.8	-16.4	-16.0	-16.8	-16.4 ± 0.8	-9.8	4.3 ^{+1.2} _{-1.7}		
452G1	lake	180	-3.5	-11.8	-13.5	-13.1	-13.9	-13.5 ± 0.4	-6.9	3.5 ^{+0.9} _{-1.3}		
452G3	g.w.	180	-4.2	-16.0	-17.7	-17.2	-18.1	-17.7 ± 0.4	-11.1	4.6 ^{+1.3} _{-1.8}		
452E	g.w.	179	-3.9	-13.8	-15.5	-15.0	-15.9	-15.5 ± 0.4	-8.9	4.0 ^{+1.1} _{-1.6}		
514	lake	170	-2.1	-15.1	-15.9	-14.8	-17.0	-15.9 ± 2.2	-11.3	4.6 ^{+1.4} _{-1.7}		
514A	lake	170	-2.0	-15.2	-16.0	-14.9	-17.1	-16.0 ± 2.2	-11.4	4.6 ^{+1.4} _{-1.7}		
511	lake	170	-0.1	-21.8	-22.6	-21.5	-23.7	-22.6 ± 2.2	-18.0	5.7 ^{+1.5} _{-2.1}		
440D	lake	164	-4.5	-16.3	-17.1	-16.0	-18.3	-17.1 ± 2.2	-12.5	4.9 ^{+1.4} _{-1.8}		
440B	ped.	162	-3.8	-17.2	-18.9	-18.5	-19.3	-18.9 ± 0.8	-12.3	4.8^{+1.3}_{-1.9}		
505	lake	150	-0.2	-17.3	-18.1	-17.0	-19.2	-18.1 ± 2.2	-13.5	5.0 ^{+1.4} _{-1.9}		
508	lake	140	-3.8	-12.3	-13.1	-12.0	-14.2	-13.1 ± 2.2	-8.5	3.9 ^{+1.2} _{-1.3}		

439E	ped.	129	-4.6	-15.8	-17.5	-17.1	-17.9	-17.5 ± 0.8	-10.9	4.5	$^{+1.2}_{-1.8}$	
439D	g.w.	127	-4.3	-16.3	-18.0	-17.6	-18.4	-18.0 ± 0.8	-11.4	4.6	$^{+1.3}_{-1.8}$	
456	lake	122	-3.7	-15.5	-16.3	-15.2	-17.4	-16.3 ± 2.2	-11.7	4.7	$^{+1.4}_{-1.7}$	
504A	lake	120	-0.7	-17.8	-18.6	-17.5	-19.7	-18.6 ± 2.2	-14.0	5.1	$^{+1.4}_{-1.9}$	
439	g.w.	120	-5.2	-15.6	-17.3	-16.9	-17.7	-17.3 ± 0.8	-10.7	4.5	$^{+1.2}_{-1.8}$	
439C	ped.	120	-5.4	-15.5	-17.2	-16.8	-17.6	-17.2 ± 0.8	-10.6	4.5	$^{+1.2}_{-1.8}$	
523	ped.	105	-3.4	-16.3	-17.9	-17.5	-18.4	-18.0 ± 0.8	-11.4	4.6	$^{+1.3}_{-1.8}$	
512	ped.	100	-3.5	-15.1	-16.8	-16.3	-17.2	-16.8 ± 0.8	-9.6	4.2	$^{+1.2}_{-1.4}$	
534A	ped.	100	-5.8	-14.5	-16.1	-15.7	-16.6	-16.1 ± 0.8	-9.5	4.2	$^{+1.1}_{-1.7}$	
534C	ped.	100	-5.3	-15.4	-17.1	-16.7	-17.5	-17.1 ± 0.8	-10.5	4.4	$^{+1.2}_{-1.7}$	
534D	ped.	100	-6.7	-12.8	-14.5	-14.1	-14.9	-14.5 ± 0.8	-7.9	3.8	$^{+1.0}_{-1.5}$	
534F	ped.	100	-3.3	-14.3	-16.0	-15.6	-16.4	-16.0 ± 0.8	-9.4	4.2	$^{+1.1}_{-1.6}$	
534G	ped.	100	-2.8	-16.3	-17.9	-17.5	-18.3	-17.9 ± 0.8	-11.3	4.6	$^{+1.1}_{-1.6}$	
534I	ped.	100	-4.5	-13.8	-15.5	-15.1	-15.9	-15.5 ± 0.8	-8.9	4.1	$^{+1.1}_{-1.6}$	
534J	ped.	100	-6.1	-14.2	-15.9	-15.5	-16.3	-15.9 ± 0.8	-9.3	4.1	$^{+1.1}_{-1.6}$	
534K	ped.	100	-5.5	-12.8	-14.5	-14.1	-14.9	-14.5 ± 0.8	-7.9	3.8	$^{+1.0}_{-1.5}$	
534L	ped.	100	-3.5	-16.7	-18.3	-17.9	-18.7	-18.3 ± 0.8	-11.7	4.7	$^{+1.3}_{-1.8}$	
418B	ped.	50	-7.0	-16.2	-17.9	-17.5	-18.3	-17.9 ± 0.8	-11.3	4.6	$^{+1.3}_{-1.8}$	
418A	ped.	49	-7.1	-16.1	-17.8	-17.4	-18.2	-17.8 ± 0.8	-11.2	4.6	$^{+1.3}_{-1.8}$	
431L	g.w.	48	-8.5	-15.6	-17.2	-16.8	-17.6	-17.2 ± 0.8	-10.6	4.5	$^{+1.2}_{-1.8}$	
417D		47	-10.4	-14.9	-16.6	-16.1	-17.0	-16.6 ± 0.8	-10.0	4.3	$^{+1.2}_{-1.7}$	
431K	g.w.	42	-8.9	-15.2	-16.9	-16.5	-17.3	-16.9 ± 0.8	-10.3	4.4	$^{+1.2}_{-1.7}$	
431I	ped.	41	-8.7	-15.9	-17.6	-17.2	-18.0	-17.6 ± 0.8	-11.0	4.5	$^{+1.3}_{-1.8}$	
431H	lake	40	-8.8	-16.0	-16.8	-15.8	-18.0	-16.9 ± 2.2	-12.3	4.8	$^{+1.4}_{-1.8}$	
431G	ped.	40	-7.2	-15.7	-17.4	-17.0	-17.8	-17.4 ± 0.8	-10.8	4.5	$^{+1.4}_{-1.8}$	
417C	ped.	39	-10.4	-12.6	-14.3	-13.9	-14.7	-14.3 ± 0.8	-7.7	3.7	$^{+1.0}_{-1.4}$	
431F	ped.	29	-6.6	-16.0	-17.6	-17.2	-18.1	-17.7 ± 0.8	-11.1	4.6	$^{+1.3}_{-1.8}$	
										Mean	4.4	$^{+1.3}_{-1.7}$ km

Table D.2 **Stable isotope data for all carbonates and calculated paleo-elevations of the Oiyug Basin.** Carbonate-water fractionation factors are calculated using the average primary $T(\Delta_{47})$ for each formation and/or carbonate lithology. $\delta^{18}\text{O}_c$ of all samples except the Nianbo Fm have been previously published in Currie et al. (2005) and Currie et al. (2016). All $\delta^{18}\text{O}_w$ values are calculated using new $T(\Delta_{47})$ measurements. Carbonate oxygen isotopic compositions are reported on the VPDB scale and water oxygen isotopic compositions are reported on the VSMOW scale. Carbonate-water oxygen fractionation factors are reported in the main text. Low elevation $\delta^{18}\text{O}_w$ values: -6.6‰ for Rigongla and Gazhacun Fms; -4.6‰ for Oiyug Fm, based on WMMTs derived from (Khan et al., 2014) and Siwalik Fm paleosol carbonate data (Quade and Cerling, 1995; Quade et al., 2013). Samples are organized by carbonate type, formation, and approximate location in stratigraphic section by correlating laterally extensive units between measured sections. Error estimates for mean elevations are reported as the quadrature of the model error for each elevation estimate and 2σ analytical uncertainty.

Sample	Carbonate Type	Location in Section (m)	$\delta^{13}\text{C}$	$\delta^{18}\text{O}_c$	Mean $\delta^{18}\text{O}_w \pm 2\sigma$	$\Delta\delta^{18}\text{O}_w$	Model Elev. (km) $\pm 2\sigma$
<i>Oiyug Formation</i>							
621I	calcite marl	1580	1.3	-28.0	-30.1 ± 1.5	-25.5	6.5 +1.8/-2.3
621H	calcite marl	1584	-0.1	-27.4	-29.9 ± 1.6	-25.3	6.5 +1.8/-2.3
621F	siderite nodule	1575	12.9	-10.8	-13.2 ± 1.5	-8.6	3.6 +1.1/-1.4
Mean Elevation (km)							6.5 +1.8/-2.3
<i>Upper Gazhacun Fm.</i>							
618A	siderite nodule	690	4.2	-17.1	-18.3	-11.7	4.4 +1.3/-1.8
<i>Middle Gazhacun Formation</i>							
555	pedogenic calcite	670	-5.8	-20.0	-21.7 ± 1.8	-15.1	5.1 +1.5/-2.0
W8	dolomite nodule	680	-7.3	-7.6	-10.6 ± 1.6	-4.0	2.1 +0.6/-0.6
553	calcareous shale	677	-3.8	-13.0	-11.8 ± 1.6	-5.2	3.0 +0.9/-1.1
W7	dolomite nodule	670	-5.4	-5.5	-8.5 ± 1.7	-1.9	1.1 +0.3/-0.1
W3	dolomite nodule	654	-6.3	-5.7	-8.7 ± 1.6	-2.1	1.2 +0.4/-0.1
W2	dolomite nodule	649	-5.1	-5.5	-8.5 ± 1.7	-1.9	1.1 +0.3/-0.1
551	calcareous mudstone	647	-2.5	-11.6	-11.6 ± 1.6	-5.0	2.5 +0.7/-0.8
W1	dolomite nodule	645	-5.4	-5.8	-8.8 ± 1.6	-2.2	1.3 +0.3/-0.2
550	dolomite nodule	615	-11.3	-11.3	-14.3 ± 1.6	-7.7	3.4 +1.0/-1.3
554B	pedogenic calcite	570	-7.8	-19.7	-25.0 ± 1.7	-18.4	5.6 +1.5/-2.1
Pedogenic-derived Mean Elevation (km)							5.3 +1.5/-2.0
Lacustrine-derived Mean Elevation (km)							2.0 +0.6/-0.7
<i>Lower Gazhacun Fm.</i>							
548	pedogenic calcite	559	-8.0	-20.1	-21.5 ± 1.5	-14.9	5.0 +1.4/-2.0
165Ca	pedogenic calcite	556	-6.9	-19.8	-18.8 ± 3.4	-12.2	4.5 +1.4/-1.7
165D	pedogenic calcite	556	-7.1	-20.0	-19.0 ± 3.4	-12.4	4.5 +1.4/-1.7
165Fa	pedogenic calcite	556	-6.9	-19.7	-18.7 ± 3.4	-15.0	5.0 +1.5/-1.9
165Fb	pedogenic calcite	556	-6.8	-19.7	-18.7 ± 3.4	-15.0	5.0 +1.5/-1.9
165Fc	pedogenic calcite	556	-5.9	-18.0	-17.0 ± 3.4	-13.3	4.7 +1.5/-1.8
165G	pedogenic calcite	556	-6.8	-19.6	-18.6 ± 3.4	-14.9	5.0 +1.5/-1.9
R2	pedogenic calcite	555	-7.0	-20.2	-19.2 ± 3.4	-15.5	5.1 +1.5/-1.9
547	pedogenic calcite	540	-6.0	-19.1	-18.1 ± 3.4	-14.4	4.9 +1.5/-1.8
546	pedogenic calcite	532	-6.4	-21.1	-20.0 ± 3.4	-16.4	5.3 +1.5/-2.0
543B	groundwater calcite	452	-3.3	-19.5	-18.5 ± 3.4	-11.9	4.4 +1.4/-1.6
543A	pedogenic calcite	450	-7.6	-19.4	-16.2 ± 1.0	-9.6	3.9 +1.2/-1.6
Mean Elevation (km)							4.5 +1.5/-1.7
<i>Rigongla Fm.</i>							
579	pedogenic calcite	410	-6.2	-18.9	-19.8	-13.2	4.7 +1.4/-1.9
576	groundwater calcite	290	-3.4	-20.4	-21.3	-14.7	5.0 +1.4/-2.0
575E	groundwater calcite	285	-3.7	-11.9	-12.8	-6.2	2.9 +0.9/-1.0
575C	groundwater calcite	280	-2.6	-16.8	-17.7	-11.1	4.3 +1.3/-1.7
575B	groundwater calcite	278	-3.8	-13.9	-14.8	-8.2	3.6 +1.1/-1.3
Mean Elevation (km)							4.1 +1.3/-1.6
<i>Nianbo Fm.</i>							
W0628-3	paleosol	44	-1.5	-24.9	-26.8 ± 3.7	-20.2	5.9 +1.5/-2.1
W0628-2	lacustrine limestone	34	-4.1	-24.6	-27.0 ± 3.8	-20.4	5.9 +1.5/-2.1
W0628-1	paleosol	0	-3.5	-18.6	-21.6 ± 1.1	-15.0	5.0 +1.4/-2.0
Mean Elevation (km)							5.6 +1.5/-2.1

Table D.3 Stable isotope data for the subset of samples with Δ_{47} measurements from Oiyug and Penbo localities. $\delta^{18}\text{O}$ and $\delta^{13}\text{C}$ values were measured both on the gas bench ([a]) CO_2 in tube headspace from CO_3 dissolution in $\sim 103\%$ phosphoric acid) and MAT253 ([b]) CO_2 released from CO_3 by $>105\%$ phosphoric acid dissolution and passed through a series of water traps and a Haysep-Q chromatographic column to remove contaminants). The measured oxygen isotopic composition of the carbonate and measured $T(\Delta_{47})$ are used to calculate the oxygen isotopic value of water in equilibrium with the carbonate [c]. As some samples are interpreted as “secondary” calcite, these water values are different than those used in the elevation calculations. The Zaarur et al. (2013) thermometer [d] was applied to Δ_{47} (CDES [c], Dennis et al. (2011)) measurements.

Sample & Lithology	Weight %- CO_3^2-	$\delta^{18}\text{O}_{\text{CCO}_3}$ vPDB^a	$\delta^{13}\text{C}$ vPDB^a	$\delta^{18}\text{O}_{\text{CCO}_2}$ vSMOW^b	$\delta_{47, \text{SG-WG}}^b$	$\Delta_{47, \text{CDES}} \text{‰}_{b,c}$	$T(\Delta_{47})$ $(^\circ\text{C})^d$	$\delta^{18}\text{O}_w$ vSMOW^e	n	Formation
OIYUG BASIN										
<i>Nodular & Groundwater Calcite</i>										
621H	36	-27.4	-0.1 \pm 0.0	12.4 \pm 0.1	-9.4 \pm 0.1	0.698 \pm 0.016	13.0 \pm 3.7	-27.6 \pm 1.6	11	Oiyug
W0628-1	90	-18.6	-3.3 \pm 0.0	22.1 \pm 0.1	-2.7 \pm 0.1	0.755 \pm 0.011	0.7 \pm 2.3	-21.6 \pm 1.1	6	Nianbo
<i>Lacustrine/Marl Calcite</i>										
621I	37	-28.0	1.3 \pm 0.0	12.1 \pm 0.0	-8.4 \pm 0.0	0.689 \pm 0.015	15.0 \pm 3.5	-30.1 \pm 1.5	12	Oiyug
W0628-2	11	-24.6	-3.3 \pm 0.1	17.3 \pm 0.3	-7.6 \pm 0.2	0.572 \pm 0.027	45.7 \pm 8.3	-18.5 \pm 2.9	3	Nianbo
<i>Pedogenic Calcite</i>										
555	21	-20.0	-5.8 \pm 0.0	19.8 \pm 0.1	-7.6 \pm 0.1	0.668 \pm 0.017	19.7 \pm 4.2	-21.7 \pm 1.8	7	Middle Gazhacum
554B	51	-19.7	-7.9 \pm 0.0	20.0 \pm 0.1	-9.2 \pm 0.1	0.739 \pm 0.017	3.9 \pm 3.4	-25.0 \pm 1.7	4	Middle Gazhacum
548	29	-20.1	-8.4 \pm 0.0	19.6 \pm 0.0	-10.1 \pm 0.1	0.721 \pm 0.020	7.6 \pm 3.3	-21.5 \pm 1.5	5	Lower Gazhacum
543A	55	-19.4	-7.7 \pm 0.0	21.2 \pm 0.0	-8.0 \pm 0.0	0.625 \pm 0.010	30.1 \pm 2.6	-16.2 \pm 1.0	4	Lower Gazhacum
579	18	-18.9	-5.8 \pm 0.2	20.9 \pm 0.1	-7.0 \pm 0.3	0.711 \pm 0.020	9.8 \pm 4.3	-19.8 \pm 1.9	6	Upper Rigongla
W0628-3	6	-24.9	-1.2 \pm 0.1	14.6 \pm 0.3	-8.1 \pm 0.2	0.738 \pm 0.040	5.3 \pm 8.2	-26.8 \pm 3.7	3	Nianbo
<i>Verm Calcite</i>										
543Av	N.D.	-27.1	-2.7 \pm 0.0	14.6 \pm 0.0	-9.9 \pm 0.0	0.467 \pm 0.014	83.3 \pm 6.0	-15.1 \pm 1.7	2	Lower Gazhacum
PENBO BASIN										
<i>Lacustrine/Marl Calcite</i>										
504A	54	-17.8	-0.7 \pm 0.1	23.1 \pm 0.4	0.5 \pm 0.4	0.549 \pm 0.003	52.4 \pm 1.2	-10.5 \pm 0.4	3	Nianbo
448D	42	-12.0	-4.1 \pm 0.1	29.2 \pm 0.3	3.4 \pm 0.3	0.586 \pm 0.007	40.9 \pm 2.4	-6.7 \pm 0.9	2	Nianbo
P0929-c	29	-12.7	-3.3 \pm 0.1	28.1 \pm 0.0	3.1 \pm 0.0	0.701 \pm 0.023	11.9 \pm 5.6	-13.1 \pm 2.5	2	Nianbo
DL104-3b	34	-12.4	-2.4 \pm 0.1	28.4 \pm 0.2	4.4 \pm 0.3	0.717 \pm 0.022	8.5 \pm 5.0	-13.6 \pm 2.2	3	Nianbo
440D	N.D.	-16.3	-3.7 \pm 0.1	24.9 \pm 0.1	-0.6 \pm 0.1	0.540 \pm 0.006	55.2 \pm 1.5	-8.5 \pm 0.5	2	Nianbo
<i>Pedogenic Calcite</i>										
446D	54	-17.3	-3.0 \pm 0.1	23.5 \pm 0.1	-1.2 \pm 0.1	0.557 \pm 0.008	49.9 \pm 2.9	-10.4 \pm 1.0	3	Nianbo
440B	8	-17.2	-4.2 \pm 0.1	23.7 \pm 0.1	2.1 \pm 0.1	0.726 \pm 0.008	6.3 \pm 1.8	-18.9 \pm 0.8	2	Nianbo

Table D.4 **Carbon, oxygen, and hydrogen stable isotope values, and calculated paleo-elevations of the Lunpola basin.** Lunpola basin carbon and oxygen data were originally published in Rowley and Currie (2006) and deuterium data in Polissar et al. (2009). Carbonate oxygen and carbon isotope values are in permill VPDB. Hydrogen and oxygen isotopes of paleo-precipitation are reported in permill VSMOW. Samples with Δ_{47} measurements are bolded.

Sample	Lithology	δD_p	$\delta^{13}C$	$\delta^{18}O_c$	Mean $\delta^{18}O_w$	$\Delta\delta^{18}O_p$	Model Elevation (m) $\pm 2 \sigma$
<i>Dingqing Formation</i>							
292A	Mudstone		0.3	-5.2	-7.0	-0.4	281 +29/-123
292C	Mudstone		-0.7	-4.3	-6.2	0.4	-277 -22/+120
292D	Calcareous Sandstone		-0.5	-7.2	-9.1	-2.5	1394 +212/-621
301	Marl	-128	0.5	-8.9	-10.8	-4.2	2173 +415/-977
300B	Marl		-4.2	-7.2	-9.1	-2.5	1414 +217/-631
300A	Marl		-0.3	-5.1	-7.0	-0.4	229 +23/-100
299C	Marl	-115	2.5	-6.7	-8.5	-1.9	1131 +158/-502
299B	Marl		-6.7	-14.6	-16.5	-9.9	3974 +1086/-1757
299A	Marl	-135	2.5	-6.7	-8.5	-1.9	1131 +158/-502
298C	Marl		1.7	-5.3	-7.2	-0.6	372 +39/-163
298B	Marl		0.0	-7.1	-8.9	-2.3	1332 +199/-593
298A	Marl		-2.5	-6.1	-7.9	-1.3	795 +99-351
297B	Marl		-1.5	-4.8	-6.6	0.0	18 +2/-8
297	Limestone		-5.9	-1.3	-3.2	3.4	-2656 +20/+1103
296	Marl		-1.0	-9.2	-11.1	-4.5	2302 +454/-1036
<i>Upper Niubao Formation</i>							
310	Paleosol		-7.2	-16.1	-18.4	-11.8	4421 +1251/-1911
305B	Paleosol		-7.9	-17.7	-18.5	-11.9	4438 +1257/-1916
305D	Paleosol		-7.8	-17.6	-18.5	-11.9	4427 +1253/-1913
305G	Paleosol		-7.8	-17.5	-18.3	-11.7	4398 +1243/-1903
305I	Paleosol		-7.9	-17.3	-18.1	-11.5	4358 +1230/-1891
305J	Paleosol		-8.2	-17.8	-18.6	-12.0	4454 +1262/-1921
305L	Paleosol		-8.0	-16.8	-17.6	-11.0	4239 +1187/-1852
305O	Paleosol		-7.5	-17.3	-18.1	-11.5	4345 +1225/-1887
305P	Paleosol		-7.4	-17.4	-18.2	-11.6	4380 +1237/-1898
305Q	Paleosol		-7.5	-18.0	-18.8	-12.2	4496 +1276/-1933
305R	Paleosol		-7.5	-17.4	-18.2	-11.6	4373 +1235/-1896
305S	Paleosol		-7.1	-17.9	-18.8	-12.2	4491 +1274/-1932
305T	Paleosol		-7.3	-17.5	-18.4	-11.8	4406 +1246/-1906
309	Paleosol		-7.4	-16.5	-15.9	-9.3	3829 +1028/-1702
307	Paleosol		-7.6	-16.6	-17.4	-10.8	4191 +1169/-1835
308	Paleosol		-7.5	-16.2	-17.0	-10.4	4107 +1137/-1806
<i>Middle Niubao Formation</i>							
316	Dolomite	-91	-4.4	-13.8	-19.0	-12.4	4543 +1290/-1947
318	Shale		-0.6	-3.1	-3.4	3.2	-2445 +2/-1019
318B	Shale		-1.8	-3.3	-3.6	3.0	-2265 -12/+947
330C	Limestone	-114	-1.3	-5.0	-5.3	1.3	-861 -47/369
330b	Limestone		-1.8	-5.2	-5.5	1.1	-730 -44/+314
330A	Limestone		-1.9	-4.4	-4.7	1.9	-1354 -50/+576
329	Mudstone		-3.1	-6.1	-6.5	0.1	-96 -8/+42
328	Limestone		-0.5	-5.2	-5.6	1.0	-682 -42/+294
327	Mudstone	-92	-1.9	-13.6	-15.4	-8.8	3705 +977/-1652
326	Dolomite		-1.6	-5.2	-5.5	1.1	-723 +222/-642

Table D.5 **Carbon and oxygen stable isotope values, and calculated paleoelevations, from Nianbo Formation in the Amu Xun.** Carbonate oxygen and carbon isotope values are in permill VPDB. Isotopic values of paleo-precipitation (p) are reported in permill VSMOW. $\delta^{18}\text{O}_p$ values were calculated using the temperature-dependent calcite-water oxygen isotope fractionation equation of Kim and O’Neil (1997), and the only $T(\Delta_{47})$ evaluated as an Earth surface temperature from the Amu Xun, $25\pm 3^\circ\text{C}$ (sample S0630-3a). Bolded samples have associated clumped isotope measurements.

Sample	Lithology	$\delta^{13}\text{C}$	$\delta^{18}\text{O}_c$	Mean $\delta^{18}\text{O}_p$	$\Delta\delta^{18}\text{O}_p$	Model Elevation (m) $\pm 2\sigma$
701-3sh	Shell	-1.3	-20.0	-17.3	-10.7	4476 ⁺¹²⁵⁴ ₋₁₇₂₁
701-3mat	Limestone	-1.4	-19.8	-17.0	-10.5	4427 ⁺¹²³⁸ ₋₁₆₉₉
702wh	Vuggy Limestone	-1.0	-20.1	-17.7	-11.1	4566 ⁺¹²⁸² ₋₁₇₆₀
702gr	Vuggy Limestone	-0.9	-19.5	-17.0	-10.4	4418 ⁺¹²³⁵ ₋₁₆₉₅
703A	Limestone	-0.7	-20.0	-17.5	-10.9	4527 ⁺¹²⁷⁰ ₋₁₇₄₃
703B	Limestone	-1.1	-18.9	-16.6	-10.0	4330 ⁺¹²⁰⁶ ₋₁₆₅₆
704	Limestone	-1.8	-19.6	-17.1	-10.5	4444 ⁺¹²⁴³ ₋₁₇₀₇
705A	Limestone	-1.0	-19.9	-17.4	-10.8	4500 ⁺¹²⁶¹ ₋₁₇₃₁
705B	Limestone	-1.5	-18.3	-17.6	-11.0	4548 ⁺¹²⁷⁶ ₋₁₇₅₂
707D	Limestone	-0.9	-19.2	-16.7	-10.2	4358 ⁺¹²¹⁵ ₋₁₆₆₈
708C	Limestone	-1.1	-18.2	-17.6	-11.0	4556 ⁺¹²⁷⁹ ₋₁₇₅₆
706	Limestone Nodule	-1.4	-20.2	-17.9	-11.3	4602 ⁺¹²⁹³ ₋₁₇₇₆
707A	Limestone Nodule	-1.0	-19.1	-16.7	-10.1	4350 ⁺¹²¹³ ₋₁₆₆₅
707B	Limestone	-0.5	-18.6	-16.3	-9.7	4249 ⁺¹¹⁷⁸ ₋₁₆₁₉
707C	Limestone Nodule	-1.6	-21.3	-18.9	-12.3	4809 ⁺¹³⁵¹ ₋₁₈₆₁
707E	Fossiliferous Limestone	-0.7	-19.5	-17.1	-10.5	4445 ⁺¹²⁴⁴ ₋₁₇₀₇
708A	Limestone	-0.5	-20.0	-17.6	-11.0	4555 ⁺¹²⁷⁹ ₋₁₇₅₅
708B	Limestone	-1.3	-19.6	-17.2	-10.6	4466 ⁺¹²⁵⁰ ₋₁₇₁₆
708D	Limestone	-0.8	-20.1	-17.8	-11.2	4584 ⁺¹²⁸⁸ ₋₁₇₆₈
S0630-3	Clastic Limestone	-3.8	-22.6	-20.2	-13.6	5041 ⁺¹⁴⁰³ ₋₁₉₄₈
S0630-5	Clastic Limestone	-3.4	-21.8	-19.5	-12.9	4910 ⁺¹³⁷⁶ ₋₁₉₀₀
S0630-6	Limestone	-3.4	-22.1	-19.7	-13.1	4956 ⁺¹³⁸⁶ ₋₁₉₁₇

Table D.6 Single crystal zircon (U-Th)/He cooling ages for igneous samples from the Oiyug and Penbo basins. (U-Th)/He ages are calculated from total measured abundances in all cases, not concentrations.

Sample name & mapped unit	Aliquot	Corrected age (Ma)	FT#	²³⁸ U (nmol/g)	²³² Th (nmol/g)	¹⁴⁷ Sm (nmol/g)	⁴ He (nmol/g)	Mass (μg)	Raw age (Ma)	U (ppm)	Th (ppm)	Sm (ppm)
<i>DBRN103</i>												
<i>Rigongla Fm. Oiyug Basin</i>	X	5.18 ± 0.05	0.791	163.493 ± 1.111	305.244 ± 1.866	266.425 ± 0.594	1.231 ± 0.006	9.16	4.06	39.20	70.83	267.06
	Y	4.33 ± 0.06	0.790	56.589 ± 0.384	187.462 ± 1.143	177.31 ± 0.395	0.438 ± 0.004	9.03	3.38	13.57	43.50	177.74
	Z	5.60 ± 0.07	0.804	35.636 ± 0.245	117.664 ± 0.715	88.28 ± 0.197	0.362 ± 0.003	11.14	4.44	8.54	27.30	88.49
	Mean age (±1σ)	5.04 ± 0.65 Ma										
<i>L0706-2 granite intrusion Penbo Basin</i>												
<i>L0706-2 granite intrusion Penbo Basin</i>	X	15.10 ± 0.10	0.703	100.968 ± 0.114	200.385 ± 0.888	113.781 ± 0.109	1.992 ± 0.010	3.31	10.44	24.21	46.50	114.05
	Y	16.56 ± 0.11	0.807	48.015 ± 0.072	95.882 ± 0.540	63.609 ± 0.031	1.204 ± 0.004	11.66	13.24	11.51	22.25	63.760
	Z	12.93 ± 0.08	0.727	75.998 ± 0.175	345.718 ± 1.483	422.563 ± 0.201	1.875 ± 0.008	4.17	9.21	18.22	80.22	423.58
	Mean age (±1σ)	14.86 ± 1.83 Ma										
<i>L0706-3 granite intrusion Penbo Basin</i>												
<i>L0706-3 granite intrusion Penbo Basin</i>	X	11.50 ± 0.06	0.793	89.580 ± 0.180	473.757 ± 2.001	738.337 ± 0.301	2.347 ± 0.007	9.44	8.98	21.48	109.93	740.11
	Y	12.35 ± 0.07	0.742	179.654 ± 0.215	501.425 ± 2.131	399.745 ± 0.195	3.459 ± 0.011	4.88	9.02	43.08	116.35	400.70
	Z	14.36 ± 0.09	0.717	91.660 ± 0.177	199.523 ± 0.854	150.095 ± 0.094	1.811 ± 0.008	3.78	10.14	21.98	46.30	150.46
	Mean age (±1σ)	12.74 ± 1.47 Ma										

Correction factor for α-ejection; Farley et al. (1996)

Table D.7 $^{40}\text{Ar}/^{39}\text{Ar}$ inverse isochron age for the base of the Rigongla Formation, Oiyug basin. Isotope abundances are corrected for blank, mass discrimination, nucleogenic interferences, and post-irradiation decay. The GA1550 flux monitor (age = 98.790 ± 0.543 Ma) was used to calculate $J = 0.00169000 \pm 0.00001690$. Errors are reported at the 2σ level and include uncertainty in J. Isotope abundances are calculated with instrument sensitivity of 8.20×10^{-17} moles/fA.

Sample name & mapped unit	Aliquot	$^{36}\text{Ar}_a$ (moles)	$^{37}\text{Ar}_{Ca}$ (moles)	$^{38}\text{Ar}_{Cl}$ (moles)	$^{39}\text{Ar}_K$ (moles)	$^{40}\text{Ar}_r$ (moles)	Apparent Age (Ma)	Error (Ma 2σ)	$^{40}\text{Ar}^*$ (%)	$^{39}\text{Ar}_k$ (%)	K/Ca	Error (2σ)
<i>W0628-4</i> <i>Rigongla Fm</i> <i>Oiyug Basin</i>	1	6.27E-17	3.54E-15	6.52E-18	8.73E-15	7.09E-14	33.81	0.50	79.28	34.44	1.06	4.92E-03
	2	1.17E-16	4.33E-15	2.61E-18	7.16E-15	6.92E-14	40.19	0.63	66.66	28.22	0.71	3.25E-03
	3	8.62E-17	6.36E-15	3.56E-18	9.47E-15	8.02E-14	35.27	0.44	75.89	37.34	0.64	2.79E-03
	Inverse isochron age ($\pm 2\sigma$)	28.90 \pm 1.52 Ma										

Table D.8 Lithologies, sample locations, and carbon and oxygen stable isotope data for the Tso Jiangding.

Sample	Lithology	Orme et al. (2014) Section	Latitude (°N)	Longitude (°E)	$\delta^{18}\text{O}_c$ ‰ VPDB	$\delta^{13}\text{C}$ ‰ VPDB	% CO_3^{2-}
T0702-2	fossiliferous limestone	D/E - shallow marine	29.85989	84.84176	-16.2	-3.6	65
T0702-2Sh	shell	D/E - shallow marine	29.85989	84.84176	-15.3	-3.4	85
T0702-4	dolomitic limestone	D/E - shallow marine	29.85995	84.84175	-16.0	-3.1	86
T0702-4Sh	shell	D/E - shallow marine	29.85995	84.84175	-15.3	-2.5	14
T0702-6	fossiliferous limestone	D/E - shallow marine	29.87528	84.84125	-20.9	-1.5	22
T0702-7	limestone	D/E - shallow marine	29.87533	84.84117	-21.4	-1.6	24
T0702-8	fossiliferous limestone	D/E - shallow marine	29.87528	84.84125	-19.3	-1.0	17
T0702-8Sh	shell	D/E - shallow marine	29.87528	84.84125	-13.0	0.1	65
T0702-9	sandy limestone	D/E - shallow marine	29.87534	84.84115	-18.4	-1.0	17
T0702-10	fossiliferous limestone	D/E - shallow marine	29.87536	84.84113	-17.5	0.6	18
T0702-11	sandy limestone	D/E - shallow marine	29.87537	84.84112	-17.5	-1.1	17
T0702-13	sandy limestone	D/E - shallow marine	29.87537	84.84112	-17.8	-1.6	12
T0702-14	limey sandstone	D/E - shallow marine	29.87538	84.84109	-16.1	-1.5	7
T0702-14V	vein	D/E - shallow marine	29.87538	84.84109	-14.4	-2.1	47
T0702-16	limestone	D/E - shallow marine	29.87539	84.84107	-15.4	-1.0	26
T0702-17	limestone	D/E - shallow marine	29.87561	84.84075	-17.0	-1.1	9.5
T0702-18	fossiliferous limestone	D/E - shallow marine	29.87566	84.83996	-15.1	-0.3	42
T0702-18N1	foraminifera	D/E - shallow marine	29.87566	84.83996	-15.0	-0.3	31
T0702-19	sandy limestone	D/E - shallow marine			-17.2	-1.7	13
T0702-19V	vein	D/E - shallow marine			-16.0	0.8	45
T0703-2	limestone	G/H - fluvial/deltaic	29.89091	84.74028	-29.5	-4.0	17
T0703-4v	vein within fluvial siltstone	G/H - fluvial/deltaic	29.88997	84.74184	-15.4	-7.5	68
T0703-7	limey sandstone	G/H - fluvial/deltaic	29.88947	84.74259	-22.4	-5.7	3
T0703-8	limey sandstone	G/H - fluvial/deltaic	29.88931	84.74213	-23.7	-6.0	9
T0703-9	quartz sand-rich paleosol	G/H - fluvial/deltaic	29.88942	84.74260	-22.9	-7.7	5
T0703-10	carbonate-rich paleosol	G/H - fluvial/deltaic	29.88942	84.74265	-21.7	-9.7	37
T0703-11	paleosol calcrete	G/H - fluvial/deltaic	29.88939	84.74271	-21.4	-8.7	2
T0703-12	paleosol calcrete	G/H - fluvial/deltaic	29.88938	84.74274	-24.2	-9.2	12
T0703-12V	vein	G/H - fluvial/deltaic	29.88938	84.74274	-16.9	-7.6	41
T0703-13	limey sandstone	G/H - fluvial/deltaic	29.88929	84.74279	-20.4	-8.6	2
T0703-16	paleosol; green	G/H - fluvial/deltaic	29.88915	84.74293	-0.4	-7.4	7
T0703-17	paleosol calcrete	G/H - fluvial/deltaic			-22.4	-6.9	12

Table D.9 All Δ_{47} measurements of the Tso Jiangding samples. The inferred oxygen isotopic composition of water in equilibrium with carbonate at measured Δ_{47} -derived temperatures is listed in the far right column. * denotes measurements made on the MAT253. $\delta^{18}\text{O}_{\text{CO}_3}$ values were calculated using a $\text{CO}_2\text{-CO}_3$ acid fractionation factor (Guo et al., 2009).

Sample	$\delta^{18}\text{O}_{\text{CO}_2}^*$ VSMOW	$\delta^{18}\text{O}_{\text{CO}_3}$ VPDB	Δ_{47}^*	$\text{T}(\Delta_{47})$ $^{\circ}\text{C}$	Inferred from $\text{T}(\Delta_{47})$	
					$\alpha_{\text{CO}_3\text{-H}_2\text{O}}$	equil. $\delta^{18}\text{O}_w$ VSMOW
T0702-18	25.572	-15.192	0.536	56.6	1.022535121	-7.1
T0702-18	24.735	-15.995	0.540	55.2	1.022771413	-8.2
T0702-18	24.598	-16.127	0.563	47.9	1.024046939	-9.5
T0702-18N1	25.085	-15.659	0.653	22.9	1.028923208	-13.8
T0702-18N1	25.317	-15.436	0.641	25.9	1.028293567	-12.9
T0702-18N2	26.335	-14.459	0.469	82.2	1.018508217	-2.5
T0702-18N2	26.204	-14.585	0.482	76.6	1.019335189	-3.4
T0702-4	24.501	-16.220	0.460	86.1	1.017949414	-3.7
T0702-4	24.663	-16.065	0.465	84.0	1.01825327	-3.8
T0702-4	24.679	-16.049	0.456	87.8	1.017709723	-3.3
T0702-4Sh	24.988	-15.752	0.721	7.4	1.032392712	-17.2
T0702-6	19.407	-21.111	0.686	15.1	1.030611579	-20.8
T0702-7	21.360	-19.236	0.613	33.1	1.026831012	-15.3
T0702-7	21.236	-19.355	0.609	34.2	1.026619354	-15.3
T0702-8	21.228	-19.363	0.589	39.9	1.025522505	-14.2
T0702-8	20.896	-19.681	0.543	54.3	1.022921829	-12.0
T0702-8	20.814	-19.761	0.688	14.5	1.030748331	-19.6
T0702-8SH1	28.037	-12.825	0.467	83.1	1.018382659	-0.7
T0702-8SH2	26.493	-14.307	0.617	32.1	1.027037021	-10.6
T0702-8SH2 recleaned	26.503	-14.297	0.621	31.2	1.027223794	-10.8
T0702-8V	25.827	-14.946	0.524	61.0	1.021796155	-6.2

REFERENCES

- , 2017. 1:25000 Geological Map of Tibet Autonomous Region. URL: <http://ngac.org.cn>.
- Aikman, A.B., Harrison, T.M., Lin, D., 2008. Evidence for Early (>44 Ma) Himalayan Crustal Thickening, Tethyan Himalaya, southeastern Tibet. *Earth and Planetary Science Letters* 274, 14–23. doi:10.1016/j.eps1.2008.06.038.
- Aitchison, J.C., Xia, X., Baxter, A.T., Ali, J.R., 2011. Detrital zircon U-Pb ages along the Yarlung-Tsangpo suture zone, Tibet: Implications for oblique convergence and collision between India and Asia. *Gondwana Research* 20, 691–709. doi:10.1016/j.gr.2011.04.002.
- Ali, J.R., Aitchison, J.C., 2005. Greater India. *Earth-Science Reviews* 72, 169–188. doi:10.1016/j.earscirev.2005.07.005.
- Almqvist, B.S.G., Hirt, A.M., Herwegh, M., Leiss, B., 2011. Magnetic anisotropy reveals Neogene tectonic overprint in highly strained carbonate mylonites from the Morcles nappe, Switzerland. *Journal of Structural Geology* 33, 1010–1022. doi:10.1016/j.jsg.2011.02.002.
- An, W., Hu, X., Garzanti, E., BouDagher-Fadel, M.K., Wang, J., Sun, G., 2014. Xigaze fore-arc basin revisited (South Tibet): Provenance changes and origin of the Xigaze Ophiolite. *Bulletin of the Geological Society of America* 126, 1595–1613. doi:10.1130/B31020.1.
- Argand, E., 1924. La Tectonique de l'Asie, in: *Proceedings of the XIIIth International Geological Congress, Brussels*. pp. vol.1, pt. 5: 181–372.
- Armstrong, R.L., 1971. Glacial erosion and the variable isotopic composition of strontium in sea water. *Nature* 230, 132–133. doi:10.1038/physci230132a0.
- Barker, C.E., 1988. Geothermics of petroleum systems: Implications of the stabilization of kerogen thermal maturation after a geologically brief heating duration at peak temperature. *Petroleum systems of the United States: US Geological Survey Bulletin* 1870, 26–29.
- Beck, R.A., Burbank, D.W., Sercombe, W.J., Riley, G.W., Barndt, J.K., Berry, J.R., Afzal, J., Khan, A.M., Jurgen, H., Metje, J., Cheema, A., Shafique, N.A., Lawrence, R.D., Khan, M.A., 1995. Stratigraphic evidence for an early collision between northwest India and Asia. *Nature* 373, 55–58. doi:10.1038/373055a0.
- Bender, F., 1983. *Geology of Burma*. Gebruder Borntraeger, Berlin.
- Berner, R., Maasch, K., 1996. Chemical weathering and controls on atmospheric O₂ and CO₂: Fundamental principles were enunciated by J.J. Ebelman in 1845. *Geochimica et Cosmochimica Acta* 60, 1633–1637.
- Bershaw, J., Penny, S., Garzzone, C.N., 2012. Stable isotopes of modern water across the Himalaya and eastern Tibetan Plateau: Implications for estimates of paleoelevation and paleoclimate. *Journal of Geophysical Research* 117.

- Boggs, S., Krinsley, D., 2006. Application of Cathodoluminescence Imaging to the Study of Sedimentary Rocks. Cambridge University Press. URL: <https://books.google.com/books?id=4F6d-LzY0bYC>.
- Bojanowski, M.J., Bagiński, B., Guillermier, C., Franchi, I.A., 2015. Carbon and oxygen isotope analysis of hydrate-associated Oligocene authigenic carbonates using NanoSIMS and IRMS. *Chemical Geology* 416, 51–64. doi:10.1016/j.chemgeo.2015.10.021.
- Bollinger, L., Henry, P., Avouac, J.P., 2006. Mountain building in the Nepal Himalaya: thermal and kinematic model. *Earth and Planetary Science Letters* 244, 58–71.
- Boos, W.R., Kuang, Z., 2010. Dominant control of the South Asian monsoon by orographic insulation versus plateau heating. *Nature* 463, 218–222. URL: <http://dx.doi.org/10.1038/nature08707>http://www.nature.com/nature/journal/v463/n7278/supinfo/nature08707__S1.html.
- Boos, W.R., Kuang, Z., 2013. Sensitivity of the South Asian monsoon to elevated and non-elevated heating. *Scientific Reports* 3, 1192. URL: <http://dx.doi.org/10.1038/srep01192><http://10.0.4.14/srep01192>.
- Bouilhol, P., Jagoutz, O., Hanchar, J.M., Dudas, F.O., 2013. Dating the IndiaEurasia collision through arc magmatic records. *Earth and Planetary Science Letters* 366, 163–175. doi:10.1016/j.epsl.2013.01.023.
- Budd, D.A., Pack, S.M., Fogel, M.L., 2002. The destruction of paleoclimatic isotopic signals in Pleistocene carbonate soil nodules of Western Australia. *Palaeogeography, Palaeoclimatology, Palaeoecology* 188, 249–273.
- Bureau of Geology and Mineral Resources Xizang Autonomous Region, . Regional geology of Xizang (Tibet) autonomous region. Technical Report. Beijing. URL: https://books.google.com/books/about/Regional__geology__of__Xizang__Tibet__autonom.html?id=NCVPPwAACAAJ__pgis=1.
- Burg, J.P., Proust, F., Tapponnier, P., Chen, G.M., 1983. Deformation phases and tectonic evolution of the Lhasa block (southern Tibet, China). *Eclogae Geologicae Helvetiae* 76, 643–665.
- Burgener, L., Huntington, K.W., Hoke, G.D., Schauer, A., Ringham, M.C., Latorre, C., Díaz, F.P., 2016. Variations in soil carbonate formation and seasonal bias over >4 km of relief in the western Andes (30S) revealed by clumped isotope thermometry. *Earth and Planetary Science Letters* 441, 188–199. URL: <http://www.sciencedirect.com/science/article/pii/S0012821X16300504>, doi:<http://dx.doi.org/10.1016/j.epsl.2016.02.033>.
- Carpenter, S.J., Lohmann, K.C., 1997. Carbon isotope ratios of Phanerozoic marine cements: Re-evaluating the global carbon and sulfur systems. *Geochimica et Cosmochimica Acta* 61, 4831–4846. doi:10.1016/S0016-7037(99)00052-6.

- Carpenter, S.J., Lohmann, K.C., Holden, P., Walter, L.M., Huston, T.J., Halliday, A.N., 1991. $\delta^{18}\text{O}$ values, $^{87}\text{Sr}/^{86}\text{Sr}$ and Sr/Mg ratios of Late Devonian abiogenic marine calcite: Implications for the composition of ancient seawater. *Geochimica et Cosmochimica Acta* 55, 1991–2010. doi:10.1016/0016-7037(91)90038-7.
- Carrapa, B., Orme, D.A., DeCelles, P.G., Kapp, P., Cosca, M.A., Waldrip, R., 2014. Miocene burial and exhumation of the India-Asia collision zone in southern Tibet: Response to slab dynamics and erosion. *Geology* URL: <http://geology.gsapubs.org/content/early/2014/03/28/G35350.1.abstract>, doi:10.1130/G35350.1.
- Castanier, S., Le Métayer-Levrel, G., Perthuisot, J.P., 1999. Ca-carbonates precipitation and limestone genesis the microbiogeologist point of view. *Sedimentary Geology* 126, 9–23. URL: <http://linkinghub.elsevier.com/retrieve/pii/S0037073899000287>, doi:10.1016/S0037-0738(99)00028-7.
- Chen, H., Han, J., Ding, Z., Sun, H., Guo, Z., 2008. Chronological dating and tectonic implications of late Cenozoic volcanic rocks and lacustrine sequence in Oiyug Basin of southern Tibet. *Science in China Series D* 51, 275–283.
- Choquette, P.W., Pray, L.C., 1970. Geologic nomenclatures and classification of porosity in sedimentary carbonates. *AAPG Bulletin* 54, 207–250.
- Chung, S.L., Chu, M.F., Zhang, Y., Xie, Y., Lo, C.H., Lee, T.Y., Lan, C.Y., Li, X., Zhang, Q., Wang, Y., 2005. Tibetan tectonic evolution inferred from spatial and temporal variations in post-collisional magmatism. *Earth-Science Reviews* 68, 173–196. doi:10.1016/j.earscirev.2004.05.001.
- Clark, I., Fritz, P., 1997. *Environmental Isotopes in Hydrogeology*. Lewis Publishers, Boca Raton.
- Clark, M.K., 2012. Continental collision slowing due to viscous mantle lithosphere rather than topography. *Nature* 483, 74–7. doi:10.1038/nature10848.
- Clark, M.K., Royden, L.H., 2000. Topographic ooze: Building the eastern margin of Tibet by lower crustal flow. *Geology* 28, 703–706. doi:10.1130/0091-7613(2000)28<703:TOBTEM>2.0.CO;2.
- Clift, P.D., 2006. Controls on the erosion of Cenozoic Asia and the flux of clastic sediment to the ocean. *Earth and Planetary Science Letters* 241, 571–580. doi:10.1016/j.epsl.2005.11.028.
- Cohen, A.C., Morin, J.G., 1990. Patterns of Reproduction in Ostracodes: A Review. *Journal of Crustacean Biology* 10, 184–211.
- Colman, A.S., Holland, H., 2000. The global diagenetic flux of phosphorus from marine sediments to oceans: Redox sensitivity and the control of atmospheric oxygen levels .

- Compton, J., Mallinson, D., 1996. Geochemical consequences of increased Late Cenozoic weathering rates and the global CO₂ balance since 100 Ma. *Paleoceanography* 11, 431–446.
- Coplen, T., Brand, W., Gehre, M., Groning, M., Meijer, H., Toman, B., Verkouteren, R., 2006. New guidelines for δ¹³C measurements. *Analytical Chemistry* 78, 3439–2441.
- Craig, H., Gordon, L., 1965. Deuterium and oxygen 18 variations in the ocean and the marine atmosphere, in: Tongiorgi, E. (Ed.), *Stable Isotopes in Oceanographic Studies and Paleotemperatures*, pp. 9–130. URL: http://yncenter.sites.yale.edu/sites/default/files/shen{_}jing{_}jan{_}2013.pdf.
- Cummins, R.C., Finnegan, S., Fike, D.A., Eiler, J.M., Fischer, W.W., 2014. Carbonate clumped isotope constraints on Silurian ocean temperature and seawater δ¹⁸O. *Geochimica et Cosmochimica Acta* 140, 241–258. URL: <http://dx.doi.org/10.1016/j.gca.2014.05.024>, doi:10.1016/j.gca.2014.05.024.
- Curray, J.R., 1991. Possible greenschist metamorphism at the base of a 22-km sedimentary section, Bay of Bengal. *Geology* 19, 1097–1100. URL: <http://geology.gsapubs.org/content/19/11/1097.short>, doi:10.1130/0091-7613(1991)019.
- Currie, B.S., Polissar, P.J., Rowley, D.B., Ingalls, M., Li, S., Freeman, K.H., 2016. Multi-proxy paleoaltimetry of the late Oligocene-Pliocene Oiyug Basin, southern Tibet. *American Journal of Science* 316, 401–436. doi:10.2475/05.2016.01.
- Currie, B.S., Rowley, D.B., Tabor, N.J., 2005. Middle Miocene paleoaltimetry of southern Tibet: Implications for the role of mantle thickening and delamination in the Himalayan orogen. *Geology* 33, 181. doi:10.1130/G21170.1.
- Dansgaard, W., 1954. The O¹⁸ abundance in fresh water. *Geochimica et Cosmochimica Acta* 6, 241–260.
- Dansgaard, W., 1964. Stable isotopes in precipitation. *Tellus* 16, 436–468. doi:10.3402/tellusa.v16i4.8993.
- DeCelles, P., DM, R., Quade, J., Ojha, T.P., Garzione, C.N., Copeland, P., Upreti, B., 2001. Stratigraphy, structure, and tectonic evolution of the Himalayan fold-thrust belt in western Nepal. *Tectonics* 20, 487–509.
- DeCelles, P., Gehrels, G., Najman, Y., Martin, A., Carter, A., Garzanti, E., 2004. Detrital geochronology and geochemistry of Cretaceous-Early Miocene strata of Nepal: implications for timing and diachroneity of initial Himalayan orogenesis. *Earth and Planetary Science Letters* 227, 313–330. doi:10.1016/j.epsl.2004.08.019.
- DeCelles, P., Kapp, P., Gehrels, G., Ding, L., 2014. Paleocene-Eocene foreland basin evolution in the Himalaya of southern Tibet and Nepal: Implications for the age of initial India-Asia collision. *Tectonics* 33. doi:10.1002/2014TC003522.

- DeCelles, P.G., Castaneda, I.S., Carrapa, B., Liu, J., Quade, J., Leary, R., Zhang, L., 2016. Oligocene-Miocene Great Lakes in the India-Asia Collision Zone. *Basin Research* , 1–20doi:10.1111/bre.12217.
- DeCelles, P.G., Kapp, P., Quade, J., Gehrels, G.E., 2011. Oligocene-Miocene Kailas basin, southwestern Tibet: Record of postcollisional upper-plate extension in the Indus-Yarlung suture zone. *Bulletin of the Geological Society of America* 123, 1337–1362. doi:10.1130/B30329.1.
- DeCelles, P.G., Quade, J., Kapp, P., Fan, M., Dettman, D.L., Ding, L., 2007. High and dry in central Tibet during the Late Oligocene. *Earth and Planetary Science Letters* 253, 389–401. doi:10.1016/j.epsl.2006.11.001.
- Decrouy, L., Vennemann, T.W., Ariztegui, D., 2011. Controls on ostracod valve geochemistry: Part 2. Carbon and oxygen isotope compositions. *Geochimica et Cosmochimica Acta* 75, 7380–7399.
- Defliese, W.F., Hren, M.T., Lohmann, K.C., 2015. Compositional and temperature effects of phosphoric acid fractionation on $\Delta 47$ analysis and implications for discrepant calibrations. *Chemical Geology* 396, 51–60. doi:10.1016/j.chemgeo.2014.12.018.
- Dennis, K., Affek, H., Passey, B., Schrag, D., Eiler, J., 2011. Defining an absolute reference frame for 'clumped' isotope studies of CO₂. *Geochimica et Cosmochimica Acta* 75, 7117–7131. doi:10.1016/j.gca.2011.09.025.
- Dennis, K.J., Schrag, D.P., 2010. Clumped isotope thermometry of carbonatites as an indicator of diagenetic alteration. *Geochimica et Cosmochimica Acta* 74, 4110–4122. doi:10.1016/j.gca.2010.04.005.
- Dewey, J., Bird, J., 1970. Mountain belts and the new global tectonics. *Journal of Geophysical Research* 75, 2625–2647.
- Dewey, J.F., Burke, K.C.A., 1973. Tibetan, Variscan, and Precambrian Basement Re-activation: Products of Continental Collision. *The Journal of Geology* 81, 683–692. doi:10.2307/30058995.
- Dewey, J.F., Shackleton, R.M., Chengfa, C., Yiyin, S., 1988. The Tectonic Evolution of the Tibetan Plateau. *Philosophical Transactions of the Royal Society A: Mathematical, Physical and Engineering Sciences* 327, 379–413. URL: <http://rsta.royalsocietypublishing.org/cgi/doi/10.1098/rsta.1988.0135>, doi:10.1098/rsta.1988.0135.
- Ding, L., Kapp, P., Wan, X., 2005. Paleocene-Eocene record of ophiolite obduction and initial India-Asia collision, south central Tibet. *Tectonics* 24. doi:10.1029/2004TC001729.
- Ding, L., Lai, Q., 2003. New geological evidence of crustal thickening in the Gangdese block prior to the Indo-Asian collision. *Chinese Science Bulletin* 48, 1604–1610.

- Ding, L., Xu, Q., Yue, Y., Wang, H., Cai, F., Li, S., 2014. The Andean-type Gangdese Mountains: Paleoelevation record from the Paleocene-Eocene Linzhou Basin. *Earth and Planetary Science Letters* 392, 250–264. doi:10.1016/j.epsl.2014.01.045.
- Dodson, M.H., 1973. Closure temperature in cooling geochronological and petrological systems. *Contributions to Mineralogy and Petrology* 40, 259–274. doi:10.1007/BF00373790.
- Dupont-Nivet, G., Lippert, P.C., Van Hinsbergen, D.J., Meijers, M.J., Kapp, P., 2010. Palaeolatitude and age of the Indo-Asia collision: palaeomagnetic constraints. *Geophysical Journal International* 182, 1189–1198. URL: <http://gji.oxfordjournals.org/cgi/doi/10.1111/j.1365-246X.2010.04697.x>, doi:10.1111/j.1365-246X.2010.04697.x.
- Eagle, R.A., Schauble, E.A., Tripathi, A.K., Tütken, T., Hulbert, R.C., Eiler, J.M., 2010. Body temperatures of modern and extinct vertebrates from ^{13}C - ^{18}O bond abundances in bioapatite. *Proceedings of the National Academy of Sciences* 107, 10377–10382. URL: <http://www.pnas.org/content/107/23/10377.abstract>, doi:10.1073/pnas.0911115107.
- Ebelmen, J., 1845. Sur les produits de la decomposition des especes minerales de la famille des silicates. *Ann. des Mines* 7, 3–66.
- Edmonds, J., 1992. Himalayan tectonics, weathering processes, and the strontium isotope record in marine limestones. *Science* 258, 1594–1597.
- Eiler, J.M., 2007. Clumped-isotope geochemistry: The study of naturally-occurring, multiply-substituted isotopologues. *Earth and Planetary Science Letters* 262, 309–327. URL: <http://linkinghub.elsevier.com/retrieve/pii/S0012821X07005109>, doi:10.1016/j.epsl.2007.08.020.
- Eiler, J.M., 2011. Paleoclimate reconstruction using carbonate clumped isotope thermometry. *Quaternary Science Reviews* 30, 3575–3588. doi:10.1016/j.quascirev.2011.09.001.
- Einsele, G., Liu, B., Dürr, S., Frisch, W., Liu, G., Luterbacher, H.P., Ratschbacher, L., Ricken, W., Wendt, J., Wetzell, A., Yu, G., Zheng, H., 1994. The Xigaze forearc basin: evolution and facies architecture (Cretaceous, Tibet). *Sedimentary Geology* 90, 1–32. doi:10.1016/0037-0738(94)90014-0.
- England, P., Houseman, G., 1986. Finite strain calculations of continental deformation: 2. Comparison with the India-Asia collision zone. *Journal of Geophysical Research*: ... 91, 3664–3676. URL: <http://onlinelibrary.wiley.com/doi/10.1029/JB091iB03p03664/pdf>.
- England, P., McKenzie, D., 1982. A Thin Viscous Sheet Model for Continental Deformation. *Geophysical Journal Of The Royal Astronomical Society* 70, 295–321. URL: <http://gateway.webofknowledge.com/gateway/Gateway.cgi?GWVersion=2&SrcAuth=mekentosj&SrcApp=Papers&DestLinkType=FullRecord&DestApp=WOS&KeyUT=A1982NY30600002\%0Apapers3://publication/uuid/7F06148B-7ADE-423D-A2B2-5589A5796074>.

- England, P., Searle, M., 1986. The Cretaceous-tertiary deformation of the Lhasa Block and its implications for crustal thickening in Tibet. *Tectonics* 5, 1–14. URL: <http://doi.wiley.com/10.1029/TC005i001p00001>, doi:10.1029/TC005i001p00001.
- Farley, K.A., Wolf, R., Silver, L., 1996. The effects of long alpha-stopping distances on (U-Th)/He ages. *Geochimica et Cosmochimica Acta* 60, 4223–4229.
- France-Lanord, C., Derry, L., 1997. Organic carbon burial forcing of the carbon cycle from Himalayan erosion. *Nature* 390, 65–67.
- Friedman, I., 1953. Deuterium content of natural waters and other substances. *Geochimica et Cosmochimica Acta* 4, 89–103.
- Friedman, I., O'Neil, J., 1977. Compilation of stable isotope fractionation factors of geochemical interest. Geological Survey Professional Paper URL: <http://pubs.er.usgs.gov/publication/pp440KK>.
- Fritz, H., Abdelsalam, M., Ali, K., Bingen, B., Collins, A., Fowler, A., Ghebreab, W., Hauzenberger, C., Johnson, P., Kusky, T., Macey, P., Muhongo, S., Stern, R., Viola, G., 2013. Orogen styles in the East African Orogen: A review of the Neoproterozoic to Cambrian tectonic evolution. *Journal of African Earth Sciences* 86, 65–106.
- Gaetani, M., Garzanti, E., 1991. Multicyclic History of the Northern India Continental Margin (Northwestern Himalaya) (1). *AAPG Bulletin* 75, 1427–1446. URL: <http://archives.datapages.com/data/bulletns/1990-91/data/pg/0075/0009/0000/1427.htm>.
- Gallagher, T.M., Sheldon, N.D., 2016. Combining soil water balance and clumped isotopes to understand the nature and timing of pedogenic carbonate formation. *Chemical Geology* 435, 79–91. URL: <http://www.sciencedirect.com/science/article/pii/S0009254116302054>, doi:<http://dx.doi.org/10.1016/j.chemgeo.2016.04.023>.
- Galy, A., France-Lanord, C., Beyssac, O., Faure, P., Kudrass, H., Palhol, F., 2007. Efficient organic carbon burial in the Bengal fan sustained by the Himalayan erosional system. *Nature* 450, 407–410.
- Galy, A., France-Lanord, C., Derry, L., 1999. The strontium isotopic budget of Himalayan rivers in Nepal and Bangladesh. *Geochimica et Cosmochimica Acta* 63, 1905–1925.
- Garzzone, C.N., 2008. Surface uplift of Tibet and Cenozoic global cooling. *Geology* 36, 1003–1004. URL: <http://geology.gsapubs.org/content/36/12/1003.short>, doi:10.1130/focus122008.1.
- Garzzone, C.N., Dettman, D.L., Horton, B.K., 2004. Carbonate oxygen isotope paleoaltimetry: evaluating the effect of diagenesis on paleoelevation estimates for the Tibetan plateau. *Palaeogeography, Palaeoclimatology, Palaeoecology* 212, 119–140. URL: <http://www.sciencedirect.com/science/article/pii/S0031018204003074>, doi:10.1016/j.palaeo.2004.05.020.

- Garzione, C.N., Dettman, D.L., Quade, J., DeCelles, P.G., Butler, R., 2000. High times on the Tibetan Plateau: Paleoelevation of the Thakkhola graben, Nepal. *Geology* 28, 339–342.
- Ghosh, P., Adkins, J., Affek, H., Balta, B., Guo, W.W., Schauble, E.E.a., Schrag, D., Eller, J., Eiler, J.M., 2006a. $^{13}\text{C}/^{18}\text{O}$ bonds in carbonate minerals: A new kind of paleothermometer. *Geochimica et Cosmochimica Acta* 70, 1439–1456. URL: <http://linkinghub.elsevier.com/retrieve/pii/S0016703705009087>, doi:10.1016/j.gca.2005.11.014.
- Ghosh, P., Garzione, C.N., Eiler, J.M., 2006b. Rapid uplift of the Altiplano revealed through ^{13}C - ^{18}O bonds in paleosol carbonates. *Science (New York, N.Y.)* 311, 511–5. URL: <http://www.sciencemag.org/content/311/5760/511.short>, doi:10.1126/science.1119365.
- Gonfiantini, R., 1983. Advisory group meeting on stable isotope reference samples for geochemical and hydrological investigations, in: Report to the Director General, International Atomic Energy Agency, Vienna. p. 77.
- Gonfiantini, R., 1986. Environmental Isotopes in Lake Studies, in: Handbook of Environmental Isotope Geochemistry, Volume 2: The Terrestrial Environment B, pp. 113–168. URL: <http://linkinghub.elsevier.com/retrieve/pii/B9780444422255500085>, doi:10.1016/B978-0-444-42225-5.50008-5.
- Gonzalez, L.A., Lohmann, K.C., 1985. Carbon and oxygen isotopic composition of Holocene reefal carbonates. doi:10.1130/0091-7613(1985)13<811:CAOICO>2.0.CO.
- Gothmann, A.M., Stolarski, J., Adkins, J.F., Schoene, B., Dennis, K.J., Schrag, D.P., Mazur, M., Bender, M.L., 2015. Fossil corals as an archive of secular variations in seawater chemistry since the Mesozoic. *Geochimica et Cosmochimica Acta* 160, 188–208. doi:10.1016/j.gca.2015.03.018.
- Gourbet, L., Leloup, P.H., Paquette, J.L., Sorrel, P., Maheo, G., Wang, G., Yadong, X., Cao, K., Antoine, P.O., Eymard, I., Liu, W., Lu, H., Replumaz, A., Chevalier, M.L., Kexin, Z., Jing, W., Shen, T., 2017. Reappraisal of the Jianchuan Cenozoic basin stratigraphy and its implications on the SE Tibetan plateau evolution. *Tectonophysics* 700-701, 162–179. URL: <http://linkinghub.elsevier.com/retrieve/pii/S0040195117300537>, doi:10.1016/j.tecto.2017.02.007.
- Green, O.R., Searle, M.P., Corfield, R.I., Corfield, R.M., 2008. Cretaceous-Tertiary Carbonate Platform Evolution and the Age of the India-Asia Collision along the Ladakh Himalaya (Northwest India). *The Journal of Geology* 116, 331–353. URL: <http://www.jstor.org/stable/10.1086/588831>, doi:10.1086/588831.
- Guo, W., Mosenfelder, J.L., Goddard, W.A., Eiler, J.M., 2009. Isotopic fractionations associated with phosphoric acid digestion of carbonate minerals: Insights from first-principles theoretical modeling and clumped isotope measurements. *Geochimica et Cosmochimica Acta* 73, 7203–7225. URL: <http://www.sciencedirect.com/science/article/pii/S0016703709004104>, doi:10.1016/j.gca.2009.05.071.

- Hafkenscheid, E., Wortel, M., Spakman, W., 2006. Subduction history of the Tethyan region derived from seismic tomography and tectonic reconstructions. *Journal of Geophysical Research* 111.
- Hall, R., 2012. Late Jurassic-Cenozoic reconstructions of the Indonesian region and the Indian Ocean. *Tectonophysics* 570-571, 1–41. URL: <http://www.sciencedirect.com/science/article/pii/S0040195112002533>, doi:10.1016/j.tecto.2012.04.021.
- Hanan, B., Blichert-Toft, J., Hemond, C., Sayit, K., Agranier, A., Graham, D., Albarede, F., 2013. Pb and Hf isotope variations along the Southeast Indian Ridge and the dynamic distribution of MORB source domains in the upper mantle. *Earth and Planetary Science Letters* 375, 196–208.
- Harrison, T., Copeland, P., Kidd, W.S.F., Lovera, O.M., 1995. Activation of the Nyainqentanghla Shear Zone: Implications for uplift of the southern Tibetan Plateau. *Tectonics* 14, 658–676.
- Harrison, T.M., Copeland, P., Kidd, W.S., Yin, A., 1992. Raising tibet. *Science* (New York, N.Y.) 255, 1663–70. URL: <http://www.sciencemag.org/content/255/5052/1663>, doi:10.1126/science.255.5052.1663.
- He, B., Olack, G., Colman, A., 2012. Pressure baseline correction and high-precision CO₂ clumped-isotope ($\delta^{13}C_{\alpha}$) measurements in bellows and micro-volume modes. *Rapid communications in mass spectrometry* 26, 2837–53. URL: <http://www.ncbi.nlm.nih.gov/pubmed/23136015><http://onlinelibrary.wiley.com/doi/10.1002/rcm.6436/full>, doi:10.1002/rcm.6436.
- He, H., Sun, J., Li, Q., Zhu, R., 2011. New age determination of the Cenozoic Lunpola basin, central Tibet. *Geol. Mag* 149, 141–145. doi:10.1017/S0016756811000896.
- He, S., Kapp, P., DeCelles, P.G., Gehrels, G.E., Heizler, M., 2007. Cretaceous-Tertiary geology of the Gangdese Arc in the Linzhou area, southern Tibet. *Tectonophysics* 433, 15–37. URL: <http://linkinghub.elsevier.com/retrieve/pii/S0040195107000182>, doi:10.1016/j.tecto.2007.01.005.
- Hedges, J., Keil, R., 1995. Sedimentary organic matter preservation: an assessment and speculative synthesis. *Marine Chemistry* 49, 81–115.
- Henkes, G.A., Passey, B.H., Grossman, E.L., Shenton, B.J., Perez-Huerta, A., Yancey, T.E., 2014. Temperature limits for preservation of primary calcite clumped isotope paleotemperatures. *Geochimica et Cosmochimica Acta* 139, 362–382.
- Henkes, G.A., Passey, B.H., Wanamaker, A.D., Grossman, E.L., Ambrose, W.G., Carroll, M.L., 2013. Carbonate clumped isotope compositions of modern marine mollusk and brachiopod shells. *Geochimica et Cosmochimica Acta* 106, 307–325. URL: <http://dx.doi.org/10.1016/j.gca.2012.12.020>, doi:10.1016/j.gca.2012.12.020.

- Hetenyi, G., Cattin, R., Brunet, F., Bollinger, L., Vergne, J., Nabelek, J., Diament, M., 2007. Density distribution of the India plate beneath the Tibetan Plateau: Geophysical and petrological constraints on the kinetics of lower-crustal eclogitization. *Earth and Planetary Science Letters* .
- van Hinsbergen, D.J.J., Kapp, P., Dupont-Nivet, G., Lippert, P.C., DeCelles, P.G., Torsvik, T.H., 2011. Restoration of Cenozoic deformation in Asia and the size of Greater India. *Tectonics* 30, TC5003. URL: <http://doi.wiley.com/10.1029/2011TC002908>, doi:10.1029/2011TC002908.
- van Hinsbergen, D.J.J., Lippert, P.C., Dupont-Nivet, G., McQuarrie, N., Doubrovine, P.V., Spakman, W., Torsvik, T.H., 2012. Greater India Basin hypothesis and a two-stage Cenozoic collision between India and Asia. *Proceedings of the National Academy of Sciences of the United States of America* 109, 7659–64. URL: <http://www.pnas.org/content/109/20/7659.short>, doi:10.1073/pnas.1117262109.
- Hofmann, A., 2014. Sampling mantle heterogeneity through oceanic basalts: isotopes and trace elements. Elsevier Ltd. doi:<http://dx.doi.org/10.1016/B0-08-043751-6/02123-X>.
- Hoke, G.D., Liu-Zeng, J., Hren, M.T., Wissink, G.K., Garzzone, C.N., 2014. Stable isotopes reveal high southeast Tibetan Plateau margin since the Paleogene. *Earth and Planetary Science Letters* 394, 270–278. URL: <http://www.sciencedirect.com/science/article/pii/S0012821X14001514>, doi:10.1016/j.epsl.2014.03.007.
- Holland, H., 1978. *The Chemistry of the Atmosphere and Oceans*. Wiley, New York.
- Hoppe, P., Cohen, S., Meibom, A., 2013. NanoSIMS: Technical Aspects and Applications in Cosmochemistry and Biological Geochemistry. *Geostandards and Geoanalytical Research* 37, 111–154. doi:10.1111/j.1751-908X.2013.00239.x.
- Hough, B., Fan, M., Passey, B., 2014. Calibration of the clumped isotope geothermometer in soil carbonate in Wyoming and Nebraska, USA: Implications for paleoelevation and paleoclimate reconstruction. *Earth and Planetary Science Letters* 391, 110–120. URL: <http://www.sciencedirect.com/science/article/pii/S0012821X14000119>.
- Houseman, G.A., McKenzie, D.P., Molnar, P., 1981. Convective instability of a thickened boundary layer and its relevance for the thermal evolution of continental convergent belts. *Journal of Geophysical Research: Solid Earth* (19782012) 86, 6115–6132. doi:10.1029/JB086iB07p06115.
- Hren, M., Bookhagen, B., Blisniuk, P., Booth, A., Chamberlain, C., 2009. $\delta^{18}\text{O}$ and δD of streamwaters across the Himalaya and Tibetan Plateau: Implications for moisture sources and paleoelevation reconstructions. *Earth and Planetary Science Letters* 288, 20–32.
- Hu, X., Garzanti, E., Moore, T., Raffi, I., 2015. Direct stratigraphic dating of India-Asia collision onset at the Selandian (middle Paleocene, 59–51 Ma). *Geology* 43, 859–862. URL: <http://geology.gsapubs.org/content/early/2015/08/21/G36872.1.abstract>, doi:10.1130/g36872.1.

- Hu, X., Wang, J., BouDagher-Fadel, M., Garzanti, E., An, W., 2016. New insights into the timing of the India-Asia collision from the Paleogene Quxia and Jialazi formations of the Xigaze forearc basin, South Tibet. *Gondwana Research* 32, 76–92. doi:10.1016/j.gr.2015.02.007.
- Huntington, K.W., Budd, D.A., Wernicke, B.P., Eiler, J.M., 2011. Use of Clumped-Isotope Thermometry To Constrain the Crystallization Temperature of Diagenetic Calcite. *Journal of Sedimentary Research* 81, 656–669. doi:10.2110/jsr.2011.51.
- Huntington, K.W., Eiler, J.M., Affek, H.P., Guo, W., Bonifacie, M., Yeung, L.Y., Thiagarajan, N., Passey, B., Tripathi, a., Daëron, M., Came, R., 2009. Methods and limitations of 'clumped' CO₂ isotope ($\Delta 47$) analysis by gas-source isotope ratio mass spectrometry. *Journal of mass spectrometry : JMS* 44, 1318–29. URL: <http://www.ncbi.nlm.nih.gov/pubmed/19621330>, doi:10.1002/jms.1614.
- Huntington, K.W., Saylor, J., Quade, J., Hudson, A.M., 2015. High late Miocene-Pliocene elevation of the Zhada Basin, southwestern Tibetan Plateau, from carbonate clumped isotope thermometry. *Geological Society of America Bulletin* 127, 181–199. URL: <http://gsabulletin.gsapubs.org/content/early/2014/08/07/B31000.1.abstract>, doi:10.1130/B31000.1.
- Huntington, K.W., Wernicke, B.P., Eiler, J.M., 2010. Influence of climate change and uplift on Colorado Plateau paleotemperatures from carbonate clumped isotope thermometry. *Tectonics* 29. URL: <http://doi.wiley.com/10.1029/2009TC002449>, doi:10.1029/2009TC002449.
- Ingalls, M., Colman, A., Rowley, D.B., 2016a. Can carbonate clumped isotopes be used in tectonically complex regions?, in: *Geological Society of America Annual Meeting*.
- Ingalls, M., Rowley, D.B., Currie, B., Colman, A.S., 2016b. Large-scale subduction of continental crust implied by IndiaAsia mass-balance calculation. *Nature Geoscience* 9, 848–853. URL: <http://www.nature.com/doi/10.1038/ngeo2806>, doi:10.1038/ngeo2806.
- Ingalls, M., Rowley, D.B., Olack, G., Currie, B.S., Li, S., Schmidt, J., Tremblay, M., Polissar, P.J., Shuster, D.L., Lin, D., Colman, A.S., 2017. Paleocene to Pliocene low-latitude high elevation of southern Tibet: Implications for tectonic models of India-Asia collision, Cenozoic climate, and geochemical weathering. *Geological Society of America Bulletin* .
- Ito, E., Deckker, P.D., Eggins, S.M., 2003. Ostracodes and their shell chemistry: Implications for paleohydrologic and paleoclimatologic applications. *Paleontological Society Papers* 9, 119–151.
- Ivany, L., Lohmann, K.C., Patterson, W., 2003. Paleogene Temperature History of the U.S. Gulf Coastal Plain Inferred from d_{18O} of Fossil Otoliths, in: *From Greenhouse to Icehouse: The Marine Eocene-Oligocene Transition*, pp. 232–251.

- Jain, A., Lal, N., Sulemani, B., Awasthi, A., Singh, S., Kumar, R., Kumar, D., 2009. Detrital-zircon fission-track ages from the Lower Cenozoic sediments, NW Himalayan foreland basin: Clues for exhumation and denudation of the Himalaya during the India-Asia collision. *Geological Society of America Bulletin* 121, 519–535. URL: <http://gsabulletin.gsapubs.org/content/121/3-4/519.short>, doi:10.1130/B26304.1.
- Janssen, C., Wenk, H.R., Wirth, R., Morales, L., Kemnitz, H., Sulem, J., Dresen, G., 2016. Microstructures and their implications for faulting processes -Insights from DGLab core samples from the Gulf of Corinth. *Journal of Structural Geology* 86, 62–74. URL: <http://dx.doi.org/10.1016/j.jsg.2016.03.008>, doi:10.1016/j.jsg.2016.03.008.
- Kalnay, E., Kanamitsu, M., Kistler, R., Collins, W., Deaven, D., Gandin, L., Iredell, M., Saha, S., White, G., Woollen, J., Zhu, Y., Chelliah, M., Ebisuzaki, W., Higgins, W., Janowiak, J., Mo, K., Ropelewski, C., Wang, J., Leetmaa, A., Reynolds, R., Jenne, R., D., J., 1996. The NCEP/NCAR 40-Year Reanalysis Project. *Bulletin of the American Meteorological Society* 77, 437–471.
- Kapp, P., DeCelles, P.G., Leier, A.L., Fabijanic, J.M., He, S., Pullen, A., Gehrels, G.E., Ding, L., 2007. The Gangdese retroarc thrust belt revealed. *GSA Today* 17, 4–9. doi:10.1130/GSAT01707A.1.
- Kapp, P., Murphy, M.A., Yin, A., Harrison, T.M., Ding, L., Guo, J., 2003. Mesozoic and Cenozoic tectonic evolution of the Shiquanhe area of western Tibet. *Tectonics* 22. doi:10.1029/2001TC001332.
- Keating-Bitonti, C.R., Ivany, L.C., Affek, H.P., Douglas, P., Samson, S.D., 2011. Warm, not super-hot, temperatures in the early Eocene subtropics. *Geology* 39, 771–774. URL: <http://geology.gsapubs.org/content/39/8/771.abstract>, doi:10.1130/G32054.1.
- Keith, M., Weber, J., 1965. Systematic relationships between carbon and oxygen isotopes in carbonates deposited by modern corals and algae. *Science* 150, 498–501.
- Kerrick, D., Caldeira, K., 1993. Paleatmospheric consequences of CO₂ released during early Cenozoic regional metamorphism in the Tethyan orogen. *Chemical Geology* 108, 201–230.
- Khan, M.A., Spicer, R.A., Bera, S., Ghosh, R., Yang, J., Spicer, T.E., Guo, S.x., Su, T., Jacques, F., Grote, P.J., 2014. Miocene to Pleistocene floras and climate of the Eastern Himalayan Siwaliks, and new palaeoelevation estimates for the NamlingOiyug Basin, Tibet. *Global and Planetary Change* 113, 1–10. URL: <http://www.sciencedirect.com/science/article/pii/S0921818113002749>, doi:10.1016/j.gloplacha.2013.12.003.
- Kim, S.T., O’Neil, J.R., 1997. Equilibrium and nonequilibrium oxygen isotope effects in synthetic carbonates. *Geochimica et Cosmochimica Acta* 61, 3461–3475. URL: <http://linkinghub.elsevier.com/retrieve/pii/S0016703797001695>, doi:10.1016/S0016-7037(97)00169-5.
- Klootwijk, C.T., Bingham, D.K., 1980. The extent of greater India, III. Palaeomagnetic data from the Tibetan Sedimentary series, Thakkhola region, Nepal Himalaya. *Earth and*

- Planetary Science Letters 51, 381–405. URL: <http://www.sciencedirect.com/science/article/pii/S0012821X80902198>, doi:10.1016/0012-821X(80)90219-8.
- Kobashi, T., Grossman, E.L., Yancey, T.E., Dockery, D.T., 2001. Reevaluation of conflicting Eocene tropical temperature estimates: Molluskan oxygen isotope evidence for warm low latitudes. *Geology* 29, 983–986. doi:10.1130/0091-7613(2001)029<0983:ROCETT>2.0.CO.
- Koppers, A., 2002. ArArCALC - software for Ar-40/Ar-39 age calculations. *Computers and Geosciences* 28, 605–619.
- Kornfeld, D., Eckert, S., Appel, E., Ratschbacher, L., Sonntag, B.L., Pfänder, J.A., Ding, L., Liu, D., 2014. Cenozoic clockwise rotation of the Tengchong block, southeastern Tibetan Plateau: A paleomagnetic and geochronologic study. *Tectonophysics* 628, 105–122. URL: <http://www.sciencedirect.com/science/article/pii/S0040195114002133>, doi:10.1016/j.tecto.2014.04.032.
- Kump, L., Brantley, S., Arthur, M., 2000. Chemical weathering, atmospheric CO₂, and climate. *Annual Review of Earth and Planetary Sciences* 28, 611–667.
- Kutzbach, J.E., Guetter, P.J., Ruddiman, W.F., Prell, W.L., 1989. Sensitivity of climate to late Cenozoic uplift in southern Asia and the American west: Numerical experiments. *Journal of Geophysical Research* 94, 18393. doi:10.1029/JD094iD15p18393.
- Laske, G., Masters, G., Ma, Z., Pasyanos, M., 2013. Update on CRUST1.0 - A 1-degree Global Model of Earth's Crust, in: European Geophysical Union, Geophysical Research Abstracts. URL: <http://meetingorganizer.copernicus.org/EGU2013/EGU2013-2658.pdf>.
- Lawrimore, J., Menne, M., Gleason, B., Williams, C., Wuertz, D., Vose, R., Rennie, J., 2011. An overview of the Global Historical Climatology Network monthly mean temperature data set, version 3. *Journal of Geophysical Research* 116. doi:10.1029/2011JD016187.
- Le Pichon, X., Fournier, M., Jolivet, L., 1992. Kinematics, topography, shortening, and extrusion in the IndiaEurasia collision. *Tectonics* 11, 1085–1098. URL: <http://onlinelibrary.wiley.com/doi/10.1029/92TC01566/full>.
- Leary, R., Orme, D.A., Laskowski, A.K., DeCelles, P.G., Kapp, P., Carrapa, B., Dettinger, M., 2016. Along-strike diachroneity in deposition of the Kailas Formation in central southern Tibet: Implications for Indian slab dynamics. *Geosphere* 12, 1198–1223. URL: <http://geosphere.gsapubs.org/content/12/4/1198.abstract>, doi:10.1130/GES01325.1.
- Lee, C., 2014. Physics and chemistry of deep continental crust recycling, in: *Treatise on Geochemistry*. 4 ed.. Elsevier Ltd, pp. 423–456.
- Lee, H., Chung, S., Wang, Y., Zhu, D., Yang, J., Song, B., Liu, D., Wu, F., 2007. Age, petrogenesis and geological significance of the Linzizong volcanic successions in the Linzhou

- basin, southern Tibet: Evidence from zircon U-Pb dates and Hf isotopes. *ACTA PETROLOGICA SINICA* 23, 493–500. URL: [\http://ntur.lib.ntu.edu.tw/handle/246246/206245](http://ntur.lib.ntu.edu.tw/handle/246246/206245){\#}.VXXi8FnBzGc.
- Lee, H.Y., Chung, S.L., Lo, C.H., Ji, J., Lee, T.Y., Qian, Q., Zhang, Q., 2009. Eocene Neotethyan slab breakoff in southern Tibet inferred from the Linzizong volcanic record. *Tectonophysics* 477, 20–35. doi:10.1016/j.tecto.2009.02.031.
- Leech, M., Singh, S., Jain, A., Klemperer, S., Manickavasagam, R., 2005. The onset of IndiaAsia continental collision: Early, steep subduction required by the timing of UHP metamorphism in the western Himalaya. *Earth and Planetary Science Letters* 234, 83–97. URL: [\http://www.sciencedirect.com/science/article/pii/S0012821X05001573](http://www.sciencedirect.com/science/article/pii/S0012821X05001573), doi:10.1016/j.epsl.2005.02.038.
- Lefebvre, C., Barnhoorn, A., van Hinsbergen, D.J.J., Kaymakci, N., Vissers, R.L.M., 2011. Late Cretaceous extensional denudation along a marble detachment fault zone in the Kirsehir massif near Kaman, central Turkey. *Journal of Structural Geology* 33, 1220–1236. doi:10.1016/j.jsg.2011.06.002.
- Leier, A., Quade, J., DeCelles, P., Kapp, P., 2009. Stable isotopic results from paleosol carbonate in South Asia: Paleoenvironmental reconstructions and selective alteration. *Earth and Planetary Science Letters* 279, 242–254. URL: [\http://www.sciencedirect.com/science/article/pii/S0012821X09000120](http://www.sciencedirect.com/science/article/pii/S0012821X09000120), doi:10.1016/j.epsl.2008.12.044.
- Leier, A.L., DeCelles, P.G., Kapp, P., Ding, L., 2007. The Takena Formation of the Lhasa terrane, southern Tibet: The record of a Late Cretaceous retroarc foreland basin. *Geological Society of America Bulletin* 119, 31–48. URL: [\http://gsabulletin.gsapubs.org/content/119/1-2/31.abstract](http://gsabulletin.gsapubs.org/content/119/1-2/31.abstract), doi:10.1130/B25974.1.
- Leloup, P.H., Lacassin, R., Tapponnier, P., Schärer, U., Zhong, D., Liu, X., Zhang, L., Ji, S., Trinh, P.T., 1995. The Ailao Shan-Red River shear zone (Yunnan, China), Tertiary transform boundary of Indochina. *Tectonophysics* 251, 3–84. URL: [\http://www.sciencedirect.com/science/article/pii/0040195195000704](http://www.sciencedirect.com/science/article/pii/0040195195000704), doi:10.1016/0040-1951(95)00070-4.
- Li, C., van der Hilst, R.D., Meltzer, A.S., Engdahl, E.R., 2008. Subduction of the Indian lithosphere beneath the Tibetan Plateau and Burma. *Earth and Planetary Science Letters* 274, 157–168. URL: [\http://linkinghub.elsevier.com/retrieve/pii/S0012821X08004500](http://linkinghub.elsevier.com/retrieve/pii/S0012821X08004500), doi:10.1016/j.epsl.2008.07.016.
- Li, C., Yanai, M., 1996. The Onset and Interannual Variability of the Asian Summer Monsoon in Relation to Land-Sea Thermal Contrast. *Journal of Climate* 9, 358–375. doi:10.1175/1520-0442(1996)009<0358:T0AIV0>2.0.CO;2.
- Li, S., Currie, B.S., Rowley, D.B., Ingalls, M., 2015. Cenozoic paleoaltimetry of the SE margin of the Tibetan Plateau: Constraints on the tectonic evolution of the region. *Earth and Planetary Science Letters* 432, 415–424. URL: [\http://dx.doi.org/10.1016/j.epsl.2015.09.044](http://dx.doi.org/10.1016/j.epsl.2015.09.044), doi:10.1016/j.epsl.2015.09.044.

- Licht, A., Van Cappelle, M., Abels, H.A., Ladant, J.B., Trabucho-Alexandre, J., France-Lanord, C., Donnadieu, Y., Vandenberghe, J., Rigaudier, T., Lécuyer, C., 2014. Asian monsoons in a late Eocene greenhouse world. *Nature* 513, 501–506.
- Liu, J., Song, X., Yuan, G., Sun, X., Yang, L., 2014. Stable isotopic compositions of precipitation in China. *Tellus* 66.
- Mack, G., Rasmussen, K., 1984. Alluvial-fan sedimentation of the Cutler Formation (Permian-Pennsylvanian) near Gateway, Colorado. *Geological Society of America Bulletin* 95, 109 LP – 116. URL: <http://gsabulletin.gsapubs.org/content/95/1/109.abstract>.
- Mack, G.H., 1992. Paleosols as an Indicator of Climatic Change at the Early-Late Cretaceous Boundary, Southwestern New Mexico. *Journal of Sedimentary Research* Vol. 62, 483–494. doi:10.1306/D426792E-2B26-11D7-8648000102C1865D.
- Mack, G.H., James, W., Monger, H., 1993. Classification of paleosols. *Geological Society of America Bulletin* 105, 129–136.
- Marshall, D.J., 1988. *Cathodoluminescence of Geological Materials*. Unwin Hyman Boston etc., Boston.
- Matte, P., Mattauer, M., Olivet, J.M., Griot, D.A., 1997. Continental subductions beneath Tibet and the Himalayan orogeny: a review. *Terra Nova* 9, 264–270. URL: <http://doi.wiley.com/10.1111/j.1365-3121.1997.tb00026.x>, doi:10.1111/j.1365-3121.1997.tb00026.x.
- McKenzie, D., 1969. Speculations on the consequences and causes of plate motions. *Geophysical Journal of the Royal Astronomical Society* 18, 1–32.
- McKenzie, D., Priestley, K., 2008. The influence of lithospheric thickness variations on continental evolution. *Lithos* 102, 1–11. doi:10.1016/j.lithos.2007.05.005.
- Métivier, F., Gaudemer, Y., Tapponnier, P., Klein, M., 1999. Mass accumulation rates in Asia during the Cenozoic, 280–318.
- Métivier, F., Gaudemer, Y., Tapponnier, P., Klein, M., 2002. Mass accumulation rates in Asia during the Cenozoic. *Geophysical Journal International* 137, 280–318. URL: <http://gji.oxfordjournals.org/content/137/2/280.short>, doi:10.1046/j.1365-246X.1999.00802.x.
- Miller, K.G., Fairbanks, R.G., Mountain, G.S., 1987. Tertiary oxygen isotope synthesis, sea level history, and continental margin erosion. *Paleoceanography* 2, 1–19. doi:10.1029/PA002i001p00001.
- Misra, S., Froelich, P.N., 2012. Lithium isotope history of Cenozoic seawater: changes in silicate weathering and reverse weathering. *Science* 335, 818–823.
- Mo, X., Niu, Y., Dong, G., Zhao, Z., Hou, Z., Zhou, S., Ke, S., 2008. Contribution of syn-collisional felsic magmatism to continental crustal growth: A case study of the Paleogene Linzizong volcanic succession in southern Tibet. *Chemical Geology* 250, 49–67.

- Molnar, P., England, P., Martinod, J., 1993. Mantle dynamics, uplift of the Tibetan Plateau, and the Indian Monsoon. *Reviews of Geophysics* 31, 357. URL: <http://doi.wiley.com/10.1029/93RG02030>, doi:10.1029/93RG02030.
- Molnar, P., Stock, J.M., 2009. Slowing of India's convergence with Eurasia since 20 Ma and its implications for Tibetan mantle dynamics. *Tectonics* 28, n/a–n/a. URL: <http://doi.wiley.com/10.1029/2008TC002271>, doi:10.1029/2008TC002271.
- Monger, H.C., Daugherty, L.A., Lindemann, W.C., 1991. Microbial precipitation of pedogenic calcite. doi:10.1130/0091-7613(1991)019<0997:MPOPC>2.3.CO;2.
- Monger, H.C., Gallegos, R.A., 2000. Biotic and abiotic processes and rates of pedogenic carbonate accumulation in the southwestern United States - relationship to atmospheric CO₂ sequestration, in: Lal, R., Kimble, J.M., Eswaran, H., Stewart, B. (Eds.), *Global Climate Change and Pedogenic Carbonates*. June. chapter 17, pp. 273–289.
- Moreno-Azanza, M., Bauluz, B., Canudo, J.I., Gasca, J.M., Torcida Fernández-Baldor, F., 2016. Combined Use of Electron and Light Microscopy Techniques Reveals False Secondary Shell Units in Megaloolithidae Eggshells. *PLoS ONE* 11, e0153026. URL: <http://dx.doi.org/10.1371/journal.pone.0153026>, doi:10.1371/journal.pone.0153026.
- Munnecke, A., Westphal, H., Reijmer, J.J.G., Samtleben, C., 1997. Microspar development during early marine burial diagenesis: A comparison of Pliocene carbonates from the Bahamas with Silurian limestones from Gotland (Sweden). *Sedimentology* 44, 977–990. doi:10.1111/j.1365-3091.1997.tb02173.x.
- Murphy, M.A., Yin, A., Harrison, T.M., Dürr, S.B., Z, C., Ryerson, F.J., Kidd, W.S.F., X, W., X, Z., Dürr, S.B., Z, C., Ryerson, F.J., Kidd, W.S.F., X, W., X, Z., 1997. Did the Indo-Asian collision alone create the Tibetan plateau? *Geology* 25, 719. URL: <http://geology.gsapubs.org/content/25/8/719.abstract>[http://geology.gsapubs.org/cgi/doi/10.1130/0091-7613\(1997\)025\(0719:DTIACA\)3E2.3.CO;2](http://geology.gsapubs.org/cgi/doi/10.1130/0091-7613(1997)025(0719:DTIACA)3E2.3.CO;2), doi:10.1130/0091-7613(1997)025<0719:DTIACA>2.3.CO;2.
- Nabelek, J., Hetenyi, G., Vergne, J., Sapkota, S., Kafle, B., Jiang, M., Su, H., Chen, J., Huang, B.S., Team, H.C., 2009. Underplating in the Himalaya-Tibet collision zone revealed by the Hi-CLIMB experiment. *Science* 325, 1371–1374.
- Najman, Y., Appel, E., Boudagher-Fadel, M., Bown, P., Carter, A., Garzanti, E., Godin, L., Han, J., Liebke, U., Oliver, G., Parrish, R., Vezzoli, G., 2010. Timing of India-Asia collision: Geological, biostratigraphic, and palaeomagnetic constraints. *Journal of Geophysical Research* 115, B12416. URL: <http://doi.wiley.com/10.1029/2010JB007673>, doi:10.1029/2010JB007673.
- Najman, Y., Carter, A., Oliver, G., Garzanti, E., 2005. Provenance of Eocene foreland basin sediments, Nepal: Constraints to the timing and diachroneity of early Himalayan orogenesis. *Geology* 33, 309. URL: <http://geology.gsapubs.org/content/33/4/309.short>, doi:10.1130/G21161.1.

- Najman, Y., Garzanti, E., 2000. Reconstructing early Himalayan tectonic evolution and paleogeography from Tertiary foreland basin sedimentary rocks, northern India. *Geological Society of America Bulletin* 112, 435–449. URL: <http://gsabulletin.gsapubs.org/content/112/3/435.short>, doi:10.1130/0016-7606(2000)112.
- O'Brien, P.J., 2000. The fundamental Variscan problem: high temperature metamorphism at different depths and high pressure metamorphism at different temperatures, in: Franke, W., Haak, V., Oncken, O., Tanner, D. (Eds.), *Orogenic Process: Quantification and Modelling in the Variscan Belt*. The Geological Society of London, London, pp. 369–386.
- Orme, D.A., 2015. Basin evolution and exhumation of the Xigaze forearc and Indus-Yarlung suture zone, Tibet. Dissertation. University of Arizona. URL: <http://search.proquest.com/docview/1719260649/previewPDF/27F90D95281246A2PQ/1?accountid=14657>.
- Orme, D.A., Carrapa, B., Kapp, P., 2014. Sedimentology, provenance and geochronology of the upper Cretaceous-lower Eocene western Xigaze forearc basin, southern Tibet. *Basin Research*, 1–25 URL: <http://doi.wiley.com/10.1111/bre.12080>, doi:10.1111/bre.12080.
- Orme, D.A., Laskowski, A.K., 2016. Basin Analysis of the Albian–Santonian Xigaze Forearc, Lazi Region, South-Central Tibet. *Journal of Sedimentary Research* 86, 894–913. doi:10.2110/jsr.2016.59.
- Palmer, M., Edmond, J., 1989. The strontium isotope budget of the modern ocean. *Earth and Planetary Science Letters* 92, 11–26.
- Palmer, M., Edmond, J., 1992. Controls over the strontium isotope composition of river water. *Geochimica et Cosmochimica Acta* 56, 2099–2111.
- Passey, B.H., Henkes, G.A., 2012. Carbonate clumped isotope bond reordering and geospeedometry. *Earth and Planetary Science Letters* 351–352, 223–236. URL: <http://www.sciencedirect.com/science/article/pii/S0012821X12003883><http://linkinghub.elsevier.com/retrieve/pii/S0012821X12003883>, doi:10.1016/j.epsl.2012.07.021.
- Passey, B.H., Levin, N.E., Cerling, T.E., Brown, F.H., Eiler, J.M., 2010. High-temperature environments of human evolution in East Africa based on bond ordering in paleosol carbonates. *Proceedings of the National Academy of Sciences of the United States of America* 107, 11245–9. URL: <http://www.pubmedcentral.nih.gov/articlerender.fcgi?artid=2895143&tool=pmcentrez&rendertype=abstract><http://www.pnas.org/content/107/25/11245.short>, doi:10.1073/pnas.1001824107.
- Pearson, P.N., Ditchfield, P.W., Singano, J., Harcourt-Brown, K.G., Nicholas, C.J., Olsson, R.K., Shackleton, N.J., Hall, M.A., 2001. Warm tropical sea surface temperatures in the Late Cretaceous and Eocene epochs. *Nature* 413, 481–7. URL: <http://dx.doi.org/10.1038/35097000>, doi:10.1038/35097000.

- Peters, N.a., Huntington, K.W., Hoke, G.D., 2013. Hot or not? Impact of seasonally variable soil carbonate formation on paleotemperature and O-isotope records from clumped isotope thermometry. *Earth and Planetary Science Letters* 361, 208–218. URL: <http://linkinghub.elsevier.com/retrieve/pii/S0012821X12005869>, doi:10.1016/j.epsl.2012.10.024.
- Polissar, P.J., Freeman, K.H., 2010. Effects of aridity and vegetation on plant-wax δD in modern lake sediments. *Geochimica et Cosmochimica Acta* 74, 5785–5797. URL: <http://dx.doi.org/10.1016/j.gca.2010.06.018>, doi:10.1016/j.gca.2010.06.018.
- Polissar, P.J., Freeman, K.H., Rowley, D.B., McInerney, F.a., Currie, B.S., 2009. Paleoaltimetry of the Tibetan Plateau from D/H ratios of lipid biomarkers. *Earth and Planetary Science Letters* 287, 64–76. URL: <http://linkinghub.elsevier.com/retrieve/pii/S0012821X09004531><http://www.sciencedirect.com/science/article/pii/S0012821X09004531>, doi:10.1016/j.epsl.2009.07.037.
- Powell, C., Roots, S., Veevers, J., 1988. Pre-breakup continental extension in East Gondwanaland and the early opening of the eastern Indian Ocean. *Tectonophysics* 155, 261–283. URL: <http://www.sciencedirect.com/science/article/pii/0040195188902697>, doi:10.1016/0040-1951(88)90269-7.
- Quade, J., Breecker, D.O., Daeron, M., Eiler, J.M., 2011. The paleoaltimetry of Tibet: An isotopic perspective. *American Journal of Science* 311, 77–115.
- Quade, J., Cater, J.M., Ojha, T.P., Adam, J., Mark Harrison, T., 1995. Late Miocene environmental change in Nepal and the northern Indian subcontinent: Stable isotopic evidence from paleosols. *Geological Society of America Bulletin* 107, 1381–1397. URL: <http://gsabulletin.gsapubs.org/content/107/12/1381.abstract>, doi:10.1130/0016-7606(1995)107.
- Quade, J., Cerling, T.E., 1995. Expansion of C4 grasses in the late Miocene of northern Pakistan: Evidence from stable isotopes in paleosols. *Palaeogeography, Palaeoclimatology, Palaeoecology* 115, 91–116.
- Quade, J., Cerling, T.E., Bowman, J.R., 1989. Development of Asian monsoon revealed by marked ecological shift during the latest Miocene in northern Pakistan. *Nature* 342, 163–165. doi:10.1038/340301a0, [arXiv:nature.vol.342.30nov1989](https://arxiv.org/abs/nature.vol.342.30nov1989).
- Quade, J., Eiler, J., Daëron, M., Achyuthan, H., 2013. The clumped isotope geothermometer in soil and paleosol carbonate. *Geochimica et Cosmochimica Acta* 105, 92–107. URL: <http://linkinghub.elsevier.com/retrieve/pii/S0016703712006849><http://www.sciencedirect.com/science/article/pii/S0016703712006849>, doi:10.1016/j.gca.2012.11.031.
- Quade, J., Garzzone, C., Eiler, J., 2007. Paleoelevation reconstruction using pedogenic carbonates. *Reviews in Mineralogy and Geochemistry* 66, 53–87.

- Ratschbacher, L., Frisch, W., Chen, C., Pan, G., 1992. Deformation and motion along the southern margin of the Lhasa block (Tibet) prior to and during the India-Asia collision. *Journal of Geodynamics* 16, 21–54. doi:10.1016/0264-3707(92)90017-M.
- Raymo, M., Ruddiman, W., 1992. Tectonic forcing of late Cenozoic climate. *Nature* 359, 117–122.
- Raymo, M., Ruddiman, W., Froelich, P.N., 1988. Influence of late Cenozoic mountain building on ocean geochemical cycles. *Geology* 16, 649–653.
- Replumaz, A., Tapponnier, P., 2003. Reconstruction of the deformed collision zone between India and Asia by backward motion of lithospheric blocks. *Journal of Geophysical Research Solid Earth* 108.
- Richter, F., Rowley, D., DePaolo, D., 1992. Sr isotope evolution of seawater: the role of tectonics. *Earth and Planetary Science Letters* 109, 11–23. URL: <http://www.sciencedirect.com/science/article/pii/0012821X9290070C>.
- Ringham, M.C., Hoke, G.D., Huntington, K.W., Aranibar, J.N., 2016. Influence of vegetation type and site-to-site variability on soil carbonate clumped isotope records, Andean piedmont of Central Argentina (32–34S). *Earth and Planetary Science Letters* 440, 1–11.
- Robinson, R.A., Brezina, C.A., Parrish, R.R., Horstwood, M.S., Bird, M.I., Walters, A.S., Oliver, G.J., 2014. Large rivers and orogens: The evolution of the Yarlung TsangpoIrrawaddy system and the eastern Himalayan syntaxis. *Gondwana Research* 26, 112–121. URL: <http://www.sciencedirect.com/science/article/pii/S1342937X13002281>, doi:10.1016/j.gr.2013.07.002.
- Roca, J.R., Wansard, G., 1997. Temperature influence on development and calcification of *Herpetocypris brevicaudata* Kaufmann, 1900 (Crustacea: Ostracoda) under experimental conditions. *Hydrobiologia* 347, 91–95. doi:10.1023/A:1003067218024.
- Roddaz, M., Said, A., Guillot, S., Antoine, P.O., Montel, J.M., Martin, F., Darrozes, J., 2011. Provenance of Cenozoic sedimentary rocks from the Sulaiman fold and thrust belt, Pakistan: implications for the palaeogeography of the Indus drainage system. *Journal of the Geological Society* 168, 499–516. URL: <http://jgs.lyellcollection.org/content/168/2/499.short>, doi:10.1144/0016-76492010-100.
- Rowley, D., 1996. Age of initiation of collision between India and Asia: A review of stratigraphic data. *Earth and Planetary Science Letters* 145, 1–13. URL: <http://www.sciencedirect.com/science/article/pii/S0012821X96002014>.
- Rowley, D.B., 1998. Minimum Age of Initiation of Collision Between India and Asia North of Everest Based on the Subsidence History of the Zhepure Mountain Section. *The Journal of Geology* 106, 220–235. URL: <http://www.jstor.org/stable/10.1086/516018>, doi:10.1086/516018.

- Rowley, D.B., 2007. Stable Isotope-Based Paleoaltimetry: Theory and Validation. *Reviews in Mineralogy and Geochemistry* 66, 23–52. URL: <http://rimg.geoscienceworld.org/content/66/1/23.abstract>, doi:10.2138/rmg.2007.66.2.
- Rowley, D.B., Currie, B.S., 2006. Palaeo-altimetry of the late Eocene to Miocene Lunpola basin, central Tibet. *Nature* 439, 677–81. URL: <http://www.ncbi.nlm.nih.gov/pubmed/16467830><http://dx.doi.org/10.1038/nature04506>, doi:10.1038/nature04506.
- Rowley, D.B., Garzione, C.N., 2007. Stable Isotope-Based Paleoaltimetry. *Annual Review of Earth and Planetary Sciences* 35, 463–508. URL: <http://www.annualreviews.org/doi/abs/10.1146/annurev.earth.35.031306.140155>, doi:10.1146/annurev.earth.35.031306.140155.
- Rowley, D.B., Pierrehumbert, R.T., Currie, B.S., 2001. A new approach to stable isotope-based paleoaltimetry: implications for paleoaltimetry and paleohypsometry of the High Himalaya since the Late Miocene. *Earth and Planetary Science Letters* 5836, 1–17. doi:10.1016/S0012-821X(01)00324-7.
- Rozanski, K., Araguas-Araguas, L., Gonfiantini, R., 1993. Isotopic patterns in modern global precipitation, in: *Climate Change in Continental Isotopic Records*. American Geophysical Union, Washington, D. C., pp. 1–36. doi:10.1029/GM078p0001.
- Ruddiman, W.F., Kutzbach, J.E., 1989. Forcing of late Cenozoic northern hemisphere climate by plateau uplift in southern Asia and the American west. *Journal of Geophysical Research* 94, 18409. doi:10.1029/JD094iD15p18409.
- Saunders A, Norry M, Tarney J, 1988. Origin of MORB and Chemically-Depleted Mantle Reservoirs: Trace Element Constraints. *Journal of Petrology* , 415–445.
- Saylor, J.E., Quade, J., Dettman, D.L., DeCelles, P.G., Kapp, P.a., Ding, L., 2009. The late Miocene through present paleoelevation history of southwestern Tibet. *American Journal of Science* 309, 1–42. URL: <http://www.ajsonline.org/cgi/doi/10.2475/01.2009.01>, doi:10.2475/01.2009.01.
- Schmidt, J.L., Zeitler, P.K., Pazzaglia, F.J., Tremblay, M.M., Shuster, D.L., Fox, M., 2015. Knickpoint evolution on the Yarlung river: Evidence for late Cenozoic uplift of the southeastern Tibetan plateau margin. *Earth and Planetary Science Letters* 430, 448–457. URL: <http://dx.doi.org/10.1016/j.epsl.2015.08.041>, doi:10.1016/j.epsl.2015.08.041.
- Schnurrenberger, D., Russell, J., Kelts, K., 2003. Classification of lacustrine sediments based on sedimentary components. *Journal of Paleolimnology* 29, 141–154. doi:10.1023/A:1023270324800.
- Shenton, B.J., Grossman, E.L., Passey, B.H., Henkes, G.A., Becker, T.P., Laya, J.C., Perez-Huerta, A., Becker, S.P., Lawson, M., 2015. Clumped isotope thermometry in deeply buried sedimentary carbonates: The effects of bond reordering and recrystallization. *Bulletin of the Geological Society of America* 127, 1036–1051. doi:10.1130/B31169.1.

- Snell, K.E., Eiler, J.M., Dettman, D.L., Grotzinger, J., Koch, P.L., 2012. Evaluating the Geochemical Consequences of Aragonite-to-Aragonite Diagenesis in Freshwater Fossil Bivalves. AAPG Annual Meeting URL: <http://resolver.caltech.edu/CaltechAUTHORS:20130814-153842490papers2://publication/uuid/E809CE7C-4E06-471A-AEF3-6D0086923DD9>.
- Snell, K.E., Koch, P.L., Druschke, P., Foreman, B.Z., Eiler, J.M., 2014. High elevation of the 'Nevadaplano' during the Late Cretaceous. *Earth and Planetary Science Letters* 386, 52–63.
- Snell, K.E., Thrasher, B.L., Eiler, J.M., Koch, P.L., Sloan, L.C., Tabor, N.J., 2013. Hot summers in the Bighorn Basin during the early Paleogene. *Geology* 41, 55–58. URL: <http://geology.gsapubs.org/content/41/1/55.abstract>, doi:10.1130/G33567.1.
- Solomon, S., Walkden, G., 1985. the Application of Cathodoluminescence To Interpreting the Diagenesis of an Ancient Calcrete Profile. *Sedimentology* 32, 877–896. URL: <file:///Users/KatiesLaptop/Dropbox/documents/Papers2/Articles/1985/SOLOMON/SOLOMONSedimentology1985.pdf>{\%}0Apapers2://publication/uuid/AA7BF875-76C4-4DD8-93D7-331239857C71.
- Spicer, R.A., Harris, N.B.W., Widdowson, M., Herman, A.B., Guo, S., Valdes, P.J., Wolfe, J.A., Kelley, S.P., 2003. Constant elevation of southern Tibet over the past 15 million years. *Nature* 421, 622–4. URL: <http://dx.doi.org/10.1038/nature01356>, doi:10.1038/nature01356.
- St-Onge, M.R., Rayner, N., Palin, R.M., Searle, M.P., Waters, D.J., 2013. Integrated pressure-temperature-time constraints for the Tso Morari dome (Northwest India): implications for the burial and exhumation path of UHP units in the western Himalaya. *Journal of Metamorphic Geology* 31, 469–504. URL: <http://doi.wiley.com/10.1111/jmg.12030>, doi:10.1111/jmg.12030.
- Stolper, D.A., Eiler, J.M., 2015. The kinetics of solid-state isotope-exchange reactions for clumped isotopes: A study of inorganic calcites and apatites from natural and experimental samples. *American Journal of Science* 315, 363–411. doi:10.2475/05.2015.01.
- Stumm, W., Morgan, J., 1981. *Aquatic chemistry: an introduction emphasizing chemical equilibria in natural waters*. 2 ed., Wiley-Interscience, New York.
- Suarez, M.B., Passey, B.H., Kaakinen, A., 2011. Paleosol carbonate multiple isotopologue signature of active East Asian summer monsoons during the late Miocene and Pliocene. *Geology* 39, 1151–1154. URL: <http://geology.gsapubs.org/content/39/12/1151.abstract>, doi:10.1130/G32350.1.
- Tapponnier, P., Peltzer, G., Le Dain, A.Y., Armijo, R., Cobbold, P., 1982. Propagating extrusion tectonics in Asia: New insights from simple experiments with plasticine. *Geology* 10, 611–616. URL: <http://geology.gsapubs.org/content/10/12/611.short>, doi:10.1130/0091-7613(1982)10.

- Taylor, M.H., 2003. Conjugate strike-slip faulting along the Bangong-Nujiang suture zone accommodates coeval east-west extension and north-south shortening in the interior of the Tibetan Plateau. *Tectonics* 22, 7407–7407. URL: <http://www.agu.org/pubs/crossref/2003/2002TC001361.shtml>, doi:10.1029/2002TC001361.
- Tremblay, M., Fox, M., Schmidt, J., Tripathy-Lang, A., Wielicki, W., Harrison, T., Zeitler, P., Shuster, D.L., 2015. Erosion in Southern Tibet shut down at ~10 Ma due to enhanced rock uplift within the Himalaya. *Proceedings of the National Academy of Sciences* 112, 12030–12035.
- Urey, H., 1952. *The Planets: Their Origin and Development*. Yale University Press, New Haven.
- VanDeVelde, J.H., Bowen, G.J., Passey, B.H., Bowen, B.B., 2013. Climatic and diagenetic signals in the stable isotope geochemistry of dolomitic paleosols spanning the PaleoceneEocene boundary. *Geochimica et Cosmochimica Acta* 109, 254–267. doi:10.1016/j.gca.2013.02.005.
- Vasconcelos, C., McKenzie, J.A., Warthmann, R., Bernasconi, S.M., 2005. Calibration of the d18O paleothermometer for dolomite precipitated in microbial cultures and natural environments. *Geology* 33, 317–320. doi:10.1130/G20992.1.
- van der Voo, R., Spakman, W., Bijwaard, H., 1999. Tethyan subducted slabs under India. *Earth and Planetary Science Letters* 171, 7–20.
- Wan, X., Wang, L., Wang, C., Luba, J., 1998. Discovery and significance of Cretaceous fossils from the Xigaze Forearc Basin, Tibet. *Journal of Asian Earth Sciences* 16, 217–223. doi:10.1016/S0743-9547(98)00012-9.
- Wang, C., Dai, J., Zhao, X., Li, Y., Graham, S.A., He, D., Ran, B., Meng, J., 2014. Outward-growth of the Tibetan Plateau during the Cenozoic: A review. *Tectonophysics* 621, 1–43. URL: <http://www.sciencedirect.com/science/article/pii/S0040195114000729>, doi:10.1016/j.tecto.2014.01.036.
- Wang, C., Li, X., Liu, Z., Li, Y., Jansa, L., Dai, J., Wei, Y., 2012. Revision of the Cretaceous-Paleogene stratigraphic framework, facies architecture and provenance of the Xigaze forearc basin along the Yarlung Zangbo suture zone. *Gondwana Research* 22, 415–433. doi:10.1016/j.gr.2011.09.014.
- Wang, J., Chen, Y., 1999. Sedimentary formation characteristics of hydrocarbon generation and oil exploration prospects of Wuyu basin in Tibet. *Petroleum Exploration and Development* 26, 14–17.
- Wang, J., Hu, X., Jansa, L., Huang, Z., 2011. Provenance of the Upper CretaceousEocene Deep-Water Sandstones in Sangdanlin, Southern Tibet: Constraints on the Timing of Initial India-Asia Collision. *The Journal of Geology* 119, 293–309. URL: <http://www.jstor.org/stable/10.1086/659145>, doi:10.1086/659145.

- Wang, Y., Deng, T., Biasatti, D., 2006. Ancient diets indicate significant uplift of southern Tibet after ca. 7 Ma. *Geology* 34, 309–312. doi:10.1130/G22254.1.
- Wilke, F.D., O'Brien, P.J., Gerdes, A., Timmerman, M.J., Sudo, M., Khan, M.A., 2010. The multistage exhumation history of the Kaghan Valley UHP series, NW Himalaya, Pakistan from U-Pb and $^{40}\text{Ar}/^{39}\text{Ar}$ ages. *European Journal of Mineralogy* 22, 703–719. URL: <http://eurjmin.geoscienceworld.org/content/22/5/703.short>, doi:10.1127/0935-1221/2010/0022-2051.
- Willems, H., Zhang, B., 1993. Cretaceous and Lower Tertiary Sediments of the Tibetan Tethys Himalaya in the Area of Gamba (South Tibet, PR China), in: Willems, H. (Ed.), *Geoscientific investigations in the Tethyan Himalayas*. Universitat Bremen, Bremen, pp. 3–27.
- Wittlinger, G., Farra, V., Hetenyi, G., Vergne, J., Nabelek, J., 2009. Seismic velocities in southern Tibet lower crust: a receiver function approach for eclogite detection. *Geophysical Journal International* 177, 1037–1049.
- Wu, Z., Barosh, P.J., Zhonghai, W., Daogong, H., Xun, Z., Peisheng, Y., 2008. Vast early Miocene lakes of the central Tibetan plateau. *Bulletin of the Geological Society of America* 120, 1326–1337. doi:10.1130/B26043.1.
- Xia, J.B., 1983. Cenozoic of Baingoin and its borders, Xizang (Tibet), Contribution to the Geology of the Qinghai-Xizang Plateau 3, Ministry of Geology and Mineral Resources. Technical Report.
- Xu, Z., 1980. The Tertiary and its petroleum potential in the Lunpola Basin, Tibet. *Oil Gas Geology* 1, 153–158.
- Xu, Z., Zhao, J., Wu, Z., 1985. On the Tertiary continental basins and their petroleum potential in Qinghai-Xizang (Tibet) Plateau with Lunpola Basin as example, Contribution to Geology of Qinghai-Xizang (Tibet) Plateau. Technical Report.
- Yakovlev, P., Clark, M., 2014. Conservation and redistribution of crust during the IndoAsian collision. *Tectonics* 33, 1016–1027. URL: <http://onlinelibrary.wiley.com/doi/10.1002/2013TC003469/full>.
- Yin, A., Harrison, T.M., 2000. Geologic evolution of the Himalayan - Tibetan orogen. *Annual Review* 28, 211–280.
- Yuan, F., Sheng, Y., Yao, T., Fan, C., Li, J., Zhao, H., Lei, Y., 2011. Evaporative enrichment of oxygen-18 and deuterium in lake waters on the Tibetan Plateau. *Journal of Paleolimnology* 46, 291–307. doi:10.1007/s10933-011-9540-y.
- Zaarur, S., Affek, H.P., Brandon, M.T., 2013. A revised calibration of the clumped isotope thermometer. *Earth and Planetary Science Letters* 382, 47–57. URL: <http://linkinghub.elsevier.com/retrieve/pii/S0012821X13004019>, doi:10.1016/j.epsl.2013.07.026.

- Zaarur, S., Olack, G., Affek, H.P., 2011. Paleo-environmental implication of clumped isotopes in land snail shells. *Geochimica et Cosmochimica Acta* 75, 6859–6869. doi:10.1016/j.gca.2011.08.044.
- Zachos, J., Pagani, M., Sloan, L., Thomas, E., Billups, K., 2001. Trends, rhythms, and aberrations in global climate 65 Ma to Present. *Science* 292, 686–693.
- Zachos, J.C., Opdyke, B.N., Quinn, T.M., Jones, C.E., Halliday, A.N., 1999. Early cenozoic glaciation, antarctic weathering, and seawater $87\text{Sr}/86\text{Sr}$: is there a link? *Chemical Geology* 161, 165–180. URL: <http://www.sciencedirect.com/science/article/B6V5Y-3XNK494-9/2/0ddafe248b9dccbda1fcbb4277d9847>, doi:10.1016/S0009-2541(99)00085-6.
- Zhang, C.L., Horita, J., Cole, D.R., Zhou, J., Lovley, D.R., Phelps, T.J., 2001. Temperature-dependent oxygen and carbon isotope fractionations of biogenic siderite. *Geochimica et Cosmochimica Acta* 65, 2257–2271. doi:10.1016/S0016-7037(01)00596-8.
- Zhang, K., 2000. Cretaceous palaeogeography of Tibet and adjacent areas (China): tectonic implications. *Cretaceous Research* 21, 23–33. URL: <http://www.sciencedirect.com/science/article/pii/S019566710090199X>, doi:10.1006/cres.2000.0199.
- Zhang, P.Z., Shen, Z., Wang, M., Gan, W., Burgmann, R., Molnar, P., Wang, Q., Niu, Z., Sun, J., Wu, J., Hanrong, S., Xinzhao, Y., 2004. Continuous deformation of the Tibetan Plateau from global positioning system data. *Geology* 32, 809.
- Zhang, R., Jiang, D., Zhang, Z., Yu, E., 2015. The impact of regional uplift of the Tibetan Plateau on the Asian monsoon climate. *Palaeogeography, Palaeoclimatology, Palaeoecology* 417, 137–150. URL: <http://linkinghub.elsevier.com/retrieve/pii/S0031018214005458>, doi:10.1016/j.palaeo.2014.10.030.
- Zhou, S., Mo, X., Zhao, Z., Qiu, R., Niu, Y., Guo, T., Zhang, S., 2010. Biosynthetic origin of the saw-toothed profile in $\delta^{13}\text{C}$ and δD of n-alkanes and systematic isotopic differences between n-, iso- and anteiso-alkanes in leaf waxes of land plants. *Journal of Asian Earth Sciences* 37, 246–258.
- Zhu, B., Kidd, W., Rowley, D., Currie, B., Shafique, N., 2005. Age of Initiation of the IndiaAsia Collision in the EastCentral Himalaya. *The Journal of Geology* 113, 265–285. URL: <http://www.jstor.org/stable/10.1086/428805>, doi:10.1086/428805.
- Zhu, Y., Fang, X., Gao, J., Yi, H., Wang, S., Zhang, W., 2006. Oligo-Miocene depositional facies of the Wuyu basin, southern Tibetan Plateau. *Acta Sedimentologica Sinica* 24, 775–782.